Studies on Synthesis, Structural and Electrical Properties of Complex Oxide Thin Films: Ba1-xSrxTiO3 and La2-xSrxNiO4

Thesis Advisor | Author

Professor Shriram Ramanathan | **Adrian A. Podpirka**

Studies on Synthesis, Structural and Electrical Properties of Complex Oxide Thin Films: $Ba_{1-x}Sr_xTiO_3$ and $La_{2-x}Sr_xNiO_4$

Abstract

High performance miniaturized passives are of great importance for advanced nanoelectronic packages for several applications including efficient power delivery. Low cost thin film capacitors fabricated directly on package (and/or on-chip) are an attractive approach towards realizing such devices. This thesis aims to explore fundamental frequency dependent dielectric and insulating properties of thin film high-*k* dielectric constant in the perovskite and perovskite-related complex oxides. Throughout this thesis, we have successfully observed the role of structure, strain and oxygen stoichiometry on the dielectric properties of thin film complex oxides, allowing a greater understanding of processing conditions and polarization mechanisms.

In the first section of the thesis, we explore novel processing methods in the conventional ferroelectric, barium strontium titanate, $Ba_{1-x}Sr_xTiO_3$ (BST), using ultraviolet enhanced oxidation techniques in order to achieve improvements in the dielectric properties. Using this method, we also explore the growth of BST on inexpensive non-noble metals such as Ni which presents technical challenges due to the ability to oxidize at high temperatures. We observe a significant

lowering of the dielectric loss while also lowering the process temperature which allows us to maintain an intimate interface between the dielectric layer and the metal electrode.

The second section of this thesis explores the novel dielectric material, Lanthanum Strontium Nickelate, $La_{2-x}Sr_xNiO_4$ (LSNO), which exhibits a colossal dielectric response. For the first time, we report on the colossal dielectric properties of polycrystalline and epitaxial thin film LSNO. We observe a significant polarization dependence on the microstructure due to the grain/grain boundary interaction with charged carriers. We next grew epitaxial films on various insulating oxide substrates in order to decouple the grain boundary interaction. Here we observed substrate dependent dielectric properties associated with induced strain. We also observe, due to the *p*-type carriers in LSNO, *pn* junction formation when grown epitaxially on the conducting oxide degenerate *n*-type Nb-doped $SrTiO_3$. Finally we explore the growth mechanism of epitaxial LSNO as a function of high oxygen content. Due to the ability for LSNO to take in interstitial oxygen, a reoriented growth is observed at a critical thickness, thereby allowing us to vary anisotropy as a function of deposition conditions.

Table of Contents

Table of Figures

Published Work

A. Podpirka, B. Viswanath, and S. Ramanathan. Heteroepitaxy of $La_{1.875}Sr_{0.125}NiO_4$ thin films on $SrTiO_3$: orientation evolution and dielectric (under review).

A. Podpirka, A. Tselev and S. Ramanathan. Synthesis and frequency-dependent dielectric properties of epitaxial $La_{1.875}Sr_{0.125}NiO_4$ thin films. (under review).

S. D. Ha, M. Otaki, R. Jaramillo, **A. Podpirka** and S. Ramanathan. Stable metal-insulator transition in epitaxial SmNiO3 thin films, *Journal of Solid State Chemistry*, in press, 2012

A. Podpirka and S. Ramanathan. Heteroepitaxial $La_{2-x}Sr_xNiO_4$-Nb-doped SrTiO3 Junctions: Synthesis and Rectification Characteristics. *J. Electrochemical Society* **159**, H72 (2012).

M.W. Cole, R.C. Toonen, S.G. Hirsch, M. Ivill, E. Ngo, C. Hubbard, S.Ramanathan and **A. Podpirka**. An elegant post-growth process science protocol to improve the material properties of complex oxide thin films for tunable deivce applications. *Integrated Ferroelectrics* **126**[1] 34 (2011).

A. Podpirka, and S. Ramanathan. Thin film colossal dielectric constant oxide $La_{2-x}Sr_xNiO_4$: Synthesis, dielectric relaxation measurement and electrode effects. *Journal of Applied Physics* **109**, 014106 (2011).

A. Podpirka, K.B. Viswanath and S. Ramanathan. Active low temperature oxidation as a route to minimize electrode-oxide interface reactions in nanoscale capacitors. Journal of Applied Physics. *Journal of Applied Physics.* **108**, 024106 (2010).

M.W. Cole, E. Ngo, **A. Podpirka,** S. Ramanathan, M. Ivill, R.C. Toonen, S.G. Hirsch, and C. Hubbard. Improved material properties of complex oxide thin films for applications in phased array antennas. *Earth and Space 2010: Engineering, Science, Construction and Operations in Challenging Environments* 3444 (2010).

A. Podpirka, and S. Ramanathan. Tranference numbers for in-plane carrier conduction in thin film nanostructured Gadolinia-Doped Ceria under varying oxygen partial pressure. *Journal of American Ceramic Society* **92**[10] 2400 (2009).

M. W. Cole, **A. Podpirka**, and S. Ramanathan. A post-growth processing methodology to achieve barium strontium titanate thin films with low dielectric loss and high tenability for reconfigurable tunable devices. *Journal of Material Science* **44**, 5332 (2009).

A. Podpirka, M.W. Cole, and S. Ramanathan. Effect of photon irradiation on structural, dielectric and insulating properties of $Ba_{0.60}Sr_{0.40}TiO_3$ (BST) thin films. *Applied Physics Letters* **92**, 212906 (2008).

Acknowledgments

The Ph.D. is a long and arduous journey, requiring sacrifice and commitment. Completing it is more than the product of one's work; it is also a testament to the people who supported the endeavor. Without those people, this degree is impossible—and to them I am tremendously grateful. So now comes the difficult part of actually putting that gratitude into words. I've frequently thought about how this acknowledgment will sound. It definitely seems easier than it is. Now it is my turn.

I would like to first acknowledge my advisor, Prof. Shriram Ramanathan, for guiding me through my entire degree. He was always available to discuss the project, challenge me by questioning my work, provide feedback, and give me the resources to do the necessary experiments. He was always passionate about the project which rubbed off on me and gave the freedom to work at my own pace (as long as I had results and a paper ready!). He gave me the freedom when I needed it and hustled me along when I was lagging. I could not have asked for a better advisor.

I would also like to thank my thesis committee, Prof. Frans Spaepen and Prof. Roy Gordon, who made the qualifier and defense process painless and gave interesting suggestions, great feedback, and thought-provoking questions. More importantly, they were available throughout my graduate school career, both for guidance and for helpful discussions.

I am greatly indebted to my funding sources that allowed me to work on these projects; I am very lucky those sources fit so well with my interests. My first project was sponsored by the Army Research Lab under the direction of Dr. Melanie Cole. Thinking about the application of my work to real-world problems greatly influenced my experiments and allowed me to make

relevant advances. In the past 3 years, my project has also been supported by a Semiconductor Research Corporation (SRC) grant. I would like to thank our industry liaisons, Dr. Larry Mosley and Dr. Rajasekaran Swaminathan from Intel that gave helpful feedback in our monthly meetings.

The Center for Nanoscale Systems (CNS) staff at Harvard has been extremely helpful with running all the experiments necessary for lithography, deposition, and characterization. In particular, I would like to thank Greg Lin for help on XPS, Steve Hickman for photolithography, and Jason Tresback for the low temperature probe station.

I am grateful for all the mentoring I have received in x-ray diffraction throughout my time at Harvard. Scott Speakman at MIT has been a tremendous part of this work, especially pertaining to the epitaxial and textured films. He was always available to discuss the experiments, help with alignment, and otherwise assist me. Anyone who has ever worked with x-rays knows just how important this is!

Of course, I wouldn't even be here without the prior foundation I received in my undergraduate training. I would like to acknowledge the material science department at Columbia University for providing the background necessary. In particular, I would like to thank Prof. Baily, Prof. Siu-Wai Chan, Prof. O'brien, Prof. Labowitz and Prof. Guha who shaped my understanding of the field. Working with Prof. Chan and Prof. Laibowitz and taking the classes of Prof. Guha and Prof. Baily definitely steered me towards thin film oxide electronics.

Any degree that takes this long requires some sense of normalcy. Throughout my youth, I have grown up being a part of the Ukrainian scouting organization, PLAST. From my first year in Boston, I have worked as a scout counselor with a troop. Although often time-consuming, being a scout counselor was a great way to complement my studies. Working with

youth and acting as a mentor has allowed me to better know myself. The group of friends that I know from scouting and my scout fraternity *Лісові Чорти* has helped me through the years. The camps I have run and the friends I have made have allowed me to keep the continuity from my youth that is such an intricate part of my life. The Ukrainian community in Boston has been a big part of this continuity, as has the Ukrainian club at Harvard. Having weekly pierogies after church on Sunday and celebrating the holidays with the community gave that sense of home that gives the sanity check needed to complete each week!

Similarly, hockey at Harvard, with Dudley House and the summer league has been an outlet for all my frustrating experiments. A special thanks to Mark who passed the list on to me. A shout out to all the regulars who were at the weekly skate with me: Dave, Pardo, Rod, Philip, Dan, Alex, Tim, Jon, Dustin, Orest and Jesse. Having free ice at Harvard definitely tacked on a few years to this Ph.D!

The beauty of going to school at Harvard is to be surrounded by the best and the brightest. Students and postdocs at Harvard have given me great discussions, terrific collaboration, and a great all-around experience. We struggled through classes together and together stressed over our qualifiers. So I would like to thank my lab and office mates with whom I have had the pleasure to work these past few years. Although I have crossed paths with many through these years, I especially wanted to single out Karthik, Dima, Bo, Masaru, Ko, Charbel, Dan, Jason, Gulgun, You, Viswanath, Brian, Alex and Gokul. Also, I want to thank Don at Rowland for all the machining these past few years.

We are defined by the people we hold as our friends and I have been blessed by a number who have been with me through all the high points and the low points of my graduate school career. It is those who stick by in thick and thin that are true friends. To Aleks and Molly for

putting me up every visit and listening to me complain so much, to Subtelny who has worked so hard alongside me with scouts every weekend, to Rositsa for the excellent help with x-ray diffraction, to Rob, Russel and Frank who were there for me whenever I came to New York and needed that beer in the tough times, to Aaron, Eric, Jess, Libby and the rest of the rowers who have been an extended family to me, to Hiten for always letting me crash in London and showing me what jingoistic British patriotism was, to Gorana for being the best roommate, Bro (Article 22 of the Bro code), and wingwoman that anyone could ask for and traveling the world with me, to Maria for educating me that Sweden is the greatest country in the world, to Vanessa for not murdering me as a roommate, to Bill for his passionate sports debates and to Taylor for the political debates that have made this office an interesting as well as awkward place! There have been countless more that I could not possibly fit into this acknowledgement. Thank you all!

In graduate school some of my closest friends became the coworkers who sat with me day in and day out – Kian, Raf and Sieu. Our annual pilgrimage to Hells night has definitely been a highlight of culinary disaster! Working alongside them has been a great experience and I can only wish that my coworkers in the coming years can be like them. In particular, Kian has been a true Bro and a great roommate these past few years.

My best friends have been with me every step of the way; Pavlo, Xrysta, Tanya and Chris, Petro and Duzyj and Anya. Really, I really can't thank you enough for being there through it all, traveling with me, partying with me and just being there for me. Graduate school is a huge commitment but through it all, true friends are a constant. I couldn't have asked for a better bunch of friends.

Finally, yet most importantly, I want to thank my family. They have been so supportive of this degree. My brothers, Roman and Victor, gave me so much; visiting me randomly, laughing

and fighting with me, dealing with the me through my frustration and sending me anything I have forgotten from home. You both have definitely shaped my world! My father, who throughout my entire life stressed the importance of education and provided me with everything I needed to obtain it. You have given me everything I could have ever imagined. I can only hope I have made you proud. Most importantly, I want to thank my mother, to whom I dedicate this thesis. She sat with me through homework, never gave up on me, took me to speech therapy classes when I struggled in school, worked with me through all those college apps, drove me to all the practices and lessons, even came to take care of me in grad school when I was sick. She supported me in all of my endeavors. This degree is a reflection of all the hard work and sacrifices my parents put into raising me. I really cannot have asked for a more supportive and close-knit family.

Dedication

This thesis is dedicated to my mother, Roxolana Podpirka, who always believed in me and my work and never let me give up. Though she didn't see this day, she was with me every step of the way. I miss you more than words can describe.

<u>After my first publication</u>

Adio,

It's fascinating.. if only I knew what it said. Congratulations! Its not everbody that can say what most people don't understand …and in so many words. I'm really proud of you. And we can discuss your paper next time I see you because of course I am going to read it.

Love, Mama

1 Introduction

1.1 Complex Oxides

The three *transition series* form the short group of elements in the periodic table, interposed between the longer main groups, highlighted in Figure 1. The occurrence of these elements as well as the varied properties of their compounds is a feature of the progressive filling of *d* orbitals across the series. These transition metal elements readily form oxides. The functionality of such compounds when considering monoxide MO_x where *M* is the transition metal is quite significant even with the simplest compounds. Transition metal oxides range from good insulators (HfO_2) which is now replacing SiO_2 in gate dielectrics to Metals (RuO_2).[1,2] Transition metal compounds show transitions from a metallic to a non-metallic state as a function of temperature and strain (VO_2) however, as complexity of the oxides increases, so does the physics.[3,4]

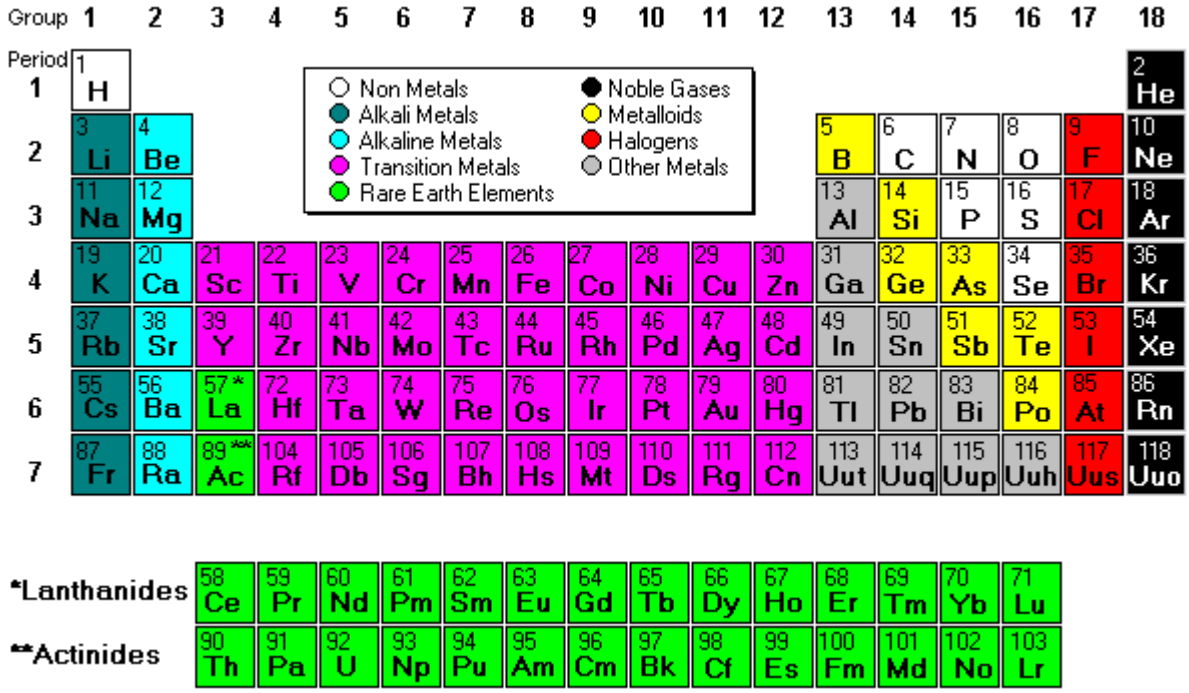

Figure 1: Periodic Table of Elements. Transition metals are shaded in purple. Reprinted with permission from Ref.[5]. Copyright 2011, Model Science Software Inc.

The more complex ternary and higher-order oxides possess even more exotic properties such as ferroelectrics, colossal magnetic resistance, colossal dielectric constants and high temperature superconductivity.[6,7,8,9] One family of transition metal oxides that has received a disproportionate amount of attention consists of compounds with the chemical formula ABO_3 that crystallize into the perovskite structure, shown in the center of Figure 2. The A and B sites can support metal cations with a wide range of size and valence giving rise to a large diversity of physical phenomena as shown in Figure 2. No other material group has shown such varied characteristic by the doping of different cations while maintaining the same crystal structure. Control over the positional ordering of the cations provides an additional tool for mediating the electronic response when the A or B site contain mixtures of two (or more) different atoms.

Perovskites can be descried in terms of close packing of AO_3 layers where the B site cations occupy all of the resultant BO_6 oxygen octahedral. When the AO_3 layers are arranged in cubic close packing, the BO_6 octahedra are connected through corner sharing and the structure is termed a cubic perovskite. In an ideal cubic perovskite the A and B cations realize their equilibrium bond distances to oxygen without inducing any distortion of the unit cell and $d_{A-O} = \sqrt{2(d_{B-O})}$. This leads to cubic symmetry and a resulting Goldschmidt tolerance factor of 1 where $t = r(_A + r_O) / \sqrt{2(r_B + r_O)}$.[10] The cation radius may vary significantly which plays an important role in the crystal structure and in turn, the final electronic properties of the material. Interestingly, when dealing with thin films, these properties can be induced through epitaxial growth and strain engineering.

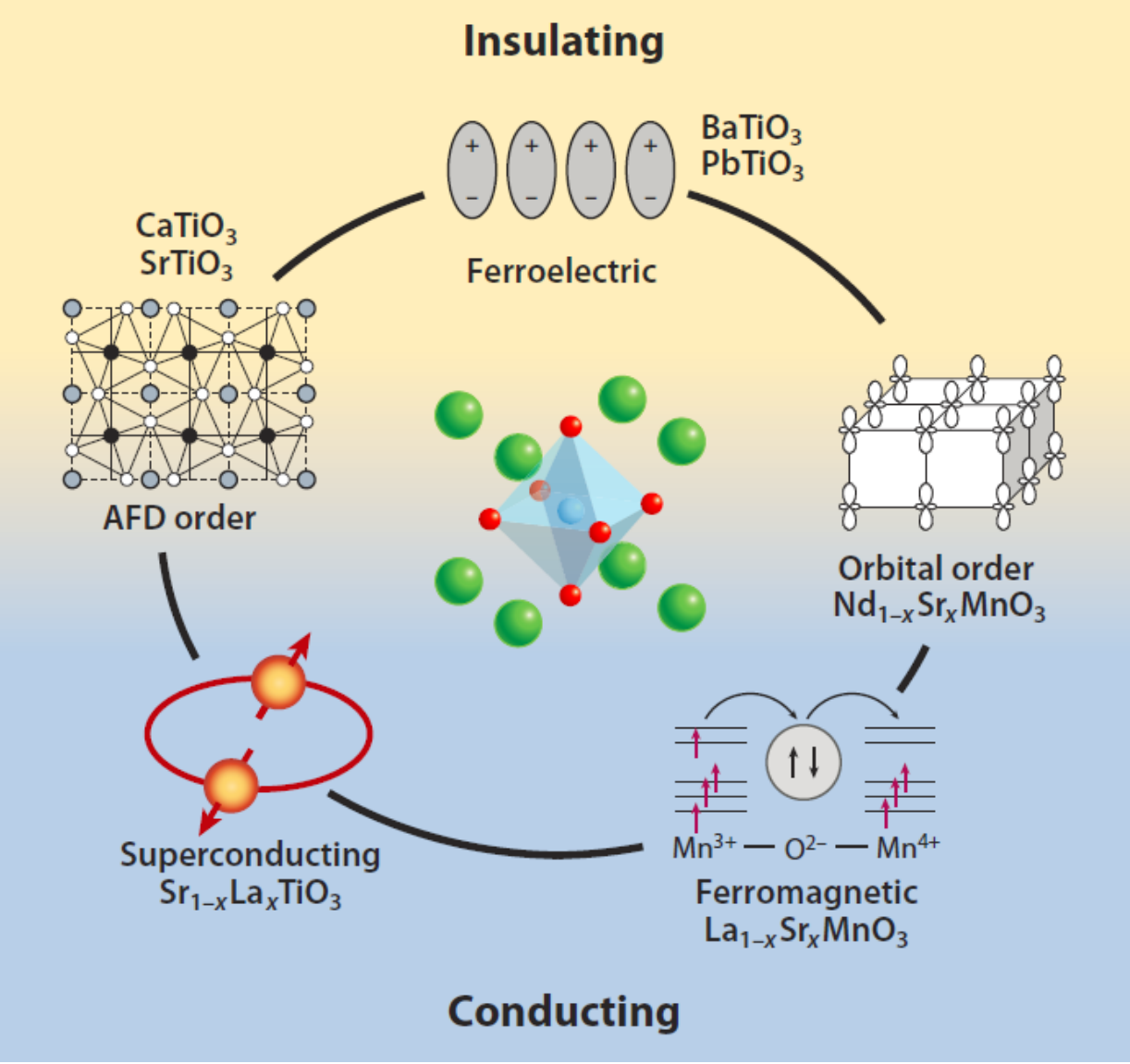

Figure 2: The perovskite ABO_3 structure is given in the center (A site – green, B site – blue, O site – red). Due to the interplay of competing energies, properties can be varied significantly with small variation in doping and strain. Reprinted with permission from Ref. [11]. Copyright 2011, Annual Reviews.

Related to the perovskites, and built upon its initial structure is the layered Ruddlesden-Popper phase. Ruddlesden-popper structure is a perovskite structure with a rocksalt layer on either end as shown in Figure 3. The structure is known commonly as the K_2NiF_4. In the past 20

years, the key stimulus to study the K_2NiF_4 structure has arisen from the high-T_c superconductors La_2CuO_4.[12] Due to similarity in the crystal structure, nickelates are being investigates to better understand the origins of superconductivity in layered perovskites. However, layered nickelates also contain rich physics from large intercalation of oxygen into the lattice, to charge ordering and high ionic conductivity which will be discussed in more detail is chapter 1.3.2.2

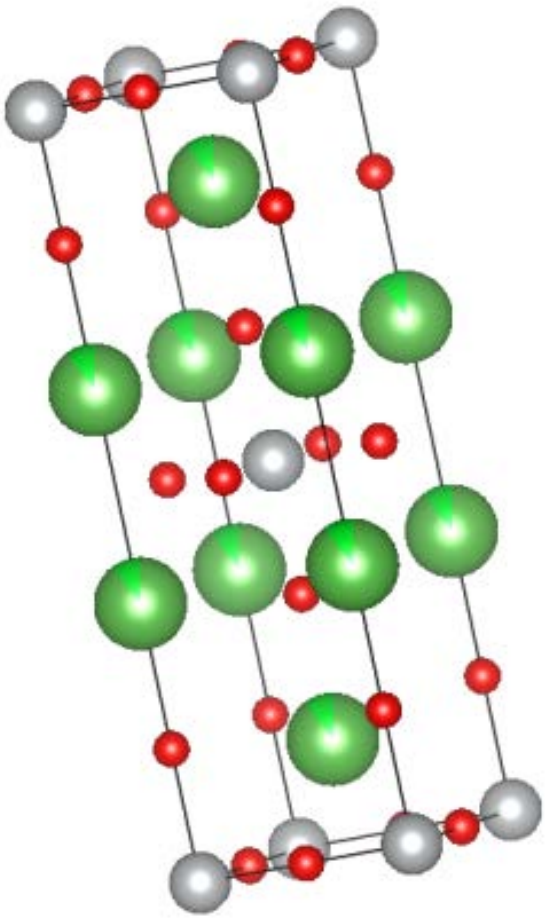

Figure 3: K_2NiF_4 structure (Tetragonal; I4/mmm). Fluorine site is red, Nickel site is grey and Potassium site is green. Created with Ref.[13].

Among complex oxides, the ABO_3 and related layered compounds stand out for their unique properties. The subtle interplay between competing energy scales in complex oxides results in a variety of orderings of the spin, charge and orbital degrees of freedom. Charge

transport can exhibit colossal magnetoresistance, metal-to-insulator transitions or insulator-to-superconductor transitions in strongly correlated compounds. Cooperative alignment of electric dipoles or spins leads to ferroelectricity or ferromagnetism, respectively. Tilting and buckling of oxygen octahedral, which results from antiferrodistortive structural ordering can couple to other modes in the system, driving structural and electronic phase transitions. All these transformations can be seen in Figure 2.[11] With the wealth of functional properties, complex transition metal oxides are rich picking ground for physicists, engineers and material scientists alike.

In this thesis, the properties of two complex oxides in thin film form will be discussed: $Ba_{1-x}Sr_xTiO_3$ (BST) and $La_{2-x}Sr_xNiO_4$ (LSNO), pertaining mostly to their dielectric properties. The first part of the thesis delves into the solid solution of $BaTiO_3$ and $SrTiO_3$ with the chemical structure $Ba_{1-x}Sr_xTiO_3$ (BST) which displays large paraelectric polarization. In this material we investigate the effect of oxygen stoichiometry on the dielectric properties and investigate novel processing methods for growth on non-noble electrodes. The second material studied is of the ruddlesden-popper phase, $La_{2-x}Sr_xNiO_4$ which has been shown to display colossal dielectric response due to hopping transport polarization and charge ordering as well as large intercalation of oxygen which leads to interesting growth mechanisms.

1.2 Dielectric Materials

A definitive guide to dielectric phenomena is given in the work by Kao.[14] Simply put, a dielectric is an electrical insulator that can be polarized by the application of an electric field. Where the term insulator is used in dc limit for a material with low electrical conductivity, the term dielectric is used almost exclusively in the ac limit, referring to highly polarizable material. One of the most important electrical properties of dielectric materials is the relative permittivity of the material, referred to interchangeable as the dielectric constant. The dielectric constant of a material is the measure of the polarizability of the material with the application of an applied alternating electric field. The polarizability of a material is strongly dependent on the chemical structure and the imperfections (defects) of the material as well as on other physical parameters including temperature, pressure and processing conditions.

Dielectric materials are made up of atoms or molecules that possess one more of the five basic types of electric polarization:

- Electronic polarization
- Atomic or ionic polarization
- Dipolar polarization
- Spontaneous polarization
- Interface or space charge polarization

Each type of polarization requires a different time scale to perform; this is why the degree of the overall polarization depends on the time variation of the electric field. The time scale is closely dependent on the size of the polarized species. A schematic of the frequency polarization is given in Figure 4 which shows different species polarizing at different frequencies.

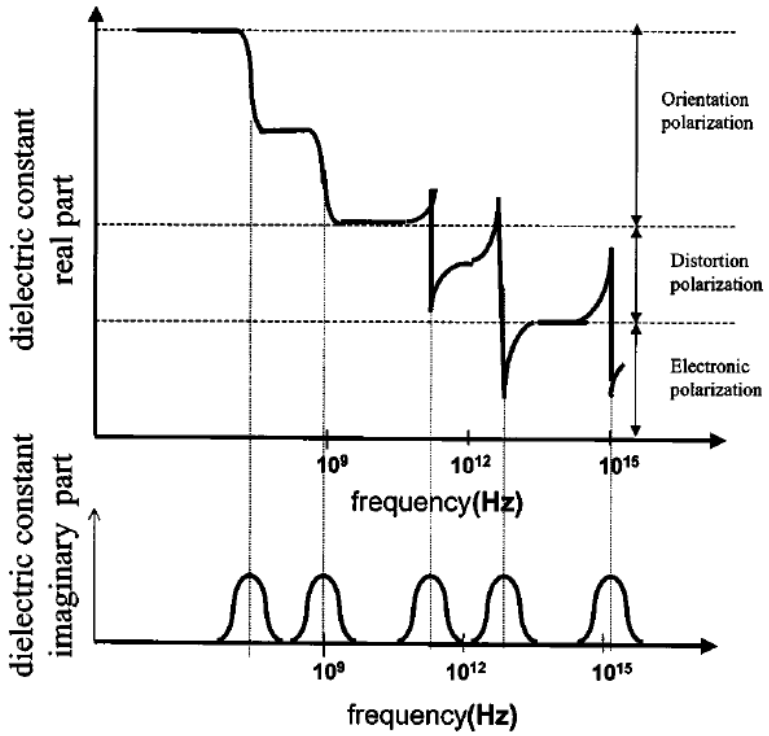

Figure 4: General view of the polarization mechanisms as a function of frequency showing approximate mechanism as to where polarization takes place. Reprinted with permission from Ref.[15]. Copyright 2003, American Institute of Physics.

We consider a perfect dielectric material which implies that inside the material no mobile charge carriers (electrons, holes or ions) present. By placing such a dielectric material between two charged plates, the system will tend to attract this piece of material into the vacuum space between the two plates in order to reduce the potential energy of the system. This causes the potential between the plates produced by the original charge to decrease to a smaller value. With the charge on the plates remaining constant, the ratio of the electric field in the space between the charged plates with that of the electric field of the dielectric material. This ratio is the dielectric constant.

A simple parallel plate capacitor, also considered a metal-insulator-metal (MIM), consists of two plates of area *A* separated by a dielectric material of thickness *d*. We find that the surface

charge depends on the applied voltage and the quantity measured is the capacitance. In the simple parallel-plate capacitor, the capacitance is given by $C = \frac{\varepsilon_r \varepsilon_o A}{d}$ where ε_r is the relative permittivity of the material (or dielectric constant) and ε_o is the permittivity of free space. The voltage and the charge are related by the form $Q = CV$.

When the relaxation time is much faster than the frequency of the applied electric field, polarization occurs instantly. When the relaxation time is much slower than the frequency of the applied electric field, no polarization (of that mechanism) occurs. When the relaxation time and the frequency of the applied field are similar, a phase lag occurs and energy is absorbed. This is called dielectric loss. It is quantified by the relationship $\tan\delta = \frac{\varepsilon_r^{''}}{\varepsilon_r^{'}}$ where $\varepsilon_r^{'}$ is the real part of the dielectric constant and $\varepsilon_r^{''}$ is the imaginary part of the dielectric constant.

There are three major mechanisms of electronic polarization in moderate electric fields (i.e. at fields much lower than the inner atomic or molecular fields) and when the materials has very low conductivity (i.e. the concentration of charge carriers inside the materials is so low that if effects can be negligible). These mechanisms are:

- Electronic polarization: The electric field causes deformation or translation of the originally symmetrical distribution of the electron clouds of atoms or molecules. This is essentially the displacement of the outer electron clouds with respect to the inner positive atomic core.
- Atomic or ionic polarization: Electric field causes the atoms or ions to be displaced relative to each other. This is essentially the distortion of the normal lattice vibration.
- Orientation polarization: This polarization occurs in materials consisting of molecules. The electric field causes the reorientation of the dipoles toward the direction of the field.

Both the electronic polarization and the atomic polarization are due mainly to the elastic displacement of electron clouds and lattice vibration within the atom or molecules. Their interaction is an intramolecular phenomenon, and the restoring force against the displacement is relatively insensitive to temperature so electronic and atomic or ionic polarization processes are only slightly dependent on temperature. Orientation polarization is a rotational process and often times only observed in molecules. Under an external force, it changes to a dynamic equilibrium. When the external field is removed, it relaxes back to its original state.

At higher fields and in "lossy" materials, carrier injection becomes important. For materials consisting of a high concentration of charge carriers (i.e. with a high conductivity), polarization can occur due to the migration of charge carriers to form space charges at interfaces or grain boundaries. This type of polarization is called *space charge* polarization.

The total polarizability of materials, α, comprises the summation of its polarization mechanisms $\alpha = \alpha_e + \alpha_i + \alpha_o + \alpha_d$ where α_e, α_i, α_o, α_d are the polarizabilities due to electronic, atomic, orientational and space charge polarizations, respectively. In the following section we will discuss the specific mechanisms dealing with the polarization of ferroelectrics as well as colossal dielectric response materials.

1.2.1 Ferroelectrics

Ferroelectric materials have a permanent electric dipole and due to this, exhibit a spontaneous polarization. Of the 32 point groups, 11 of them are center symmetric which disqualifies them from ferroelectricity. With the application of an external electric field, positive and negative charged atoms will be displaced with respect to the equilibrium position in the unit cell. Of the remaining 21 non-centrosymmetric point groups, they may have one or more polar axes and show piezoelectric effects (except cubic 432). Among the 21 point groups without an

inversion center, there are 10 polar groups which possess a unique polar axis. These crystals may display spontaneous polarization parallel to the polar axis. All ferroelectric crystals belong to a pyroelectric crystal class and have the additional property that an external field can reverse their spontaneous polarization. Thus ferroelectric character cannot be solely determined from crystallography. This reversible polarization manifests itself as a hysteresis loop in the response of polarization to an external applied field.

A ferroelectric crystal shows a reversible spontaneous electric polarization and a hysteresis loop that can be observed in certain temperature regions. For example, in widely studied material, $BaTiO_3$, the perovskite crystal is elongated along the c-axis and the resulting distortion is termed tetragonal distortion. The body centered Ti atom does not have a preference where to move and creates a built-in polarization along the c axis. With the application of an electric field, the loosely bound Ti will be polarized which brings about the large dielectric constant. Above this temperature region, there is a phase transformation that changes the symmetry of the crystal. In the case of $BaTiO_3$, symmetry is changed to a cubic structure. This transition point is called the Curie temperature, T_c, and the crystal begins to exhibits paraelectric dielectric behavior. This occurs since the Ti atom is now energetically favored to sit in the center of the crystal. At $T>Tc$ anomalous behaviors follows the Curie-Weiss relation $\varepsilon_r = \frac{C}{T - T_C}$ where C is known as the Curie constant. In Figure 5 the Curie temperature (~120°C) of $BaTiO_3$ is shown. As the crystal structure changes with temperature, the dielectric constant (shown along the a-axis and c-axis of the crystal) varies drastically. At 120°C the crystal is cubic and the permittivity along the a-axis and c-axis are equivalent. As the crystal structure changes, there is a change in the dielectric properties of the crystal. More material specific properties of ferroelectrics will be discussed in further in Chapter 1.3.2.1.

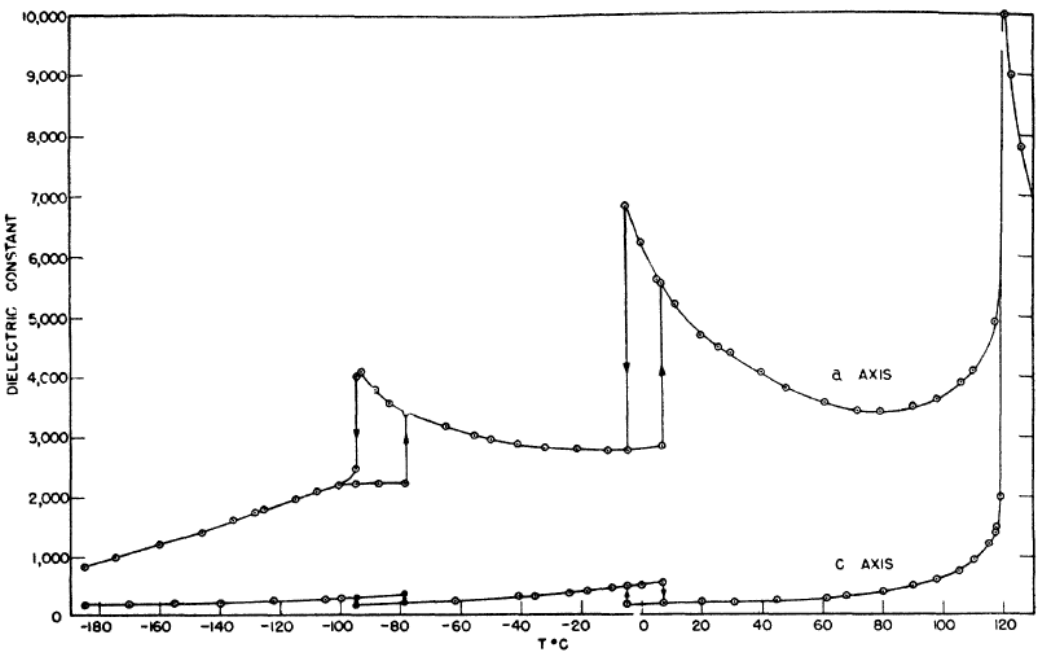

Figure 5: Dielectric constant as a function of temperature for a $BaTiO_3$ crystal. Reprinted from Ref.[16]. Copyright 1949 by the American Physical Society.

1.2.2 Colossal Dielectric Constant Materials

A comprehensive review of the physics behind Colossal Dielectric Constant materials is given by work from the Loidl group.[17,18] Most capacitor materials with high dielectric constant are based on ferroelectric which reach values of dielectric constants exceeding 10^4. However, as mentioned previously, dielectrics exhibit strong temperature dependent dielectric constants, limiting their application into electronic devices. At the moment, the most widely studied non-ferroelectric material exhibiting colossal dielectric response is $CaCu_3Ti_4O_{12}$ (CCTO) which was first reported on 2000.[19] The advantage of a material such as CCTO to standard ferroelectric based dielectrics is its nearly temperature independent colossal dielectric response at around room temperature. Only below approximately 200K and as a function of frequency does the

colossal dielectric response show a strong frequency dependence of the magnitude of 100. Typical behavior of colossal dielectric materials is shown in Figure 6.

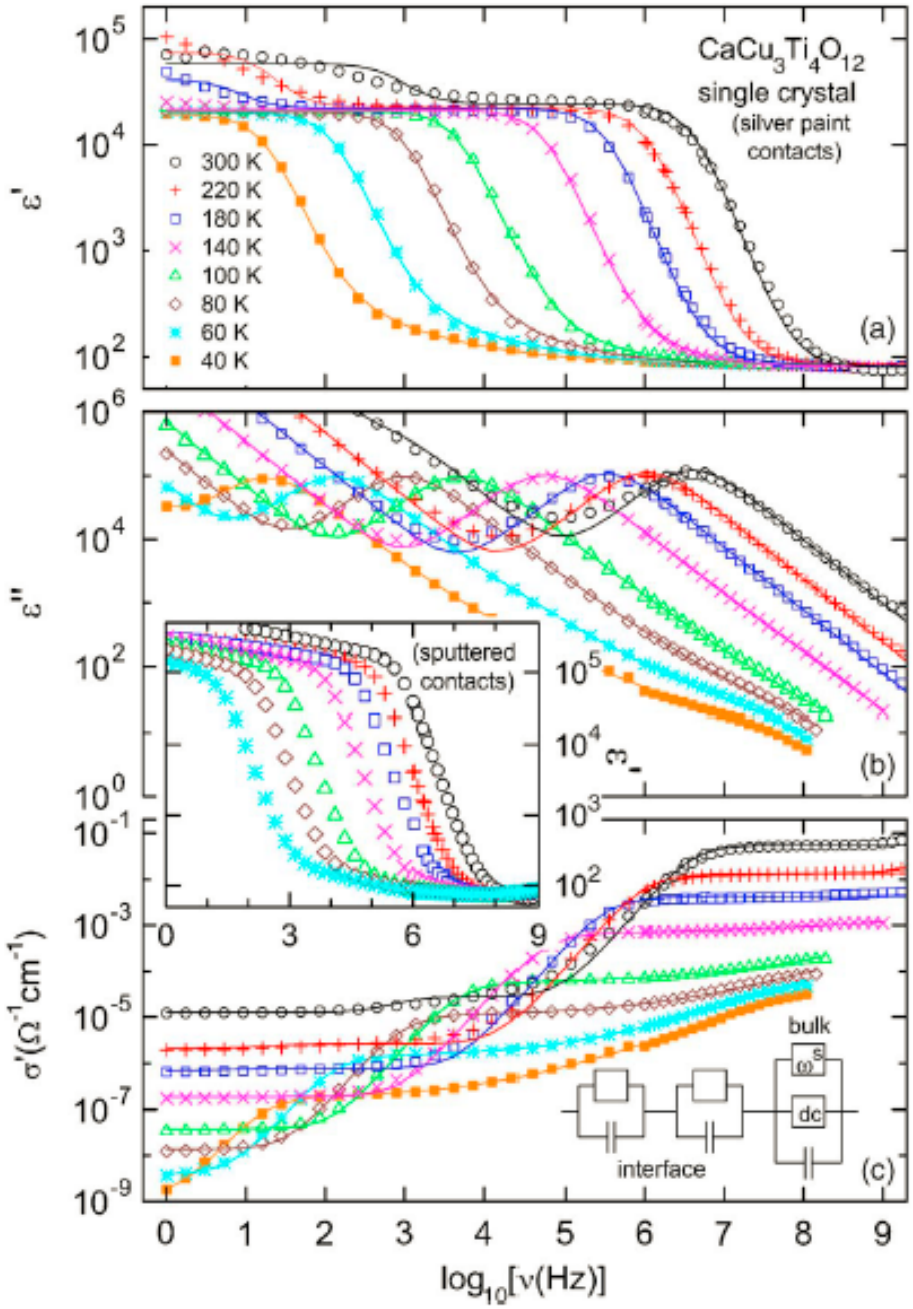

Figure 6: Behavior of CCTO single crystal showing typical colossal dielectric properties. Reprinted with permission from Ref. [20]. Copyright 2008, American Institute of Physics.

From the first discovery of CCTO, speculations of the colossal dielectric response have been put forward. From the onset, speculations on the origin lay in extrinsic properties of the material namely a barrier layer mechanism. However, certain studies still attributed the response to intrinsic properties of the film. It is commonly accepted that a barrier mechanism is the correct explanation for the response however the nature of these barriers leading to the dielectric response is still open to debate. These include surface barrier layer, internal barrier layer or a combination of the two.

Since CCTO was first discovered to have giant dielectric response, there has been an ongoing search for new and better materials. Many of the isostructural materials have been synthesized in order to discover colossal dielectric response however none have come to give the large dielectric of CCTO.[21] Completely different structural transition metal complex oxides have shown interesting dielectric response, namely LSNO, which generate a different mechanism for the large dielectric response.[22]

1.2.2.1 Mechanism for Colossal Dielectric Response

To date, the most prominent mechanisms for the colossal dielectric response are as seen in relaxor ferroelectrics,[23,24] charge density wave formation,[25] hopping charge transport,[26] metal insulator transition[27] or combinations of the previous effects. For the sake of brevity, we will focus on two of these mechanisms that we observe in this thesis, namely the hopping charge transport and various interface effects leading the increased dielectric response.

1.2.2.2 Hopping Charge Transport

Hopping conductivity is the most common charge transport process in transition metal oxides. Hopping conduction is the typical charge transport process of localized charge carriers.

In electronic conductors, electrons or holes can be localized due to disorder leading to polaron formation. This disorder may arise from substitutional doping, defects in the lattice or non-stoichiometry.[28,29,30,31] Depending on the width and the height of the potential barrier, a charged particle on one site may hop or tunnel to the other site. The hopping conductivity leads to a characteristic frequency dependent power law developed by Jonscher[32] and widely referred to as the Universal Dielectric Response. The equation is given as such $\sigma' = \sigma_0 \upsilon^s$ where s <1. This response can be understood as the transport of localized charge carriers with such models as variable range hopping. Due to Kramer–Kronig relation, the υ^s power law also leads to a corresponding power law in the imaginary part of the ac conductivity, namely $\sigma'' = \tan(s\pi/2)\sigma_0 \upsilon^s$. Since the dielectric constant is directly related to σ'' by $\varepsilon' = \sigma''/(2\pi\upsilon\varepsilon_0)$ hopping conduction is expected to lead to a power law of $\varepsilon' \propto \upsilon^{s-1}$. Thus, as s<1, the dielectric constant can reach colossal magnitudes at low frequency. This also leads to $\tan(s\pi/2)$ on the order of unity. The dielectric loss $\varepsilon'' = \sigma'/(2\pi\upsilon\varepsilon_o)$ is extremely high leading many of these systems to be unsuited for device application.[33]

1.2.2.3 Interfaces

A detailed study of the interface response is given in *Dielectrics and Waves*.[34] Interfaces of any kind can generate very high apparent values of the dielectric constant because they can act as parallel-plate capacitors with very small plate distances. This effect is known as a Maxwell-Wagner (MW) polarization effect. MW relaxation is a phenomenon having been discussed extensively first by Maxwell and later by Wagner in the 19th century.[35,36] Its frequency response spectrum is similar to that of Debye relaxation (dipole relaxation). MW relaxation occur for a variety of heterogeneities, including a depletion layer between a sample and electrode, interfacial

layer of grain boundaries and electronic heterogeneities which may occur from charge ordering. Domain boundaries are also suggested as another source at which M-W relaxation can occur.[37]

The heterogeneity associated with different contacts (electrodes, interfaces, and grain boundaries) can be modeled by a two layer model shown in Figure 7 which consists of two *RC (R*=resistance and *C*=capacitor) circuits in series, one for the contact and the other for the sample. The dielectric properties of the system can be characterized by the conductivities σ_i (*i*=1,2) permittivities ε_i and thickness d_i with the real and imaginary parts of the complex permittivity can be written as[38,39]

$$\varepsilon^* = \varepsilon' - j\varepsilon'' = \varepsilon_r \varepsilon_o - j\frac{\sigma}{\omega}$$

where

$$\varepsilon'(\omega) = \varepsilon_\infty + \frac{\varepsilon_s - \varepsilon_\infty}{1 + (\omega\tau)^2}$$

$$\varepsilon''(\omega) = \frac{(\varepsilon_s - \varepsilon_\infty)\omega\tau}{1 + (\omega\tau)^2} + \frac{\sigma}{\omega\varepsilon_0}$$

From Figure 7, the static limit, ε_s and the high frequency limit, ε_∞ are given by

$$\varepsilon_s = \varepsilon'(\omega = 0) = \frac{\varepsilon_1 d}{d_1}$$

$$\varepsilon_\infty = \varepsilon'(\omega \to \infty) = \frac{d\varepsilon_1\varepsilon_2}{(d_2\varepsilon_1 + d_1\varepsilon_2)}$$

By extending this analysis of the two layer system in the terms of conductivity, it can be shown that the dielectric dispersion of a two layer system can be described to be Debye-like but the high frequency and low frequency terms can be described in terms of the two materials sharing an interface

$$\varepsilon_s = \varepsilon'(\omega = 0) = \frac{d(d_1\varepsilon_1\sigma_2^2 + d_2\varepsilon_2\sigma_1^2)}{(d_2\sigma_1 + d_1\sigma_2)^2}$$

$$\varepsilon_\infty = \varepsilon'(\omega \to \infty) = \frac{d\varepsilon_1\varepsilon_2}{(d_1\varepsilon_2 + d_1\varepsilon_2)}$$

where the relaxation time for the interfacial polarization is given as

$$\tau = \frac{\varepsilon_1 d_1 + \varepsilon_2 d_2}{\sigma_1 d_2 + \sigma_2 d_1}$$

where $d=d_1+d_2$, ω and ε_0 is the thickness of the entire layer, the angular frequency and the permittivity of free space, respectively.

The relaxation time and therefore the dispersion frequency are related to the permittivity and conductivity values of both materials. The cause for the effect can be explained as follows: The dielectric material between the two plates has a net total impedance and therefore must give a constant current through the structure. Since the two materials transfer charge in different ways (by conduction or polarization), there exists a discontinuity at the interface between the materials where the mode of charge transfer changes. Where one transfers charge principally by conduction and the other by polarization, an accumulation of charge at the interface occurs. Therefore, a dipole is created at the interface. Interfaces in a material, i.e. electrical inheterogeneities, grain boundaries, etc. lead to a significant interfacial effects.

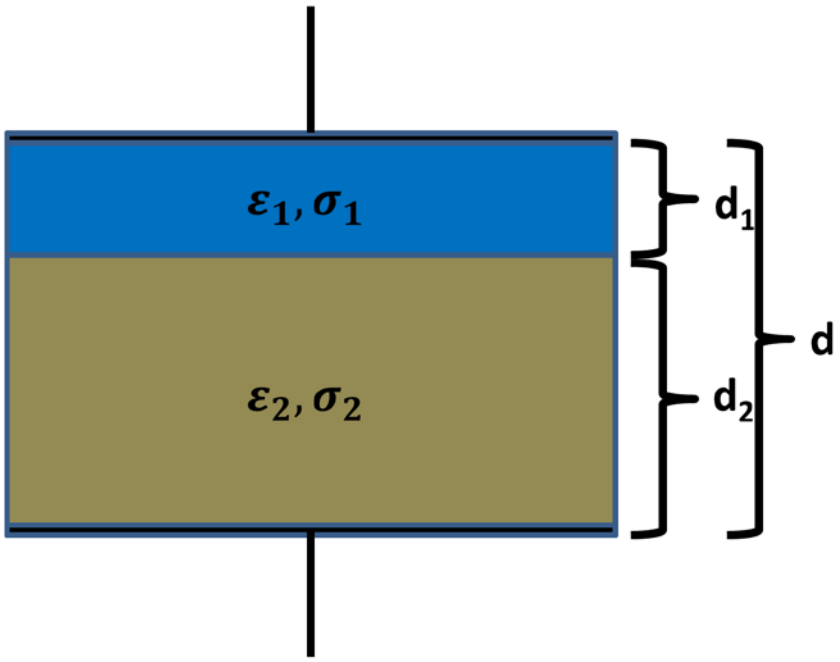

Figure 7: Maxwell-Wagner two layer capacitor model. Adapted from *Dielectrics and Waves* (Ref.[34]).

Of significant interest to this dissertation is the spontaneously arising interfaces caused by electronic phase separating arising from charge ordering in certain transition metal complex oxides. This phenomena has been seen in systems exhibiting high T_c superconductivity (La_2CuO_4), magnetoresistance manganites and nickelates.[40] The system $La_{2-x}Sr_xNiO_4$ has attracted significant interest due to stripe like and checkerboard ordering in much of its phase diagram.[41] Due to the process of charge ordering, internal interfaces develop leading to the enhanced observed polarization. This leads to a Maxwell-Wagner type response and can be regarded as quasi-intrinsic. These interfaces may lead to delayed dispersion due to the fine length scale or can be coupled with other mechanisms to give a higher apparent polarization.

1.3 Motivation of Thesis

1.3.1 Bypass Capacitors for Next Generation System on Package Technology

Tremendous progress has been made in the past four decades in miniaturizing and integrating transistors and capacitors for logic applications onto silicon in keeping with the semiconductor industry's decades-old defining paradigm of Moore's Law. By comparison, passive components (resistors, capacitors and inductors) on the circuit-board level have made only incremental advances in size and density, sometimes referred to as the system integration law and shown in Figure 8.[42] Passive components refer to non-active elements, including capacitors, resistors and inductors and usually tens to hundreds of discrete passive components are mounted on the circuit board. Consequently, passive components occupy an increasingly larger area and mass fraction of electronic systems and are a major hurdle to the miniaturization of many electronic systems.

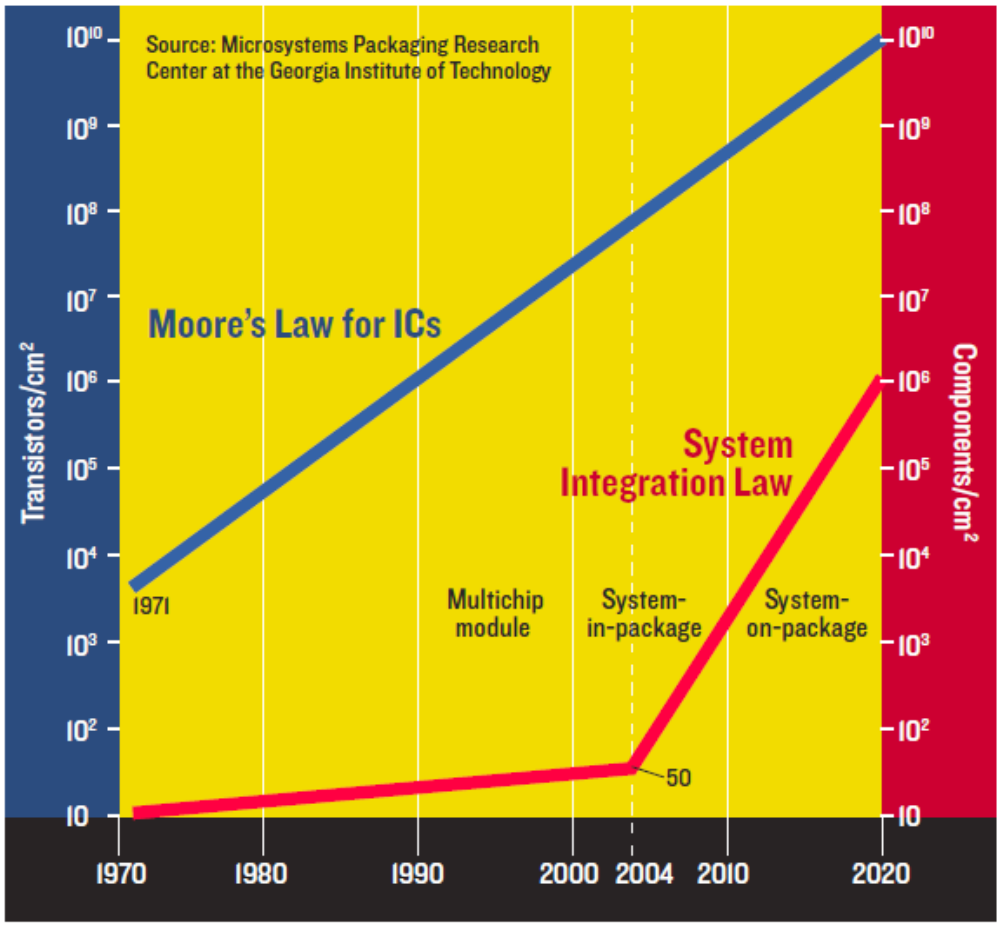

Figure 8: Moore's Law and System Integration Law. Reprinted with permission from Ref. [42]. Copyright 2006, IEEE.

Embedded passive components could be defined as passive components sandwiched between the interconnecting layers of a circuit board, including printed wiring board and ceramic tape. The goal of embedded passive components is to take surface mount technology (SMT) from top and/or bottom of the board and to bury those components in the board thickness as seen in the evolution and predictions in Figure 9. By moving from SMT to embedded passives, significant improvement in performance and size can be obtained. Reduced system mass, volume and footprint with the integration of the package into the substrate leaves more room on the surface for the ICs. Improved electrical performance is achieved due to lower parasitics,

particularly lower inductance due to shorter signal transmission as well as minimizing loop inductance.[43] Embedded passives may also improve reliability by the elimination of solder joints. The eventual goal is to achieve what is known System on Package (SoP) technology which allows for all passives to be integrated along with some active components into the packaging board. A look at the future concept is seen in Figure 10. This is reviewed in detail by in *Fundamentals of Microsystems Packaging*.[44]

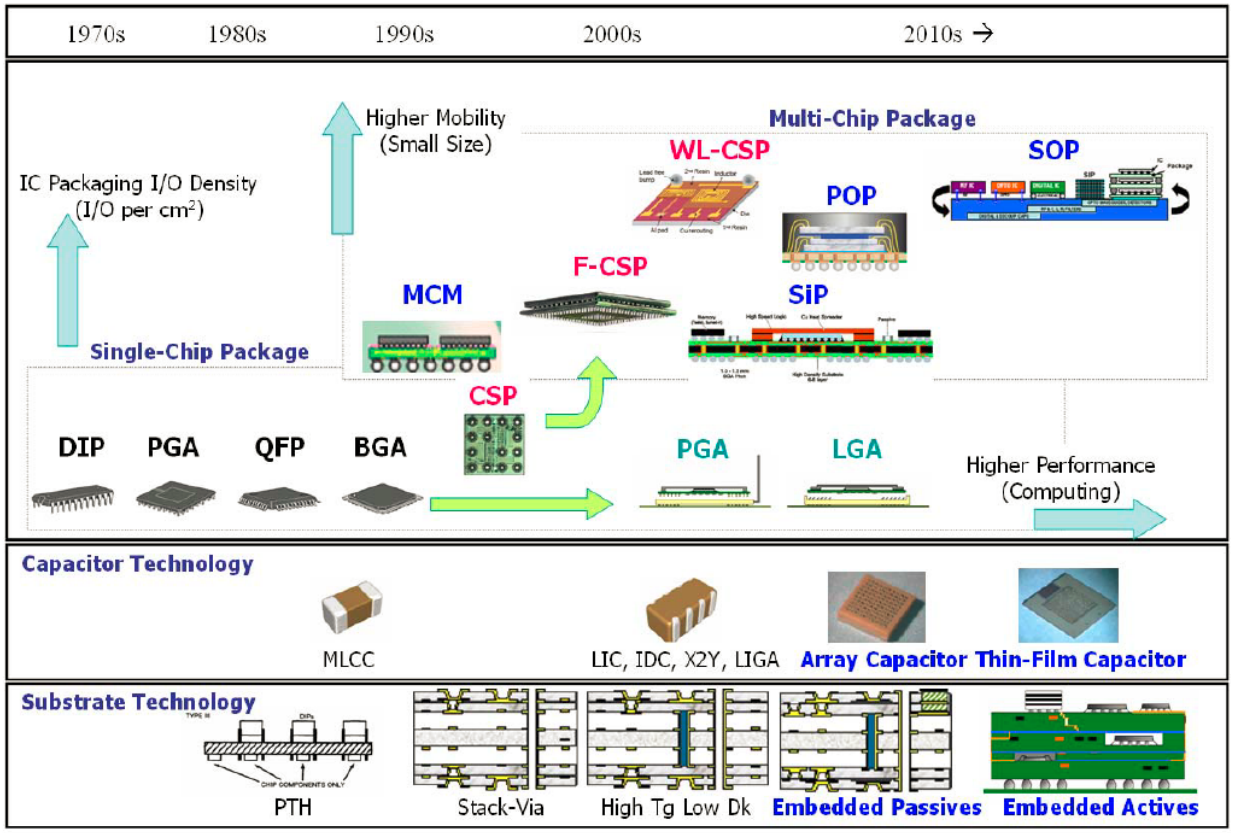

Figure 9: Projected evolution from Surface Mount Technology (SMT) to Embedded Passives. Reprinted with permission from Ref.[45].

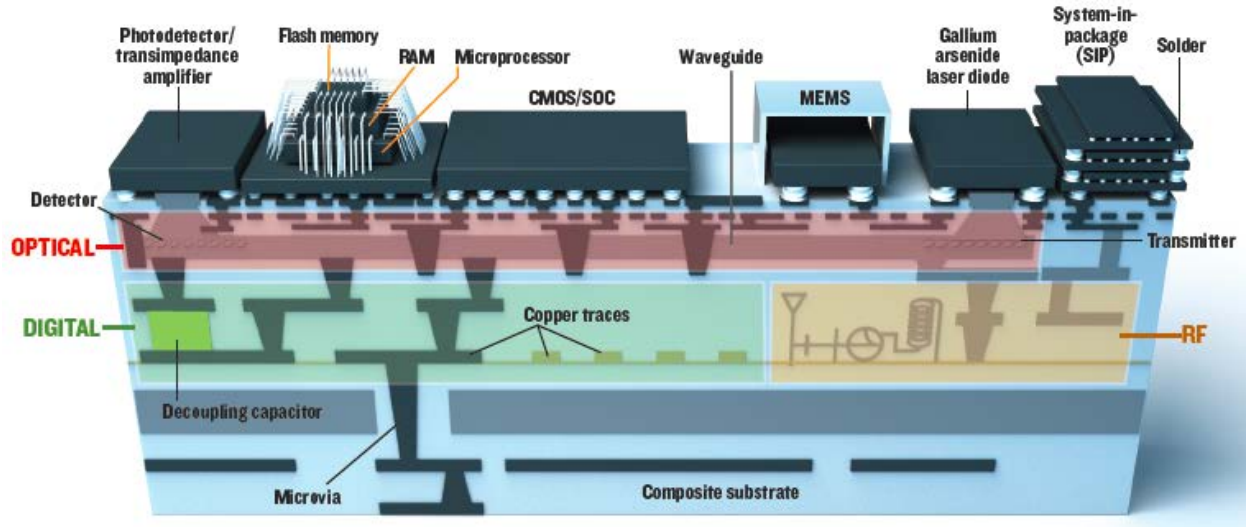

Figure 10: Future view of a System-on-Package. Note the placement of the decoupling capacitor. Reprinted with permission from Ref.[42]. Copyright 2006, IEEE.

In order to reach this goal, thin film capacitors (decoupling or bypass capacitors) on non-noble metallic foils need to be developed to replace the existing bulk ceramic surface mounts. These thin film capacitors could be embedded directly beneath the IC rather than spread out across the printed wiring boar. Thus would decrease the amount of area the wiring board requires and improve speed and performance directly related to the distance between the capacitor and the IC.

In order to achieve these goals, key technical issues must be surmounted. The growth of high quality dielectric materials with dielectric density on the order of 10-100 $\mu F/cm^2$ would be needed as well as the growth of these materials at low enough temperatures to allow for the incorporation with existing dielectric circuit boards and IC components. These materials (preferably non-noble to reduce cost) should be readily incorporated into the supply chain. To date, thin film capacitor technology has not yet been developed that would satisfactorily replace current bulk ceramic capacitors of all capacitance values used in modern electronic packages.

The challenge here is to identify a material suitable for dielectric processing where thin film properties of this material can be compatible with the semiconductor industry roadmap. This requires us to identify materials that should be researched to try to achieve these targets.

1.3.2 Material Studied

In this thesis, the properties of two complex oxides in thin film form will be discussed: $Ba_{1-x}Sr_xTiO_3$ and $La_{2-x}Sr_xNiO_4$. The first part of the thesis delves into the solid solution of $BaTiO_3$ and $SrTiO_3$ with the chemical structure $Ba_{1-x}Sr_xTiO_3$ (BST) which displays large paraelectric polarization. With this material we investigate the effect of oxygen stoichiometry on the dielectric properties and investigate novel processing methods for growth on non-noble electrodes.

The second material studied is the Ruddlesden-Popper phase, $La_{2-x}Sr_xNiO_4$, which has been shown to display colossal dielectric response as well as large intercalation of oxygen which leads to interesting growth mechanisms.

1.3.2.1 BST

Barium Strontium Titanate (BST), $Ba_xSr_{1-x}TiO_3$, where $0 \le x \le 1$ is a solid solution of $BaTiO_3$ and $SrTiO_3$. BST has a perovskite crystal structure with the formula ABO_3. In BST, the A site is occupied by Ba and St (oxidation state of +2) atoms while B site is occupied by Ti (oxidation state of +4) while O ion is in the -2 oxidation state. Ba^{2+} and Sr^{2+} are located in the eight corners of the cubic crystal cell and O^{2-} is located at the face of the cube while the $Ti^{4+}$is located at the center of the cubic cell.

$BaTiO_3$ as discussed earlier is a ferroelectric at room temperature (T_c = 120C) while $SrTiO_3$ is a quantum paraelectric with no T_c. The lattice parameter and T_c depends on the ratio

of Ba:Sr as seen in Figure 11 and Figure 12. Electrical properties are also greatly dependent on the stoichiometry of the material, in particular the cation ratio and oxygen concentration. An important application based property of BST is the ability to change the dielectric constant and dielectric loss tangent near the Curie temperature by an externally applied field, which makes this material ideally suited for electrically tunable devices such as phase shifters and filters. This is due to the paraelectric phase having a centrosymetric tunability.[46,47]

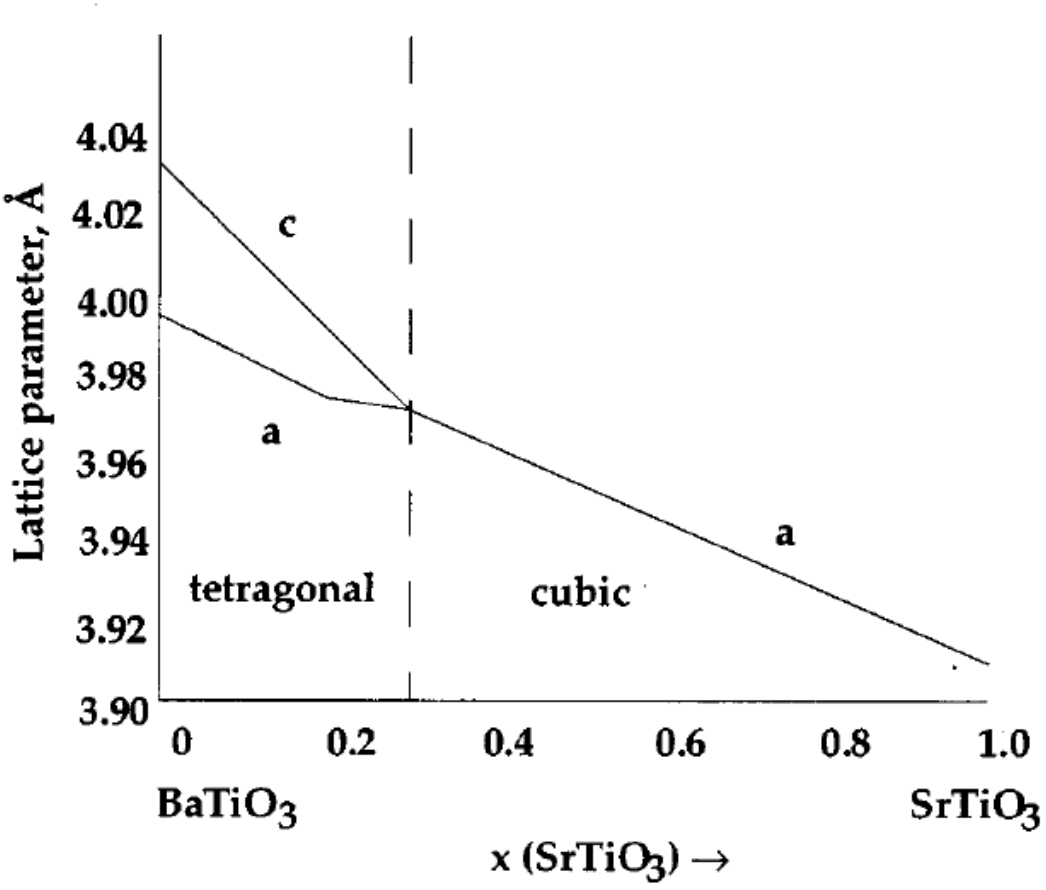

Figure 11: Effect of cation ratio on the crystal structure of BST. Reprinted with permission from Ref. [48]. Copyright 1997, American Institute of Physics.

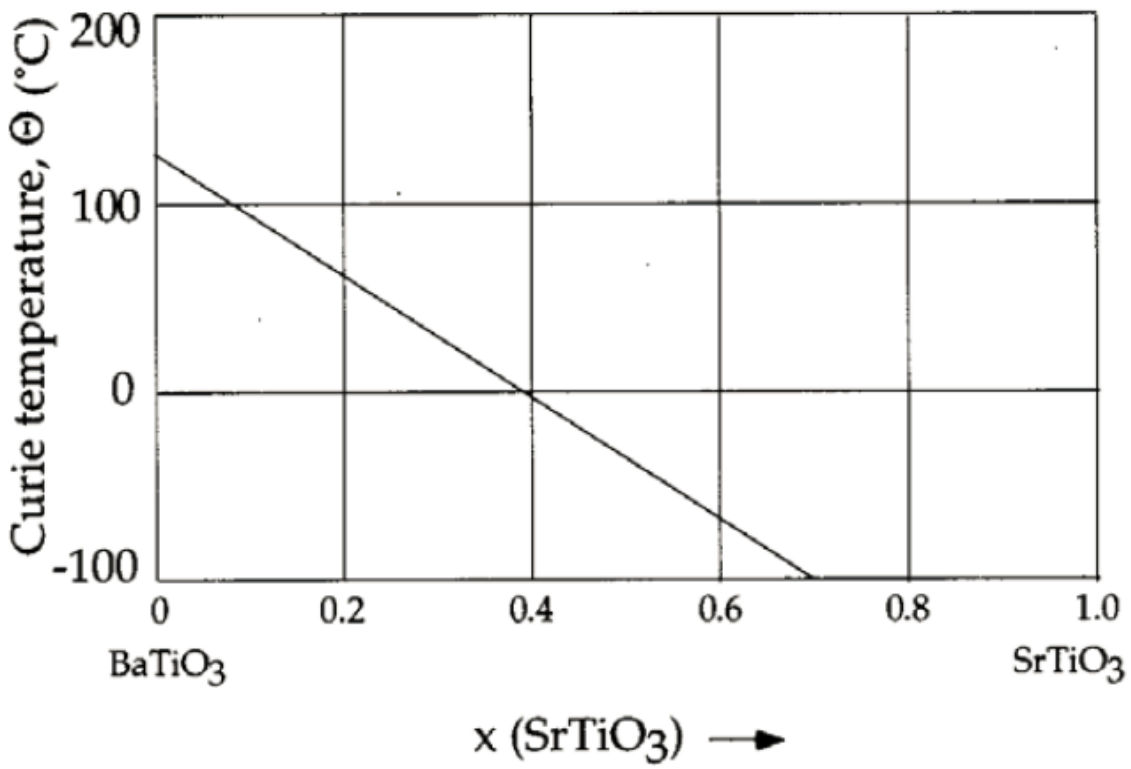

Figure 12: Effect of cation ratio on the Curie temperature of BST. Reprinted with permission from Ref.[48]. Copyright 1997, American Institute of Physics.

Besides the concern for the cation ratio, great emphasis is placed on the oxygen stoichiometry. Due to charge balance, oxygen vacancies lead to *n*-type conductivity by the equation, $O_O^x = V_O^{\bullet\bullet} + 2e' + \frac{1}{2}O_2(g)$. Kroger-Vink notation is used where O_O^x is the Oxygen on the oxygen site with a neutral charge, $V_O^{"}$ is the vacancy on the oxygen site with a net positive charge, and two electrons with a negative charge each to balance the equation. Oxygen vacancy therefore gives the lattice more *n*-type carriers and greatly increases the leakage in the material. In order to consider device application, where a robust low loss dielectric must be used, maintaining stoichiometry is of great concern. Measuring the electronic conductivity as a function of low partial pressure has shown a dramatic dependence on the partial pressure and therefore oxygen content of the material as seen in Figure 13. The slope of the graph, showing a

-1/4 dependence indicates an *n*-type conductivity at low partial pressures and a p-type conductivity at high partial pressures. When depositing thin film material or growing bulk samples of BST, the crystal may become oxygen deficient. This also occurs with the deposition of electrodes due the process of impinging the metal material onto the surface. In order to make high quality material, ways to reintroduced lost oxygen must be developed.

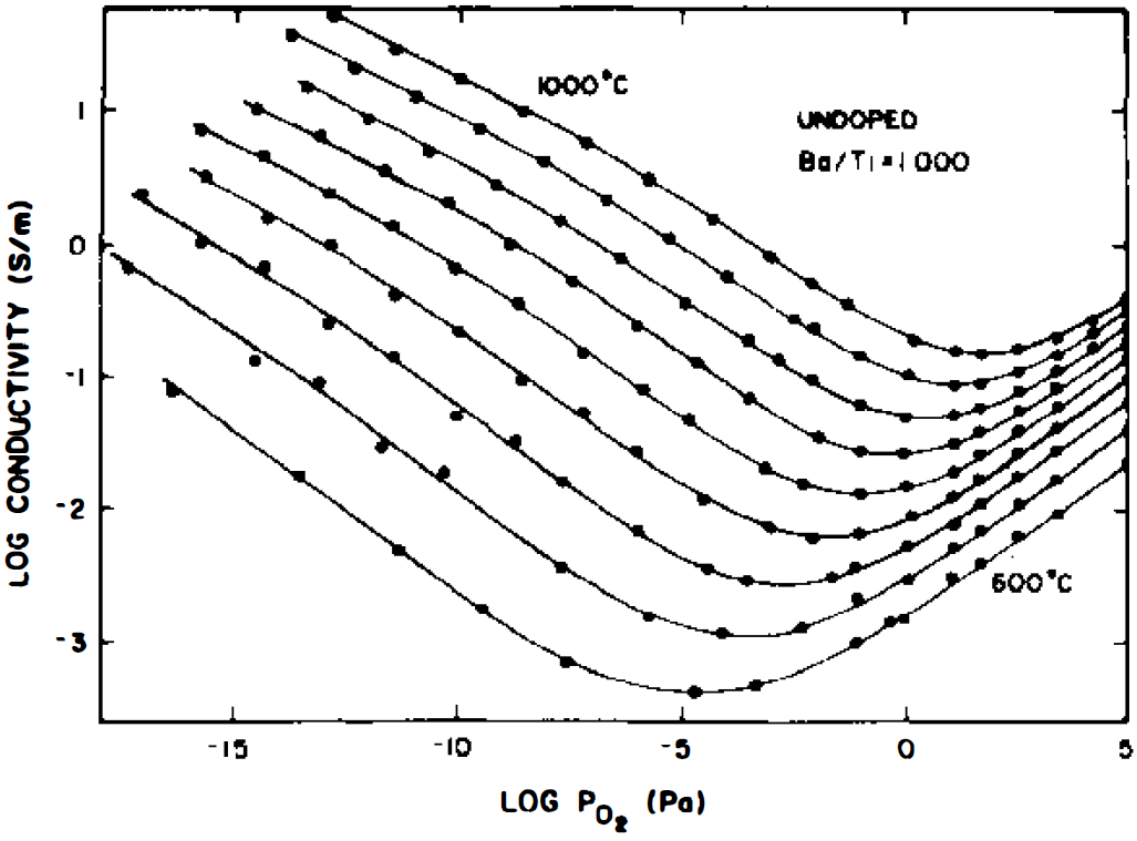

Figure 13: Electrical conductivity in polycrystalline $BaTiO_3$ as a function of partial pressure. Reprinted with permission from Ref.[49]. Copyright 1985, Annual Reviews.

1.3.2.2 LSNO

Since the discovery of high T_c superconductivity by Bednorz and Muller in 1986, there has been a deep interest into the $La_{2-x}Ba_xCuO_4$ structure as well as isostructural materials in order to understand the physical properties leading to the anomalous superconductivity. This

discovery has led to theoretical and experimental interest in understanding other doped layered antiferromagnets. It has become apparent that doped antiferromagnets exhibit ordered phases involving both spin and charge. This has led to the discovery of striped spin-charge ordered phase in non-superconducting layered cuprates. These findings underline the importance of understandings charge stripe ordering.

The basic crystal structure of $La_{2-x}Sr_xNiO_{4+\delta}$ (LSNO) which has a crystal structure that is typical of doped layered antiferromagnets is shown in Figure 3. LSNO does not superconduct but is isostructural to the cuprate superconductors of $La_{2-x}Sr_xCuO_4$. The structure is made of layers of Ni-O conduction layers that are separated by spacer layers of La/Sr-O in the body centered tetragonal unit cell. Substitution of one atom of La by one atom of Sr in the space layer, introduces one hole into the conduction layer. So the spacer layer provides the charge carriers for the conduction layer which is responsible for the electrical properties of the material. This also occurs with the doping of oxygen interstitials into the lattice since LSNO, due to its K_2NiF_4 structure, readily takes up oxygen.[50] The concentration of holes in LSNO is given by the equation $p = x + 2\delta$. Oxygen excess in La_2NiO_4 is associated with the incorporation of interstitial oxygen anions into the rock salt layers.[51] This ability leads to high oxygen mobility and potential application in as materials in fuel cells. Moreover, they show strong electrocatalytic activity towards the oxygen reduction and have their thermal expansion coefficients close to those of the conventional electrolytes used in the SOFC device.[52] These properties have been shown to strongly enhance the cathodic electrochemical performance. Previous data has shown that La_2NiO_4 exhibits lower polarization resistance than lanthanum strontium manganite perovskite, a common cathode material.[53]

At high temperatures, the holes doped in the conduction layer are randomly distributed. Upon cooling, charges then line up into periodically spaced lines of charges. These lines are known as charge-stripes and they are centered either on the ionic metal sites or oxygen sties of the conduction layer depending on the material. Upon further reducing the temperature the spins of the metallic sites (Ni_{2+} spins in the case of LSNO) on the conduction layer order antiferromagnetically between the charge stripes. The ordering of the spins is drastically affected by the charge ordering. The charge stripes act as spin antiphase domain walls. As mentioned previously, the basic physics behind the charge ordering and the hole formation will be a driving force in understanding the dielectric properties of the LSNO.[41]

The ability to stripe order has been associated with a colossal increase in dielectric properties. Due to the novelty of the material, an understanding of all the intricacies of this material is still in its infancy. This thesis attempts to shed light on the dielectric properties of LSNO.

2 Outline of Thesis

This dissertation presented here is divided into two main sections. Chapter 4 deals with the material BST. In the first work (Chapter 4.1), we investigate the role of oxygen non-stoichiometry in BST thin films and a novel route using photon assisted annealing in order to achieve lower losses. In the following section (Chapter 4.2), we investigate the photon assisted annealing method we previously developed and use it as a route to producing high quality BST thin films on non-noble electrodes, namely Ni. This was done in a multi-step process using high temperature, low partial pressure annealing and photon assisted low temperature reoxidation to reform the near surface of the BST thin film

From the previous work on BST, we observed that the upper limit for capacitance density for the BST thin films was approximately 1-2 $\mu F/cm^2$ which was too low for next generation system on package technology. A novel material with a much higher dielectric constant needed to be investigated. Chapter 5 deals with the material LSNO which was chosen due to a recent paper by Krohns *et al.*[54] which showed giant dielectric properties ($\sim 10^5$) well into the gigahertz range. Chapter 5.1 deals with the growth and characterization of polycrystalline thin film LSNO by reactive sputtering from metal targets. Due to the difficulty in obtaining a stoichiometric target from a vendor, this processing route was explored. Dielectric results showed hopping conduction leading to a giant dielectric response as well as interface effects from grain-grain boundary and electrode effects. These results were interpreted as MW type polarization. Chapter 5.2 deals with the epitaxial growth of LSNO on Nb doped $SrTiO_3$. Nb doped $SrTiO_3$ is a highly degenerate n-type semiconductor which acts metallic. Due to the hole doping by the addition of Sr into the LSNO lattice and the mechanism for dielectric response in LSNO, *pn*

junctions were fabricated which were investigated fully. This allowed for an understanding of the carrier conduction in the LSNO thin film. After developing an understanding on the growth of epitaxial thin film LSNO, we investigated the electrical properties as a function of substrate induced strain as well as texturing as discussed in chapter 5.3 . By varying the substrates (single crystal $LaAlO_3$, $SrTiO_3$, $SrLaAlO_4$ and Al_2O_3), we were able to grow LSNO under compressive and tensile strain as well as fiber textured. Dielectric properties in thin film form showed extremely high response on the order to 10^7 with moderate losses. Properties varied significantly between samples due to substrate induced strain. In chapter 5.4, we study the growth and reorientation phenomena associated hyper oxygenated LSNO thin films. We observe that at a critical thickness, the film reorients and continues growth in the new orientation. This is attributed to the ability for oxygen to be incorporated into the lattice as well as the tensile strain produced by the $SrTiO_3$ substrate. Due to the ability to vary the orientation, functional properties can be obtained due to the anisotropy of the crystal which once seemed unobtainable on certain substrates.

Throughout this thesis, we have successfully observed the role of structure and oxygen stoichiometry on the dielectric properties of thin film complex oxides, allowing a greater understanding of processing conditions and polarization mechanisms.

3 Experimental Methods

3.1 Thin Film Deposition and Processing

3.1.1 Sputtering

A thorough description of sputtering is given by Wasa *et al.*[55] Sputtering is a thin film physical vapor deposition technique performed in a vacuum chambers that relies on the collision of plasma to eject material from targets onto substrates. In sputtering a glow discharge plasma of molecules (usually of a noble gas such as Ar) is accelerated into the target. The accelerated plasma impacts the target and ejects the target material. Sputtered atoms ejected are not in thermodynamic equilibrium and tend to deposit on all surfaces of the sputtering chamber. The average number of atoms ejected from the target per incident ion is called the sputter yield and depends on the ion incident angle, energy of the ion, the masses of the ion and target atoms and the surface binding energy of atoms in the target. A schematic of the sputtering process is shown in Figure 14.

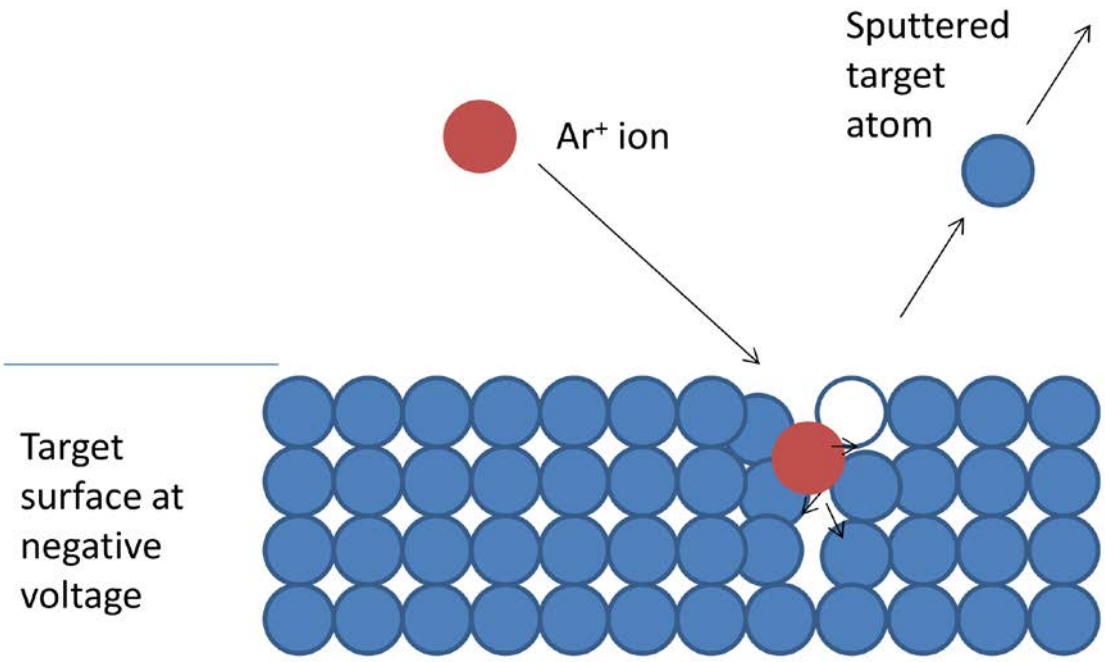

Figure 14: Schematic drawing of the sputtering process.

3.1.1.1 DC Sputtering

DC sputtering is the simplest of such techniques requiring two electrodes: the cathode where the target is placed and the plasma is generated and the anode where the substrate is held. An electric field with sufficient strength is applied between the anode and cathode to accelerate the ionized inert gas to produce highly energetic incident particles. This method is most often used when depositing metals, such as co-sputtering nickel in chapter 5.1 as well as metalizing silicon substrates with platinum as used in chapter 4.1.

3.1.1.2 RF Sputtering

When sputtering insulating material, since the sputtering discharge cannot be sustained due to the buildup of positive charge at the surface, a different method must be used. To sustain the plasma discharge, an alternating current must be used, usually at the RF frequency of

13.56MHz. At these frequencies, ions can no longer follow the switching and electrons can neutralize positive charge build up on the surface thereby leading to ejection of material and sputter deposition. The heave Argon ions (process gas) bombard the target, transferring their kinetic energy to the target, causing the atoms at or near the surface of the target to be ejected and deposit on the substrate surface.

This method is important when sputtering insulating materials as well as when reactive sputtering such as in the presence of oxygen. Reactive sputtering of metals sometimes requires an RF source if the metal is known to oxidize rapidly, such as is the case with depositing La and Sr (chapter 5.1). Reactive sputtering is often used to improve stoichiometry of the films due to the loss of the anion during the deposition process. The anion (oxygen in this thesis) due to its size as well as its reactivity will have a lower mean free path and may end up sticking onto a wall of the chamber rather than leading to a 1:1 transfer from the target to the substrate. By bleeding in oxygen and forming atomic oxygen during the deposition process, oxygen stoichiometry can be increased.

3.1.1.3 Magnetron Sputter Deposition

In order in increase the efficiency and the rate of sputtering, magnet is placed below the cathode to trap free electrons in the applied magnetic field above the surface of the target which increases the deposition rate by increasing the ionization of the sputtering gas. These trapped electrons increase the probability of ionization by several orders of magnitude allowing sputtering pressure to decrease and leading to smoother film surfaces.

For this thesis, sputtering was performed from stoichiometric oxide targets of BST, LSNO as well as reactive co-sputtering from La/Sr mosaic targets, Ni and Pt targets.

3.1.2 Electron beam deposition (E-beam)

E-beam evaporation is a technique to deposit thin films by evaporating a material with an electron beam. While in vacuum, the electrons are thermionically emitted from heated filaments. A transverse magnetic field is applied that serves to deflect the electron beam to focus it onto the hearth and evaporate the material held in the crucible. Due to the ultrahigh vacuum conditions, the evaporated material reaches the substrate as a molecular flow. The key benefit of using e-beam deposition is, wherein sputtering is multidirectional producing a cloud of materials, e-beam deposition is a unidirectional flow of material, producing sharp edged when growing contacts using shadow masks as well as photolithographic patterning. A schematic diagram of e-beam deposition is given in Figure 15. In this thesis, electrical contacts are deposited using e-beam evaporation of various metals through shadow masks. Interdigitated electrodes are deposited using e-beam deposition of 10 nm Ti as an adhesion layer and 100nm Au as the electrode as well as the deposition of material though shadow masks.

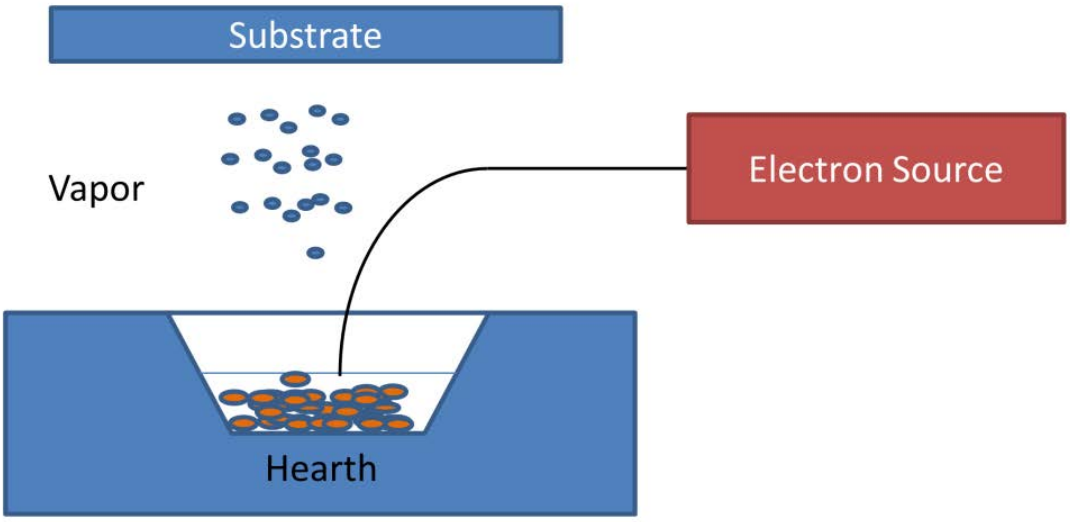

Figure 15: Schematic diagram of e-beam deposition.

3.1.3 Processing Parameters and Post-processing techniques

The success of growth of complex oxides by sputtering is attributed to the growth process and nucleation in thin film which is related to the thermodynamics and kinetics of 2-dimensional crystal growth. Numerous parameters are involved in the entire process of growth. Substrate temperature, process gas pressure and composition and sputtering power are among the most critical in the growth of thin films.

3.1.3.1 Room Temperature Growth

Due to the sputtering process being a physical bombardment of ions to the surface, room temperature growth of thin films leads to an amorphous layer of atoms at the surface in nearly the composition of the target. Due to the ability of ejecting atoms from the surface of the target, the composition of the material deposited on the substrate will vary slightly from the composition of the target. This however, is mostly limited to the size of the atoms deposited, whereas larger atoms that are ejected have a longer mean free path and a higher probability of ending up on the substrate, smaller atoms such as oxygen have a greater probability of interacting with other particles and not ending up on the substrate.

In room temperature grown films, high temperature post processing annealing is required to reach proper crystal phase such as seen in chapter 4.1, 4.2 and 5.1 . This post processing annealing step often leads to polycrystalline thin films where the crystallite size is often defined by the thickness of the film as well as the annealing temperature. Growth of polycrystalline films generally beings with the thermally activated nucleation of islands of the film material on the surface. Initial crystallographic orientation of the film that minimize surface and interface energies are favored over other mechanism and the nucleation rates for clusters with lower

energy orientations. This can lead to textured growth.[56] When sputtering as a function of temperature, difference structural evolution is seen as a function of temperature as first discussed by Thornton in 1977.[57] A schematic of the work down by Thornton is shown in Figure 16.

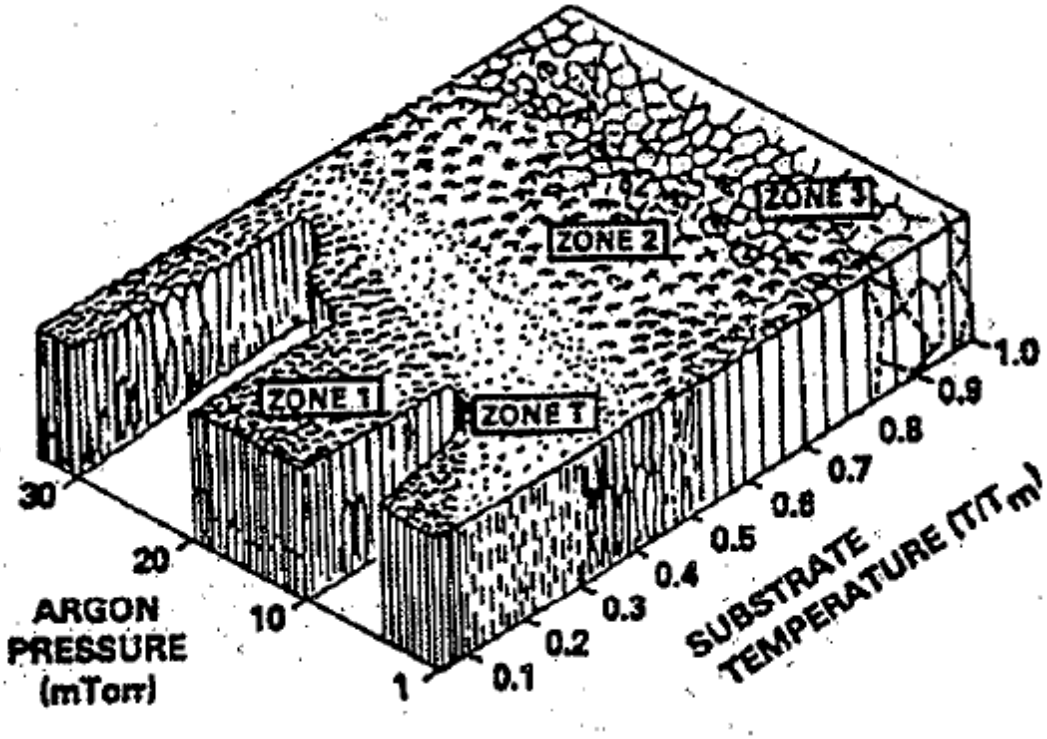

Figure 16: Structural evolution in polycrystalline films as a function of substrate temperature and argon gas sputtering pressure. Reprinted with permission from Ref. [57]. Copyright 1977, Annual Reviews.

In this same light, the flow of process gas is required to improve stoichiometry as well as limit the formation of certain phases and crystallography. When post deposition processing of oxide films is performed, an understanding of the oxidation-reduction reactions of constituent materials must me understood.

Using the simplest oxidation reaction of a metal M, $2M_{(s)} + O_{2(g)} \equiv 2MO_{(s)}$. The standard Gibbs free energy change for a reaction is given by $\Delta G^o = -RT \ln K$ where

$K = \frac{a_{MO}^2}{a_M^2 pO_2}$, R is the gas constant, T is the temperature, K is the equilibrium constant and a is the activity.[58] Assuming the activities of a pure solid to be unity, the free energy change can be written as

$$\Delta G^o = -RT \ln \frac{1}{pO_2}$$

In an Ellingham diagram, an oxide is stable above the line and the metal is stable below the line. This allows one to vary the partial pressure during post processing in order to avoid oxidation of material (as will be seen with the selective oxidation in chapter 4.2) or promote the oxidation of others. The partial pressure as a function of temperature for the oxidation is derived and plotted in Figure 17. This allows for regions to be accessed where thermodynamic stability can be obtained for different compounds.

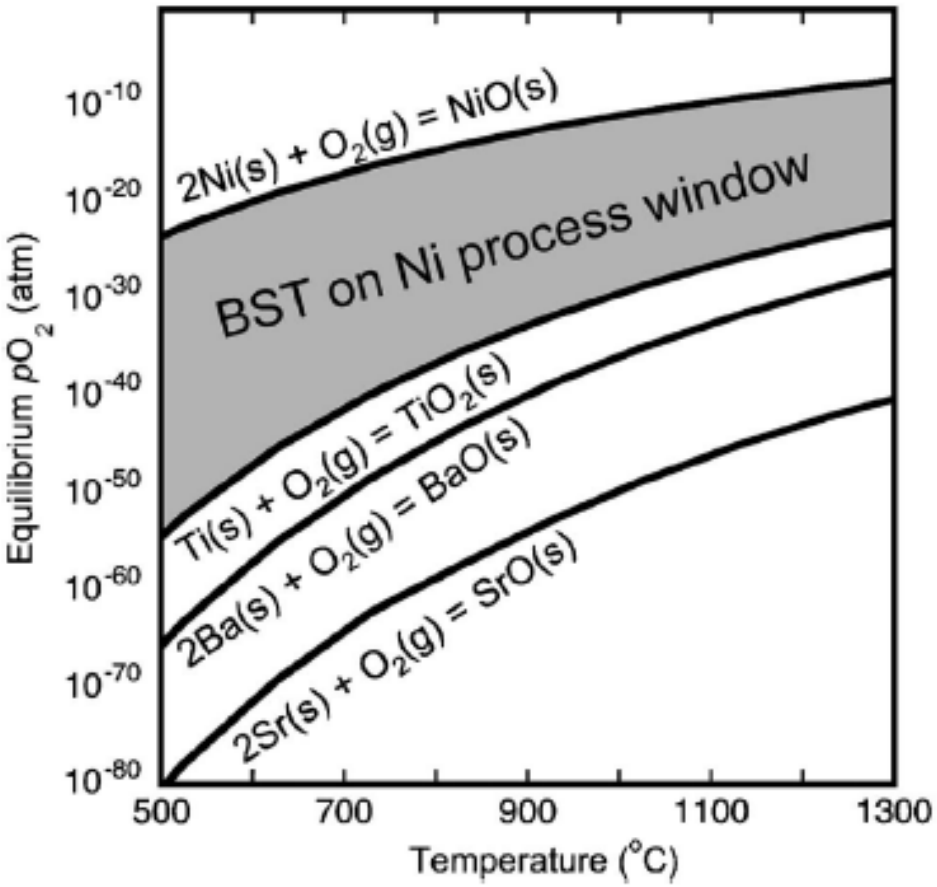

Figure 17: *pO_2 vs* temperature diagram showing processing window in which oxides of Ba, Sr and Ti are stable with metallic Ni as derived from elligham diagrams. Reprinted with permission from Ref.[59]. Copyright 2008, American Institute of Physics.

Since thermodynamics often leads to limitations in processing, kinetically driving oxidation is often necessary as will be seen in chapter 4.1and 4.2.

With post-growth annealing, in order to control the partial pressure of oxygen, a water-hydrogen reaction is utilized. By varying the flow rate of forming gas (5% H_2) with Argon and by using a Yttrium stabilized tube in the process area (coated on both sides by platinum to form a half-cell reaction), a voltage is obtained from the difference in oxygen content across the half cell. The voltage (emf) is given by the equation

$$emf = \frac{RT}{4F}\ln\left(\frac{P_{O_2}^{'}}{P_{O_2}^{''}}\right)$$

Where F is the Faraday constant, R is the universal gas constant, T is the temperature $P_{O_2}^{''}$ is the air (~0.21) reference and $P_{O_2}^{''}$ is the concentration of the gas in the cell.

3.1.3.2 Epitaxial Growth of oxide thin films

When considering the growth of epitaxial films, it is critical to determine the proper substrate, temperature, processing gas conditions and gun power. One of the key components for the growth of epitaxial films lay in the choice of substrate as shown in chapter 5.3. Near lattice matching must be chosen to ensure oriented growth. The proper amount of thermal energy (substrate heating) is needed to allow for the redistribution of atoms at the surface into the lowest energetic (epitaxial) formation. Process gas pressure is another substantial parameter in sputter deposition, impacting composition and growth. As stated earlier, oxygen must be included in order to promote stoichiometry in the films. Gun power also leads to a substantial parameter when considering epitaxial growth. The higher the rate, the less time the adatoms at the surface have to find the minimal energy state, and mosaicity in the film will begin to develop, sometimes referred to as island growth.

3.2 Ultraviolet Photon Film Synthesis

3.2.1 Photochemistry of Oxygen

The ability of ultraviolet (UV) light to decompose molecules has been known for a long time. For photon assisted oxide film synthesis, the creation of active oxygen species and ozone is important due to the ability to incorporate oxygen species beyond thermodynamic limitation. As early as the early 1980s, Young and Tiller [60] have shown that UV assisted oxidation plays a significant role in the thermal oxidation of Silicon. This stems from the fact that the absorption of the oxygen molecule leading to its dissociation as well as the availability of "hot" electrons in the conduction band. This suggests that electron injection into the oxide layer (when creating oxide layers on metals using UV enhanced oxidation) was responsible for the dissociation of O_2 into $O\text{-}O^-$ near the metal/oxide interface.[61] The ability of UV enhanced oxidation stems from the ground state of Oxygen being approximately 5.115eV.[62] The photon absorption in the region 175nm-200nm is called the Schumann-Runge system. The Schumann-Runge bands converge to the limit at 175nm corresponding to the production of ozone and atomic oxygen at the threshold wavelengths of 242.4nm and 175 nm as given in the form

$$O_2 \xrightarrow{h\nu} O + O$$
$$O + O_2 + M \xrightarrow{h\nu} O_3 + M$$

where M is a third body.

By using high intensity mercury arc lamp whose characteristic radiation falls at 254nm and 185nm due to the resonance spectrum of Mercury, full dissociation of oxygen will occur. UV exposure experiments were performed in a custom built load lock attached furnace allowing controlled annealing conditions. An image of the custom UV annealing setup in the load lock

chamber is given in Figure 18. Not shown in the image is the heating unit on the load lock cover.

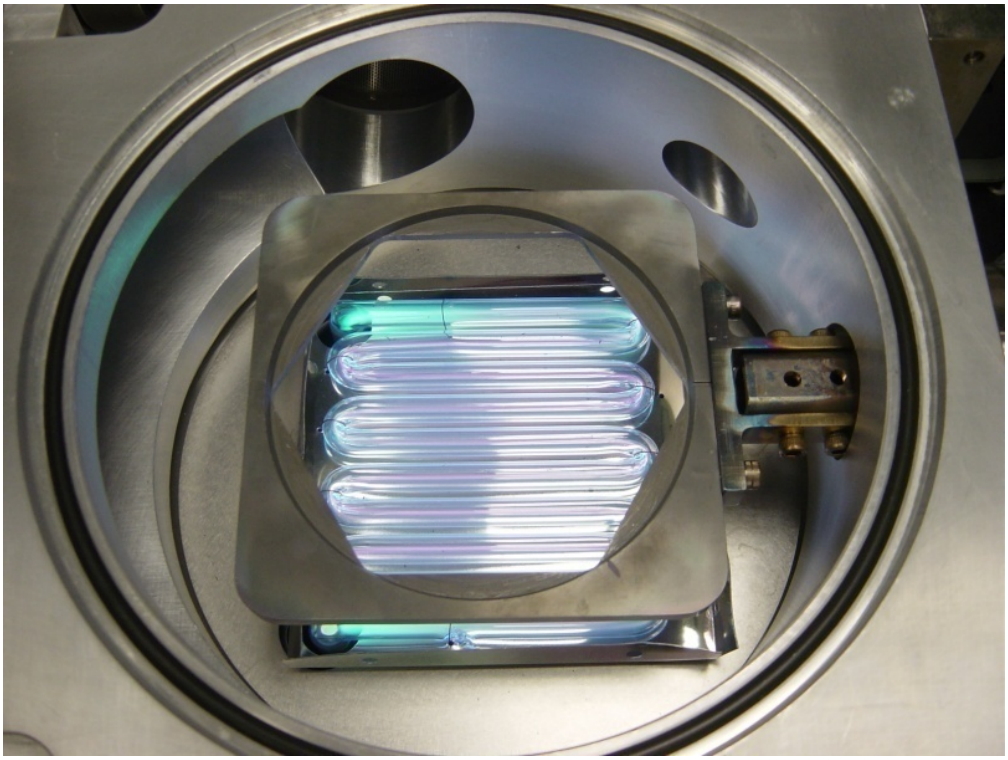

Figure 18: Load lock UV annealing setup that were used in these experiments.

3.2.2 Recent Review of UV enhanced oxidation

It was recently has shown that the use of UV enhanced oxidation can significantly oxidize films as well as remove defects present in the growth process. Essary *et al.* showed that the UV enhanced oxidation and nitridation techniques can be used on Hafnium in order to fully oxidize high-K gate materials at low temperatures.[63] Srivastava *et al*. showed that UV enhanced growth led to improved structure and electrical properties in BST thin films in pulse laser deposition (PLD) grown BST thin films.[64] Work by Tsuchiya *et al.* has shown the oxidation enhancement using UV in fluorite structured films. [65] These recent works have shown light enhanced oxidation enables the formation of stoichiometric metal oxides, eliminate defects in the

film and significantly lower the processing temperature conventionally associated with the formation of the oxide.

3.3 X-Ray Characterization

3.3.1 Fundamentals of Diffraction

A thorough description of x-ray diffraction is given in the book *Elements of Modern X-Ray Physics.*[66] The discovery of x-rays dates back to 1895 by Wilhelm Conrad Rontgen in Wurzburg.[67] It was not until von Laue, in 1912, obtained the first diffraction pattern from a crystal of Copper sulfate did the ability of understand the periodic nature of lattices became known. In 1913, W.H. Bragg and W. L. Bragg studied a number of crystals and laid the foundations of crystallography, which allows for the probing of the long range atomic structure of materials. The Braggs' won the Nobel prize in physics for the analysis of crystal structures by means of x-rays in 1915.

The scattered amplitude of a diffracted x-ray beam is proportional to the Fourier transform of the electron density distribution of the material. The Fourier transform of some function in real space, $g(\vec{r})$, where $(\vec{r})$ is a real space vector given by

$$F[g(\vec{r})] = \int g(\vec{r}) e^{-i\vec{k}\bullet\vec{r}} d\vec{r}$$

Where $\vec{k}$ is a reciprocal space vector. The reciprocal lattice is the Fourier transform of the electron density distribution, $\rho(\vec{r})$, of the structure.

The incident x-ray $\vec{k}_0$ is a plane wave in the direction $\hat{k}_0$, which is the same in reciprocal and real space

$$\vec{k}_0 = \frac{2\pi}{\lambda}\hat{k}_0$$

In kinematic diffraction theory, scattering is perfectly elastic, which states that there is no change in energy between the scattered ray, $\vec{k}_h$, and the incident ray, $\vec{k}_0$

$$|\vec{k}_h| = |\vec{k}_0| = \frac{2\pi}{\lambda}$$

The scattering vector, $\vec{k}$, is the difference between the scattered vector and the incident vector.

$$\vec{k} = \vec{k}_h - \vec{k}_0$$

Using the magnitude of the scattering vector is determined by the geometry of the scattered and incident vector for a given scattering angle 2θ, as shown in Figure 19B.

$$|\vec{k}| = \frac{4\pi \sin\theta}{\lambda}$$

Equation 1

If the scattering is off one electron, the amplitude of the scattering vector is the electron scattering factor, $f_e(k)$. If the scattering is off an atom, where $\vec{r}$ is the position from the nucleus, the scattered amplitude is

$$f_i(\vec{k}) = \int f_e(k) n_i(\vec{r}) e^{-i\vec{k}\bullet\vec{r}}\, d\vec{r}$$

where $n_i(\vec{r})$ is the electron density distribution. A molecule with atoms at real space positions, $\vec{r}_i$, can be described by

$$\sum_i \delta(\vec{r} - \vec{r}_i)$$

where i represents each atom in the molecule and $\delta(\vec{r} - \vec{r}_i)$ is the delta Dirac function. The electron density distribution for each atom is $n_i(\vec{r}) * \delta(\vec{r} - \vec{r}_i)$ where * is the convolution operator. The total electron density distribution is

$$b(\vec{r}) = \sum_i n_i(\vec{r}) * \delta(\vec{r} - \vec{r}_i)$$

The total scattered amplitude from a molecule is

$$\mathbf{F}(\vec{k}) = f_e(\vec{k})F[b(\vec{r})] = f_e\sum_i F[n_i(\vec{r})] \bullet F[\delta(\vec{r}-\vec{r}_i)] = \sum_i f_i(\vec{k}) \bullet F[\delta(\vec{r}-\vec{r}_i)]$$

where the convolution theorem

$$F[g_1(\vec{r}) * g_2(\vec{r})] = F[g_1(\vec{r})] \bullet F[g_2(\vec{r})]$$

has been used. Since $F[\delta(\vec{r}-\vec{r}_i)] = e^{-i\vec{k}\bullet\vec{r}_i}$

$$\mathbf{F}(\vec{k}) = \sum_i f_i(\vec{k}) e^{-i\vec{k}\bullet\vec{r}_i}$$

which is called the structure factor. A crystal structure is described by a lattice function

$$L(\vec{r}) = \sum_i \delta(\vec{r}-\vec{a}_i)$$

where $\vec{a}$ are the vectors to all of the positions of the lattice sites. The electron density distribution of the structure is

$$\rho(\vec{r}) = b(\vec{r}) * L(\vec{r})$$

The scattered amplitude therefore given by

$$A = f_e(\vec{k})F[\rho(\vec{r})] = f_e(\vec{k})F[b(\vec{r})] \bullet F[L(\vec{r})] = \mathbf{F}(\vec{k}) \bullet L'(\vec{k})$$

where $L'(\vec{k})$ is the reciprocal lattice. The scattered intensity is

$$I = AA^* = |\mathbf{F}(\vec{k})|^2 \bullet L'(\vec{k})$$

where A^* is the complex conjugate of A. The intensity is non-zero only when $\vec{k} = \vec{b}$, where $\vec{b}$ is a reciprocal lattice vector. For a give interplanar spacing, d

$$|\vec{b}| = \frac{2\pi m}{d}$$

Equation 2

where m is an integer. Equating Equation 1 and Equation 2 gives Bragg's law, $m\lambda = 2d\sin\theta$. Visually, Braggs law can be visualized as seen in Figure 19A.

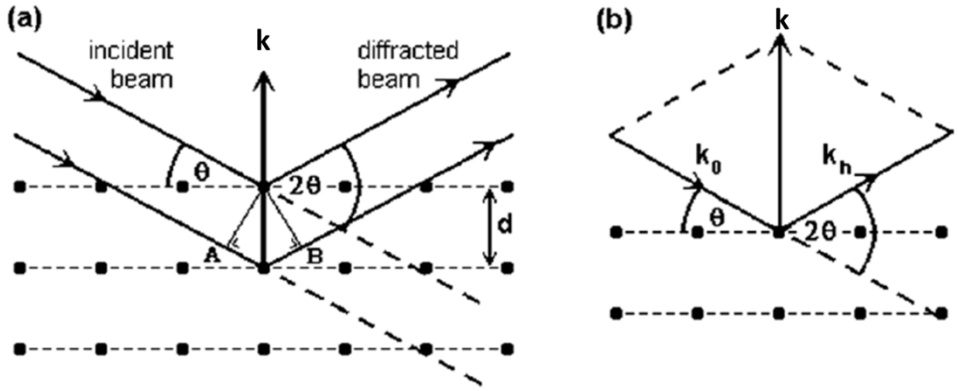

Figure 19: (a) Bragg's Law and the (b) relationship of the incident, diffracted and scattering vectors with respect to the crystal. Plants of atoms are indicated by dotted lines. Reprinted with permission from Ref.[69]. Copyright 2009, IOP Publishing LTD.

The structure factor explains why some peaks are not observed in the diffraction pattern of a crystal. The diffracted peaks should be delta functions. However, they are broadened by the finite size of the sample, temperature and experimental equipment such as the width of the x-ray source and the detector slits.

3.3.2 X-Ray Diffraction (XRD)

One of the simplest setup for an x-ray diffractometer is the rotating axis of the specimen and detector as defined as the θ and 2θ axis, respectively. The detector can be rotated about the sample and set at any desired angular position. The crystal planes that are parallel to the surface that satisfy braggs law are diffracted and allow for the probing of the lattice image. In the case of polycrystalline samples, due to the random rotation of the grains, all grains should satisfy all Bragg conditions through the entire scan. However, if a film is highly textured or epitaxial, peak

positions will be missing due to the orientation of the grains. If this is the case, other diffraction methods must be employed to find the peaks. In the following sections, different methods pertaining to diffraction in polycrystalline, textured and epitaxial films will be discussed.

3.3.3 Glancing Incidence X-Ray Diffraction (GIXRD)

In the analysis of polycrystalline thin films, a glancing incident scan is commonly used to observe the reflection peaks. The sample is placed at an angle ω with respect to the x-ray beam and kept constant while the detector is scanned across 2θ. The detector is rotated around the sample at a consistent rate. This allows the x-rays to be incident on the film and maximize the x-ray volume of the thin film sample. Since the film is polycrystalline, many grains are being exposed at the same moment thus satisfying Bragg's law and showing all peaks present. It must be noted that this scan can only be utilized for polycrystalline samples and that any texturing and orientation will not be observed. A drawing of glancing incidence diffraction is given in Figure 20.

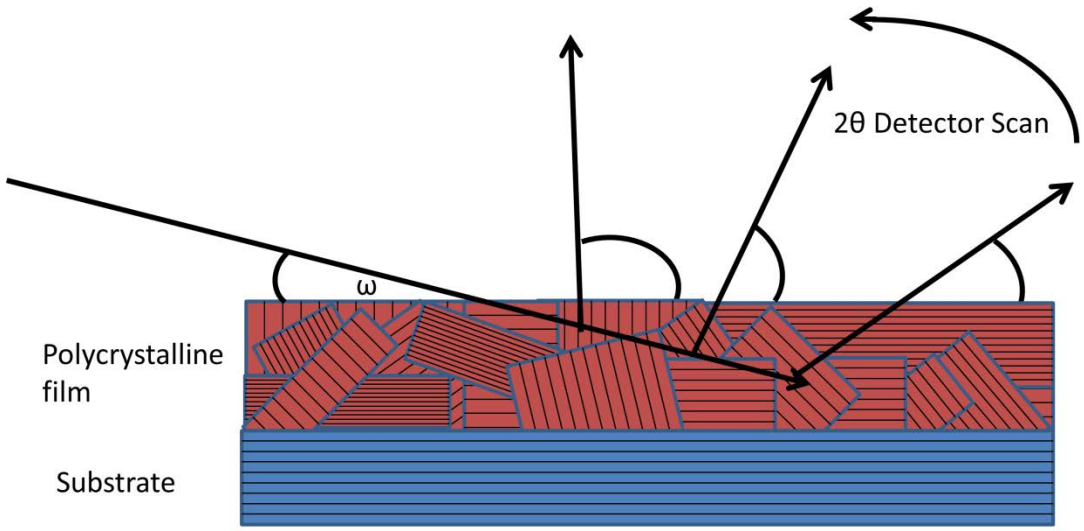

Figure 20: Measurement geometry of a glancing incidence x-ray diffraction scan. Note the random orientation of the grains allowing for the satisfaction of Bragg's law. Striped lines indicate lattice planes.

3.3.4 X-Ray Reflectivity (XRR)

A thorough review of reflectivity is given in the work by Chason and Mayer.[68] The characterization of surfaces and interfaces in the near-surface regime of materials and layered structures has become a field of extensive research activity in the last decade. Investigations include the study of surface and interface roughness, sub-surface composition, crystallinity, electron density, mechanical damage and its variation as a function of depth over the first 100 nanometers of the material.

X-ray reflectivity provides a wealth of information on thickness and interfacial properties on the nanometer scale, such as layer thickness, the layers electronic densities, surface and interface roughness and roughness morphology. The reflectometry method is, therefore, well suited for the study of surfaces and thin layers.

The index of refraction for x-ray is given by

$$n = 1 - \delta - i\beta$$

where δ can be defined as

$$\delta = r_e N_e \lambda^2 / 2\pi$$

and where the wavelength λ is far from the absorption edge. N_e is the electron density and $r_e = e^2 / mc^2$, classical electron radius. β is related to the linear absorption coefficient μ by $\beta = \mu\lambda / 4\pi$. Total reflection occurs at a critical angle (α_c) for which transmission into the film becomes 0. Neglecting the absorption (for β=0) the index of refraction of the medium which follows Snell-Descartes law gives us

$$n \cong 1 - \delta = \frac{\cos\alpha_i}{\cos\alpha_t}$$

where α_i is the angle of incidence and α_t is the angle of transmission. Expanding the cosine for small angles gives us the critical angle

$$\alpha_c \approx \sqrt{2\delta}$$

For a single thin film layer, the maxima and minima of the reflection of fringes, which is proportional to the thickness of the film, appears as

$$\alpha_i^2 = 2\delta + (m_i + \Delta m)^2 \lambda^2 / 4d^2$$

where δ is the thickness of the film, m_i is the integer, Δm is the value of ½ or 0. If the mass density of the film is higher than that of the substrate, $\Delta m = 1/2$ for the maximum and Δm for the minimum and vice versa. This method was used in all chapters to determine growth rate and thickness. A typical x-ray reflectivity curve, showing the thickness and critical angle is given in Figure 21.

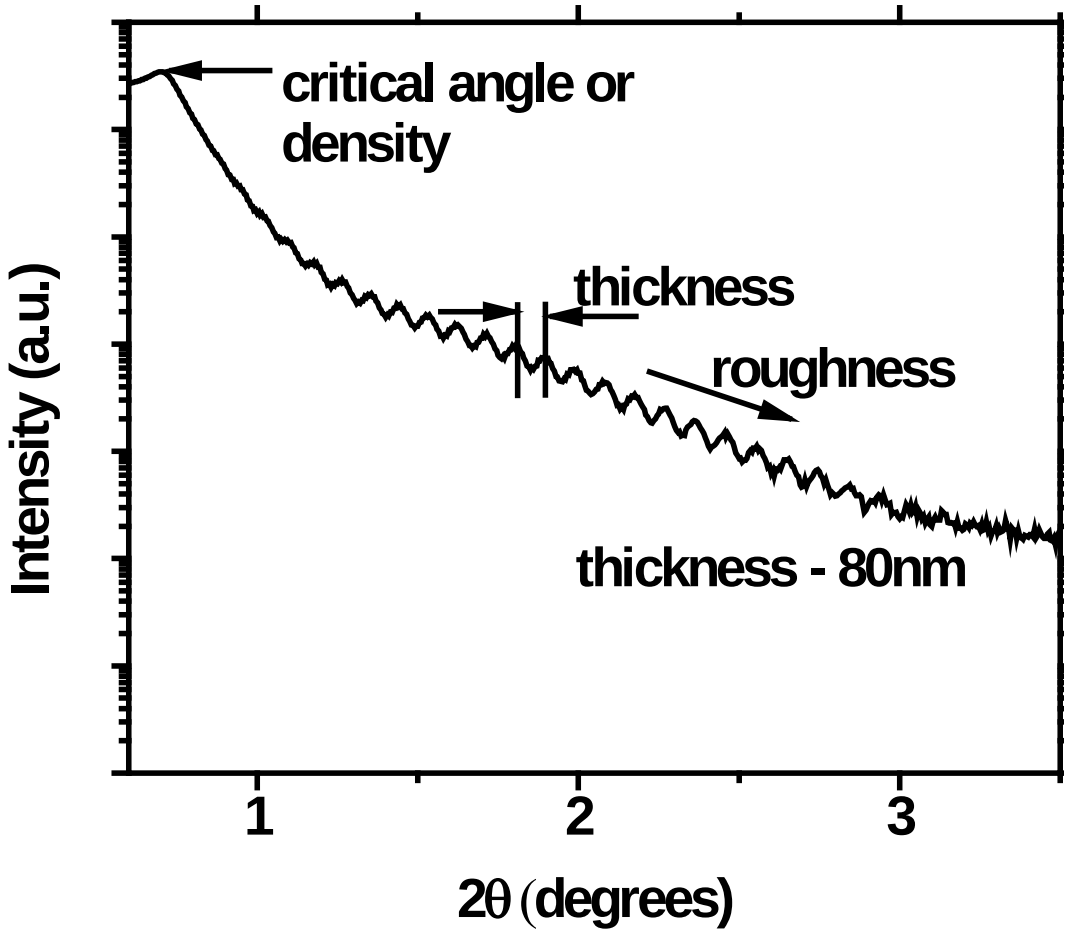

Figure 21: X-ray reflectivity diagram.

3.3.5 Azimuthal Scan (ϕ Scan)

Azimuthal scan is a scan mode used to determine the in-plane ordering between film and substrate by rotating the substrate around the phi position at a known Bragg reflection angle and at a known χ angle. The technique is used to evaluate the epitaxial relationship between the film and substrate by indexing the film peaks to known substrate peaks and analyzing the offset and symmetry of reflections.

To take an azimuthal scan, we must choose a diffraction peak diffrerent from 00*l* which is located at a tilted configuration i.e. $\chi \neq 90^0$ The appropriate χ is determined from the interplanar angle of the planes of interest to the surface normal. Symmetry of the crystal from pole projections can determine the reflections in the ϕ scan. A typical pattern is given in Figure 22.

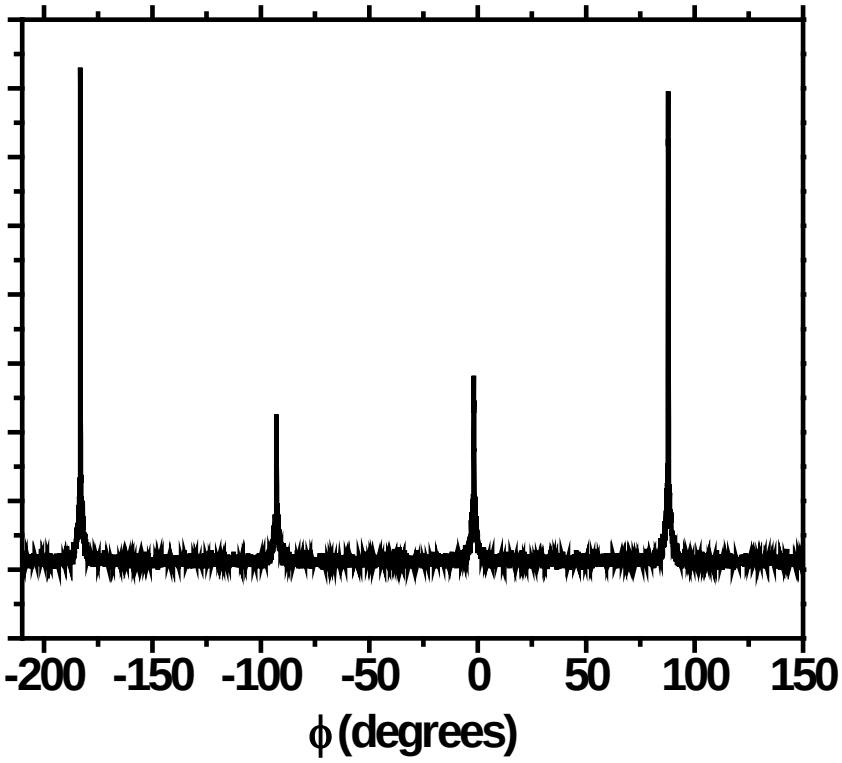

Figure 22: Typical ø scan observed showing four- fold symmetry.

3.3.6 Rocking Curve

A rocking curve is used to determine if the film is in registry with the substrate or has good mosaicity. This scan is performed by holding the detector at a 2θ peak position and rocking the sample through an angle, ω ,in small increment around the peak as shown in Figure 23A. For polycrystalline samples, no peak should be observed in the rocking curve. For mosaic films, columnar growth and textured, a diffuse peak should be observed like that is Figure 23C

whereas in epitaxial films, very sharp and narrow rocking curves are observed such as shown in Figure 23B. The width of the rocking curve peaks is an indication on the quality of the film and a convenient measure to determine proper growth conditions.

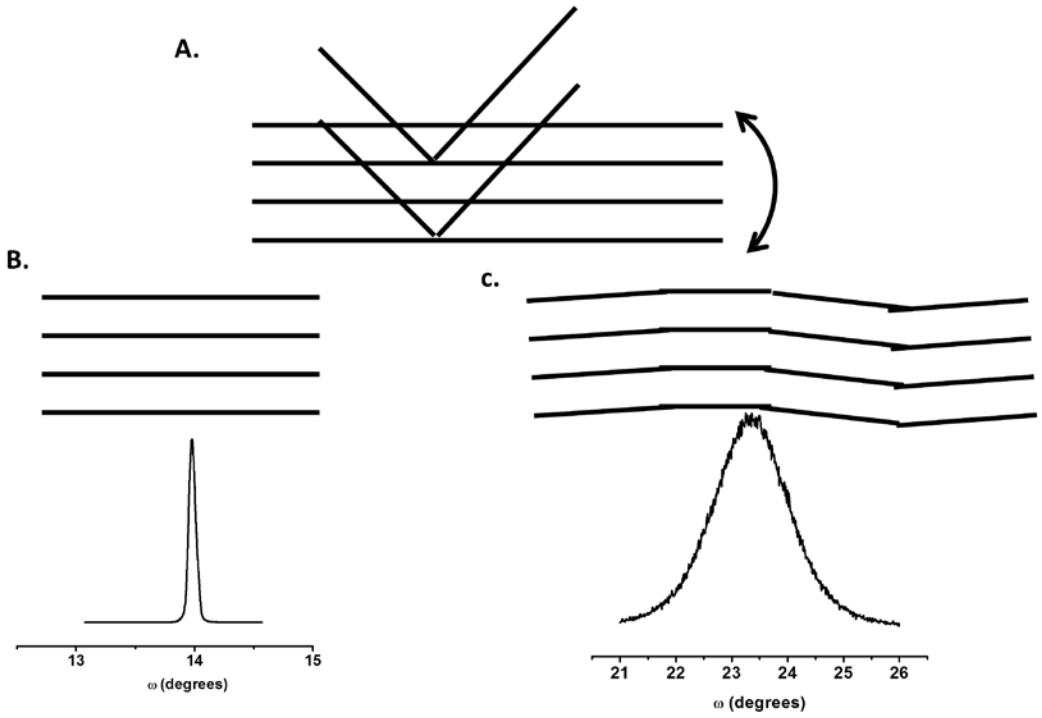

Figure 23: (A) Schematic drawing of ray diagram showing a rocking curve. (B) Rocking curve for a single crystal sample. Note the lattice planes that are all contributing to the diffraction at precisely the same moment. (C) Rocking curve for a mosaic or textured sample. Note the lattice plane mosaicity contributing to the broadening.

3.3.7 Reciprocal Space Map (RSM)

An excellent and thorough review of x-ray diffraction is given in Moram and Vickers work on the diffraction of III-nitrides.[69] Reciprocal space mapping is a term used to describe an x-ray diffraction technique which seeks to extract information from thin epitaxial films through understanding the registry of the x-ray diffraction pattern of the film to that of the substrate. The crystal acts as a 3D diffraction grating so as the sample and/or detector are moved, a 3D array of

diffraction can be investigated. Each set of crystal planes will produce a diffraction spot, with the positions and shapes of the diffraction spot being inversely related to the spacing of the crystal plane and size of the crystallite. The crystal planes are associated with real space and the diffraction spots with reciprocal space. These diffraction spots make up the 3D reciprocal lattice.

In order to construct the reciprocal lattice, reciprocal lattice points associated with every crystal plane are plotted for both the substrate and for the epitaxial film. Once an area is accessed to have diffraction intensity from the substrate and film peak, a collection of 2θ-ω scans (usually performed asymetrically in order to align the beam parallel to the substrate) is performed while incrementally changing the position of ω. From the information obtained, a clean understanding of the growth, strain, relaxation and mosaicity of the film can be described. A section through reciprocal space is given in Figure 24. The Ewald sphere construction is often used to illustrate this. The same vectors are shown along with a sphere of radius $1/\lambda$. This sphere shows which part of reciprocal space we can explore with k, given a particular wavelength λ and angle θ. As θ increases the length of the scattering vector k increases up to a maximum possible length of $2/\lambda$. There the sphere touches a spot, diffraction occurs. Regions of reciprocal space where the sample block a beam are shown in grey and inaccessible.

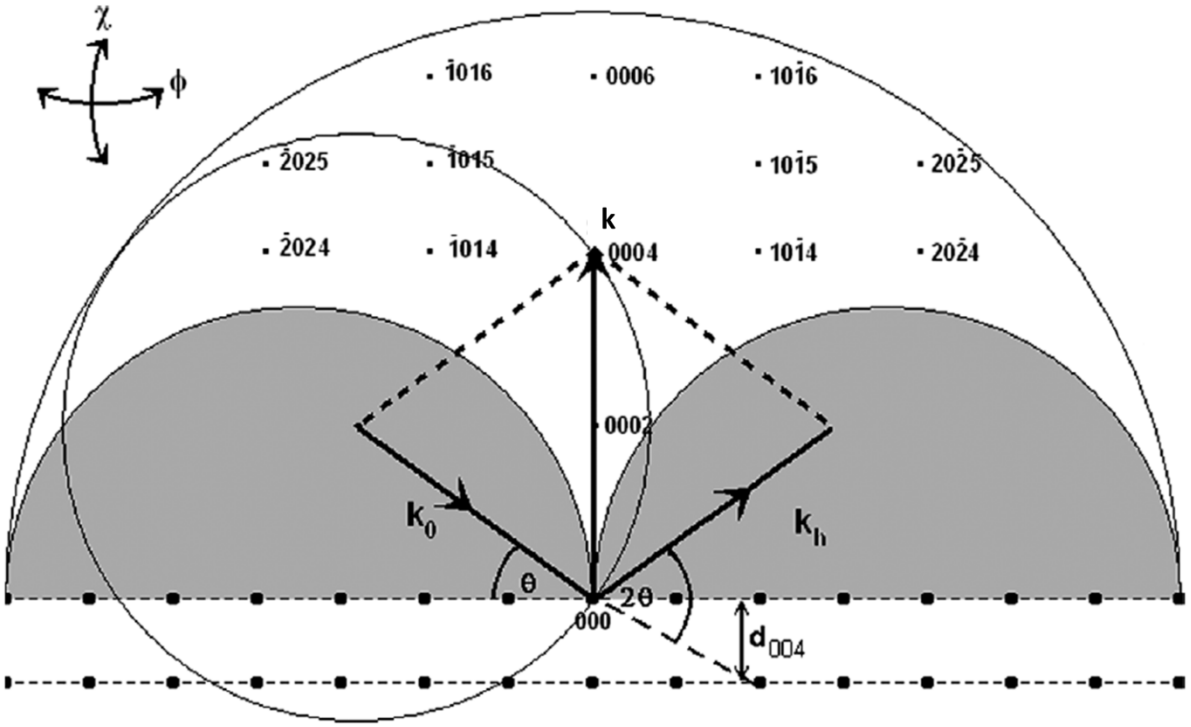

Figure 24: Reciprocal Space Map showing the Ewald sphere construction. Reprinted with permission from Ref.[69]. Copyright 2009, IOP Publishing LTD.

3.3.7.1 Analysis of Reciprocal Space Maps

After a series of coupled of ω/2θ Bragg scans take place, they are then converted to the scattering vectors q_x and q_z and displayed as contour plots. The scattering vectors are given as

$$q_x = \frac{1}{\lambda}\{\sin\omega\Delta\omega - \sin(\varphi-\omega)(\Delta\varphi-\Delta\omega)\}$$

$$q_z = \frac{1}{\lambda}\{\cos\omega\Delta\omega + \cos(\varphi-\omega)(\Delta\varphi-\Delta\omega)\}$$

where ω and $\varphi-\omega$ are the angles between incident beam, diffraction beam and the sample surface, respectively. $\Delta\omega,\Delta\varphi$ are the deviations of incident and diffraction beams from their

Bragg conditions. For the symmetric reflection, $\omega=\theta$, $\varphi-\omega=\theta$; while for the grazing indicence asymmetric reflection $\omega=\theta-\Phi$, $\varphi-\omega=\theta+\Phi$. θ is the Bragg angle, Φ is the angle between the diffraction lattice plane and the sample surface.

3.3.7.1.1 Strain

When a film is deposited onto a single crystalline substrate, the lattice may be fully strained, fully relaxed or an intermediate, partially relaxed state. For a fully strained film, the matching of the in-plane lattice vector of the film to the substrate necessitates that both the symmetric and asymmetric x-ray reflections of the substrate and film lie vertically above each other in reciprocal space. For a fully relaxed layer, the in-plane vector is free of substrate constraints. Neglecting mosaicity and other effects for the time being, the film and substrate reflections for a fully relaxed layer will lie along a radial line through the origin. Figure 25 and Figure 26 clearly shows the effect of strain and relaxation in reciprocal space maps. Degree of relaxation is given by a relaxation triangle as shown in Figure 27 and described elsewhere.[71]

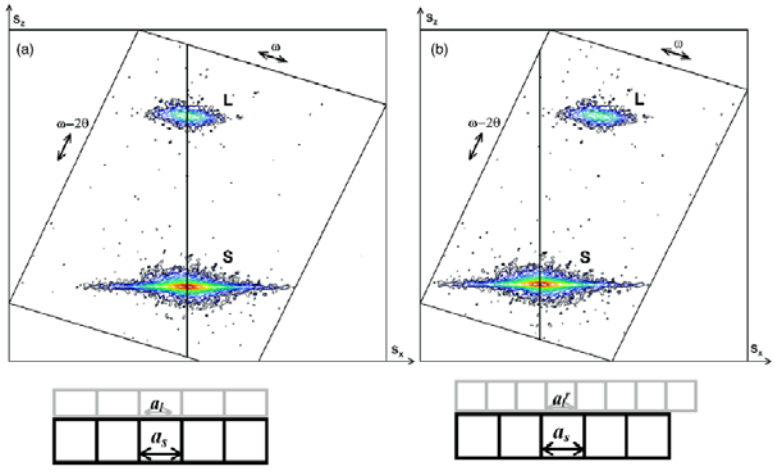

Figure 25: RSM data for a (a) strained and (b) partially relaxed film. Reprinted with permission from Ref.[69]. Copyright 2009, IOP Publishing LTD.

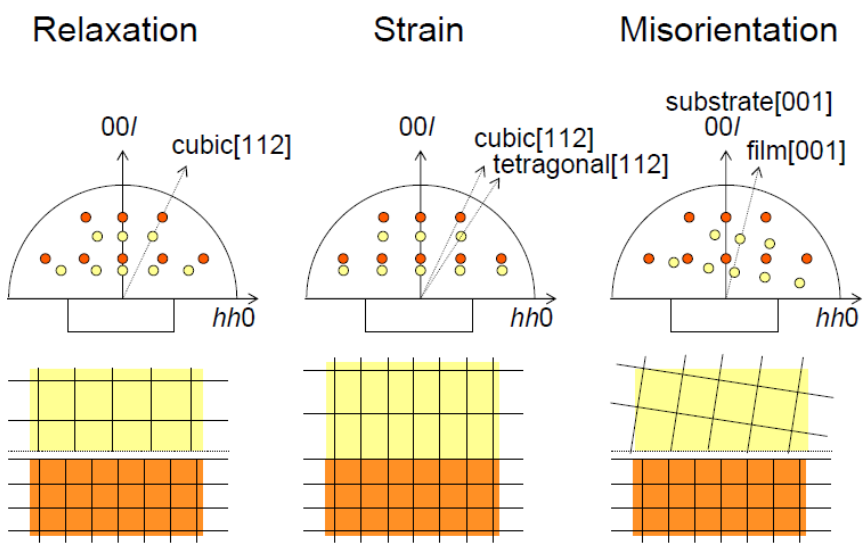

Figure 26: Reciprocal Space Maps showing the effects of relaxation, strain and misorientation. Reprinted with permission from Ref.[70]. Copyright 2010, Rigaku Corporation.

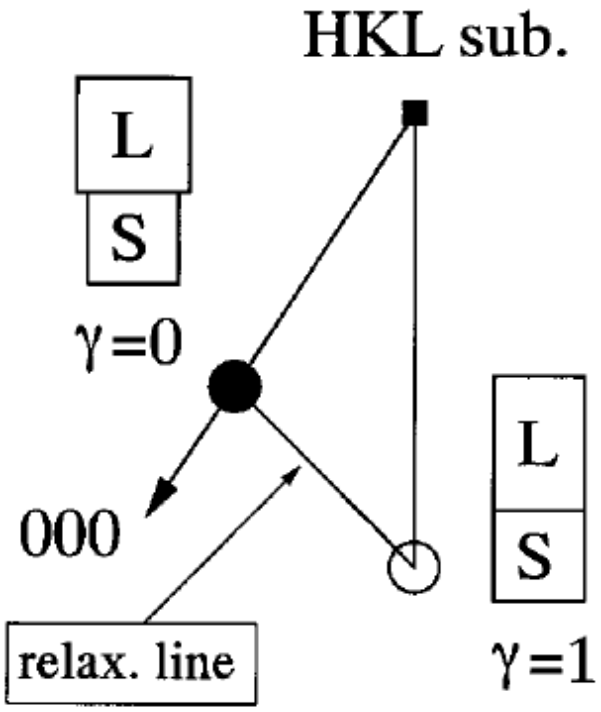

Figure 27: Schematic diagram showing the degree of relaxation in epitaxial films. Reprinted with permission from Ref.[71]. Copyright 1997, American Institute of Physics.

3.3.7.1.2 Mosaicitiy

Often a "perfect" epitaxial film is not grown. Perfect epitaxy is defined as a single extended crystal having perfect registry with the orientation of the underlying layer. Textured epitaxy is close to, but varies from the underlying substrate both within the surface plan and parallel to the surface normal. The orientation of mosaic crystal components are determined by the underlayer. The crystals in general extend through the layer depth but will have limited dimensions laterally. The distribution of tilts of mosaic blocks in a layer will exhibit itself as an extended region of scattering as the sample is rocked in the x-ray beam. In scattering space, this will manifest itself as a broadening of the film peak in the out of plane vector i.e. horizontal.

From the shape and the size of the broadened peak, a correlation function can be calculated in order to quantify the degree of mosaicity. A schematic of a reciprocal space map showing mosaicity is given in Figure 28.

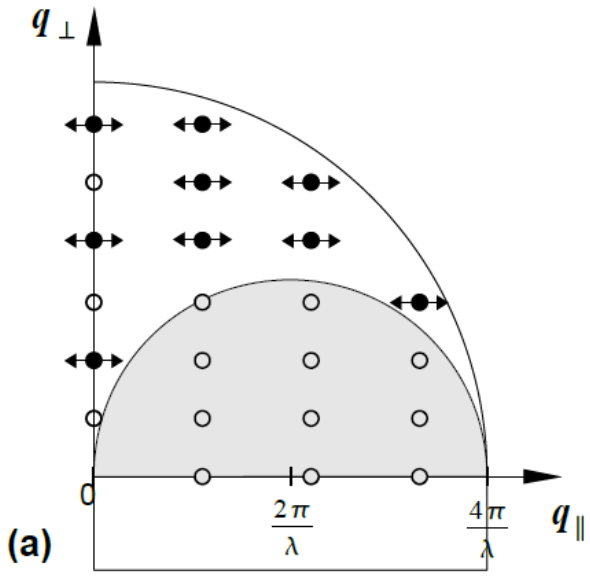

Figure 28: Spreading of the reciprocal space map as a function of mosaicity. Reprinted from Ref.[72].

3.3.8 Pole Figures

An x-ray pole figure is a representation of the orientations of all the grains in a material. Pole figures are a way of representing the orientation relationship between the sample coordinate system and the crystal coordinate system. The crystal coordinate system is defined with respect to the unit cell of the crystal and is described by the three Euler angles of θ, χ and ϕ since poles are symmetric with respect to inversion. The relationship is described by the intensities of the reflection observed and visualized on a 2D surface known as a stereographic projection.

In order to form a pole figure, General Area Detector Diffractometer systems (GADDS) should be used due to the constraints required to scan such a large area of the sample. The basic

setup of such a system is shown in Figure 29. Through a combination of movements of ϕ and χ with at different 2θ positions, a complete stereographic projection of a film is obtainable.

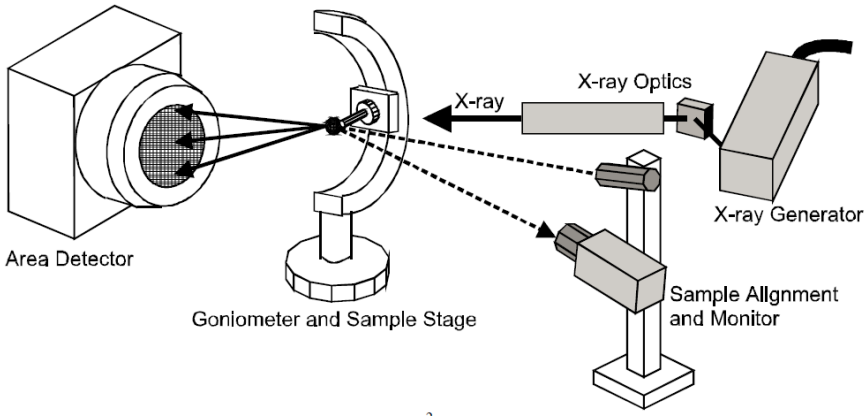

Figure 29: Setup for GADDS scan. Reprinted with permission of ICDD from Ref.[73]. Copyright 2000, International Centre for Diffraction Data.

Figure 30 shows the diffracted x-ray from a (a)single crystal sample showing discrete reflections and a (b) polycrystalline sample which shows diffraction cones formed by large number of randomly oriented crystallite grains. Each diffraction cone corresponds to the diffraction from a family of crystalline planes in all participating grains. Texture is used to refer to the crystallographic texture: non-random distribution of crystallographic grain orientations in a polycrystalline sample. Pole figure analysis is done in chapter 5.3 and 5.4.

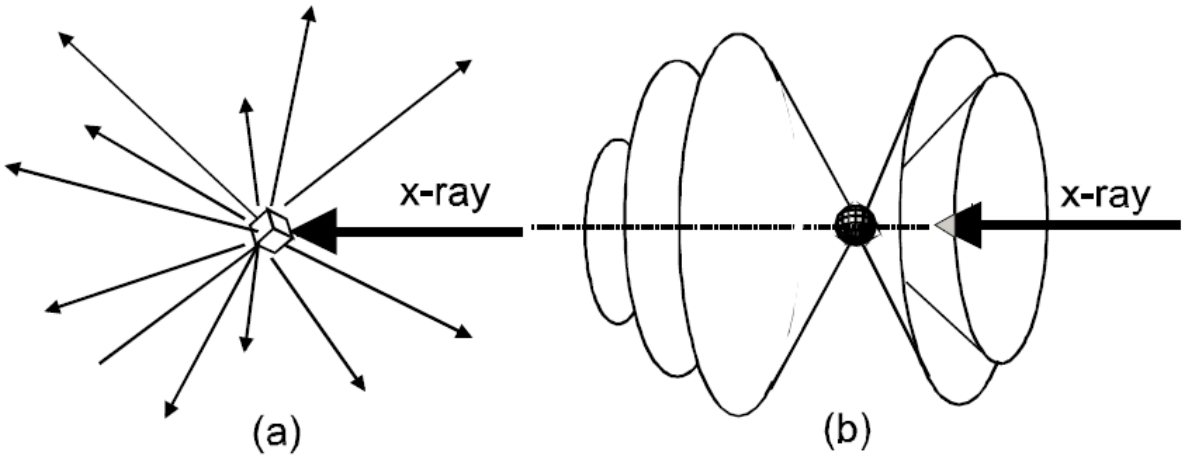

Figure 30: (a) diffraction poles from a single crystal (b) diffraction cones from a polycrystalline material. Reprinted with permission of ICDD from Ref.[73]. Copyright 2000, International Centre for Diffraction Data.

3.4 Electrical Measurements

3.4.1 Electrical Contacts

The choice of electrode contact materials must meet certain requirements such as high conductivity, sufficient resistance against oxidation, good adhesion and interfacial smoothness to reduce leakage current as well as form a good schottky barrier for contact to the dielectric. Pt is a common material used in this study do to its high work function (~5.6eV), high temperature stability and high conductivity however it suffers from poor adhesion and hillock formation.[74] Pt requires an adhesion layer if it is to be used as a bottom electrode. Ni has also been used as a bottom electrode material however it requires low oxygen partial pressure annealing. Ni also has a high work function (~5.15eV) allowing it to form a large schottky barrier.

In the study using interdigitated capacitors, Au was used to form contacts. A 10nm thick Ti adhesion layer was used due to the poor adhesion of Au to surfaces. Au has good electrical

conductivity, resistance to oxidation and a high work function (~5.3eV). In all studies, the usual thickness of electrode materials was approximately 100nm.

The study of LSNO being used as a *pn* junction with Nb doped $SrTiO_3$ (chapter 5.2) was not entirely planned so the use of Pt electrodes was not ideal since ohmic contacts should be used however, this did not change the rectification observed at the interface. Rectification was verified using different work function metals.

3.4.2 Metal-Insulator-Metal Devices and Interdigitated Capacitor Devices

Metal-insulator-metal devices (MIMs) and Interdigitate Capacitors (IDCs) are the two basic types of geometries used to measure the capacitance of a thin film. In the MIM structure, the thin film layer is sandwiched between two metallic layers. The film is deposited directly onto the bottom metal electrode. Top electrodes are deposited through a shadow mask. On the other hand, the IDC structure allows for flexibility in the choice of insulating substrate since the metal electrodes are only deposited on the surface of the film through a photolithograph process.

In general, IDC devices are simpler to fabricate requiring only a single metallization step compared to multiple steps. Another advantage of IDCs is that the thin film can be directly deposited onto the substrate and can therefore be annealed at higher temperatures. In the case of MIM devices, the difference in the coefficient of thermal expansion for the multiple layers of the bottom electrode may impose limitations to annealing temperature as well as morphology.

For MIM configurations, the capacitance value is given by $C = \frac{\varepsilon_r \varepsilon_o A}{d}$ where ε_r is the relative permittivity of the material and ε_o is the permittivity of free space. A schematic of the structure is given in Figure 31.

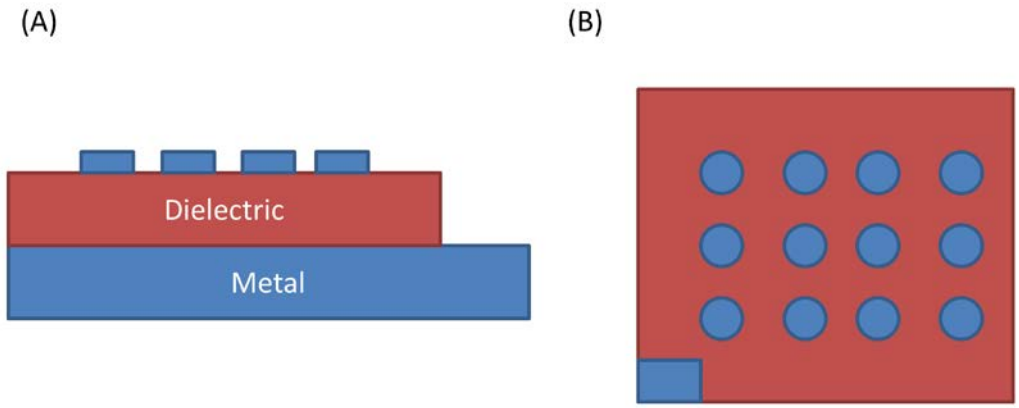

Figure 31: (A) Cross section view of MIM structure. (B) Top view of MIM structure.

A schematic image of an IDC is given in Figure 32. Dielectric constant of a film can be calculated using the known semi-empirical relations as described by Kidner *et al.*[75,76] For IDC configurations, the equation relating the measured capacitance per unit length (pF/m) to the electrode geometry and the film and substrate relative permittivity (ε_f and ε_s) is given as

$$C = K_{p,\varepsilon}[1 + \varepsilon_s + (\varepsilon_f - \varepsilon_s)F_\varepsilon]$$

where

$$C = \frac{C_m}{FL * N}$$

C_m is the measured capacitance in units of picofarads, FL is effective length of the fingers in units of meters, and N is the number of sections of fingers given by $N=2P-1$ where P is the number of finger pairs in the IDC pattern.

.

Figure 32: Schematic image of an IDC structure

The relative permittivity of the film measured in the IDC configuration is described by the functions $K_{p,\varepsilon}$ and F_ε that are dependent on the dimensionless parameters for the electrode (w/L) and film thickness (h/L) where w is the electrode width, L is the inter-electrode spacing and h is the film thickness. The subscript p denotes $K_{p,\varepsilon}$ is valid only for periodic electrode arrangements where stray capacitances can be neglected. The subscript ε denotes $K_{p,\varepsilon}$ and F_ε were determined from an analysis of the capacitive properties. The functions are given as

$$\mathrm{K}_{\mathrm{p},\varepsilon} = 137.79\left(\frac{w}{L}\right)^5 - 320.72\left(\frac{w}{L}\right)^4 + 288.22\left(\frac{w}{L}\right)^3 - 120.47\left(\frac{w}{L}\right)^2 + 28.55\left(\frac{w}{L}\right)$$

$$F_\varepsilon = 1 - \exp\left[-2.2\left(\frac{h}{L}\right)^2 - 3.9\frac{h}{L}\right]$$

3.4.3 Impedance Spectroscopy

A thorough review of the impedance spectroscopy technique can be found in the work by Barsoukov and Macdonald.[77] Impedance spectroscopy is an experimental tool for the characterization of electrical properties of materials. The technique is based on analyzing the a.c. response of a system to a sinusoidal perturbation and subsequent calculation of the impedance as a function of the frequency of the perturbation. The technique enables an evaluation and separation of contributions to the overall electrical properties in the frequency domain due to

differences in impedance of the electrode/material interface, migration of charge carriers across grain and grain boundaries and other phenomena.

With impedance spectroscopy, a sinusoidal signal of low amplitude is applied across a sample and the complex impedance and phase shift are measured as an output. The impedance can be represented as a real (*Z'*) and imaginary (*Z"*) component. Depending on material and hypothesized process, an electrical equivalent circuit can be constructed made of capacitors, inductors, resistors and other elements.

Transforms can be used in order to obtain related values from the impedance. A few transformations are listed below.[78,79] The real and imaginary parts of complex dielectric constant, ε are represented as:

$$\varepsilon' = \frac{Z''}{\omega C_o (Z'^2 + Z''^2)}$$

$$\varepsilon'' = -\frac{Z'}{\omega C_o (Z'^2 + Z''^2)}.$$

The real and imaginary parts of complex electric modulus, *M* are represented as:

$$M' = \omega C_0 Z''$$

$$M'' = \omega C_0 Z'.$$

The loss tangent is given as

$$\tan\delta = \frac{\varepsilon''}{\varepsilon'} = \frac{M''}{M'}$$

the radial frequency, ω, is given as

$$\omega = 2\pi f$$

with *f* being the frequency and the vacuum capacitance C_o is given as

$$C_0 = \frac{\varepsilon_0 A}{d}$$

with *A* is the area of the electrode and *d* is the thickness of the dielectric layer.

3.4.4 Metal-Semiconductor and *pn* Junctions

In a sense, dielectric complex oxides are not pure insulator which is usually a result of slight changes in stoichiometry. For the case of BST, due to the loss of oxygen, n-type conductivity is present. In LSNO, the doping of Sr and oxygen leads to p-type conductivity. When a semiconductor is brought together with the metal, band bending occurs in the semiconductor and to a much smaller extent in the metal. The difference in the metal work function and the electron affinity of the semiconductor drives electron diffusion from the semiconductor to the metal surface region. In essence, the two materials must come together in a manner such that the Fermi energy is continues across the junction. This will force band bending in the semiconductor. This leads to a depletion of charge in the semiconductor which is balanced by accumulation in the metal.

The schottky barrier height is given by $\Phi_{SB} = \phi_M - \chi$ where ϕ_M is the metal work function and χ is the electron affinity of the semiconductor. The quantitative expression for band bending and depletion width is given by solving Poisson's equation under the depletion approximation.

Band bending associated with the space charge predominately occurs in the semiconductor since the density of carriers is far greater in the metal. The charge depletion creates a potential drop across the junction which corresponds to the band bending. The application of a bias will shift the Fermi energy in the semiconductor relative to that at the

equilibrium. A forward bias (positive on the metal) reduces this barrier while a negative bias increases the barrier. Current flow is given by

$$I = I_0[\exp(\frac{eV_a}{k_b T}) - 1]$$

A *pn* junction can be thought of as a special case of a schottky junction, where the *p*-type semiconductor is thought of as the metal. Due to the lower density of carriers, bending occurs in both the p and n type sides.

A review of this topic can be found in the book by Sze *et al.*[80]. A more thorough approach and the understanding from a materials point of view is given in Chapter 4.2 and 5.2.

3.5 Transmission Electron Microscopy (TEM)

Review of transmission electron microscopy is given in William and Carter.[81] TEM is an efficient and versatile tool for the characterization of nanoscale materials and in particular thin films. The resolution of the state of the art microscopes has reached into the sub-angstrom level and a variety of detection modes are available including bright field, dark field angle annular dark field allowing for z-contrast, selected area diffraction, energy dispersive x-ray analysis and energy-loss spectroscopy.

The resolution of a microscope is approximated by the Rayleigh criteria

$\delta = \frac{0.61\lambda}{\mu \sin\beta}$ where δ is the resolution, λ is the wavelength, μ is the refractive index of the viewing medium and β is the semi angle of collection of the magnifying lens. Wavelength of electrons is given by de Broglie wavelength $\lambda = \frac{h}{(2m_0 eV)^{1/2}}$ where h is the Planck's constant, m_0 is the electron mass, e is the elementary charge, and V is the acceleration voltage of the

electron gun. Limitations in optics has been greatly reduced with the development of aberration corrected TEMs.

TEM work was performed in CNS using the JEOL 2010F microscope. TEM work in this thesis was done by B. Viswanath.

4 BST

4.1 Photon Assisted Oxidation in BST

4.1.1 Abstract

The effect of ultra-violet (UV) photons assisted annealing on the structural, dielectric, and insulating properties of barium strontium titanate (BST) thin films was investigated. Isothermal-temporal annealing experiments revealed that the films annealed utilizing UV-assist possessed enhanced crystallization, and lattice parameters closer to bulk values with respect to conventional thermal annealed films. The leakage current density and dielectric loss of the films was significantly reduced by employing UV-assisted annealing without degradation of film tunability. Mitigation of oxygen vacancies, associated with the UV-assisted annealing, is deemed responsible for the improvement of the dielectric and electrical properties of the BST thin films.

4.1.2 Introduction

Thin film barium strontium titanate, $Ba_{1-x}Sr_xTiO_3$, (BST) is a promising dielectric material for active elements in tunable devices such as filters, varactors, delay lines, phase shifters, and voltage controlled oscillators.[82,83,84,85,86] It is the nonlinearity of its dielectric properties with respect to applied dc voltage that makes BST attractive for these device applications. Of particular interest to both the commercial and military sector is the realization of "affordable" electronically tunable filters. Although the possibility of using BST thin film varactors in tunable filters has been recognized for quite some time, this application space has not been fully exploited since most filter applications place a high premium on insertion-loss in the pass-band while maintaining high tunability. To date, the technology for BST fabrication has

not been able to satisfy the required balance of these two material properties while still maintaining excellent reliability and device affordability.

Conventional approaches for lowering thin film BST dielectric loss include: acceptor doping,[87] modification of film stress,[85,88] film texturing,[89] ferroelectric-low loss oxide material layering,[90] and improving the film/electrode interface quality by utilization of refractory metals and/or addition of buffer layers between the film and bottom electrode.[91] Although these techniques have led to lower dielectric losses, these approaches often lead to severe degradation of the films tunability and frequently involve complex non-industry standard film processing steps which in turn compromise device affordability. Thus, there is a critical need to develop different material designs and/or film processing methods that enable maintenance of BST Q-factor (low dielectric loss/insertion loss) without compromising the material tunability (η~2:1) and other required filter performance metrics, such as device impedance matching (ε_r<500), film resistivity/conductivity (leakage current ~μA range) and long-term reliability (long-term performance under extended applied voltage and temperature). In this section, we report on the fabrication of BST thin films via a combinational processing technique which blends RF-sputtering and photon (in the ultra-violet range) irradiation annealing to achieve balanced BST material properties. While growth of BST films by UV-enhanced pulsed laser deposition has been reported earlier,[92] this work elucidates kinetic effects post-processing.

4.1.3 Experimental

The $Ba_{0.60}Sr_{0.40}TiO_3$, BST (60/40), thin films (~100 nm thickness) were RF sputtered from a stoichiometric $Ba_{0.60}Sr_{0.40}TiO_3$ ceramic target onto Pt-Si and r-plane sapphire substrates. An off-axis sputtering configuration was employed, with a target-substrate distance of 30 mm, and the sputtering gas consisting of argon. The as-deposited films were annealed via

conventional substrate thermal annealing and UV-assisted photon irradiation annealing. Both sets of films were *in situ* annealed at variable temperatures (615 -783^{o}C) and times (15-225 min.) in a custom built load lock annealing chamber adjoined to the sputtering chamber. The annealing chamber was specially designed with a substrate heater and precision oxygen partial pressure control, as well as equipped with an *in-situ* photon sources facing the sample for performing UV-assisted anneals. The UV photon source produces radiation between 185 and 254 nm and is operated at 50 mW/cm^2. In order to evaluate the effects of the UV-assisted annealing with respect to conventional *in situ* thermal annealing, the films were characterized for structural, dielectric, and insulating properties. The dielectric properties were measured in the metal-insulator-metal (MIM) device configuration using Pt top and bottom electrodes.

4.1.4 Results

In order to minimize the effect of x-ray peak interference and evaluate/compare the structural properties of both the UV annealed and conventional thermally annealed BST films, glancing incidence x-ray diffraction (GIXRD) was conducted using BST films grown on r-plane sapphire without electrode metallization. Specifically, the films were annealed for 60 min. at temperatures ranging from 615 to 783°C with and without UV treatment in an oxygen environment. The x-ray patterns of the conventionally annealed BST thin films and the films annealed with UV-assist are shown in Figure 33**.** The annealed film showed no evidence of secondary phase formation, as no peaks other than (100), (110), (111), (200), and (211) BST peaks were observed. It should be noted that for the conventional thermally annealed BST films there was a slight shift of the x-ray peaks to lower angles (corresponding to larger interplanar spacing) with respect to that of the UV-assist annealed BST films. This downshift in the peak position is indicative of the fact that the lattice parameter of the conventionally thermal annealed

BST films, based on the (110) x-ray peak, i.e. at 700°C $a_{conventional\ anneal}$ = 4.01 Å as opposed to $a_{UV\text{-}assisted\ anneal}$ = 3.99 Å, was slightly larger than that for the film annealed with UV-assist. To further detail this observed difference in lattice parameter between the two annealing methods the experimental calculated lattice parameters, using the (110) x-ray peak, for both sets of films are shown as a function of variable annealing temperatures in Figure 34. The dotted-dashed line in Figure 34 represents the JCPDF #00-034-0411 lattice parameter for bulk ceramic $Ba_{0.60}Sr_{0.40}TiO_3$. It is likely that the UV-treated films display structural characteristics closer to that of bulk BST, i.e., lattice parameter closer to bulk with respect to the conventionally annealed BST film, advocating a reduction in film stress resultant of defect (oxygen vacancies) annihilation in the film with respect to the non UV-treated films. Oxygen vacancies affect the nearest neighbor distance by reducing the Coulomb attractive force between cations and anions, resulting in an increased lattice parameter.[93] The oxygen vacancy site, being a prevalent defect in perovskite oxide films, has a net positive value thus repelling the Ba, Sr, and Ti atoms causing a distortion in the lattice parameter. It is likely that the influx of activated oxygen during UV annealing allows for a greater compensation of the vacancies resulting in the reduction of the lattice parameter, and ultimately alleviating film strain by filling oxygen vacancies. Extrapolating the data, it is important to note that UV treatment can allow for the reduction in fabrication temperature by roughly 100-150°C with respect to the non-UV treated films while maintaining the same degree of stoichiometry and crystallinity. The reduction in growth temperature is extremely important for tunable devices fabrication due to material selectivity and thermal sensitivity.[94] The UV radiation also athermally excites the film enhancing mobility and allows for a greater degree of crystallization.[95]

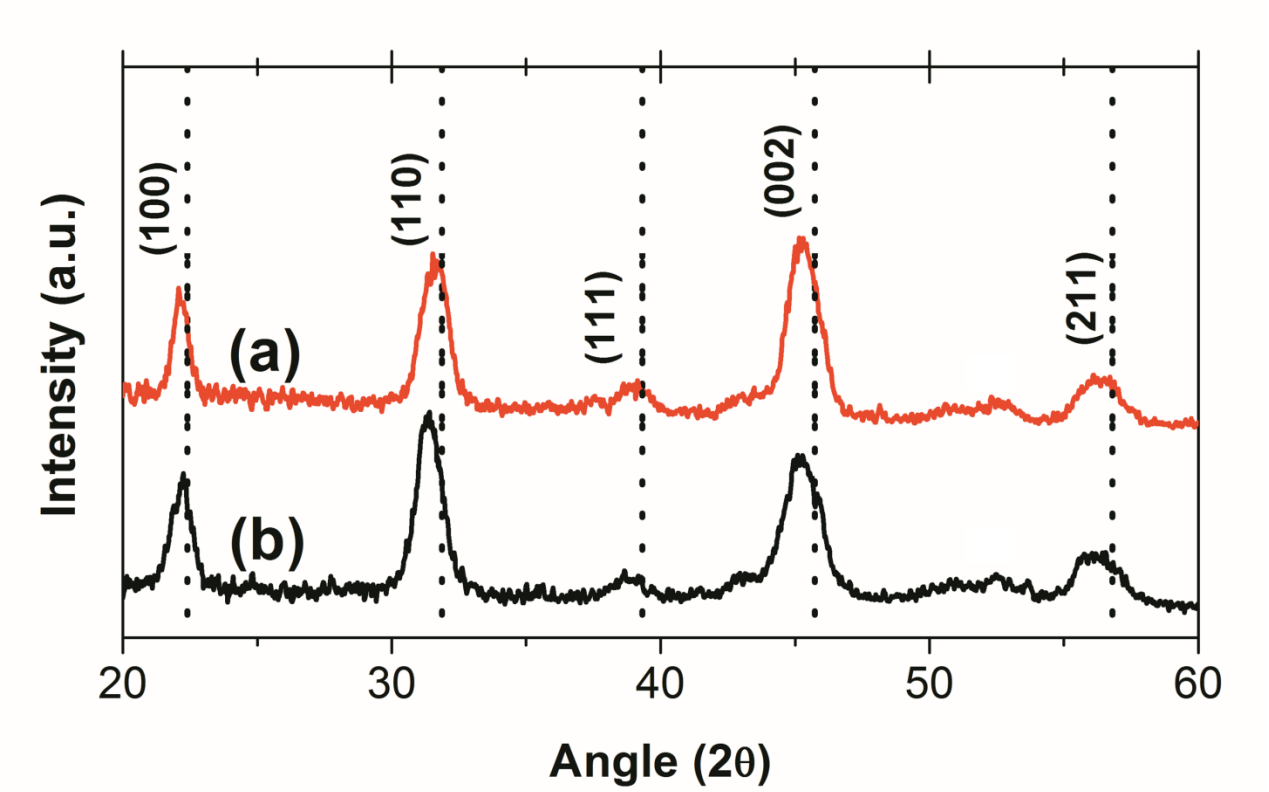

Figure 33: GIXRD patterns of BST thin films annealed at 700°C for 60 minutes (a) with UV treatment and (b) without UV treatment. Dotted lines represent the BST (60/40) bulk peak position (JCPDF #00-034-0411).

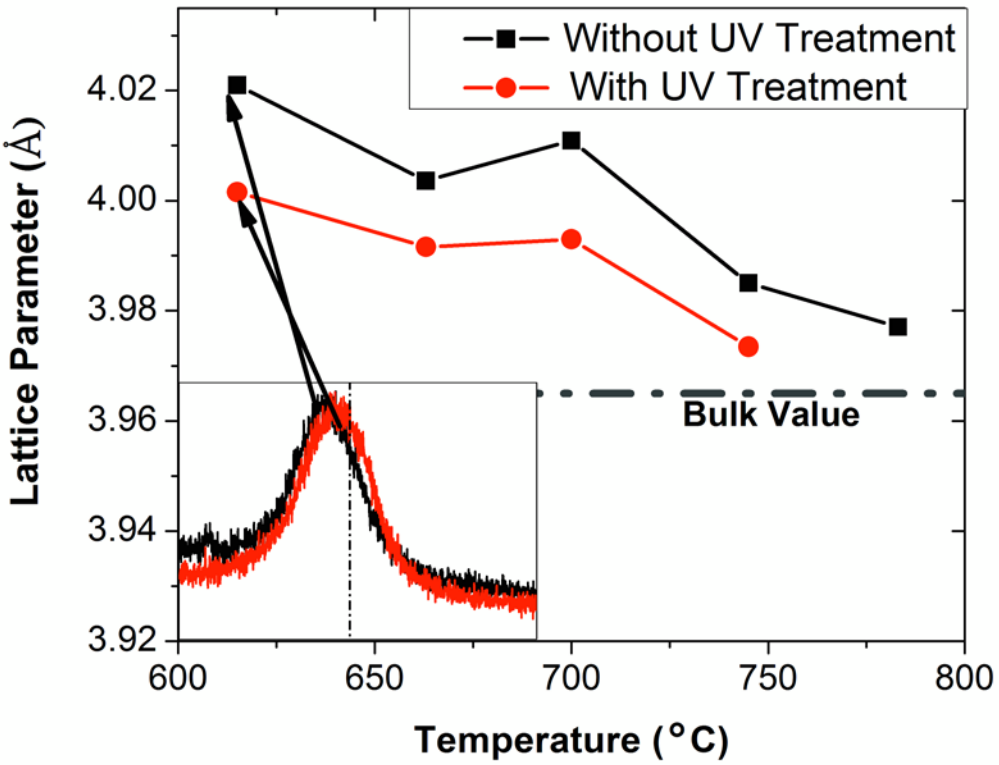

Figure 34: Change in lattice parameter as a function of annealing temperature for BST films annealed with (red filled circles) and without (black filled squares) UV-assist.

In order to determine the temporal effects of UV treatment on the BST films' structural quality, both sets of films were isothermally annealed at 700^{o}C as a function of variable annealing time from 15-225 min. Figure 35a and Figure 35b shows the change in full-width-at-half-maximum (FWHM) and lattice parameter of BST films annealed with and without UV-assist, respectively. The steep decrease in FWHM, observed for both sets of films, as the time is increased from 15 to 30 min., suggests an increase in the grain size over a relatively short time interval. The decrease in FWHM as a function of annealing time is more pronounced for the UV treated film with respect to that of the conventionally annealed film. It is also important to note that for both sets of films the FWHM appears to approach a near-steady state after annealing for

75 min., i.e., additional annealing time does not drastically enhance the films grain size. Furthermore, the data in Figure 35a (narrower FWHM of UV-assist treated film) demonstrates that for equivalent time and temperature conditions, the film annealed with UV-assist is either more developed (possesses a higher degree of crystallinity/larger grain size) and/or possesses less residual stress, than the film annealed without UV-assist.

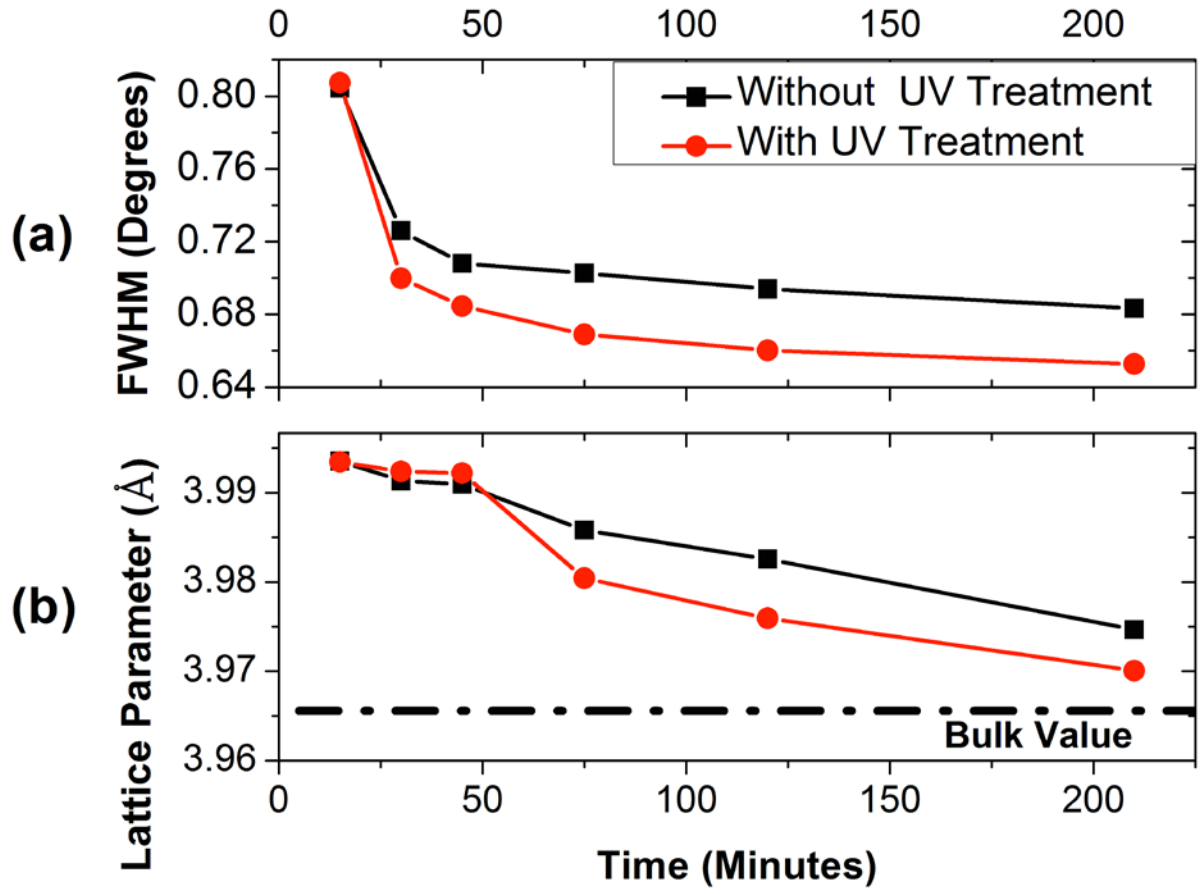

Figure 35: The variation in (a) FWHM and (b) lattice parameter of the 700°C annealed UV-assist (red filled circles) and non-UV treated (black filled squares) BST (60/40) films as a function of annealing time.

Figure 35b displays the variation in lattice parameter as a function of increasing annealing time for films annealed at 700^{o}C with and without UV-assist. After annealing for ~45

minutes there is a divergence in the lattice parameter such that at the same annealing time the lattice parameter of the UV-assist annealed film has contracted substantially with respect to that of the non-UV annealed film and hence the lattice parameter is closer to that of bulk BST. This result suggests that UV irradiation has a dramatic effect on the film structure whereby, the more pronounced lattice parameter contraction observed for the UV treated films advocates that UV irradiation leads to a reduction in oxygen vacancies, hence yielding lower residual stress in the UV-annealed film.

Figure 36 displays the permittivity and tunability of the two sets of films as a function of applied bias. The permittivity of the UV annealed ($\varepsilon_{v=0}$= 96) BST film is slightly lower than that of the non-UV annealed film ($\varepsilon_{v=0}$= 108). This may be related to the lattice parameter difference in the two samples as the ionic displacement is reduced lowering the net polarization. This decrease in polarization lowers the dielectric constant which can result in lower dielectric loss.[96] The permittivity for both sets of films is reasonable (i.e., ε_r<500), for device impedance matching purposes,[97,98] thereby allowing efficient power transfer in the device. What is also important in Figure 36 is the tunability data, whereby tunability (η) is defined as $\eta = \Delta C/C_o$, and ΔC is the change in capacitance relative to zero-bias capacitance C_o. More importantly, what is most significant is that the tunability is virtually the same for both annealing treatments, with a maximum of ~35 % at $\pm$10V applied bias. This tunability value is very reasonable for practical filter applications. Furthermore, the measured dielectric loss for both sets of films established that the dissipation factor for the UV-treated film was found to be reduced by ~ 20% with respect to that of the non-UV treated film.[99] This data is aligned with the lattice parameter findings (Figure 34) and is in support of the UV-assist's consequence to mitigate oxygen vacancies, thereby resulting in improved dielectric loss.

Leakage current is one of the limiting factors for the suitability of a dielectric material for filter/tunable device applications.[97] Conduction mechanism of BST thin films is primarily through Schottky emission in which leakage currents are controlled by the barrier height.[100] Large leakage currents arise from excess oxygen vacancies since a higher concentration of oxygen point defects will give the BST n-type conductivity. These vacancies arise during deposition or post-deposition anneals due to the low molecular mass of the oxygen with respect to the other deposited atoms.[84] Shye *et al.*[101] reported on post deposition anneals in oxygen activated through plasma treatment. Craciun *et al.*[92,95,102] have reported on the effect of UV exposure during growth of oxide films including BST by pulsed laser deposition. Ramanathan *et al.*[103] have shown that UV irradiation can enhance the oxidation rate of metal films enabling formation of stoichiometric oxides. It has been argued that the major factors that influence leakage characteristics of BST films are oxygen vacancies generated during deposition, annealing of the BST film in low oxygen environments and during sputtering of the top electrode, and mechanical damage imposed by sputtering of the top electrode.[84] The leakage current characteristics of BST thin films were measured using MIM capacitors. The relation of the leakage current density versus the applied bias is shown for both the UV-assist and conventionally thermal annealed BST films in Figure 37. In contrast to conventional thermal annealing, the UV annealed BST film has a significantly lower leakage current density in reverse bias (bias voltage is defined as negative when a negative voltage is applied to the top Pt electrode). For example, the current density of the UV-assist annealed BST film is 7.73×10^{-7} A/cm^2 at -2.0 V applied bias and this value is significantly lower than that for the thermal annealed film (6.11×10^{-5} A/cm^2) for the same electric field. The oxygen vacancies generated at the top BST electrode by the sputtering process as well as the oxygen vacancies in the film from

the initial sputtering conditions may act as electron trap sites causing high leakage currents in the Pt/BST/PT capacitor structure. Since the UV radiation increases the influx of oxygen through the film, the vacancies are annihilated and thus the leakage current is decreased. Our results agree well with reported literature on the effect of oxygen annealing on leakage currents.[101,104]

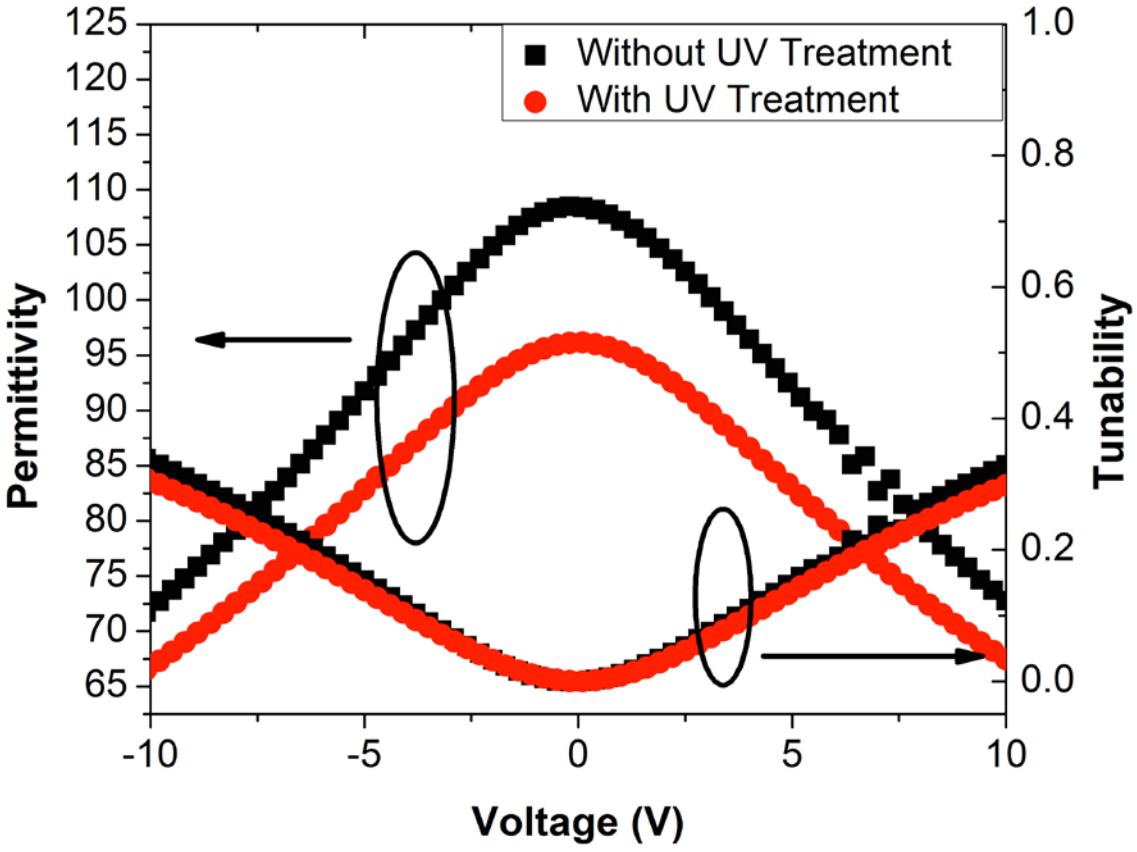

Figure 36: Dielectric response as a function of applied bias for the BST films annealed at 700°C with (red filled circles) and without UV-assist (black filled squares).

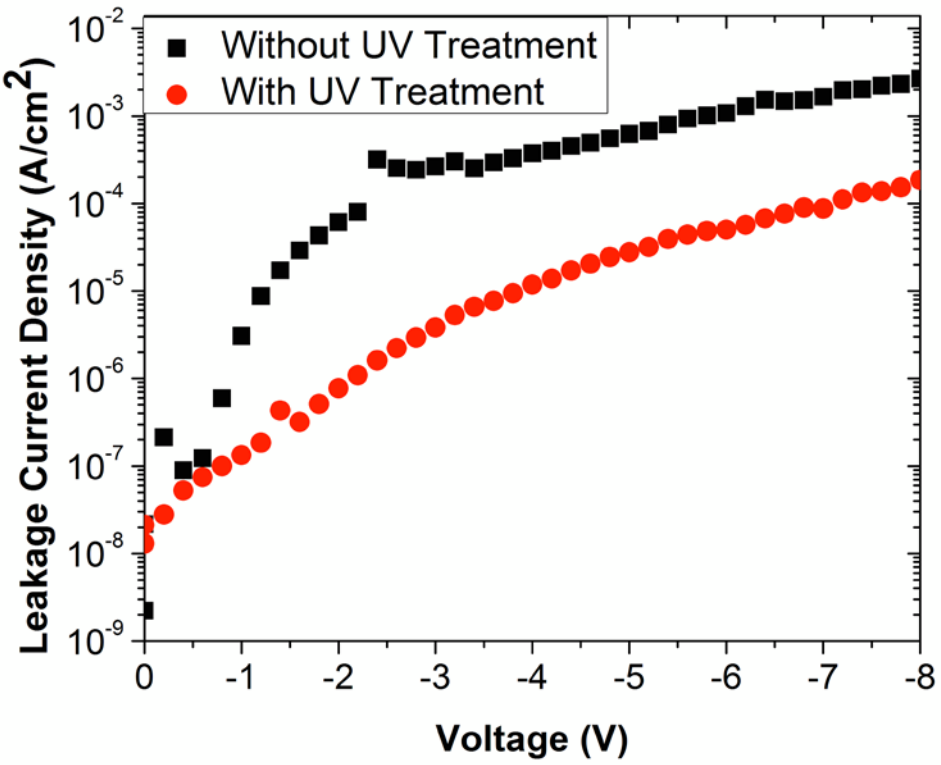

Figure 37: Variation of leakage current density with applied reverse bias for the BST thin films annealed at 700°C with (red filled circles) and without UV-assist (black filled squares).

4.1.5 Conclusion

In summary, this study demonstrates the potential for utilizing photon irradiation assisted annealing to achieve enhanced balanced material properties. Specifically, compared to conventional thermal annealed BST films, the UV-assist annealed films possessed improved leakage current characteristics and dielectric loss with sustained tunabilities. The improved dielectric response, reduced leakage current and more pronounced lattice parameter contraction observed for the UV treated films suggests that UV exposure plays a significant role in the annihilation of oxygen vacancies serving to improve the film's material properties.

4.2 Novel Processing Route for BST on Non-noble metal substrates

4.2.1 Abstract

The electrical characteristics of reactive metal-oxide interfaces are largely dependent on the thermodynamics and kinetics of interfacial reactions that may occur during synthesis and further processing conditions. Such reactions may lead to undesirable properties such as increased loss tangent, frequency dispersion or asymmetric capacitance. Metals such as Ni are being explored as electrodes in various electronic packaging as well as on-chip de-coupling capacitors and this presents a challenge to advance processing routes that render utilization of high-dielectric constant oxide thin films. In this section, we demonstrate that photon-assisted oxidation enables a unique low temperature processing route to synthesize reduced loss $(Ba,Sr)TiO_3$ thin film based capacitors with Ni bottom electrodes. Our results show a decrease in the dielectric loss tangent in photon-assisted oxidized films compared to conventionally reoxidized at an applied field of 0.33MV/cm, tan δ of .08 vs .63, respectively. Leakage currents showed a significant decrease, 7.8 A/cm^2 for conventional re-oxidation versus 0.046 A/cm^2 for photon assisted, at an applied field of 0.33 MV/cm. The results are of relevance to processing reactive materials wherein athermal routes are necessary to avoid interfacial reactions.

4.2.2 Introduction

Thin films of $Ba_{1-x}Sr_xTiO_3$ (BST) have attracted a great deal of attention due to their high dielectric constant and low loss, which make them promising for integrated capacitors, dynamic random access memories (DRAM) and related technologies.[105,106,107,108,109] The application of

BST into integrated passives (bypass capacitors) in system-on-package (SOP) technology could enable the realization of much faster and smaller devices due to decrease in impedance by placing the capacitor closer to the integrated circuit as well as leading to a decrease in area of surface mounted capacitors.[110,111]

Literature pertaining to BST thin films has almost entirely been based on the growth of BST on noble metal electrodes such as Pt due to the high annealing temperature coupled with high oxygen partial pressures required to obtain good crystallinity and insulating properties.[112,113] However, such electrodes would make it prohibitively expensive for wide spread implementation. In recent years, a drive has developed to grow high quality BST thin films on base metal electrodes that can be electroplated at low temperatures; i.e. Ni. The fundamental problem lies in deposition and annealing of oxide films on a reactive electrode. This process can oxidize the electrode (i.e. NiO_x) thereby leading to undesirable changes in the electrical properties of the resulting capacitor structures. Further, such reactions must also be prevented during post-processing. A process approach developed by Maria *et al.* uses a low partial pressure of oxygen (pO_2) range where BST and the base metal are thermodynamically stable (base-metal oxide cannot form). This allows for the oxide components of BST to be stable (BaO, SrO and TiO_2) along with the base metal electrode, nickel.[114,115] By maintaining these conditions, an abrupt metal/BST interface could be formed. Due to the low partial pressure oxygen anneal, oxygen vacancies are expected to be created at the open interface, however reoxidation annealing steps have been developed to improve the quality of the reduced films. These consist of lower temperature anneals (~773K) and higher partial pressure of oxygen (pO_2 approx. 10^{-8} atm.) using vacuum furnaces. This process is used to reoxidize the reduced BST film while kinetically maintaining the base metal electrode from reactions by preventing oxygen

from diffusing through the dense dielectric film.[115] However this environment is still reducing and at these temperatures and low partial pressures, oxygen incorporation is kinetically frustrated and is not maximized.[116] The high degree of oxygen vacancies therefore may still lead to high leakage and losses in the film which is detrimental to the dielectric properties. In this section, we demonstrate that photo-excitation during reoxidation at low temperatures enables high capacitance density with a striking reduction in dielectric loss and leakage currents. Photo-chemical reactions enable creation of atomic oxygen and ozone that are highly reactive and enhance oxygen incorporation into oxides at relatively low temperatures.[117,118,119] Further, creation of electron-hole pairs during photon illumination may enhance surface exchange leading to additional reduction in point defect concentration in the near-surface regions.[117,120] This approach may be of broad of relevance for processing devices incorporating reactive metal-oxide interfaces.

4.2.3 Experimental

Thin film BST was prepared by off-axis RF magnetron sputtering of stoichiometric $Ba_{0.75}Sr_{0.25}TiO_3$ 2in. ceramic targets at room temperature in 5mTorr of Ar onto platinized and nickelized sapphire. BST was grown to a thickness of 150nm while bottom electrodes (Ni or Pt) were 200nm thick. Samples were annealed with mixture of 5% H_2 in Argon bubbled through de-ionized water resulting in partial pressure of oxygen (pO_2) of approximately 10^{-22} atm of O_2 at 973K. Films were subsequently reoxidized at lower temperatures of approximately 573K in a flowing oxygen environment with and without UV-assisted oxidation. Lower temperatures of 373K and 473K were studied to determine temperature dependent effects of reoxidation. A mercury arc lamp was used as the UV source producing radiation at 185 and 254nm wavelength operated at 50 mW/cm^2 at approximately 10 cm from the substrate. Samples were heated from

the back using a halogen heating lamp. Glancing incidence x-ray diffraction studies were done on nickelized sapphire to study the structural evolution of the film as a function of annealing temperature in air and 5% H_2 in Ar (reducing atmosphere). Cross sectional TEM studies were carried out using JEOL 2100 and JEOL 2010F transmission electron microscopes on BST prepared on nickelized Silicon substrate with a 50nm Tantalum diffusion-adhesion layer between the Ni and Si. TEM specimens were prepared by mechanical grinding and dimpling followed by Ar ion milling. Thickness dependence studies on electrical properties of BST under reducing conditions were performed on samples grown on nickelized silicon. Electrical measurements were performed by depositing Pt contacts (100nm thick) at room temperature by e-beam evaporation through a shadow mask post processing to form MIM (metal/insulator/metal) capacitor devices. A schematic of the process is given in Figure 38. Electrical measurements were performed using an Agilent 4284A LCR meter probe station. Capacitance-voltage measurements were performed using a 50mV applied signal at 1MHz. DC bias was applied to the bottom electrode relative to the top electrode.

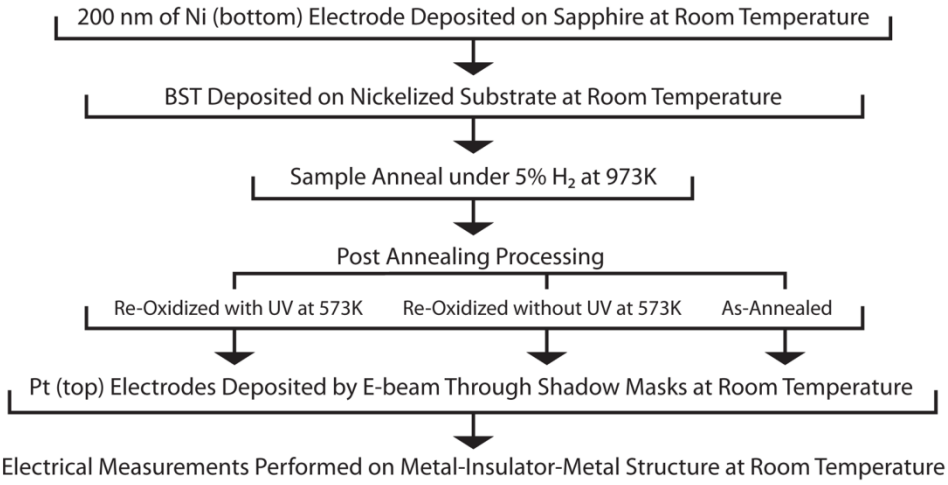

Figure 38: Flow Chart of preparation of BST films for electrical characterization

4.2.4 Results

Figure 39A and Figure 39B shows the structural evolution of thin film BST grown on nickel base electrodes under reducing (5% H_2 in Ar) and oxidizing (air) anneals at various temperatures. It is evident from the diffraction pattern that at 973K, NiO is present in air annealed samples whereas only nickel is present in reduced films (i.e. annealed under low partial pressure of O_2). Characteristic BST peaks are seen in both samples above 873K. Transmission electron microscopy studies were carried out to investigate the interfacial stability of the Ni/BST thin films annealed under various conditions. Figure 40 shows cross sectional TEM images of Ni/BST film annealed at 973 K in reducing atmosphere. Indeed, the selected area diffraction pattern recorded from the Ni/BST interface closely follows the thermodynamic prediction and shows no reflection for NiO and the observed rings are consistent with the x-ray diffraction pattern of the BST film (Figure 40A). Characteristic reflections such as (100), (110), (111) and (200) seen in both x-ray diffraction pattern and selected area diffraction pattern confirms the cubic phase of BST. Dark field image recorded using the (110) reflection of BST (Figure 40B) confirms the presence of BST film on Ni. High-resolution image taken from Ni/BST region (Figure 40C) confirms a clean interface. While annealing under reducing atmosphere leads to stability of the interface, subtle changes in stoichiometry in BST due to oxygen vacancy creation can happen.

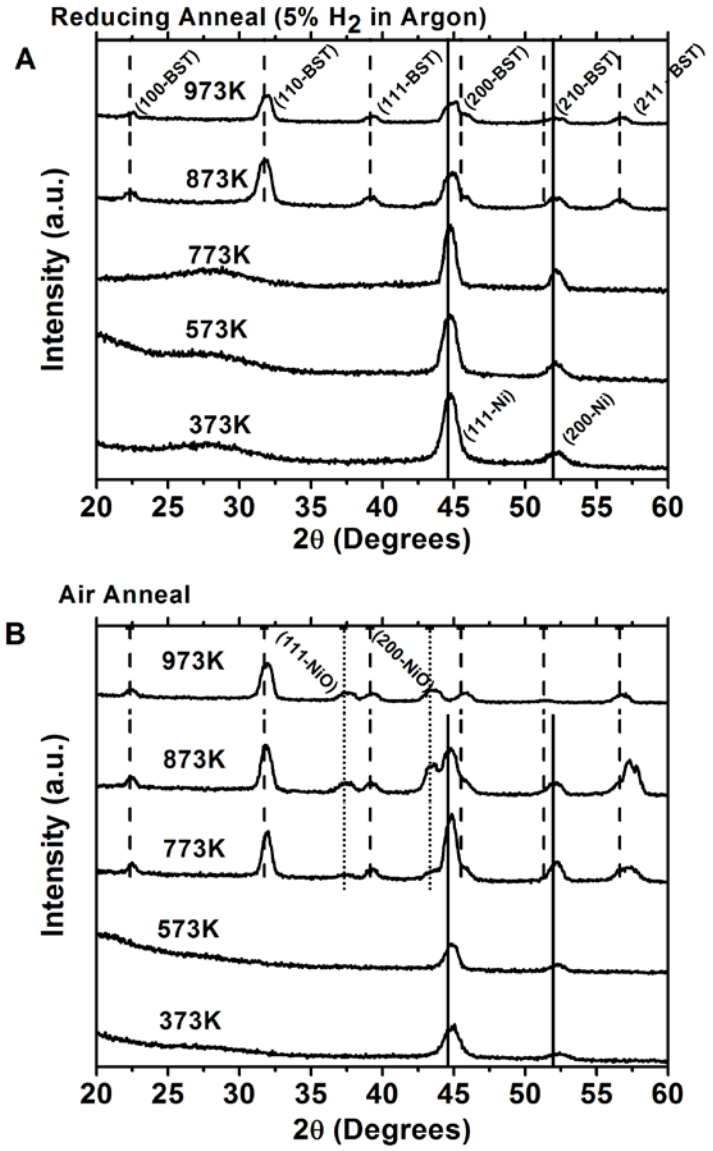

Figure 39: x-ray diffraction pattern of BST grown on nickelized sapphire annealed in reduced conditions (A) and air (B). Annealing temperatures are displayed on graph. All samples measured at room temperature. Solid vertical lines – Nickel (JCPDS# 01-071-3740), Dotted lines – Nickel Oxide (JCPDS# 00-004-0835), Dashed vertical line – BST (taken for BST(77/23) – JCPDS# 00-044-0093).

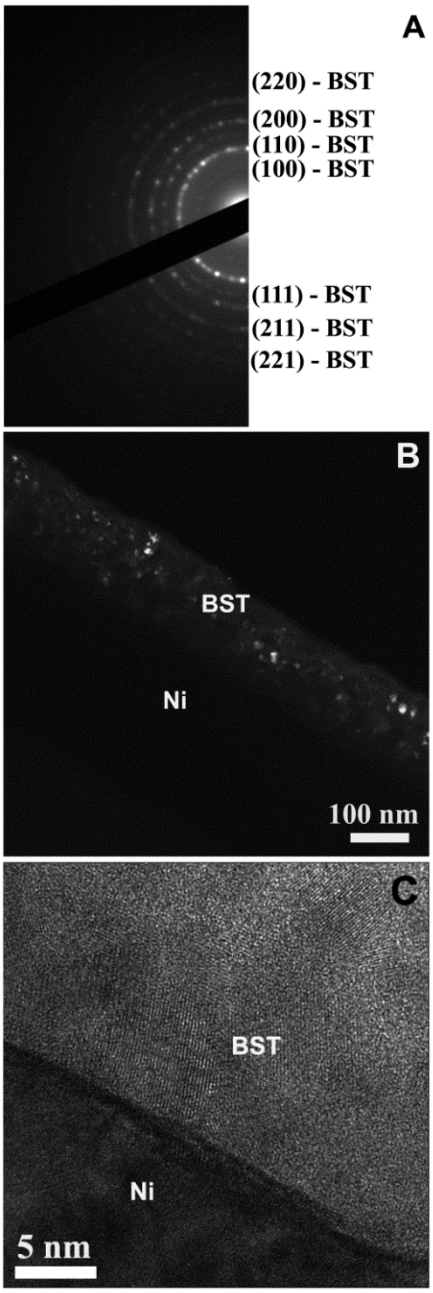

Figure 40: Cross sectional TEM micrograph of 150 nm thick BST film deposited on nickelized Si (100) substrate, annealed at 973K under reducing atmosphere. (A) Selected area diffraction pattern recorded from the Ni-BST interface. (B) Corresponding dark field image recorded using the (110) reflection of BST. (C) High-resolution image of Ni/BST interface.

Insulating and dielectric properties were measured for BST grown on nickelized sapphire annealed at 973K in reducing atmosphere as shown in Figure 41 (black squares). It has been reported that thin film BST annealed in reducing conditions contains oxygen vacancies as the predominant defects. [121] Under reducing anneal, the degraded region is limited to the top near-surface region of the film.[121,122] The increased amount of positively charged oxygen vacancies at the surface causes a lowering of the Schottky barrier height.[122,123] The oxygen vacancies (defect sites) at the surface of the film pins the Fermi level of the BST and top contact metal (Pt) close to the conduction band minimum thereby leading to a lower Schottky barrier height.[124] The increased number of oxygen vacancies lead to an increased number of electrons by the equilibrium reduction equation (in Kroger-Vink notation)[125]

$$O_O \rightarrow V_O^{\bullet\bullet} + 2e^{'} + \frac{1}{2}O_2(g)$$

where O_o represents oxygen ion on the neutral site in the BST lattice, $V_O^{\bullet\bullet}$ is the double charged vacancy created, e is the free electron and O_2 is the gaseous oxygen leaving the lattice. This reaction gives more carriers leading to higher conductivity and as a result, higher dielectric loss in the positive regime since the dielectric loss is coupled with the resistive losses of the film.[126] The dielectric loss tangent, is defined as

$$\tan\delta = \frac{\sigma}{\omega\varepsilon_o\varepsilon}$$

Equation 3

where σ is the conductance, ω is the angular frequency and $\varepsilon_o\varepsilon$ is the capacitance, is also shown for the reduced sample in Figure 41. As more carriers are present due to injection from the lowered barrier in the positive bias, the dielectric loss increases. In the negative biased regime,

due to the Schottky barrier between the insulating BST film (containing less vacancies and therefore less free electrons) and the Ni (a high work function metal similar to Pt), injected charge is at a minimum and low dielectric losses are seen as expected. Maximum dielectric constant of the reduced sample was approximately 185, which was at a slightly positive applied bias (.06MV/cm). Dielectric losses at positive applied electric field of 0.33 MV/cm was observed to be approximately 0.53.

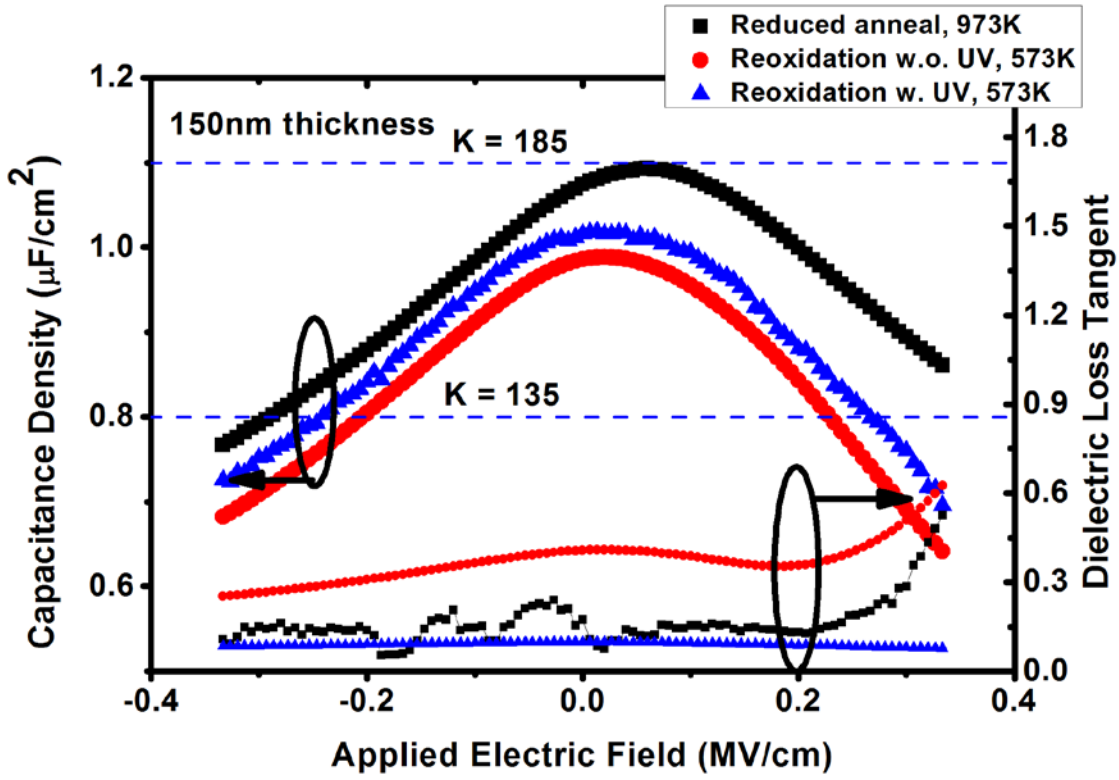

Figure 41: Capacitance density and dielectric loss tangent for 150nm thick BST thin film grown on Ni bottom electrode with Pt top contacts. Films were treated under reducing anneal at 973K (black squares) and reoxidized conventionally (red circles) or with UV-enhanced oxidation (blue triangles) at 573K. Dielectric constant equivalents of capacitance density are given by the dashed blue line and labeled accordingly.

Reduced samples of varying thickness were also prepared in order to investigate the effects of the onset of conduction in the positive biased region. Samples of thickness 100, 150, 200, and 250nm were prepared and annealed at 973K under reduced anneal for 1 hour. Pt top electrodes were deposited to make MIM capacitor devices. As shown in Figure 42, the local minima in the positive regime where the onset of increased conductivity starts is not constant as a function of applied field. The ac conductivity term being plotted is related to the dielectric loss tangent by the above equation (Equation 3). The onset of the applied field decreases as the film becomes thinner. This indicates that the thin depleted region (rich in oxygen vacancies) forms a higher fraction of the film with decreasing thickness. At 100nm, this region dominates the film and leads to an almost immediate increase in conductivity in the positive region. Upon re-oxidation, the dielectric loss should be significantly reduced due to the compensation of vacancies. However, large losses are still present in the sample annealed at 573K without UV (w.o. UV) enhanced oxidation (red circles in Figure 41). Shen *et al.*[127] describe the compensation of the oxygen vacancy as being a two step process:

$$\text{(I)} \qquad \frac{1}{2}O_2 + 2e' \xrightarrow{T_1} O^{2-}$$

$$\text{(II)} \qquad O^{2-} + V_O^{\bullet\bullet} \xrightarrow{T_2} O_O^x$$

where $T_2 > T_1$ and T_1 is in the range of 623K and T_2 being approximately 823K. Therefore oxygen vacancies may not be fully compensated at 573K.[127] The increase in dielectric loss (a dielectric loss tangent of 0.63 at 0.33MV/cm) in the non-UV re-oxidized samples is likely caused by the oxygen being trapped near the surface (i.e. not compensating the vacancy) which would form a layer with a lower resistivity leading to high loss as predicted by the Maxwell-Wagner model.[127] This has also been studied by Roy *et al.* showing blue shift of the band-gap as a function of annealing temperature.[128]

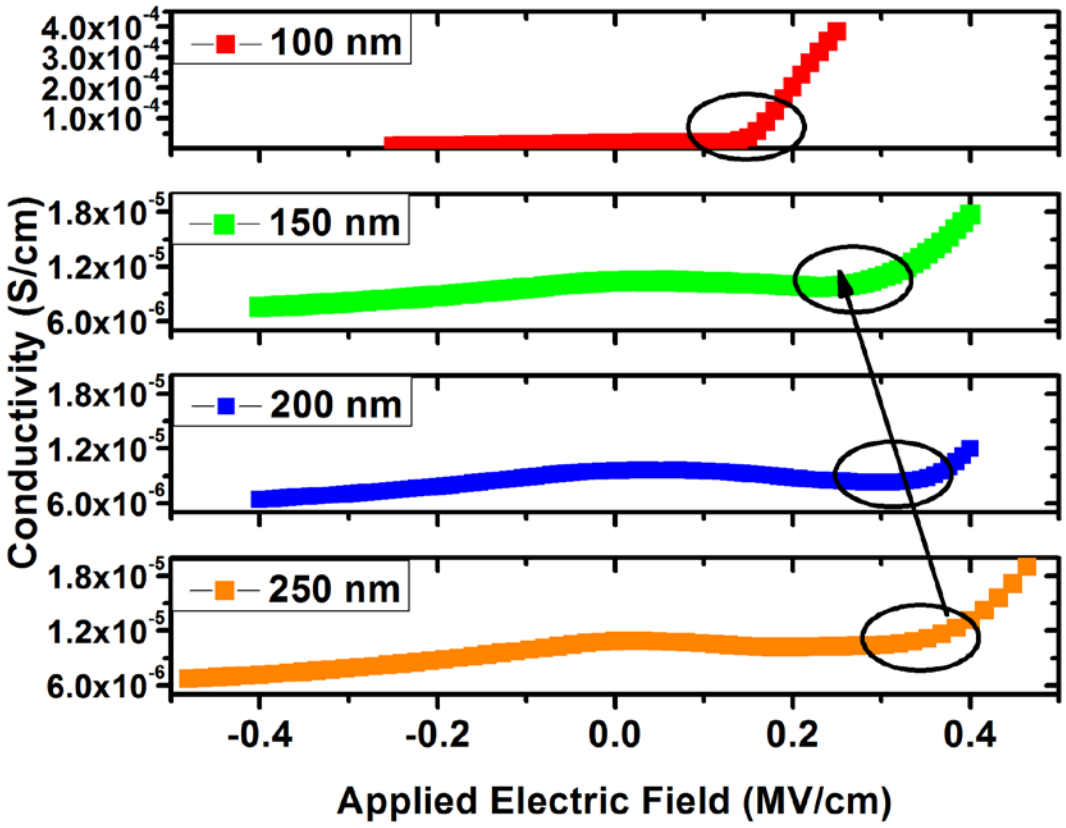

Figure 42: AC conductivity as a function of applied electric field measured at 1 Mhz for varying thickness BST samples annealed at 973K under reducing conditions. Samples prepared on nickelized silicon.

The maximum value of the capacitance density is also seen to shift closer to zero bias (.02MV/cm) indicating the accumulation of charge at the top surface. However, since the oxygen vacancies are not being compensated, an increase in loss was observed as expected. With UV (w. UV) enhanced oxidation (blue triangles in Figure 41), the additional photo-chemical interactions[129] drive oxygen ions into the vacancies thereby lowering the thermal budget required to compensate the vacancies. The temperature is low enough to kinetically impede the growth of nickel oxide as well as low enough to prevent oxygen from diffusing into the interface thereby allowing for an abrupt interface which can be seen from the values of the capacitance in

the negative regime (no significant change) and more importantly by TEM analysis which will be described below. UV irradiation, with energy larger than the band gap of BST, linearly accelerates the incorporation rate.[120,130]

The UV enhanced annealed samples showed a capacitance density maximum closer to zero bias and a *significant* decrease in loss indicating the annihilation of vacancies. Dielectric losses associated with UV enhanced oxidized films showed values of a maximum of approximately $\tan \delta \approx 0.1$ at zero applied field and approximately 0.08 at both negative and positive 0.33MV/cm. applied bias. The large improvement in dielectric loss (i.e. decrease in dielectric loss, especially that associated with the positive applied electric field) can therefore be associated with an increase in incorporation of oxygen into oxygen vacancies at lower temperatures with the help of UV irradiation and is significant with respect to the reduced sample and the conventionally annealed sample. The oxygen incorporation leads to a restoration of the Schottky barrier height by the incorporation of oxygen into the vacancies and unpinning the conduction band of the BST.[124] Similar trends for the improvement of dielectric loss under UV irradiation were seen in devices prepared with 100nm thick BST (not shown). As stated previously, the non-centro symmetry of the C-V characteristic in the reduced annealed sample in Figure 41 likely arises from an oxygen-depleted surface layer, thereby shifting the voltage maximum to the positive regime.[131,132] Upon re-oxidation, the value is shifted towards the origin. Since the work function of both Pt and Ni are approximately 5eV, the symmetry should be nearly preserved however the slight shift that is still observed may be due to the loss of oxygen during the deposition of the top contacts.

The incorporation mechanisms of oxygen into perovskite oxide surfaces has been studied previously.[133,134] The surface reaction itself is a multistep reaction comprising adsorption,

electron transfer, *O-O* bond dissociation and incorporation of atomic oxygen species into oxygen vacancies. One possible reaction for the incorporation of oxygen is given by reaction $\frac{1}{2}O_2 + V_O^{\bullet\bullet} \rightarrow 2h^{\bullet} + O_O^x$ where $h^{\bullet}$ are the positively charged holes.

This is then subdivided into several elemental steps:

1. $O_2 \rightarrow h^{\bullet} + O_2^-$

   $O_2^- + e^{'} \rightarrow O_2^{2-}$

2. $O_2^{2-} \rightarrow 2O^-$

3. $O^- + V_O^{\bullet\bullet} \rightarrow O_O^x + h^{\bullet}$

where step 1 and 3 are fast and step 2 is the rate determining step. Work has shown that the availability of free electronic species required for charge transfer is the rate determining step for oxygen surface exchange. [120] The use of a UV source enhances the amount of atomic oxygen and ozone in the system. This increases the speed of step 2 and eliminates it as the rate limiting step. This also removes the high temperature requirement described by Shen *et al.* since the high temperature step was previously required to overcome the rate determining steps.[127] It must be noted as well that Shen *et al.* lumped what is above referred to as steps 2 and 3 into one step (step II). Therefore, oxygen can be incorporated at a significantly lower temperature by using a UV source in comparison to conventional thermal annealing. This process has a significantly larger effect on the surface exposed to the UV than the bulk due to the need for diffusion of the active species. Figure 43 show the cross sectional TEM micrographs of Ni/BST film re-annealed at 573K under UV irradiation. A clean Ni/BST interface is evident from the selected area diffraction pattern (Figure 43A) and the corresponding dark field image is shown in Figure 43B. High resolution image recorded from Ni/BST interface (Figure 43C) does not show any

additional reaction layer at the interface confirming the interfacial stability of Ni/BST after re-annealing with UV irradiation under these conditions.

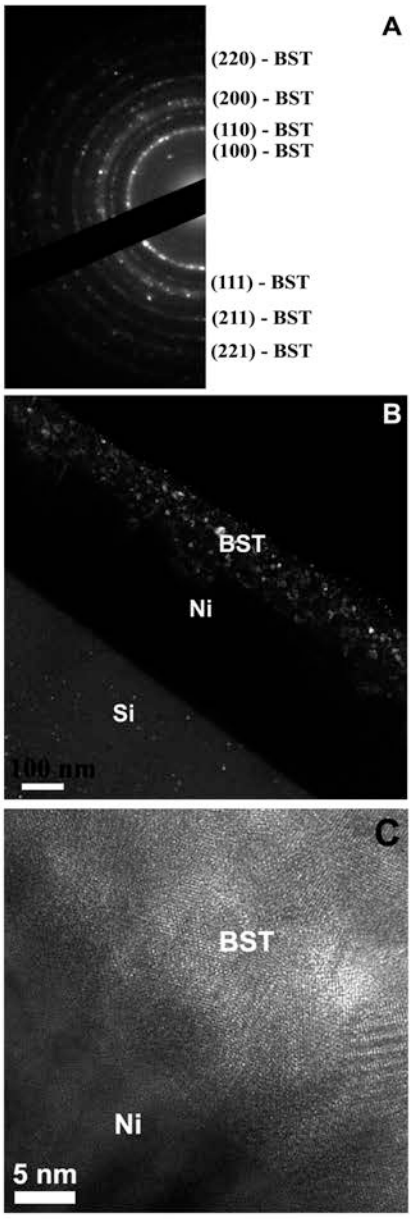

Figure 43: Cross sectional TEM micrograph of BST film grown on nickelized Si substrate, re-oxidized at 573K under UV irradiation. (A) Selected area diffraction pattern recorded from the Ni-BST interface. (B) The corresponding dark field image recorded using the (110) reflection of BST. (C) The high resolution image of Ni/BST interface revealing no additional reaction layers.

To better understand the mechanism involved in the incorporation of oxygen into the top surface, reoxidation experiments were carried out at various temperatures on films reduced at 973K. During reoxidation at 673K and above, NiO was formed, that can also be visually observed as the metal electrode oxidized. Hence, reoxidation annealing at 373K and 473K were carried out and the results are shown in Figure 44. It can be seen that at 373K, the onset of dielectric loss occurs at approximately the same point in both samples, indicating that there is no relative change in oxygen incorporation into the top surface. At 473K, the onset in the UV-annealed sample is delayed and reduced showing that oxygen incorporation has initiated at these temperatures, being assisted by photo-excitation. In the conventionally oxidized sample (without UV), onset is earlier, comparable with that found in the 373K samples, indicating no oxygen incorporation is occurring at the top surface. These results clearly demonstrate the effect of additional oxygen incorporation due to photo-excitation.

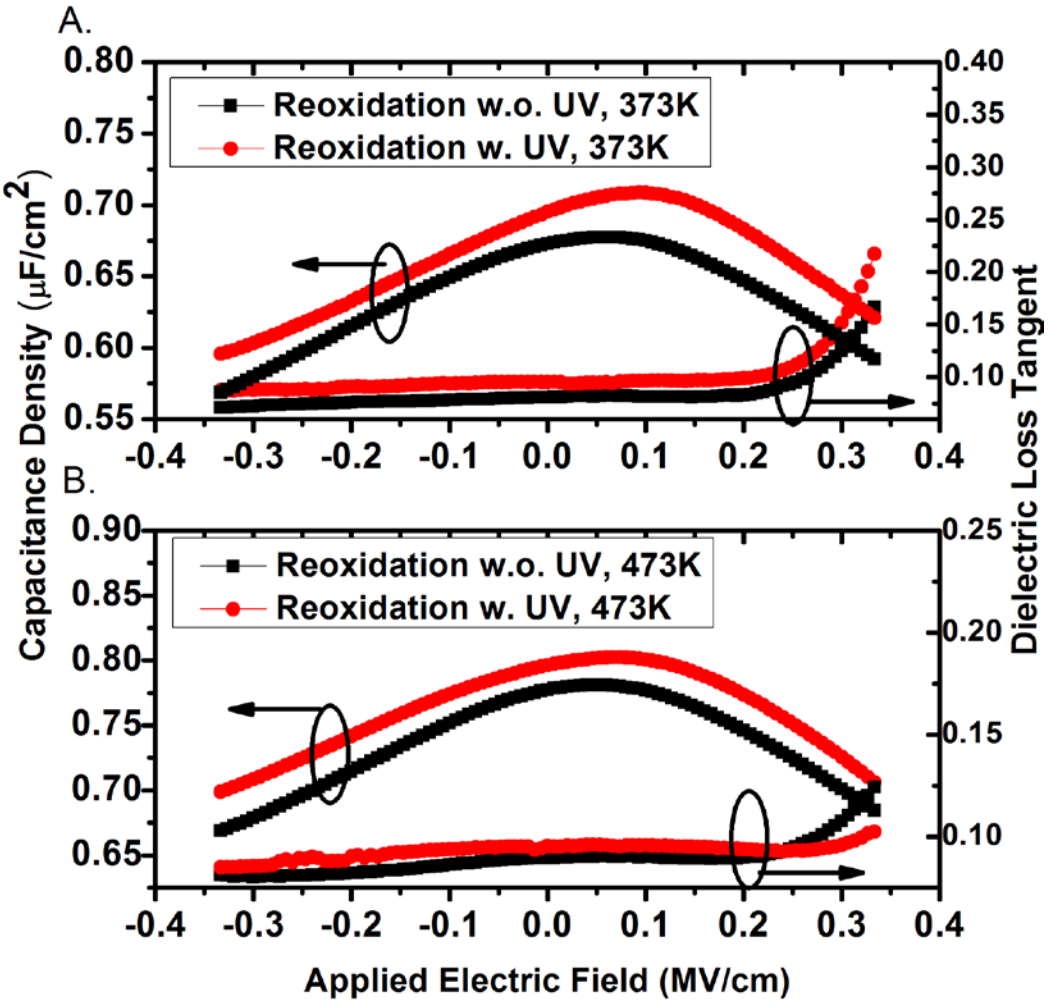

Figure 44: Capacitance density and dielectric loss tangents of reduced 150nm BST films reoxidized at 373K (A) and 473K (B) with UV and conventionally (without UV). Samples are grown with Ni bottom electrode with top Pt contact.

In order to further show that the asymmetry in the dielectric loss tangent was an effect of the oxygen vacancies at the reduced surface and not an effect of the electrode, Pt/BST/Pt capacitors were fabricated under identical conditions and annealed in reducing and in air environment as shown in Figure 45. Dielectric loss in the positive region of the reduced annealed sampled is shown to increase dramatically as was seen in the reduced and conventionally

reoxidized Ni/BST/Pt samples (Figure 41), indicating the cause of the dielectric loss increase is a result of the reduction of the top surface. Leakage current data from Ni/BST/Pt and Pt/BST/PT samples are seen in Figure 46 and Figure 47, respectively, also showed expected data in comparison to literature.[135] Leakage current was measured from 0 to 5V corresponding to an applied field of 0 to 0.33MV/cm. Leakage current for the Ni/BST/Pt sample in the positive regime (i.e. barrier associated with top depleted surface) decrease significantly with UV oxidation. The UV oxidized sample, at 0.33MV/cm had a leakage current of .046 A/cm^2 which was nearly 3 orders of magnitude below the conventional reoxidized sample (7.8 A/cm^2) and the reduced sample (~40 A/cm^2). In the negative regime, all the samples had approximately the same leakage current since the bottom contact was formed from the initial reduction anneal and the reoxidation step was in-sufficient to perturb that interface. Leakage current for the Pt/BST/Pt sample (Figure 47) in the positive bias shows high leakage when exposed to reducing anneal (11A/cm^2 at 0.33MV/cm) as opposed to the air annealed samples which show a very low leakage current ($4.6*10^{-5}$ A/cm^2 at 0.33MV/cm). This further indicates the lowering of the barrier height through the formation of oxygen vacancies at the surface when exposed to reducing annealing conditions.

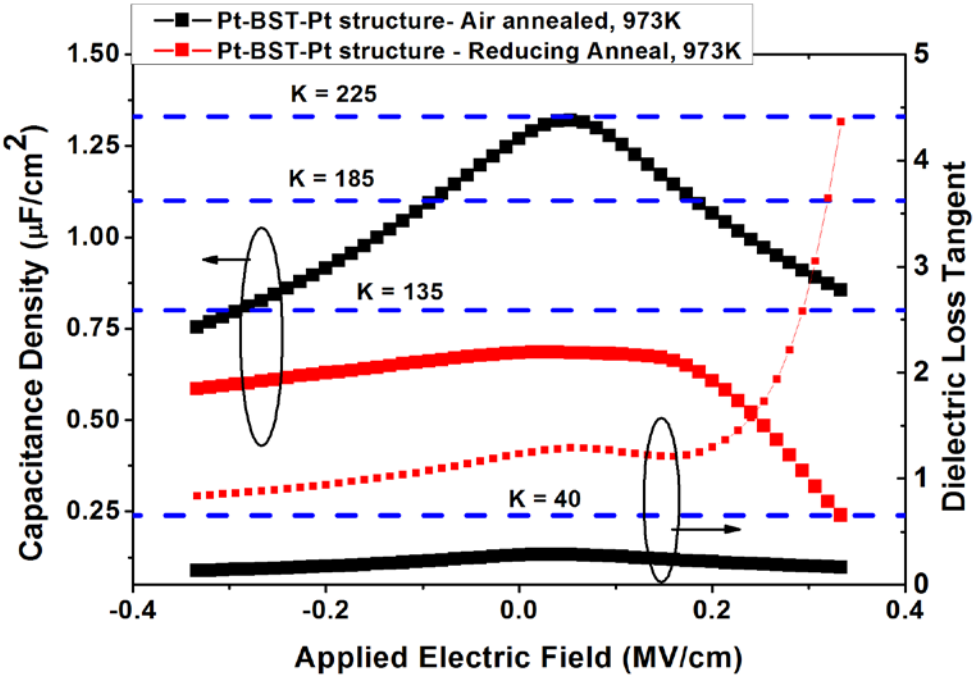

Figure 45: Capacitance density and dielectric loss tangent for 150nm thick BST thin film grown on Pt bottom electrode with Pt top contacts. Dielectric constant equivalents of capacitance density are given by the dashed blue line and labeled accordingly.

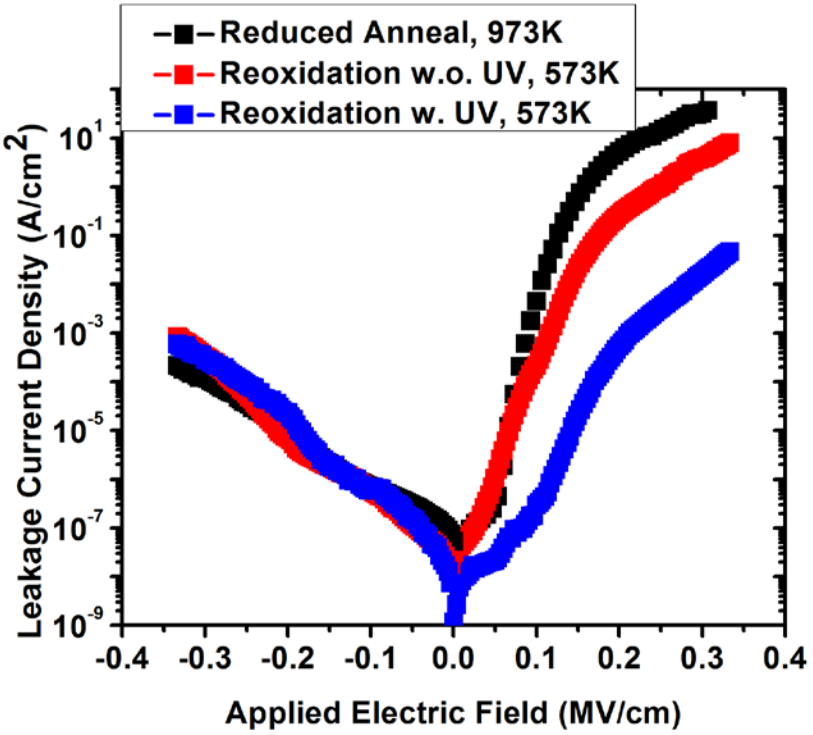

Figure 46: Leakage current density as a function of electric field for 150nm thick BST grown on Ni bottom electrode with top Pt electrode.

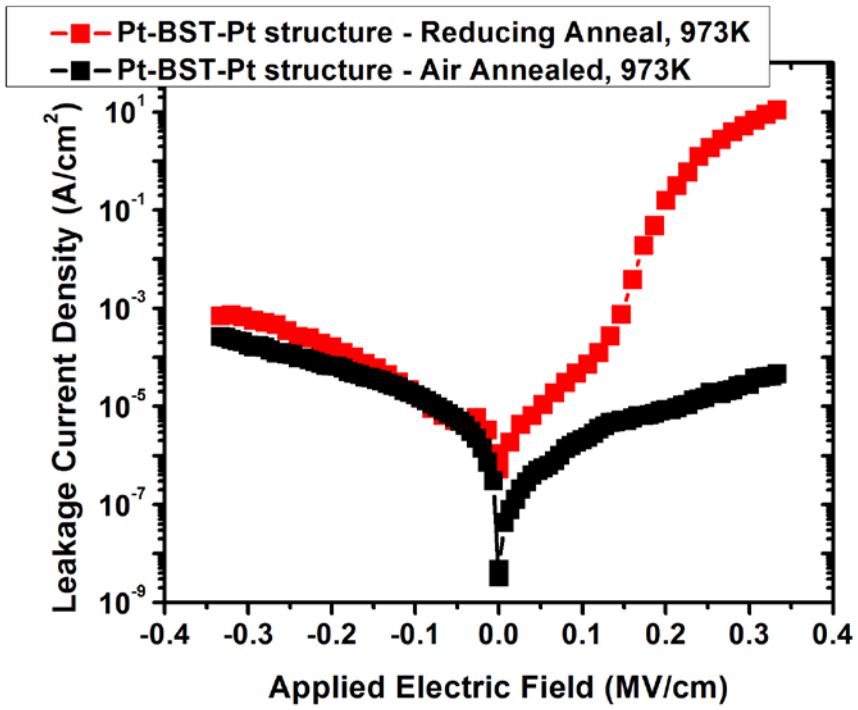

Figure 47: Leakage current density as a function of electric field for 150nm thick BST with Pt top and bottom electrodes

4.2.5 Conclusion

We have investigated active oxidation through photo-excitation as a processing route for reactive metal-oxide interfaces in the context of fabricating reduced loss nanoscale capacitors. The use of UV enhanced oxidation significantly decreases the leakage currents and losses in the film, thereby allowing for improvement in dielectric performance at lower temperatures. Improvements of nearly three orders of magnitude in leakage current and dielectric losses by a factor of eight were seen in films annealed under photo-excitation in comparison to conventionally annealed films. By limiting the thermal budget, a sharp base-metal/oxide interface can be maintained. The results could have relevance to advancing thin film capacitors for advanced packaging and power delivery.

5 LSNO

5.1 Colossal Dielectric Response in Polycrystalline Thin Film LSNO

5.1.1 Abstract

We have successfully synthesized the colossal dielectric constant (CDC) oxide $La_{2-x}Sr_xNiO_4$ (LSNO) in thin film form by reactive co-sputtering from metallic targets and careful annealing protocols. Composition and phase purity was determined through energy dispersive spectra and x-ray diffraction, respectively. The dielectric constant exceeds values of over 20,000 up to 1kHz and the activation energy for the frequency-independent conductivity plateau was extracted to be approximately 155meV from 300K to 473K, both in agreement with measurements conducted on bulk single crystals. However, unlike in single crystals, we observe early onset of relaxation in thin films indicating the crucial role of grain boundaries in influencing the dielectric response. AC conductivity at varying temperatures is analyzed within the framework of the universal dielectric law leading to an exponent of approximately 0.3, dependent on the electrode material. Impedance spectroscopy with electrodes of different work function (Pt, Pd, and Ag) was further carried out as a function of temperature and applied bias to provide mechanistic insights into the nature of the dielectric response.

5.1.2 Introduction

There is tremendous scientific and technological interest in oxides with colossal dielectric constant (CDC), on the order of 10^3-10^5.[136] Such materials could be candidates for applications

in advanced packaging or charge storage devices and studies related to charge ordering in complex oxides. Thin film dielectrics are of particular importance in the trend for miniaturization of microprocessors packaging due to the emphasis on next generation of embedded passives also referred to as the second Moore's law.[137,138] Packaging must accommodate lowering the on-chip parasitic inductance, thereby leading to technologies such as system-on-package and system-on-chip. Thin film dielectrics fabricated directly onto the die have the ability to exhibit high capacitance density (due to its minimal thickness) as well as being located close to the processor, thereby reducing inductance in bypass needs. New dielectric materials may significantly influence electronic packaging and lead the way for faster and smaller devices.

Recently, Krohns *et al.*[139] reported that bulk $La_{1.875}Sr_{0.125}NiO_4$ (LSNO) single crystals could have equally impressive or superior dielectric properties in comparison to other CDC materials, namely $CaCu_3Ti_4O_{12}$.[136,140] They observed that LSNO displays a high dielectric constant well into the GHz range, whereas many CDC materials suffer from large frequency dispersion. These properties, coupled with low dielectric losses into the gigahertz range, make this a material of interest for capacitor applications. In this section we present a detailed study on the dielectric properties of thin film polycrystalline $La_{2-x}Sr_xNiO_4$, successfully grown by reactive co-sputtering followed by careful annealing processes. To the best of our knowledge, no prior reports detail dielectric response in thin film forms of this complex oxide.

5.1.3 Experimental

Samples were prepared by co-sputtering La/Sr mosaic targets of composition 15:1 using a RF source and nickel using a DC magnetron gun in a thickness ratio of 2:1. Samples were prepared on platinized silicon (100 nm Pt/ 4nm Ti) as well as sapphire. Sputtering was performed at room temperature at 4 mTorr pressure with a gas composition of 60:3 argon to oxygen. All

samples were post-deposition annealed at 1273K in air in order to crystallize. The optimal conditions for sputter deposition and annealing to achieve phase-pure films were arrived at by extensive synthesis experiments and the results reported here are representative. Structural and compositional data was determined by glancing incidence x-ray diffraction and SEM energy dispersive x-ray spectroscopy. Sample thickness was measured by cross-sectional scanning electron microscopy to be approximately 900 nm. Electrical measurements were performed (with Solartron 1260 impedance gain analyzer and a 1287 electrochemical interface) by depositing top electrodes post-annealing by e-beam deposition through shadow masks (Pt, Pd and Ag), thus creating a metal-insulator-metal structure. The frequency range studied here ranged from 1Hz to 10^5Hz.

5.1.4 Results

As determined by EDAX measurements, the ratio of Lanthanum to strontium was approximately 17.2:1 leading to a composition of approximately $La_{1.89}Sr_{0.11}NiO_{4+\delta}$. x-ray diffraction pattern of the LSNO film shown in Figure 48 shows characteristic peaks of the K_2Ni-F_4 (I4/mmm). The calculated lattice parameter was (a=3.86Å) (b=3.86Å) (c=12.63Å) which is a minor deviation from the JCPDS data for single crystal La_2NiO_4 - (a = 3.855Å) (b=3.855Å) (c=12.652Å) (shown as vertical red lines in figure 1). No secondary phases were observed in the sample indicating phase purity. Plane-view SEM image shows a well defined polycrystalline structure with grain size on the order of approximately 150nm as shown in Figure 49.

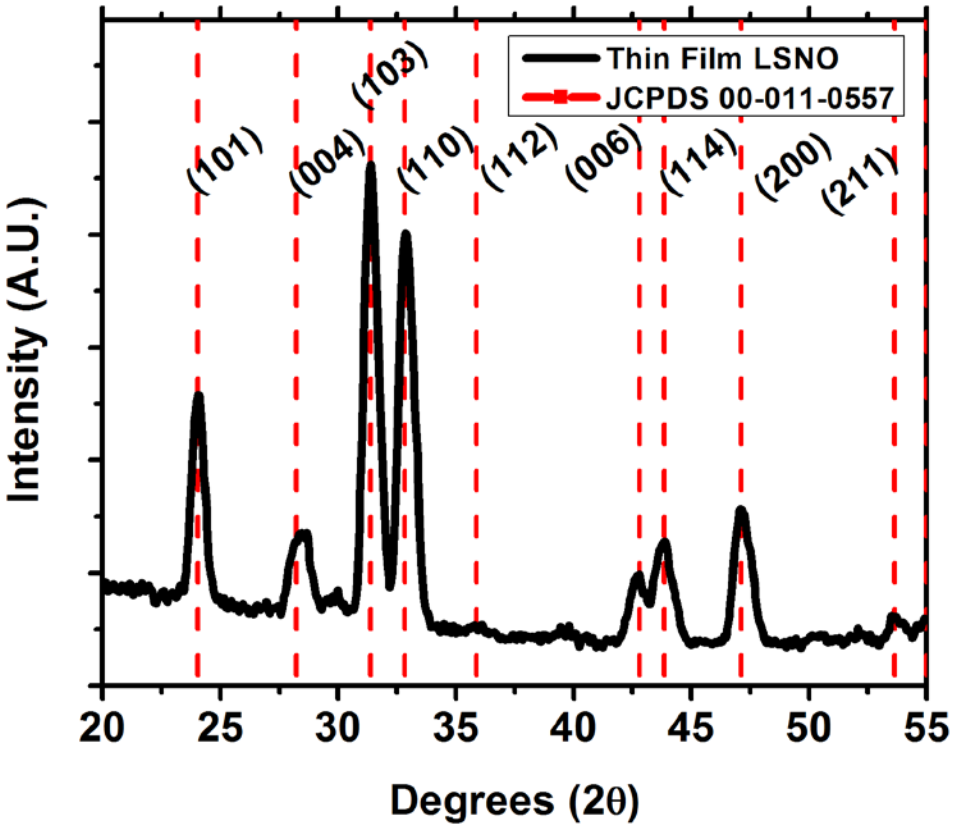

Figure 48: x-ray diffraction taken from a LSNO thin film. Vertical red dashed lines indicate La_2NiO_4 JCPDS data (file # 00-011-0557) with diffraction planes indicated above.

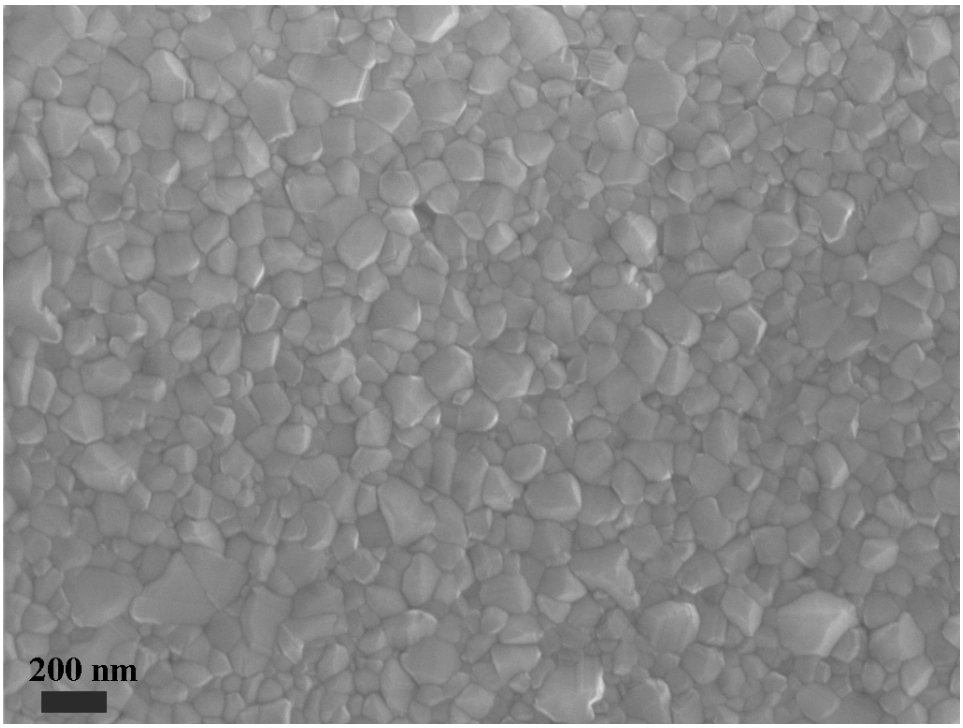

Figure 49: Plane view SEM image of LSNO surface after annealing. Grain size is approximately 150 nm.

Electrical characterization of the capacitors were performed by impedance spectroscopy with Pt top electrodes (unless otherwise noted).[141,142] The inset in Figure 50 shows representative data taken at room temperature as well as the equivalent circuit used to analyze the data. The Cole-Cole plot does not show an arc intercepting the coordinate origin indicating that under these conditions and in the studied frequency range only an extrinsic response is observed. If the capacitive response of the material was purely intrinsic, the complex impedance would intercept the origin. This plot can be modeled with two RC elements (resistor and constant phase element (CPE) in parallel) connected in series and one resistor, R_1, in order to consider the bulk resistance. The complex impedance representation can be used to determine the real and imaginary parts of the permittivity by the following equations

$$\varepsilon' = \frac{Z''}{\omega C_0 (Z'^2 + Z''^2)}$$

$$\varepsilon'' = -\frac{Z'}{\omega C_0 (Z'^2 + Z''^2)}$$

$$C_O = \frac{A}{t}\varepsilon_o$$

where C_0 is the vacuum capacitance, A is the area of the electrode, t is the thickness of the film, ω is the angular frequency, ε_0 is the permittivity of free space while Z' and Z" are the real and imaginary parts of the impedance.[143,144] The dielectric constant of the thin film measured at room temperature as a function of frequency is shown in Figure 50. A dielectric constant of approximately 20,000 is observed at low frequencies followed by a step-like decrease occurring at approximately 1 kHz leading to a strong decrease in permittivity as the frequency approaches approximately 100 khz (permittivity of the order of 10^2). This is in contrast to the results on a bulk single crystal reported by Krohns *et al.*,[139] also displayed in figure 3 for reference, who observed a low frequency dielectric constant of 50,000 which relaxed at the MHz frequency range to approximately 10^4 and maintained that well into the GHz range. Comparing with the results obtained from the Cole-Cole plot, internal defects (i.e. grain boundaries) in the material contribute to the large dielectric dispersion as higher frequencies are approached.[145] We note that our results are qualitatively similar to those reported in the literature for other CDC compounds such as CCTO, La_2MnCoO_6 as well as other bulk LSNO studies.[136,146,147] Many of these materials possess high dielectric constant and the origin may be explained by the internal barrier layer capacitor (IBLC) model where the grain and grain boundaries may have different conductivity and capacitance values that lead to Maxwell-Wagner (MW) polarization as well as the formation of a Schottky diode at the surface.[148,149,150]

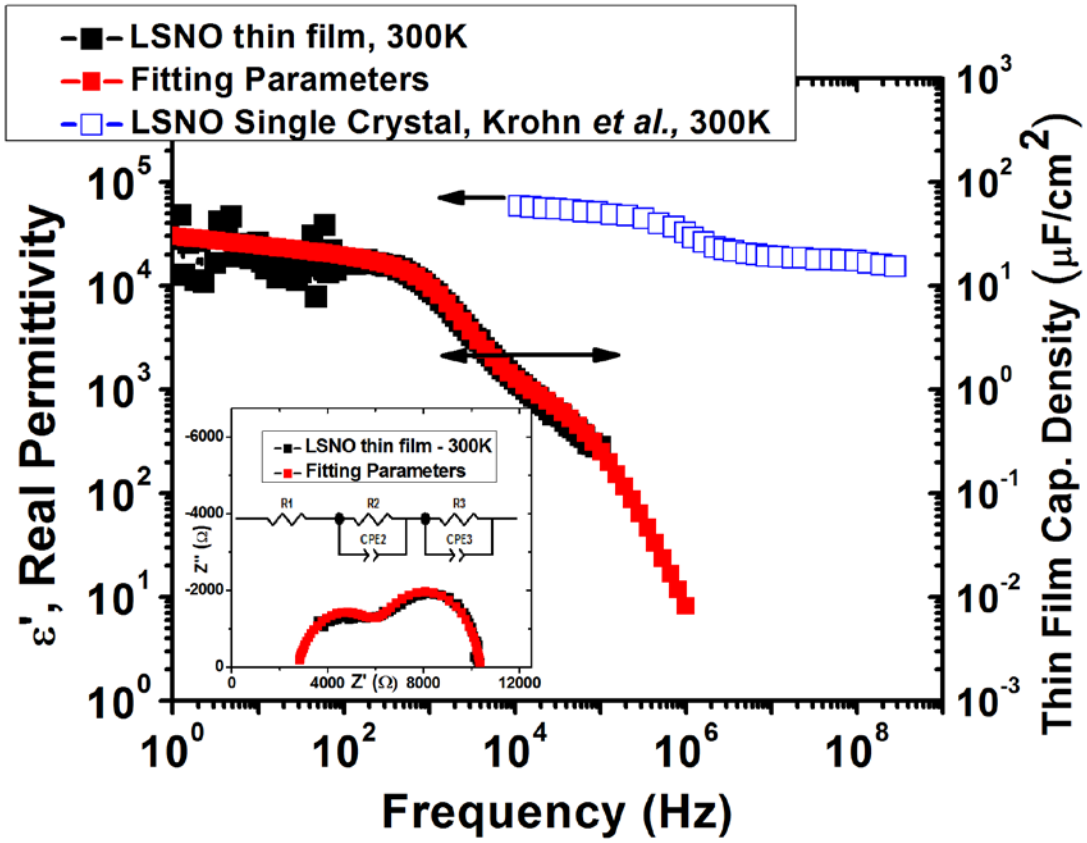

Figure 50: Dielectric constant of LSNO thin film (black squares) from this work and single crystal data (blue squares) taken at 300K from Krohns *et al.*[139] is shown for comparison. Inset is an impedance spectra from the LSNO film. Model fitting to data is plotted in red.

Temperature dependent permittivity is obtained from the impedance spectra in the range of 300-473K and plotted in Figure 51A. As the temperature increases, the onset of relaxation shifts to higher frequencies i.e. 600Hz at 300K, 1000Hz at 398K and 1200Hz at 473K. The permittivity is relatively insensitive to temperature, though increasing slightly as temperature increases as shown in Figure 51B. At 1kHz, permittivity increases from approximately 12,000 to 18,000 from 300K to 473K and 2,100 to 6,500 at 10 kHz in the same temperature range. The loss tangent at 300K (Figure 51C) decreases from ~10 at 1Hz to ~1 at 10Khz. As temperature increases, the loss tangent also increases, showing similar temperature sensitivity trends as the

real permittivity. The temperature response of the LSNO thin film is similar to that seen in other CDC material systems reported in literature.[151,152]

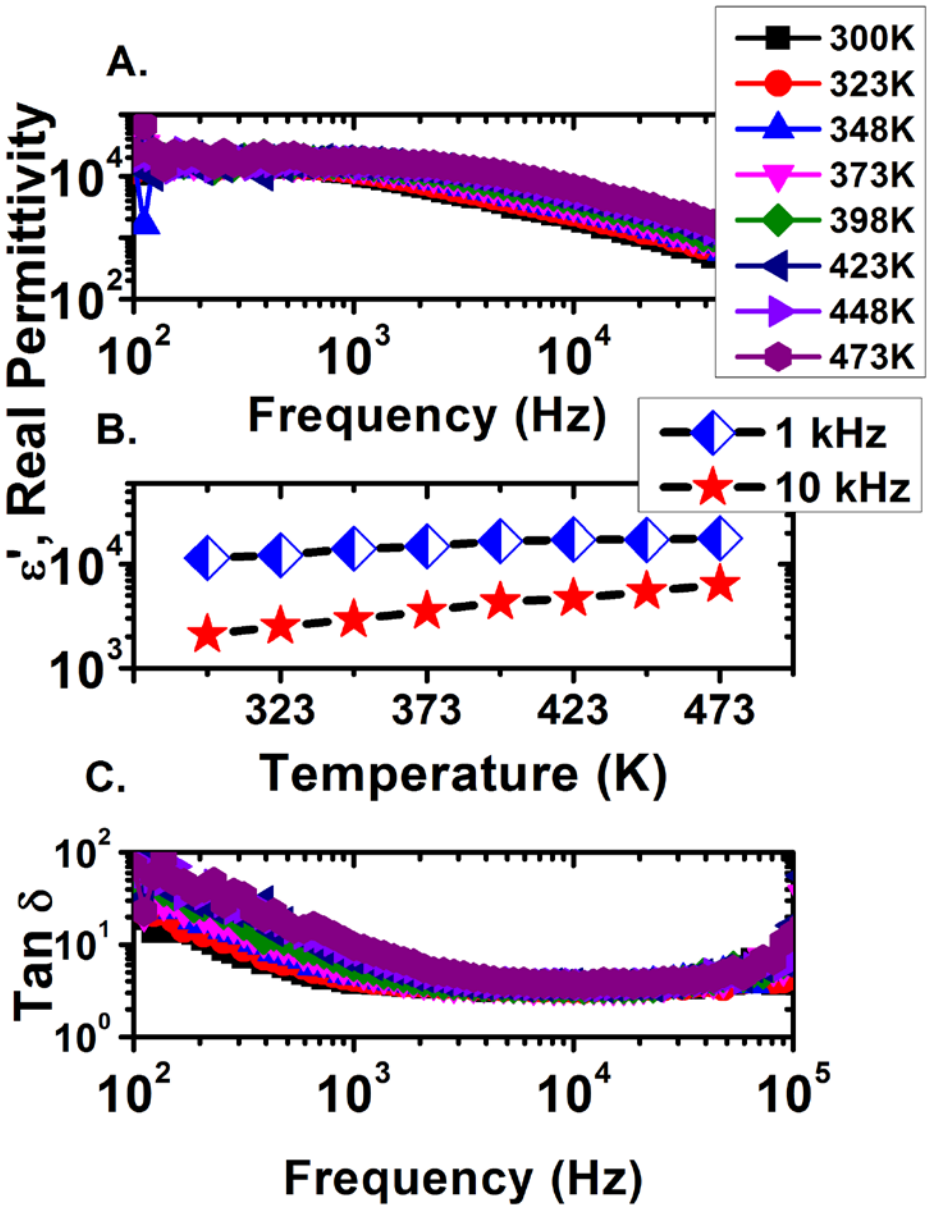

Figure 51: Dielectric response of LSNO thin films as a (A) function of frequency and (B) temperature for two representative frequencies. (C) Loss tangent as a function of frequency for various temperatures.

From the temperature dependent impedance spectra, the AC conductivity is derived by[153]

$$\sigma' = \varepsilon'' \omega$$

and plotted in Figure 52A. The intrinsic bulk response is given by the sum of dc conductivity and frequency dependent ac conductivity – for which Jonscher's universal dielectric response (UDR) is typically used.[154,155,156] The UDR is a common approach to take into account the hopping conductivity of localized charge carriers. Under these assumptions, the real part of the conductivity can be written as[145]

$$\sigma'(\omega) = \sigma_{dc} + A\omega^n$$

where n is the frequency exponent in the range 0<n<1, σ_{dc} is the dc component of the conductivity and A is the conductivity pre-factor. Both σ_{dc} and A are thermally activated quantities. The conductivity is found to be frequency independent in low frequency region. For the temperature range measured, the AC conductivity exponent was approximately 0.37 as shown in Figure 52B. n represents the degree of interaction between the mobile ions and the lattice around them. A unit value of n implies a Debye-type behavior and is attainable at low temperatures. However, as the temperature increase, the interaction between the charge carriers and the lattice increases which leads to a decrease in n. The power law corresponds to a short-range hopping of charge carriers through trap sites or in other words, the degree of interaction between mobile carriers with the surrounding lattice.[157] According to Funke, n≤1 implies that the hopping involves a translational motion with sudden hopping whereas n>1 means that the motion involves localized hopping with the species leaving the neighborhood.[158] Therefore, the exponent is indicative of the dimensionality of the motion of the charge carriers – short or long range.[159] The curve for different temperatures branches from the dc-link conductivity exhibiting weak temperature dependence, typical for ac conductivity due to hopping transport of charge carriers subjected to disorder-induced localization. Such localization may also arise from

substitutional distortion in doped semiconductors i.e. the addition of strontium into La_2NiO_4.[149] Hence in these films, localized polaronic hopping is involved in the high frequency conduction mechanism. This suggests that the relaxation may be related to the hopping conductivity. Localized charge carriers hopping in the lattice not only produces the conductivity but also gives rise to dipolar effects.[160]

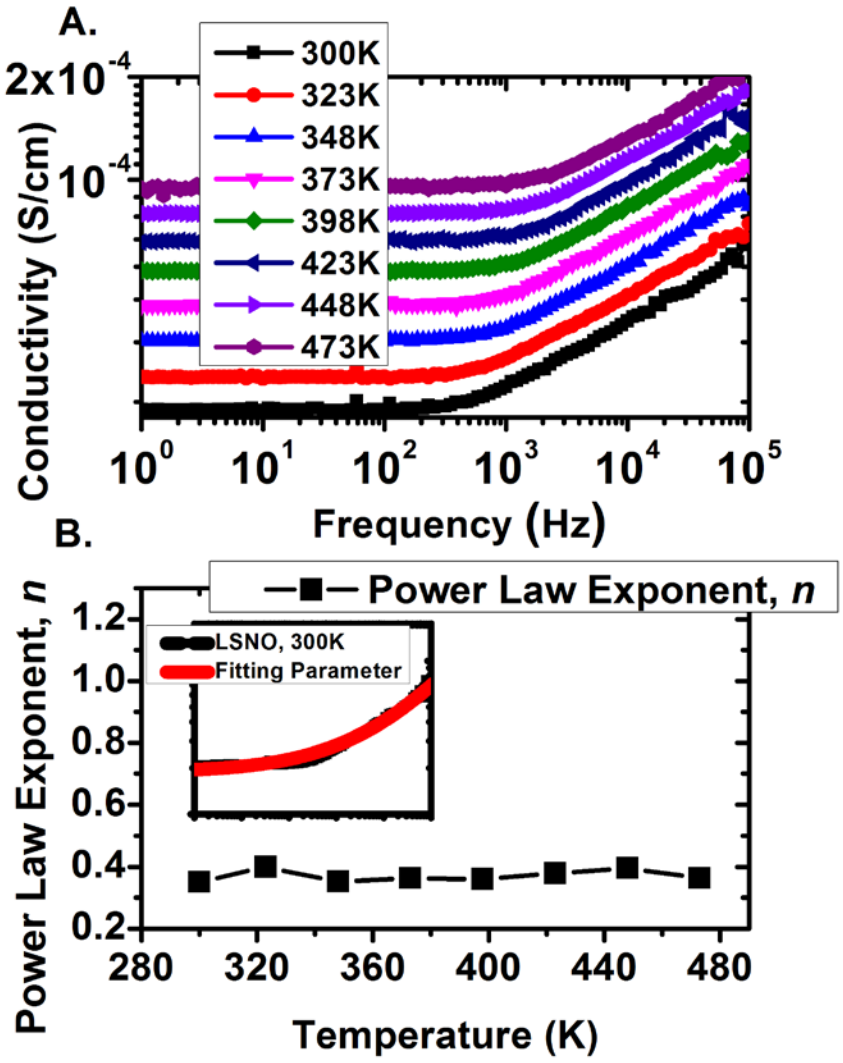

Figure 52: (A) Conductivity vs. frequency as a function of temperature. (B) Power law exponent, *n*, as a function of temperature. Inset shows representative fitting curve.

The activation energy for the DC component of the conductivity is given by the polaronic hopping relationship

$$\sigma_{dc} = \sigma_0 T^{-\alpha} \exp(\frac{-E_a}{kT})$$

where σ_0 is the pre-exponent factor, E_a is the activation energy of the mobile charge carriers, α=1 corresponds to the adiabatic case and k is the Boltzmann's constant. Good agreement between experimental data and fitting result is observed. The DC activation energy for the material is calculated to be 152meV. This value is in similar range to what has been observed in other colossal dielectric response studies (of cuprates, nickelates).[161,162,163] Previously, Wu and Neumeier and Liu *et al.* found that the electrical conduction mechanism in bulk $La_{2-x}Sr_xNiO_4$ ($0 \leq x \leq 1.2$) was due to thermally activated small polaronic hopping above the incommensurate charge ordering temperature and below which the electrical conduction mechanism changes to variable range hopping.[162,164] For bulk $La_{1.5}Sr_{0.5}NiO_4$, the incommensurate charge ordering temperature was determined to be 163K whereas the variable range hopping onset began at 485K.[162] The activation energy for the DC conduction was measured to be 124meV in the temperature range of the referenced study.[162] The relatively close values in activation energy to recent work imply that most likely localized polarons in the low frequency regime are formed and their activated hopping may contribute to the dielectric constant.[162,165]

In the study done by Krohns *et al.*,[139] a high dielectric constant of 10^4 at 300K was seen up until the Ghz range, whereas in our study we see the giant dielectric response only up to the KHz range. It should be noted that in the work by Krohns et al, the value at the GHz range is due to a secondary relaxation; lower than the initial giant dielectric response, but still possessing a large dielectric constant. We speculate the difference between this report and our thin film polycrystal LSNO is likely due to grain boundaries and a further discussion is presented below.

Nickel is a multivalent cation. Addition of strontium into the structure can lead to hole doping and a change in valence from Ni^{2+} to Ni^{3+} and resulting charge induced heterogenity.[166] Ni, like Cu, also reduces under high temperature annealing in air.[167,168] Upon cooling, not all of the microstructure is fully re-oxidized, which would aid in polaron formation and possibly semiconducting grain boundaries which would account for an arc in the Cole-Cole plot and help explain the origins of CDC behavior. The microstructure from the polycrystalline sample lead to a dielectric constant enhancement due to increased internal boundaries according to the IBLC model,[162] however it also leads to the rapid decrease in permittivity at higher frequencies. The relative ease in the creation of charge induced heterogeneities in the lanthanum nickelate type system could also contribute to the formation of surface depletion layers.

As mentioned earlier, the origin of the giant dielectric constant is extrinsic in nature arising from inhomogenieties (i.e. contacts, grain boundaries, etc.) in the structure that is being measured. As suggested by Lunkenheimer et al.,[145] the origin of giant dielectric response arises from Maxwell-Wagner type interfacial polarization onset by the electrode contact with the oxide. This contact leads to a suppression of electron concentration and thereby leading to the appearance of a depletion layer. This phenomena was looked at previously in different material systems exhibiting giant dielectric response however, while being apparent in most systems experiencing giant dielectric constants, many argue it is not necessarily the entire origin of the response.[169,170]

To understand the interfacial polarization effects in reactively sputtered LSNO thin films, we performed additional experiments to determine the effect of the contacts on the dielectric response of the film. LSNO was prepared as previously described and contacts made through electron-beam evaporation of Pt, Pd, and Ag. Impedance spectroscopy measurements were

performed using contact metal-LSNO/Pt structure with the base electrode being Pt in all cases. Figure 53 shows the dielectric response of the films with different electrodes. It is evident that all devices show giant dielectric response, irrelevant of choice of contact material. At low frequencies, the dielectric response is affected by choice of electrode. Since the work function of Pt and Pd, (approximately 5.3 and 5.15 eV, respectively)[171] is larger then Ag (4.2 eV)[172], the extent of space charge polarization arising from the contact potential will differ. The Schottky barrier being much thinner than the film thickness, the measured capacitance will be influenced by the space charge layer. The results indicate that the dielectric response of the film is sensitive to the Schottky barrier height and in turn the work function of the metal and therefore the contribution of the low frequency dielectric response arise from interfacial polarization. At sufficiently high frequencies, the bulk intrinsic dielectric properties of the polycrystalline sample should be observed however in this region, we do not have data to estimate the bulk capacitance and we cannot obtain information about the bulk permittivity, as discussed by Castro-Couceiro et al.[152] It can be found that there are only slight changes for the dielectric constant of the samples and the dispersion at higher frequencies is similar. AC conductivity results show similar response for all three top electrodes: Pt (Figure 52A), Ag (Figure 54A) and Pd (Figure 54B). Conductivity was modeled using Jonscher's power law, which showed the same behavior as the Pt-LSNO-Pt sample. Activation energy for the Pd and Ag sample in the low frequency range (DC conductivity) was ~163meV and ~155meV, (shown in Figure 55A) respectively which is comparable to that measured for the Pt electroded sample (153meV). Johnscher power law exponent again shown in Figure 55b shows similar results to that of Pt-LSNO-Pt, with Ag-LSNO-Pt laying at $0.3<n<4$ and Pd-LSNO-Pt laying at $0.2<n<0.3$, well within the range to indicate hopping conduction as previously discussed.

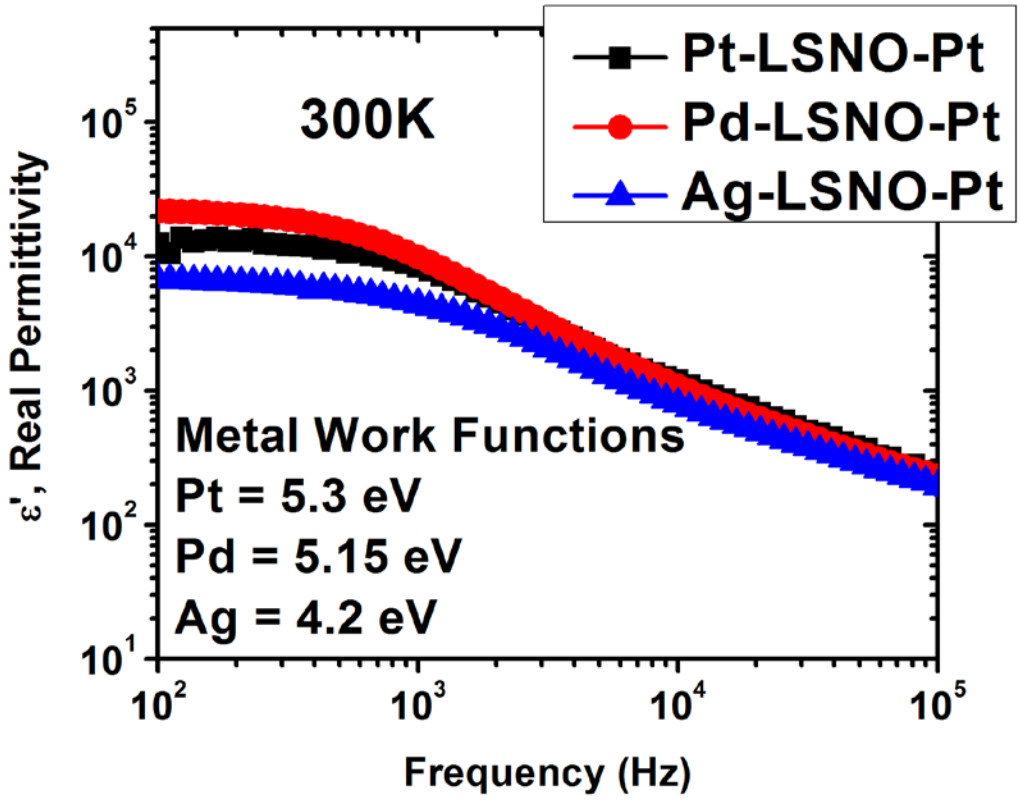

Figure 53: Dielectric permittivity as a function of frequency for Pt, Pd and Ag contacted LSNO thin films. The bottom contact is Pt in all cases synthesized identically. Metal work functions are labeled on the graph.

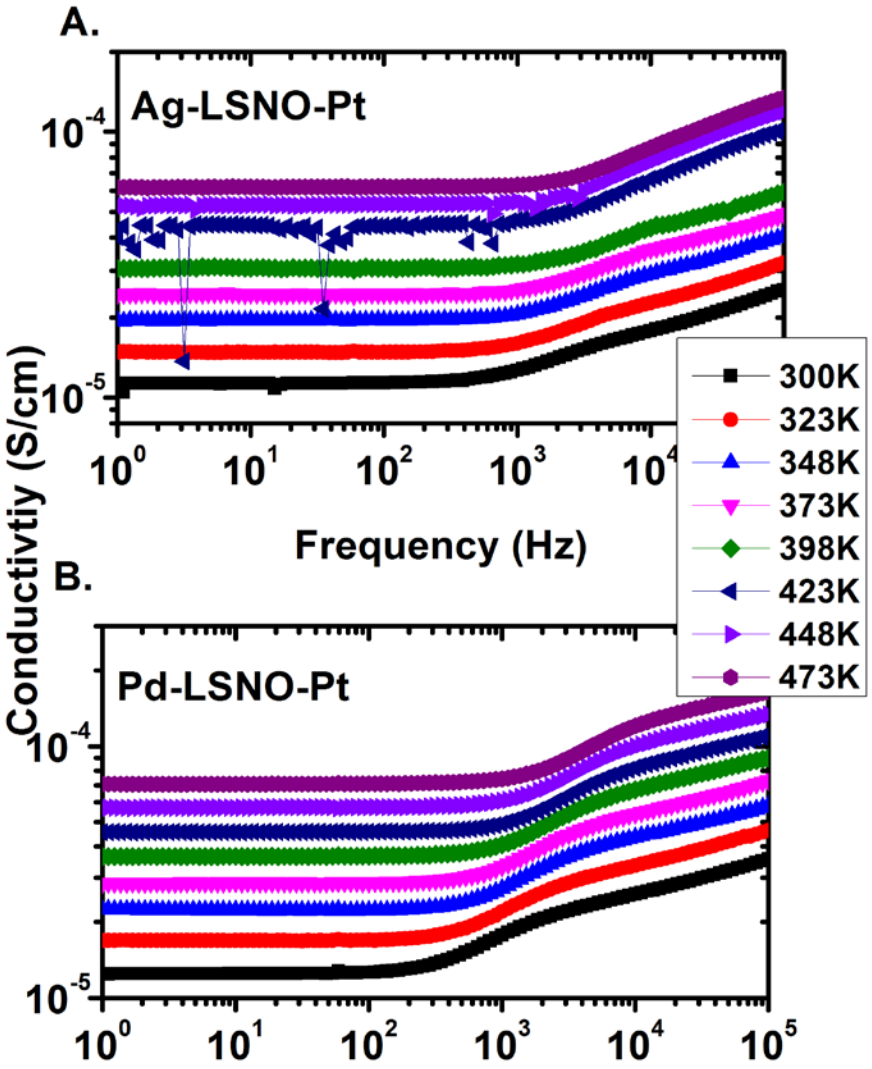

Figure 54: Conductivity as a function of frequency for (A) Ag and (B) Pd contact thin films at different temperatures.

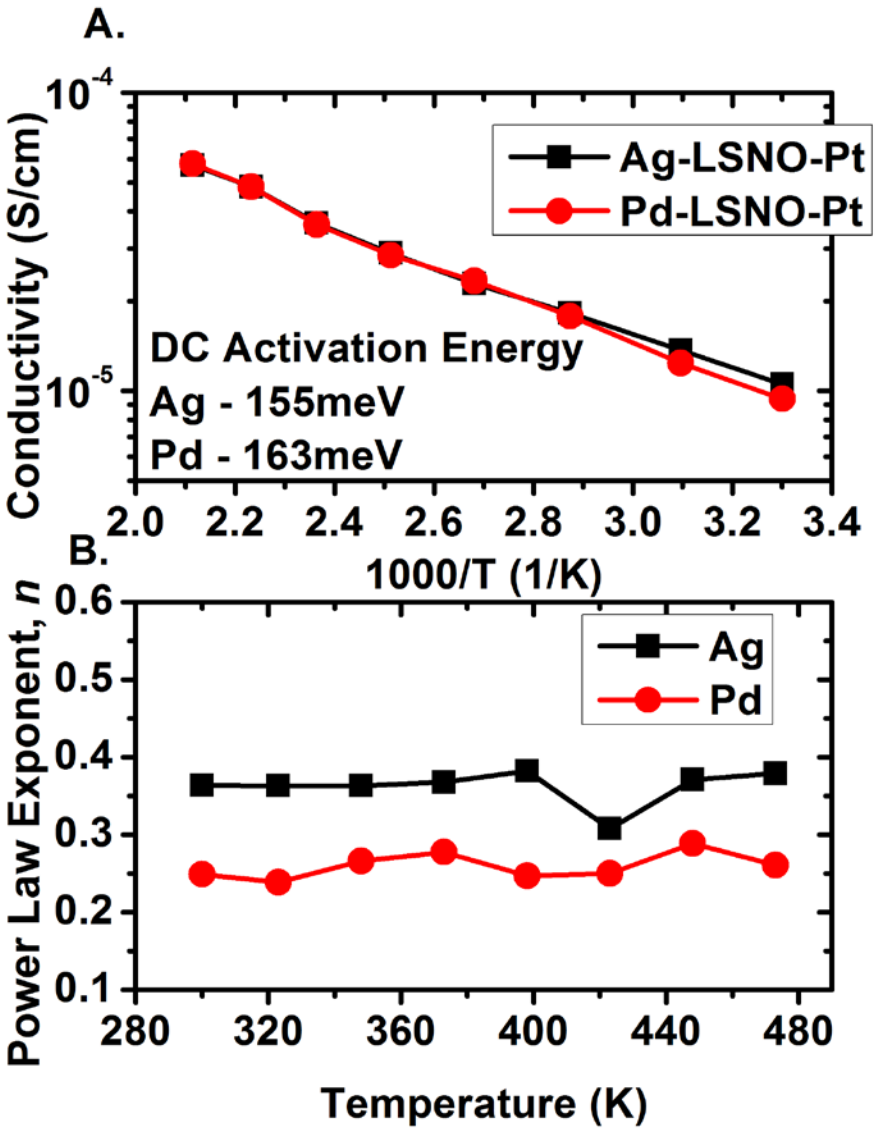

Figure 55: (A) Arrhenius relationship showing the DC activation energy for the Ag and Pd electroded films. (B) Power law exponent, *n*, for Ag and Pd contacted LSNO as a function of temperature.

Impedance spectroscopy at various voltages was then performed by sweeping the voltage from -5V to 5V in 2.5V increments for each of the samples: Pt (Figure 56), Pd (Figure 57) and Ag (Figure 58). The DC bias was applied to the top electrode relative to the bottom electrode. As the sample is biased starting from 0V, the low frequency arc decreases with the rest of the

curves remaining the same. This would indicate that the low frequency arc is formed by a depletion layer. The depletion layer width is changing as a function of the applied voltage and thereby changing the capacitive contribution as seen in the inset in Figure 56b, Figure 57b and Figure 58b where the dielectric constant decreases as a function of applied bias. Independent of the polarity of the exciting AC field, one of the two diodes at the two opposite contact interfaces is blocked and thus has a high resistance.[149] The low frequency response is strongly dependent on voltage leading to tunability of the capacitance, while the high frequency response shows little if any change. Tunability is defined here as $1-\frac{\varepsilon_V}{\varepsilon_{0V}}$ where ε_V is the dielectric constant at a specific voltage and ε_{0V} is the dielectric constant at 0V. A stepped decrease appears in the capacitance versus frequency curves, which is typical of MW relaxation,[149] indicating that the interfacial polarization dominates in the low frequency range. From these results, it is reasonable to infer that the tunability in LSNO arises primarily from interfacial polarization at low frequencies.

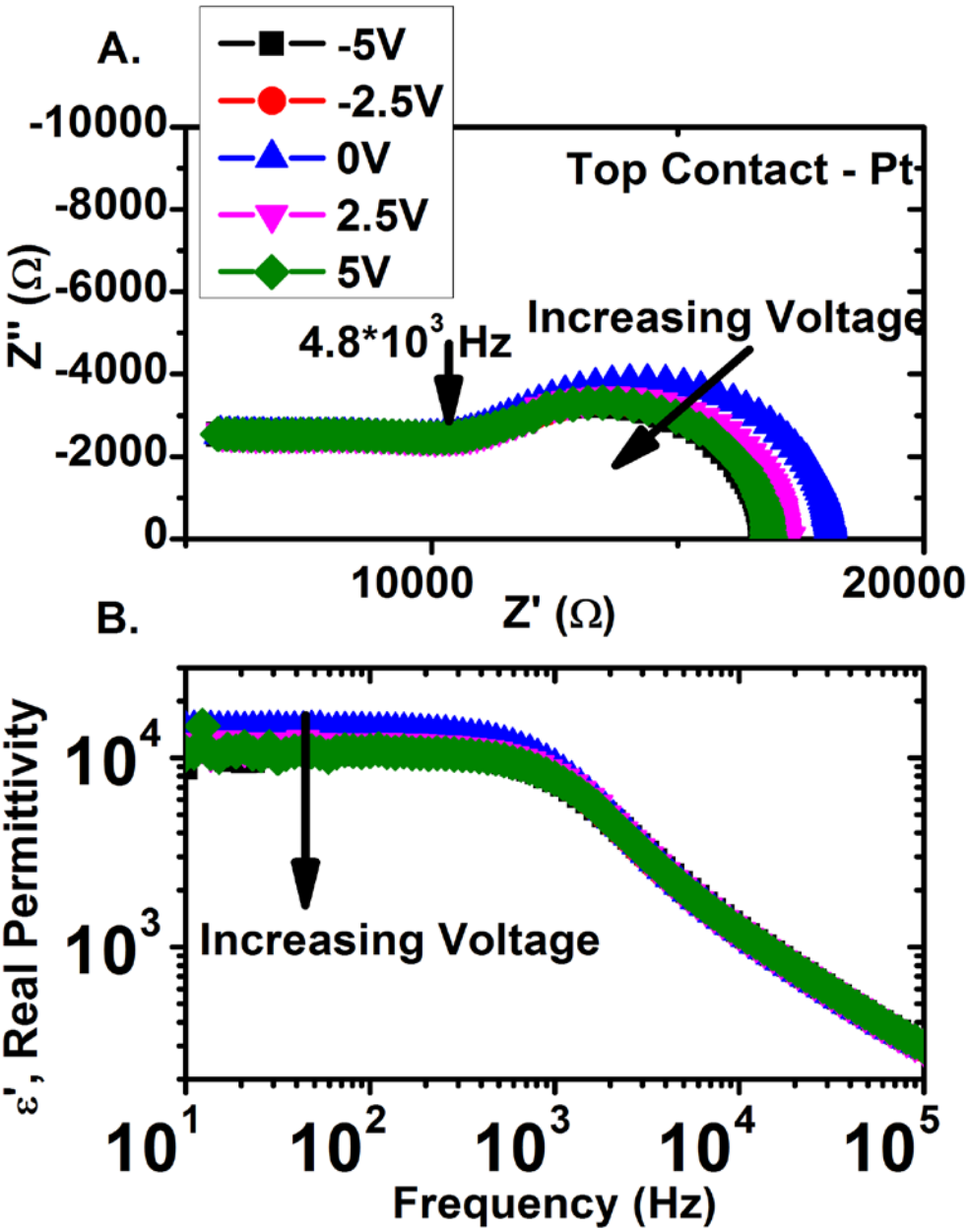

Figure 56: (A) Impedance spectra of Pt contacted LSNO thin films as a function of bias. (B) Real permittivity as a function of frequency derived from the impedance plot for different applied biases.

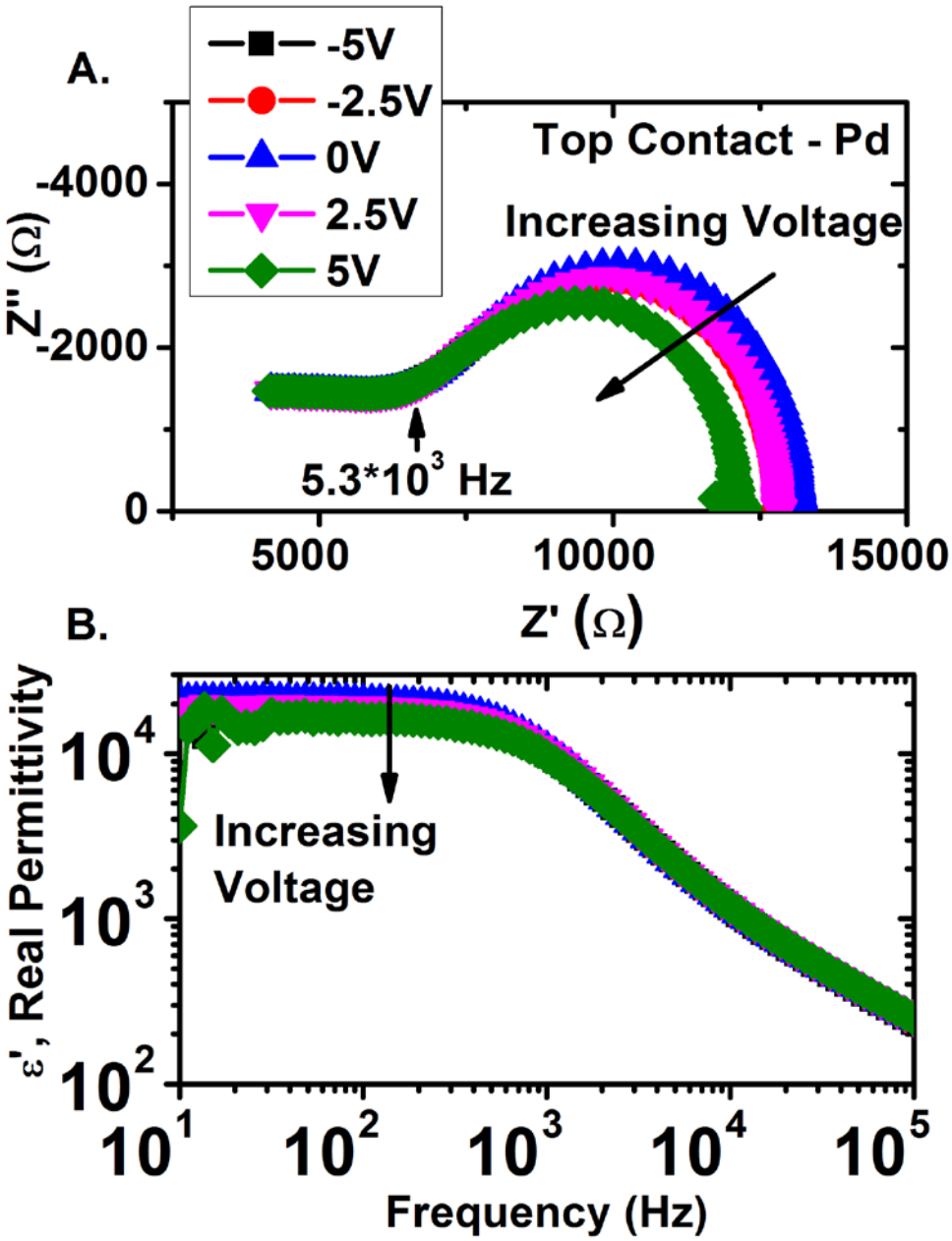

Figure 57: (A) Impedance spectra of Pd contacted LSNO thin films as a function of bias. (B) Real permittivity as a function of frequency derived from the impedance plot for different applied biases.

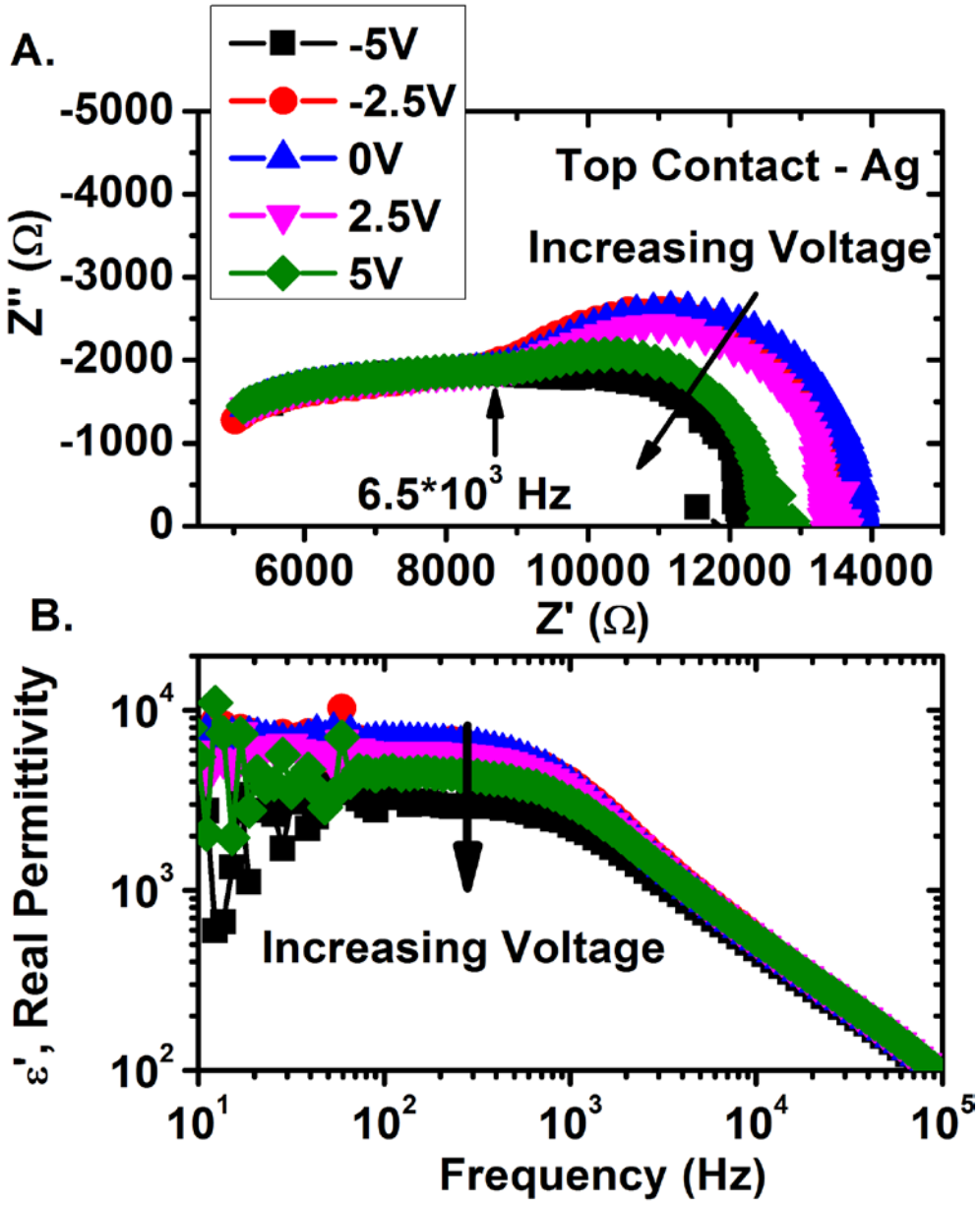

Figure 58: (A) Impedance spectra of Ag contacted LSNO thin films as a function of bias. (B) Real permittivity as a function of frequency derived from the impedance plot for different applied biases.

Dielectric response to the applied field as well as the degree of tunability is shown in Figure 59 for 100 Hz, 1 kHz and 10 kHz. By comparing the tunability, we see it is significantly

affected by the choice of materials further indicating that the interfacial polarization is dominantly caused by the electrode effect. At 100 Hz and -5V, sample with Ag electrode shows a tunability of 45%, whereas Pd and Pt contacted devices both show tunability of approximately 20%. Similar results are observed at 1kHz. At +5V, sample with Ag top electrode showed a tunability of 33% where as the Pd and Pt showed a tunability of approximately 25%. At 1kHz, Pt, Pd and Ag had approximately the same tunability of ~ 20%. At 10 kHz, there is negligible tunability since we are now past the interfacial polarization frequency range which was indicated in Figure 56, Figure 57 and Figure 58 as $4.8*10^3$ Hz, $5.3*10^3$Hz and $6.5*10^3$Hz, respectively. This result again indicates an interfacial contribution resulting from the Schottky barrier. The capacitance of the Schottky barrier depletion layer per unit area can be described as

$$C(/\,area) = \sqrt{\frac{e\varepsilon' N_d}{2(V_d + V)}}$$

where N_d, V_d and V refer to the charge carrier density, diffusion potential and the dc bias, respectively.[173] Since the work function of Ag (4.2 eV) is significantly smaller than that of both Pt (5.3 eV) and Pd (5.15 eV), the diffusion potential (i.e. built-in potential) will be smaller when an Ag electrode is used. Therefore, the capacitance of the depletion layer is more voltage sensitive and a larger tunabilty occurs as seen in Figure 59. According to Majhi et al., the apparent high capacitance originating due to electrode effects would generally have strong voltage dependence and would diminish upon the application of DC bias during capacitance measurement[174] consistent with our observations as well as other groups.[175] These results are also analogous to those obtained by K. Liu et al., and G.-Z. Liu et al. [173,176] Both these groups show the electrode effect in different oxide material systems. K. Liu et al. studied interfacial effects in $Pb(Fe_{1/2}Nb_{1/2})_{1-x}Ti_xO_3$ single crystal and separating the frequency responses to indicate the giant tunability was induced by interfacial polarization. G.-Z. Liu et al. showed similar

results for $BiFeO_3$ thin film capacitors that experiences giant dielectric response indicating that interfacial polarization results in a strong dependence of capacitance on frequency and bias voltage in the low frequency region.

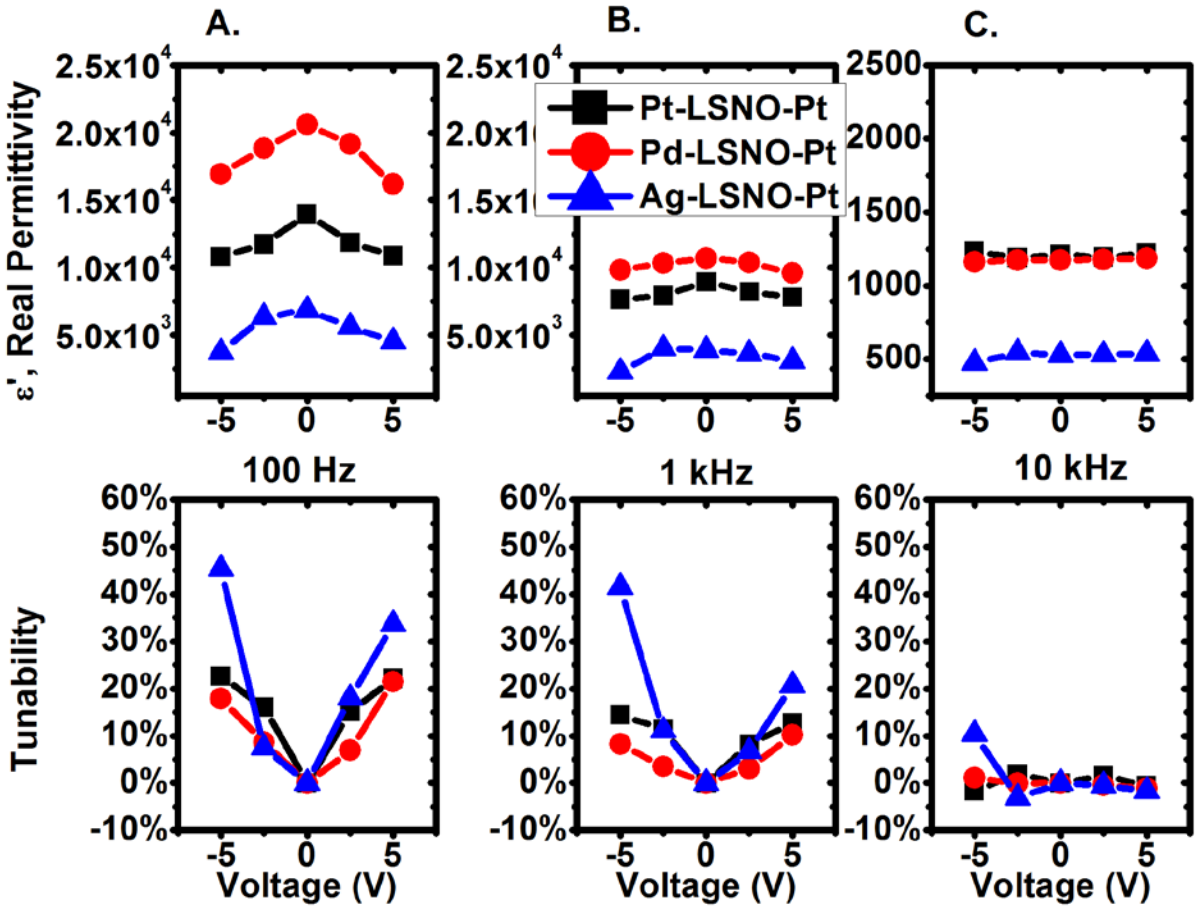

Figure 59: (Top) Dielectric constants and (Bottom) tunability of Pt, Pd and Ag contacted LSNO as a function of applied bias at (column A) 100 Hz, (column B) 1kHz, and (column C) 10 kHz.

Finally, we have explored the effect of surface depletion on the dielectric response of the LSNO films. In previous work, we have shown that UV excitation during annealing of complex oxides can significantly enhance oxygen incorporation and result in changes in conduction properties. UV irradiation creates highly reactive atomic oxygen and ozone that more easily

incorporates into near-surface regions and grain boundaries of the film.[177,178,179] In this work, two samples were prepared using the above mentioned steps (i.e. LSNO co-sputtered onto a platinized Si wafer, annealed at 1273K for 1 hour in air). One of the samples was subsequently re-annealed under UV irradiation in pure flowing oxygen at approximately 700K for 2 hours. Top platinum contacts were e-beam deposited on both samples under identical conditions. Prior to depositing top electrodes, the sheet resistance of the UV treated sample and the non-UV treated were measured. Sheet resistance for the as-annealed sample was approximately 10kΩ/sq. where the UV annealed sample had a sheet resistance of 5kΩ/sq. The resistance decreases due to increased p-type conduction in the film upon activated oxygen annealing during the UV process.[180] Since the sheet resistance decreases, we can assume that the film is becoming more semiconducting in the near surface region and should therefore experience a higher degree of dielectric enhancement. Dielectric properties of both samples are shown in Figure 60. Since the entire dielectric response curve decreases in the UV annealed sample, the UV oxidation is also affecting the grain boundaries through diffusion of the reactive species. The inset showing the impedance spectra also shows a significant shift with UV treatment while the same shape still remains and the corresponding low frequency arc is present indicating an electrode polarization. The low frequency arc arises from an electrode polarization formed by the creation of a depletion barrier. The interfacial polarization boundary has a significant shift from the non-UV treated sample ($9*10^3$Hz) to the UV treated sample ($3.9*10^4$Hz). Using UV-enhanced oxidation, active oxygen species diffuse through grain boundaries – annihilating some of the oxygen vacancies. This changes the response of the mid-frequency curve results from a change in the chemistry. Previously, when dealing with contact effects, we saw very little change in interfacial/grain boundary frequency boundary even with different contacts or voltages (shown in Figure 56,

Figure 57 and Figure 58). This is because the internal part of the film was not affected. By oxidizing the film, we significantly change the chemical characteristics of the material and are able to realize a change in the impedance response, providing additional insights into the different parts of the Nyquist plots.

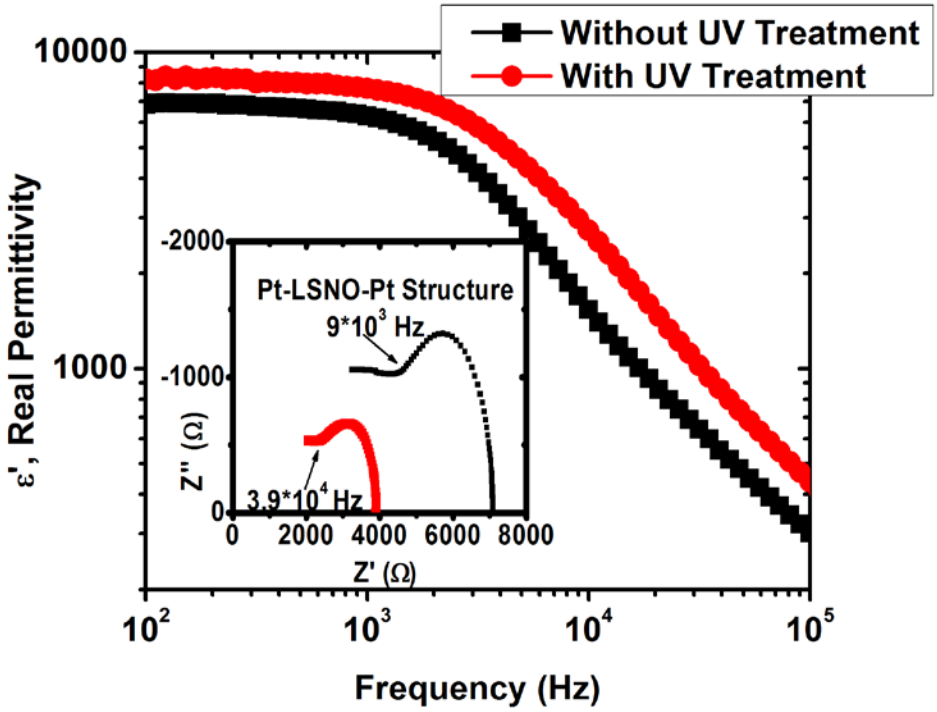

Figure 60: Dielectric constant of sample prepared without and with post processing UV annealing treatment. Inset: Impedance spectra of two previously compared samples.

5.1.5 Conclusion

In summary, we have successfully prepared LSNO thin films by reactive co-sputtering that show colossal dielectric constant at room temperature up to the KHz range. The low frequency dielectric constant and activation energy for conduction are in agreement with reported values for bulk single crystals. The low frequency giant dielectric response is influenced by the electrode work function. A lower work function electrode led to greater tunability –

further indicating the existence of a depletion layer. The early onset of dispersion in dielectric constant in our polycrystalline films is most likely due to the grain boundary contribution leading to Maxwell-Wagner type relaxation.

5.2 *pn* Junction Behavior in Epitaxial LSNO on Nb:$SrTiO_3$

5.2.1 Abstract

pn junctions formed with complex oxides may be of interest in emerging fields of electronics and energy conversion owing in part to their rich electronic structure. Here we report on the successful synthesis of epitaxial $La_{1.875}Sr_{0.125}NiO_4$ (LSNO) films on Nb doped SrTiO3 (Nb:STO) single crystals and a detailed study of their electrical properties. The junctions measured displayed highly rectifying current-voltage characteristic from 298 to 373 K. Mechanism for rectification is likely due to the formation of a *pn* junction between heavily doped n-type Nb:STO and semiconducting p-type LSNO. Capacitance-voltage (*C*-*V*) measurements as a function of temperature and frequency were used to determine the admittance of the *pn* junction. We investigate the thickness dependence of capacitance and highlight the role of defects in influencing the electronic properties of complex oxide *pn* junctions.

5.2.2 Introduction

There is growing interest in exploring all-oxide semiconductor devices for electronics and energy conversion. Transition metal-oxides display rich physical phenomena wherein electronic and magnetic properties show sharp changes dependent on temperature, phase and doping concentration. These factors significantly influence contact properties of junctions made with these systems through changes in the carrier concentration. Understanding carrier

conduction at interfaces with such materials is important from a fundamental perspective as well as device technologies in oxide electronics and opto-electronics. [181,182,183]

The study of all oxide *pn* junctions opens the possibility of developing new classes of thin film semiconductor heterostructures with tunable electronic and optical properties and the field is relatively young. It was recently shown that electron transport properties of junctions in manganites such as epitaxial $Nd_{0.5}Sr_{0.5}MnO_3$/Nb-doped $SrTiO_3$ could be explained with conventional *pn* semiconductor physics junction models.[184] Similar studies have been performed on $La_{0.5}Ca_{0.5}MnO_3$ films.[185] Similar to these systems, $La_{2-x}Sr_xNiO_4$ has attracted much interest due to charge ordering in large parts of its phase diagram, and strong charge-lattice coupling.[186,187,188] Therefore, understanding interfaces of this material system with the canonical single crystal Nb:STO substrate is of interest.

In this section, we report on the rectifying characteristics in the heteroepitaxial junction of $La_{1.875}Sr_{0.125}NiO_4$ (LSNO) on Nb-doped $SrTiO_3$ (Nb:STO), in which LSNO shows *p*-type semiconductor characteristics due to strontium doping and oxygen deficiency while the Nb:STO is a degenerate wide band gap n-type semiconductor. In LSNO, the substitution of Sr^{2+} for La^{3+} can provide holes in the O 2p band similar to the isostructural cuprates.[189] These represent some of the first studies on device junctions fabricated with this oxide system.

5.2.3 Experimental

$La_{1.875}Sr_{0.125}NiO_4$ films on single crystal (100) oriented Nb-doped $SrTiO_3$ substrates were grown by RF magnetron sputtering. Bulk precursor targets of LSNO were prepared by solid state reaction methods (ACI alloys). Great care was taken during deposition and power ramps to avoid target shattering during film growth. Substrates were chosen as 0.1%, and 0.7% Nb-doped $SrTiO_3$ (Nb:STO) due to its lattice constant of a=3.905Å being closely matched with that of a

similar composition LSNO (a=3.833Å, c=12.708Å for $La_{1.75}Sr_{0.25}NiO_4$)[190] and high carrier concentration. Films were deposited at 1123K at 4mTorr pressure with 2% oxygen in argon. The deposited samples were cooled to room temperature in the same environment. Film thickness, chosen to be 110nm and 220nm in this study on 0.7% Nb doped STO and 110nm on 0.1% Nb doped STO, was varied by changing deposition time and verified by x-ray reflectivity. Devices were formed by depositing Pt electrodes (area ~ 0.196 mm^2) onto the surface of the film with shadow masks. Contact to the Nb:STO substrates were provided by Ag paste on the backside. Contact between two Pt pads at the surface of the LSNO showed linear Ohmic conduction in the low bias regime. Electrical properties of the junction were investigated by measuring current-voltage (*J-V*) and capacitance-frequency-voltage (*C-f-V*) measured in a probe station equipped with a hot stage. Measurements were performed in frequency range of 20Hz to 1 MHz with amplitude of 50mV. The junction polarity is defined as a positive voltage applied to the top electrode contacting the LSNO film. Samples were characterized by x-ray diffraction and atomic force microscope (AFM). AFM data (not shown) revealed a root mean square roughness of ~2 nm.

5.2.4 Results

X-ray diffraction reveals sharp peaks corresponding to the K_2NiF_4 phase (tetragonal with a space group of I4/mmm) with the only peaks being the (00*l)* family from the Nb:STO and LSNO as shown in Figure 61 indicating cube-on-cube growth of the c-axis perpendicular for the 110nm sample on 0.7% wt Nb-doped STO. All measured samples showed similar orientation relationship. The rocking curve of the (006) LSNO peak showed a full width half maximum (FWHM) of 866 arc seconds for the 110m thick samples. Out of plane lattice parameter was estimated to be c=12.85Å for the 110nm film. For the 220nm films, rocking curve FWHM was

1270 arc seconds, as expected from extended defects as the film gets thicker. As a reference, the FWHM of the (002) peak Nb:STO was measured to be 220 arc seconds. The relative large width of the rocking curve of the thin films compared to the substrate indicates defects in the film. Epitaxial growth was verified through in-plane Φ scans along the (114), (103), (101) and (204) film planes as indicated in Figure 62. Four-fold symmetry is observed as expected for the tetragonal structure. The diffraction pattern was referenced to the substrate (111) plane indicating the epitaxial relationship (0k0)//(0k0) relationship as can be deduced from the alignment of the phi scan peaks. In-plane lattice constant was measured to be a=3.79Å for the 110nm film. Lattice parameter for the 220nm film was measured to be a = 3.78Å and c=12.91 Å. The lattice parameters differ from the bulk values and are likely indicative of non-stoichiometry in the oxygen content in the film. In bulk ceramic samples, it is known that there is a correlation between lattice parameter and oxygen content, that is, the higher the oxygen content, the larger the c parameter.[191] It is however challenging to perform thermo-gravimetric measurements on thin film samples to measure oxygen content.

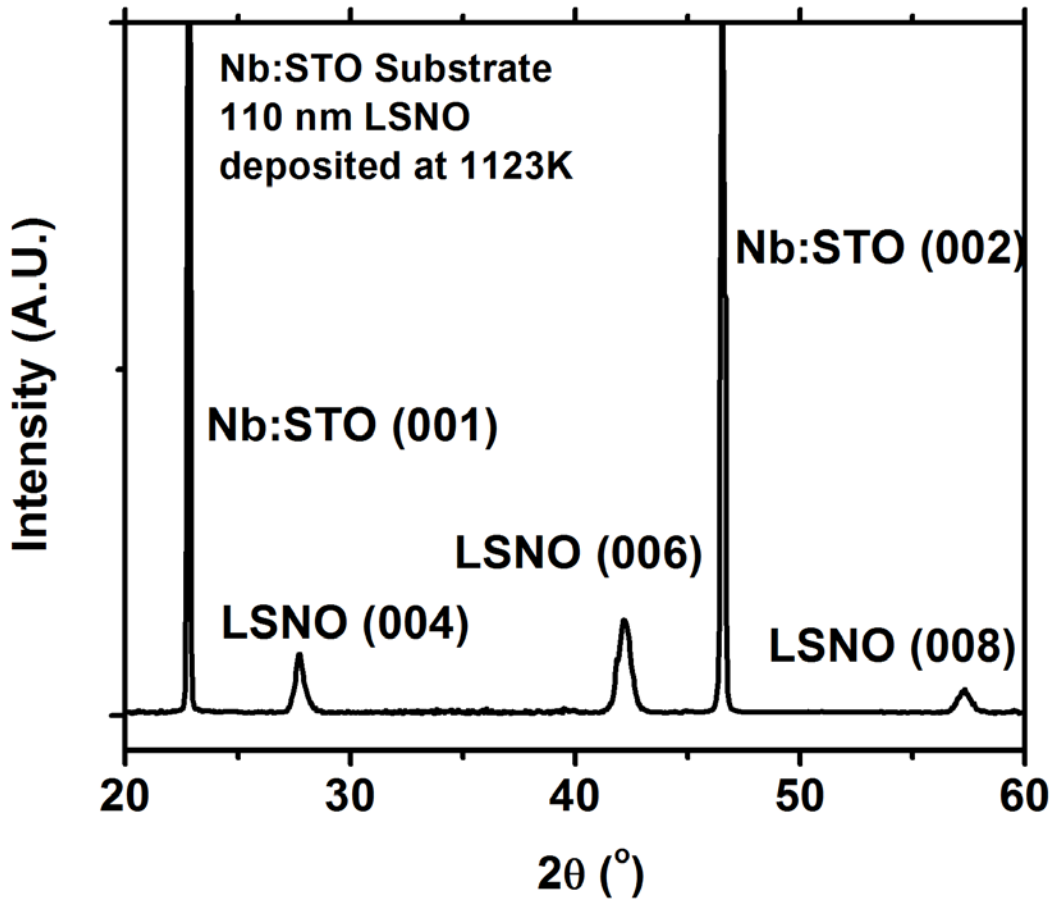

Figure 61: Diffraction pattern taken from epitaxial LSNO film of 110nm thickness on 0.7% Nb:STO substrate. (00l) family of peaks are present.

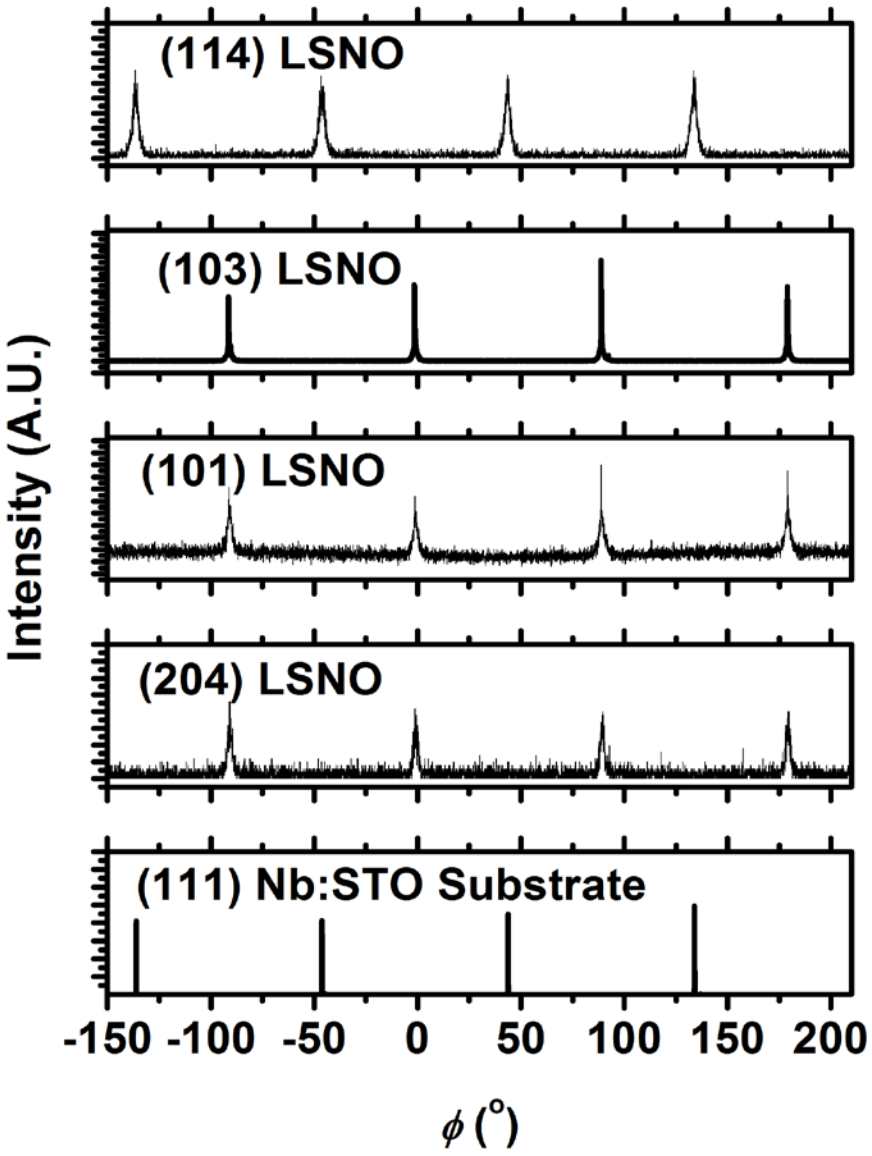

Figure 62: Epitaxial relation for 110nm thick LSNO on 0.7% Nb:STO of the (114), (103), (101) and (204) planes. (111) Nb:STO plane scanned for reference. Peaks indicate 4-fold symmetry as expected for LSNO films.

Current density-voltage characteristics (*J-V*) of the LSNO-Nb:STO junction exhibit significant asymmetric behavior in the temperature range from 298 to 373K. Good rectifying behavior is found in the whole measured temperature range and seen in all samples as shown in Figure 63A,B,C. A typical metric to judge rectifying properties for diode behavior is to compare *J(+V)/J(-V)*, namely the ratio of current at a fixed positive voltage with that at the same negative voltage. Rectifying ratio values of 317 and 432 were measured for LSNO film of thickness of 110nm and 220nm at 298K at 2V on 0.7% Nb:STO, respectively. The 110nm film on 0.1% Nb:STO had a rectifying ratio of 120 at 2V at 298K. For simplicity, 110nm thick films grown on 0.7% Nb doped STO is referred to as Nb0.7%-110nm, 220nm 0.7% Nb doped STO is referred to as Nb0.7%-220nm and 110nm 0.1% Nb doped STO is referred to as Nb0.1%-110nm. The threshold voltage at which the current increases significantly increases monotonically with decreasing temperature as seen in Figure 63 which has also been observed in other transition metal-oxide heterojunctions.[192] This is most clearly observed in the semi-log plots of Figure 63D,E,F. The increasing temperature has no obvious effect on the *J-V* curve except for a nearly rigid shift to lower voltages as indicated by the arrows in Figure 63.

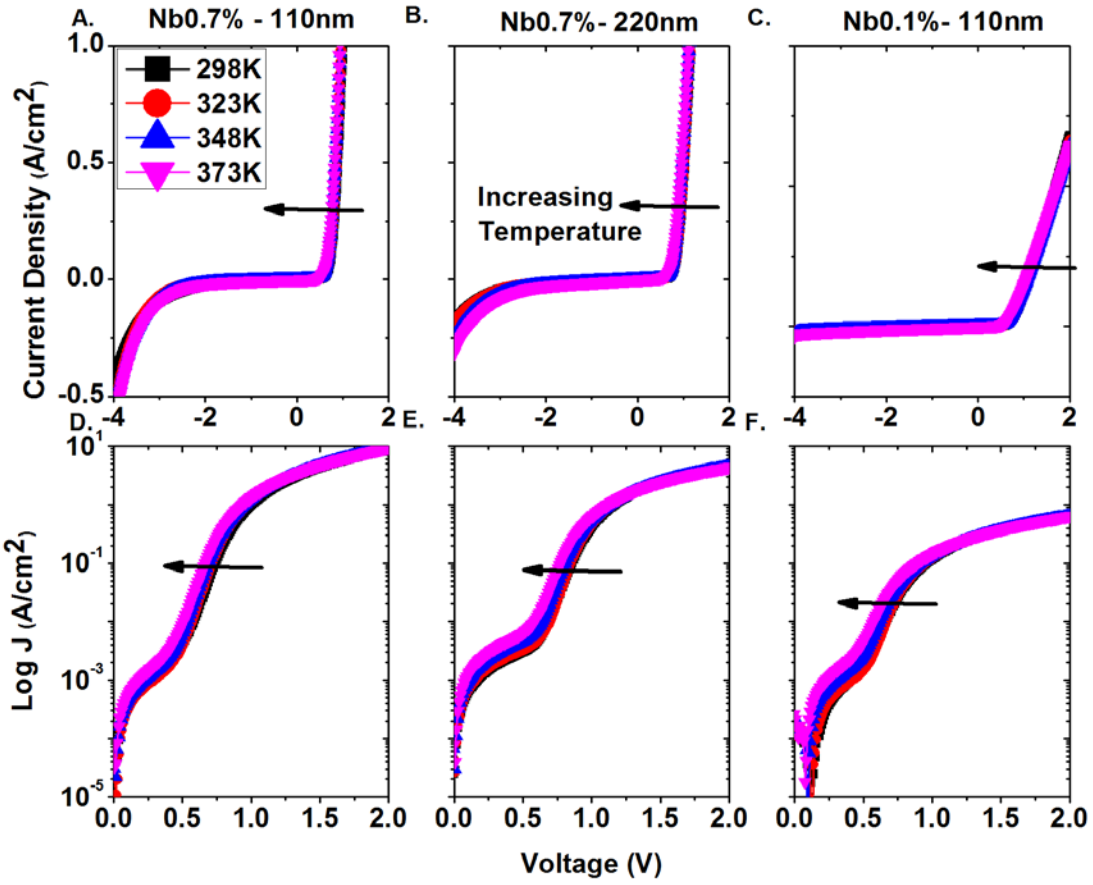

Figure 63: Linear plots of current density as a function of voltage for (A) Nb0.7%-110 nm, (B) Nb0.7%-220 nm and (C) Nb0.1%-110 nm samples. Log linear current density plot in the positive bias of (D) Nb0.7%-110 nm, (E) Nb0.7%-220 nm and (F) Nb0.1%-110 nm samples.

Typical characteristics of current density – voltage on semi-logarithmic scale is shown in Figure 63D,E,F Since we are using heavily doped degenerate Nb:STO substrates with band gap of ~3.2eV, the substrate acts as an n^+ semiconductor whereas our LSNO is a p-type conductor having a bandgap of approximately 2eV.[193] For this reason, the band structure of the junction may be regarded as a *pn* junction. The rectifying *J-V* characteristics of junctions originate from

energy band bending. When $V>k_BT/q$, we can approximate the forward bias current density (J) as[192,194]

$$J = J_{pn}^{'} \exp(\frac{qV}{nk_BT})$$

Equation 4

where $J_{pn}^{'}$ is the temperature dependent saturation current pre-factor, q is the elementary charge V is the applied voltage, n is the ideality factor, k_B is the Boltzmann constant and T is the temperature in Equation 4.

In the ideal regime where diffusion dominates transport, n is unity whereas when n equal to 2 indicates transport is dominated by recombination of charge carriers in the space charge region.[194] The linear part of the semi-log plots is extracted from Figure 63D,E,F for this analysis. We obtain a value of approximately n =2.6, 2.8 and 3.6 for samples 0.7%-110nm, 0.7%-220nm and 0.1%-110nm respectively in the linear region at 298K shown in Figure 64 as a function of temperature. The ideality constant is seen to decrease with temperature. Due to the deviation from ideality, we can assume that any one distinct mechanism is not dominating the transport. Large values for n have been observed in conventional and perovskite semiconductor junctions.[195,196] Possible reasons may include spatial barrier inhomogeneities and interface states at the junction. Ramadan *et al.*[197] came to a similar conclusion indicating that it may originate from varying distribution of Nb in doped $SrTiO_3$ due to high temperature processing.[198] Intrinsic electronic inhomogeneities of $La_{1.875}Sr_{0.125}NiO_4$ with its stripe ordering and layer structure may also play a role. The Nb0.7%-110nm and Nb0.7%-220nm samples, show relatively the same ideality of approximately 2.62 and 2.82 at 298K, respectively which decreased to approximately 2.26 and 2.35 at 373K, respectively. The slight difference in ideality arises from the relaxed thicker film having more defects. These results were also confirmed by the wider rocking curve

obtained for the thicker film. The large difference in ideality between the Nb0.1%-110 nm and Nb0.7%-110 nm samples is likely due to the substrate (since the samples were deposited at precisely the same time and conditions) or the large depletion width in the film. All reported results on ideality we show has a similar temperature dependent trend, analogous to other all-oxide junctions.[196,199,200]

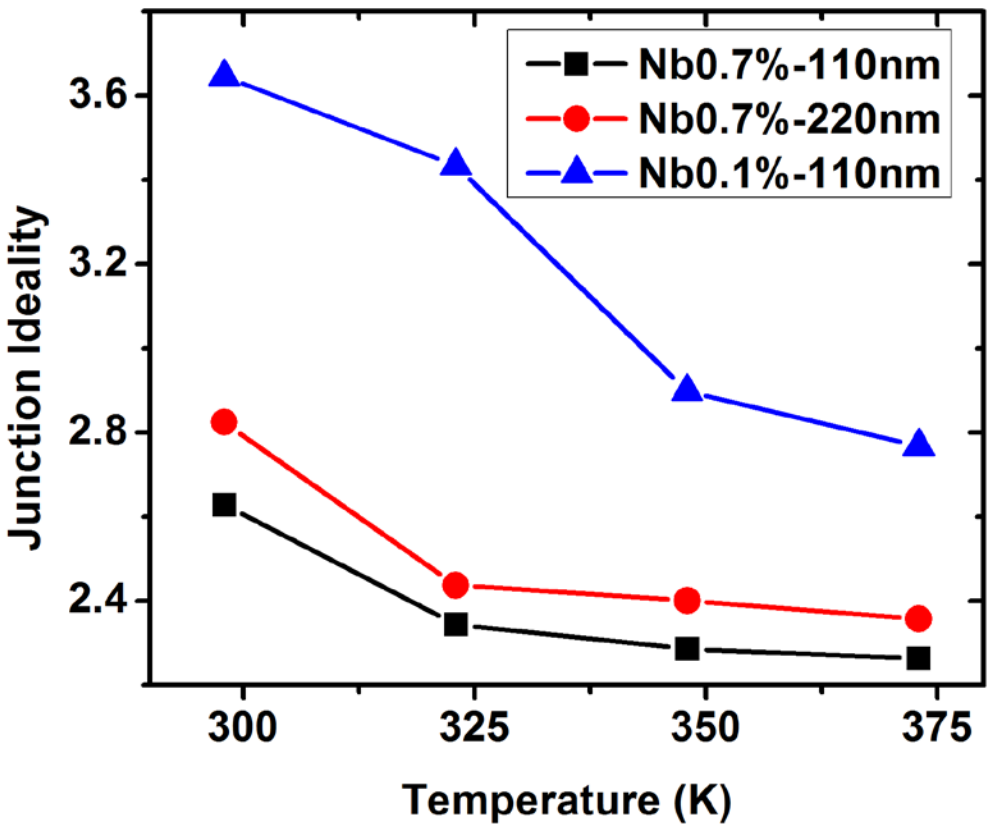

Figure 64: Ideality of the junction as derived from Figure 63 for (black squares) Nb0.7% - 110nm, (red circles) Nb0.7% - 220nm and (blue triangles) Nb0.1% - 110nm.

As the thickness of the film increases, so does the ability to rectify as seen in Figure 65A. Inset shows the linear rectification scale. There is a slight, yet noticeable shift of the *J-V* curve in the positive direction. Figure 65B shows the room temperature *J-V* characteristic for 110nm film

for both 0.1% and 0.7% Nb-doped STO. The slight non-zero offset for the minimal current in the Nb0.1%-110 nm sample is a result of the resistance of the substrate associated with contacting the bottom electrode. Due to the lower amount of carriers, the substrate is more resistive and therefore an offset is present. The threshold voltage at which current increases significantly in the 0.1% Nb-doped STO is seen to increase as expected for the lower concentration of Nb with respect to 0.7% Nb-doped STO even while taking into account the resistance of the substrate. The inset in Figure 65B shows the clear rectifying behavior of the 110nm thick films.

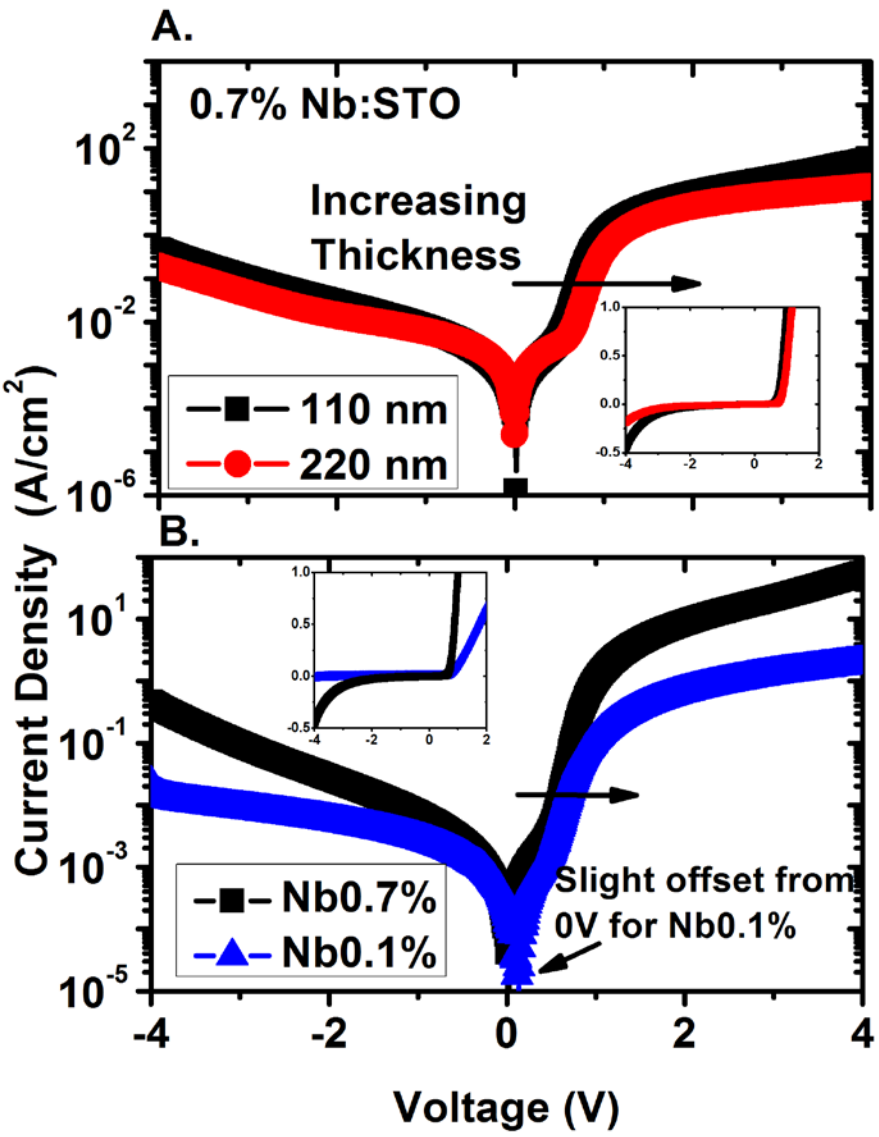

Figure 65: (A) Log-linear current density comparison of 110nm (black squares) and 220nm (red circles) samples grown on 0.7% Nb:STO. (B) Log-linear current density comparison of 110nm thick LSNO grown on 0.1% Nb:STO (blue triangles) and 0.7% Nb:STO (black squares). Inset shows linear comparison.

The capacitance-voltage (*C*-*V*) relation of the junction gives information pertinent to the interfacial energy barrier. The value of the built-in potential can be derived from the C^{-2}-*V* relationship. The depletion capacitance is defined as $C = \frac{dQ}{dV}$, where *dQ* is the incremental change in the depletion layer charge for an incremental change in the applied voltage *dV*. In the regime of the rigid band junction, the capacitance is related to the applied voltage by

$$\frac{1}{C^2} = \frac{2}{q}\left(\frac{1}{\varepsilon_n n_n} + \frac{1}{\varepsilon_p n_p}\right)(V_{bi} - V)$$

Equation 5

Where *C* is the capacitance density, *q* is the elementary charge, *V* is the applied voltage, V_{bi} is the built-in voltage, n_n and ε_n are the carrier density and the dielectric constant in Nb:STO layer, respectively and n_p and ε_p are the carrier density and the dielectric constant in LSNO layer, respectively. We estimated the built-in potential (V_{bi}) from the intercept on the voltage axis which corresponds to the difference in the Fermi level of contacting materials in the rigid band model.[194] Samples were measured at 1kHz and 10kHz at a *C*-*V* sweep from -4V to 2V as well as a function of temperature. The results are plotted in Figure 66. From the *C*-*V* relationship, the capacitance values of the Nb0.7%-110nm (Figure 66a,b) and Nb0.7%-220nm (Figure 66C,D) samples at the local maximum (~ 0.5V) were approximately the same at 15μF/cm^2 and 11μF/cm^2 for the 1 kHz and 10 kHz measurements, respectively, indicating the capacitance measured must arise from the interface (otherwise it would scale with thickness). Comparing Nb0.1%-110nm (Figure 66E,F) and Nb0.7%-110nm (Figure 66A,B) at 0.5V, the junction capacitance of the Nb0.1%-110nm samples is significantly smaller due to the low carrier concentration of the substrate and electrostatics of the carrier interaction. This is based on the depletion layer estimate of[194]

$$t_n = \left[\frac{2n_p \varepsilon_p \varepsilon_n (V_{bi} - V)}{q n_n (\varepsilon_n n_n + \varepsilon_p n_p} \right]^{1/2}$$

Equation 6

$$t_p = \left[\frac{2n_n \varepsilon_n \varepsilon_p (V_{bi} - V)}{q n_p (\varepsilon_n n_n + \varepsilon_p n_p} \right]^{1/2}$$

Equation 7

$$C = \left[\frac{q n_n n_p \varepsilon_n \varepsilon_p}{2(V_{bi} - V)(\varepsilon_n n_n + \varepsilon_p n_p)} \right]^{1/2}$$

Equation 8

where t_n and t_p are the depletion layer thickness of Nb doped $SrTiO_3$ and LSNO, respectively. The other variables have been previously defined in Equation 5 . For the calculation, ε_n is taken to be 50.[201] Carrier density in the Nb:STO layer was calculated to be ~ $2.3*10^{19}cm^{-3}$ for 0.1% Nb-doped STO and $3.5*10^{20}$ cm^{-3} for 0.7% Nb-doped STO.[202] LSNO carrier concentration in a similar composition in bulk was measured to be approximately $1*10^{19}$ cm^{-3}.[193] ε_p was taken to be 1000. Such large dielectric constant has been noted in polycrystalline thin films as well as single crystal bulk samples.[186,203] From the nominal values obtained from literature for carrier concentration as well as estimates of permittivity values, we estimate the total depletion thickness from Equation 6 and Equation 7 ($t_t=t_p+t_n$) to be on the order of 86nm for Nb0.7% and 48nm for Nb0.1%. t_p in the Nb0.7% samples has a thickness of 84nm and t_p in the Nb0.1% sample has a thickness of approximately 34nm. The larger depletion region should be found in the p-layer due to the low carrier concentration and the high permittivity.

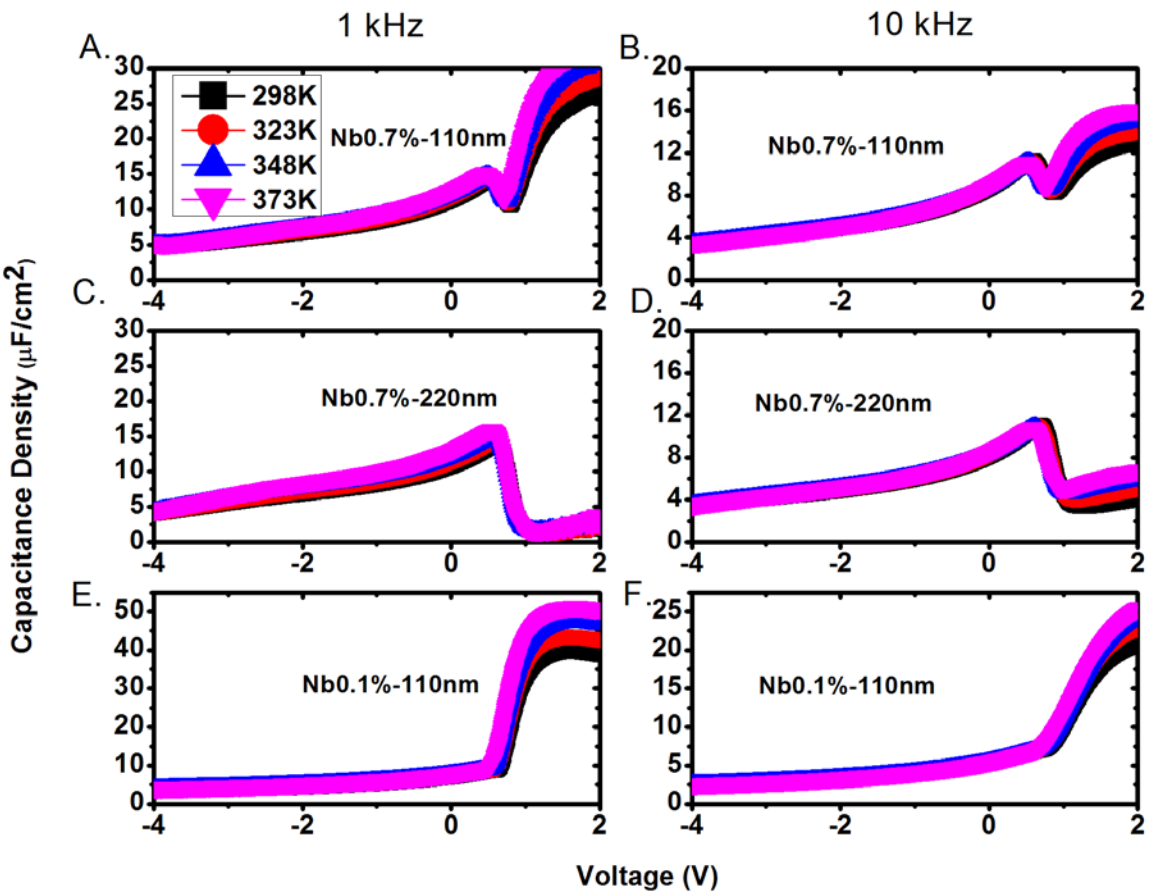

Figure 66: Capacitance-voltage curves for Nb0.7%-110 nm at (A) 1 kHz and (B) 10 kHz, for Nb0.7%-220 nm at (C) 1 kHz and (D) 10 kHz, and for Nb0.1%-110 nm at (E) 1 kHz and (F) 10 kHz.

Figure 67 shows the linear fits to Equation 8 in the low reverse bias region (between -2 and 0V). The built-in potential, derived from Figure 65, was estimated to range from 1eV to 1.55eV at 1kHz and 0.8eV to 1.2eV at 10 kHz and plotted in Figure 68 (A -1 kHz, B - 10 kHz) respectively as a function of temperature. The results of the study indicate a change in built-in potential with frequency which is non-trivial. From standard semiconductor *pn* junction physics, one might expect the built-in potential to be constant over this range. The built-in voltage

increases as a function of temperature due to the promotion of carriers in the semiconducting Nb:STO and LSNO. As the temperature increases, the amount of mobile carriers increases leading to a much thinner depletion layer and a higher capacitance. As the n-type material promotes more carriers into the conduction band and the p-type material promotes more carriers into the valence band, the separation of the Fermi levels will increase causing a slight increase in the built-in potential. The slight deviation from a straight line at large reverse bias for high doping is likely due to the leakage current and electric-field dependence of the dielectric constant for Nb:STO.[201,204]

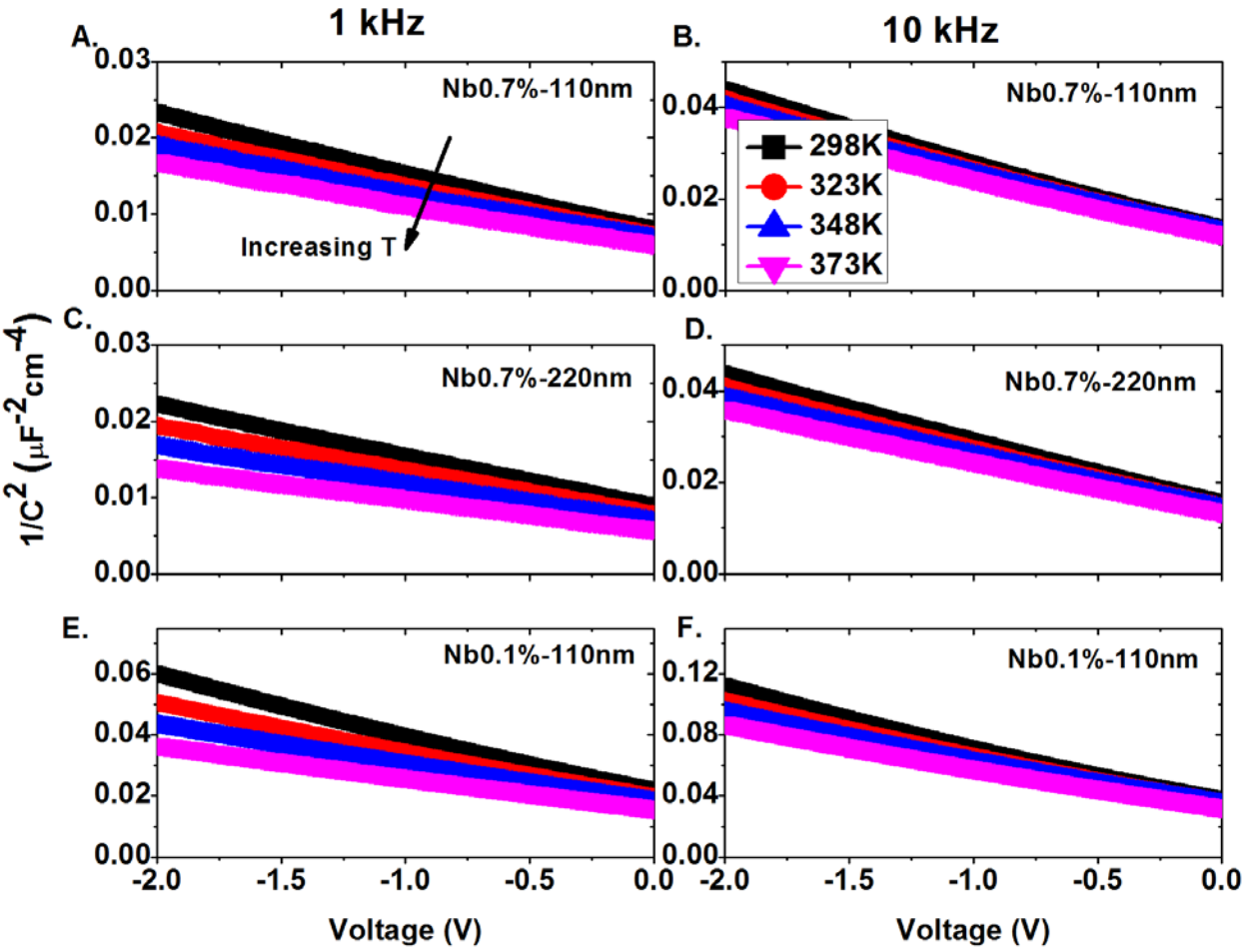

Figure 67: C^{-2}-V curves for Nb0.7%-110nm at (A) 1 kHz and (B) 10 kHz, for Nb0.7%-220nm at (C) 1 kHz and (D) 10 kHz, and for Nb0.1%-110nm at (E) 1 kHz and (F) 10 kHz as derived from Figure 66.

From Figure 68, comparing the Nb0.1%-110nm and Nb0.7%-110nm samples at 1kHz (Figure 68A) and 10 kHz (Figure 68B), we find that a larger built-in voltage is obtained in the 0.1% Nb-doped samples which is contrary to what should be obtained from standard semiconductor theory (i.e. positioning of the Fermi level). From the steep increase in built-in potential as a function of temperature and a much higher than expected built-in voltage, we may

assume that the thickness of the depletion layer, due to the low carrier concentration of the substrate, is on the order of the film thickness and thereby leading to a fully depleted film. The contribution of defects in the junction of the 0.1% Nb-doped STO substrate could also be significant. In Figure 68, the Nb0.7%-220 nm thick sample should have the same built-in potential as Nb0.7%-110nm however it is seen to be larger. The thicker film will have more defects which will cause a higher calculated built-in voltage due to the defects' response to the applied frequency. This leads to a non-trivial analysis of the junction. By comparing the values obtained at 1kHz (Figure 68A) and 10 kHz (Figure 68B), a change in built-in voltage is seen as a function of frequency and discussed further below. This may be the result of interface/trap states as described by Bruno *et al.*[200] in a similar structure.

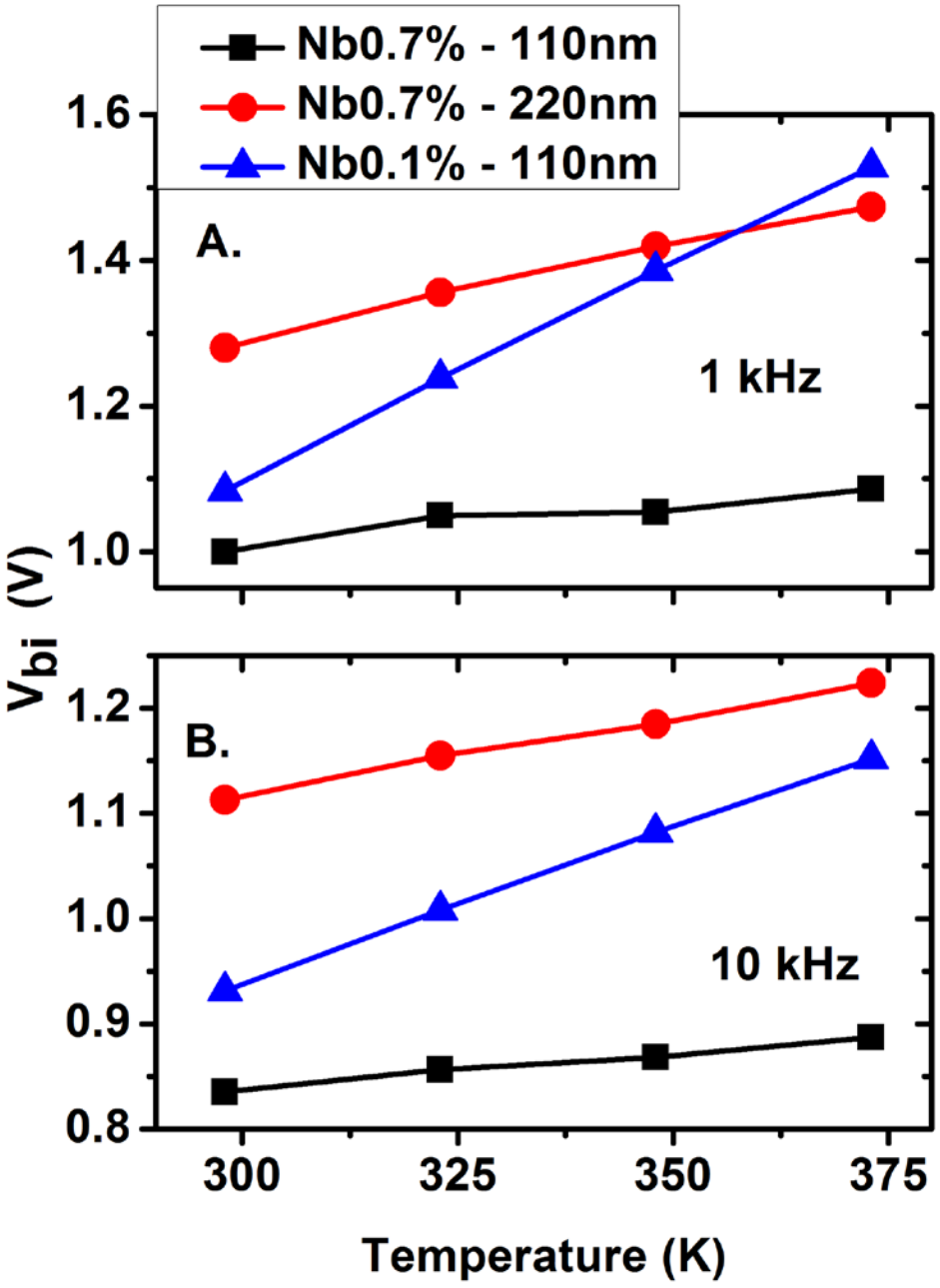

Figure 68: Built-in voltage measured at (A) 1 kHz and (B) 10 kHz plotted as a function of temperature for Nb0.7%-110 nm (black squares), Nb0.7%-220 nm (red circles) and Nb0.1%-110 nm (blue triangles).

Figure 69 shows the dielectric loss tangent. As alluded to previously, the built-in potential is of the order of ~1V which indicates that above this bias, we are in a highly conducting state and

the measured capacitance is not accurate. This is seen in Figure 69 when we observe the dielectric loss tangent response under positive bias. In the negative bias, we also see a breakdown of the junction as observed by the high loss near ~-4V.

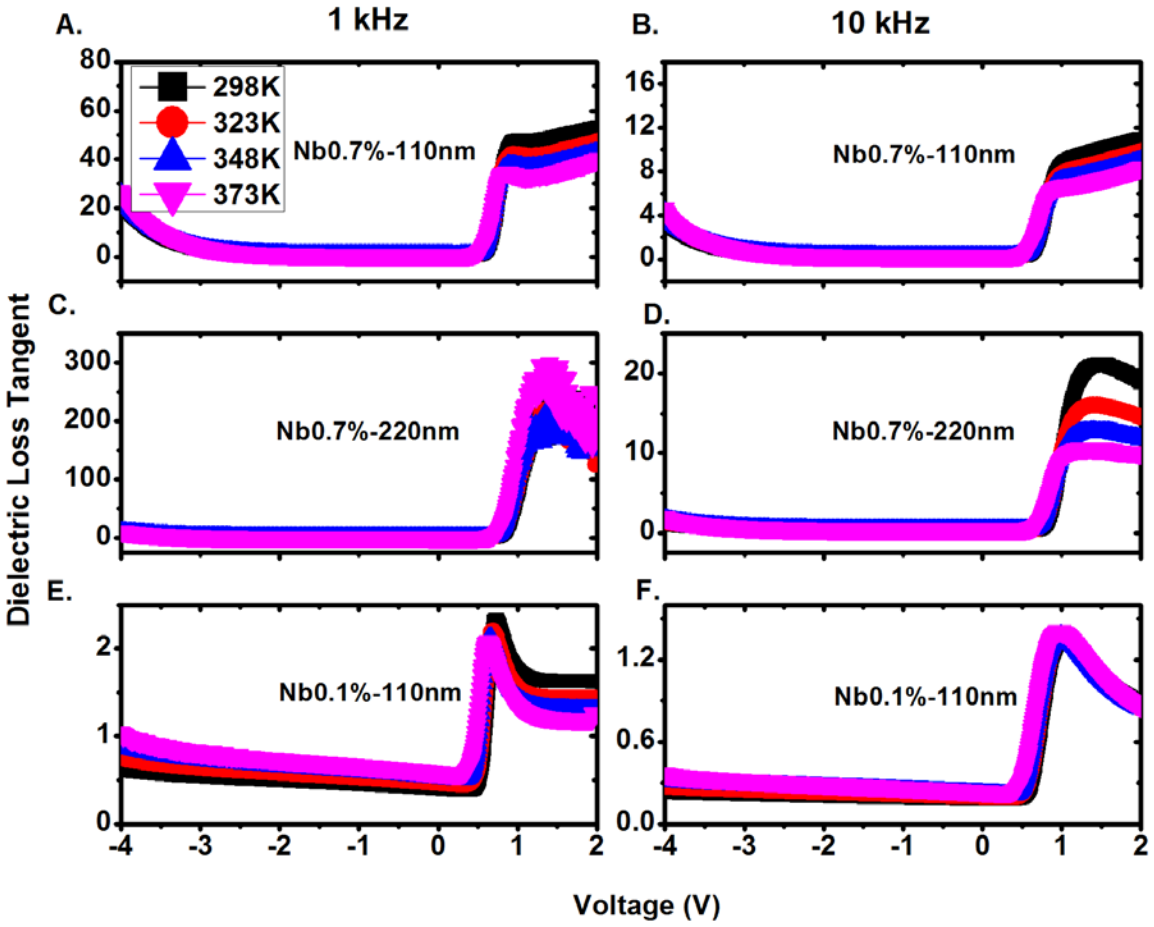

Figure 69: Dielectric loss tangent for Nb0.7%-110nm at (A) 1 kHz and (B) 10 kHz, for Nb0.7%-220 nm at (C) 1 kHz and (D) 10 kHz, and for Nb0.1%-110nm at (E) 1 kHz and (F) 10 kHz as a function of temperature.

From the above experimental results, it is clear that it is not possible to obtain the built-in potential with C^{-2}-V characteristic using a single frequency measurement over the entire temperature range. Instead, varying frequencies should be used to ascertain the relative

influence of the different contributions to the capacitance on the V_{bi} determination. We further probe this dependence by measuring *C-f-V* in the range 100 Hz to 1Mhz as seen in Figure 70. Strong frequency dispersion is seen at all applied voltages and temperatures. Low frequency dispersion of the capacitance below 1000Hz for this temperature range and applied bias has been seen elsewhere and associated with hole (like) deep levels at the LSNO side.[200] Comparing Nb0.7%-110 nm (Figure 70A) and Nb0.7%-220 nm (Figure 70B), there is a clear stepped decrease in capacitance at approximately 100 kHz in the 220nm thick sample.

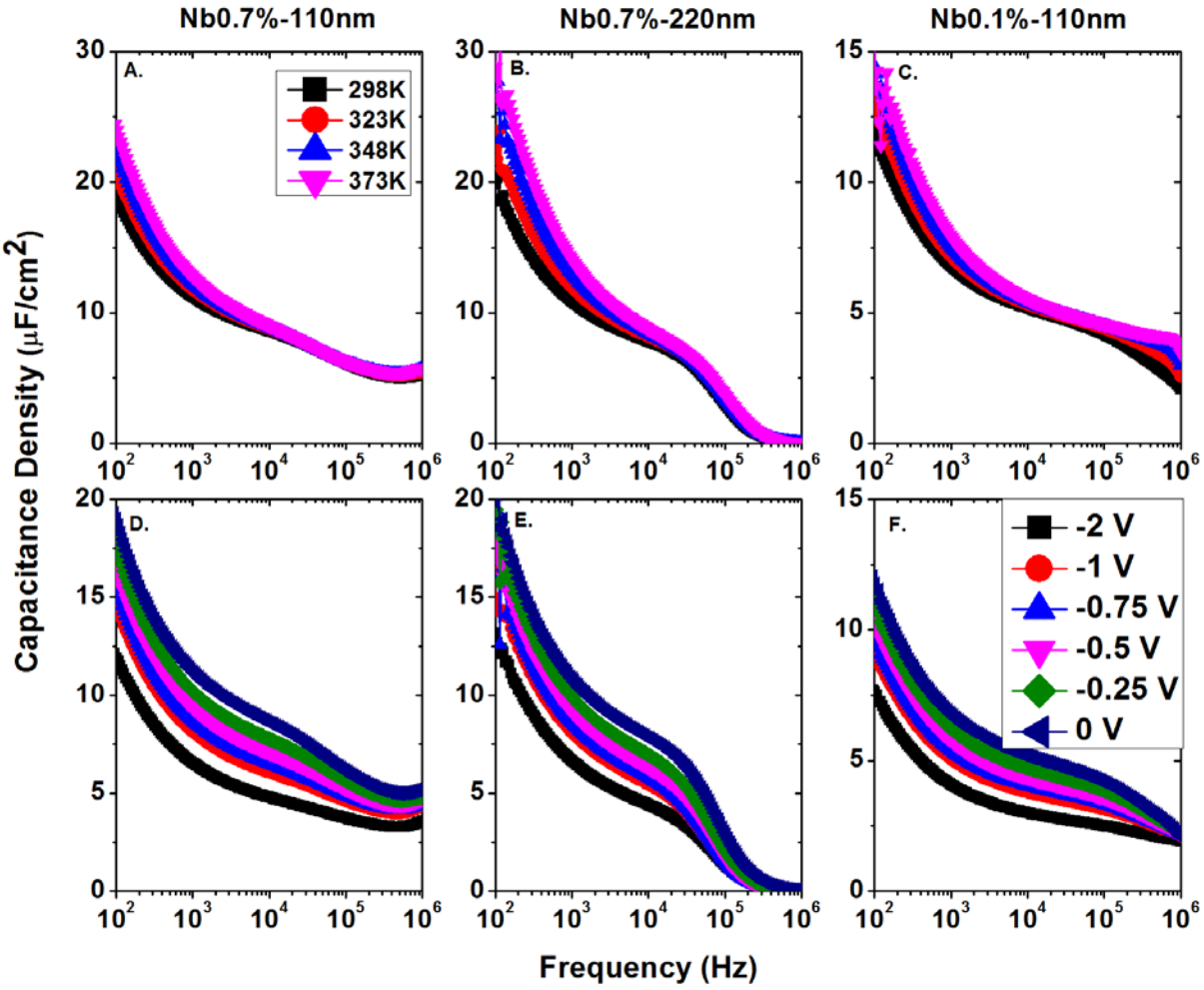

Figure 70: (Top row) Capacitance density as a function of frequency plotted at different temperatures for (A) Nb0.7%-110nm, (B) Nb0.7%-220 nm, and (C) Nb0.1%-110 nm. (Bottom row) Capacitance density as a function of applied negative bias for (D) Nb0.7%-110 nm, (E) Nb0.7%-220 nm, and (F) Nb0.1%-110 nm.

From the *J-V* curve data, the limited range of exponential behavior in these junctions around room temperature makes it difficult to deduce the primary contributions to ideality for $n>1$ although similar junctions formed with manganite electrodes appear to be well described by thermionic field emission.[199] It has been reported that interface states might be related to the

electronic reconstruction resulting from charge leakage or the disruption in the polarity at the interface.[200]

The rectification can be understood in terms of the band alignment between p-type LSNO and n-type Nb:STO. With the addition of strontium into the La_2NiO_4 lattice, impurity bands develop in the narrow bandgap (~2eV).[205] This is associated with polaronic hopping conduction. The Nb:STO is a degenerate wide bandgap semiconductor so the impurity band will lead to trap states within the gap and could lead to electronic defects.

Interface traps are detected through losses resulting from changes in their occupancy during ac measurements. Capture/emission of traps cause energy loss leading to a conductance which is noticeable when conductance (G) divided by the radial frequency (ω) is plotted as a function of frequency.[206,207] Figure 71 shows G/ω versus frequency for the samples measured in figure 10a,b,c at zero bias. Figure 71a, which corresponds to Nb0.7%-110nm, showed a broad and weak resonance. In Figure 71b, which corresponds to Nb0.7%-220nm, a peak is clearly seen at ~83kHz at 298K due to a trap/defect level in the film in resonance with the applied field. The 220nm sample shows a strong resonance peak which would be expected in the thicker film since rocking curve data indicate more defects in the film as opposed to the Nb0.7%-110 nm sample. Figure 71c, corresponding to the Nb0.1%-110 nm thin film, does not show a peak in the measured frequency range however it does exhibit an increase at higher frequency. The inset in Figure 71b plots the resonance peak of the Nb0.7%-220 nm sample and the evolution of the peak positions as a function of temperature. The resonance peak frequency increases with temperature.

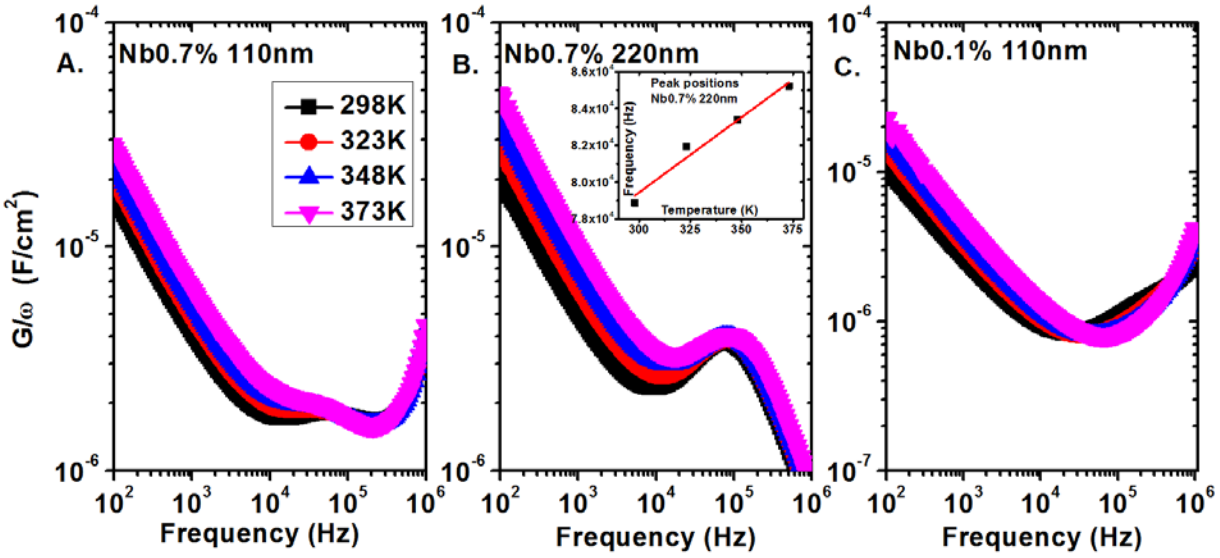

Figure 71: (G/ω) vs. frequency of (A) Nb0.7%-110 nm, (B) Nb0.7%-220 nm and (C) Nb0.1%-110 nm films measured at 0V bias as a function of temperature. Inset in Figure 71b shows the resonance frequency peak positions for the Nb0.7%-220 nm sample.

The capacitance-frequency relationship as a function of applied bias from -2V to 0V shown in Figure 70d,e,f is used to derive the built-in voltage and is plotted in Figure 72. C^{-2}-V relationship was linear at all temperature and frequency range indicating the existence of interfacial (junction) capacitance dominating all devices. However, extracting V_{bi} from the C^{-2}-V relationship indicates shows that V_{bi} decreases and then subsequently increases to a large value, indicating a loss of the validity of the flat band offset model. It was previously determined from J-V measurements that the ideality factor, n, was much larger then unity indicating defects at the interface. The frequency dependent built-in voltage in conventional semiconductor interfaces has been ascribed to defects in the *pn* junction.[208]

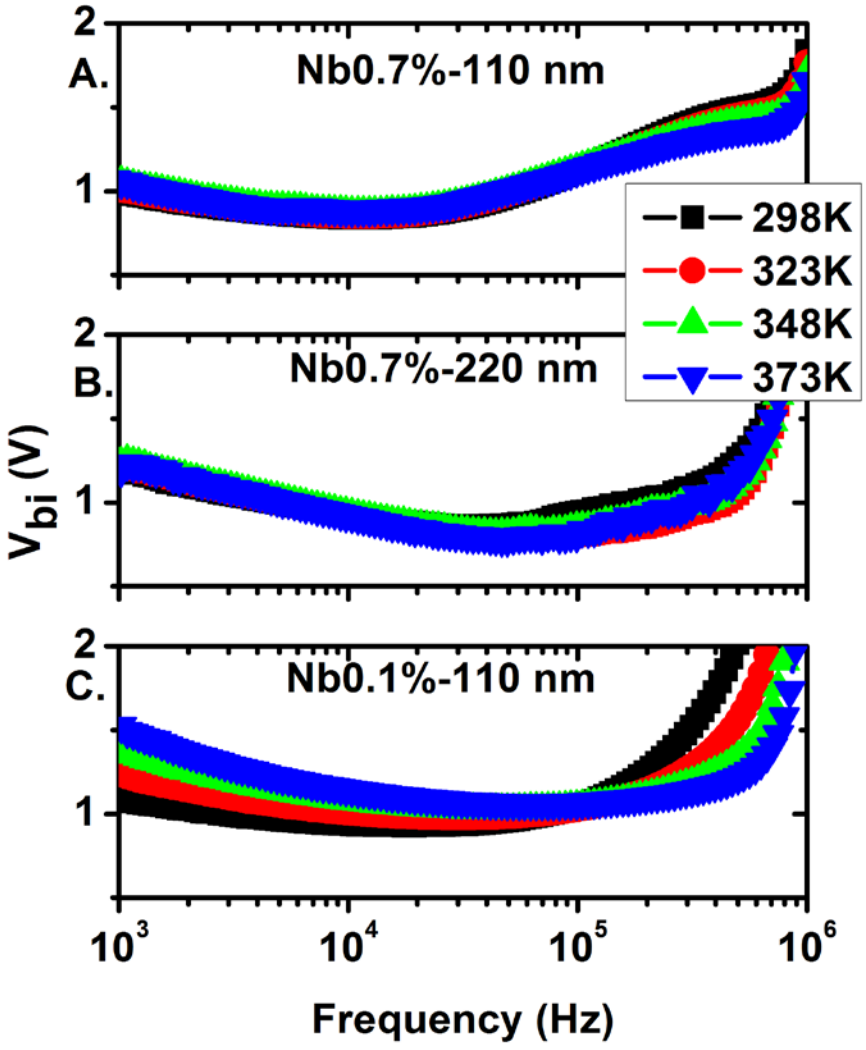

Figure 72: Built-in voltage as a function of frequency for (A) Nb0.7%-110 nm, (B) Nb0.7%-220 nm, and (C) Nb0.1%-110 nm as derived from Figure 70.

Defect chemistry of complex oxide *pn* junctions has recently been described by Saraf *et al.*[209] Defects in the depletion layer (oxygen vacancies, interstitial, dislocations, etc.) can contribute to the measured built-in voltage. At low temperatures (such as in the vicinity of room temperature), species with high ionization energies do not respond at high applied frequency.[194] In conventional *pn* junctions, frequency dependent built-in voltage may arise due to deep level

trap centers. This characteristic originates from the slow thermal emission rate of deep dopants which are unable to follow the high frequency voltage modulation and contribute to the space-charge in the space charge layer. At high temperatures, this characteristic is increased to higher frequency, because the thermal emission rate of the deep dopants increase.[210,211] Defects therefore leads to shifts expected from standard conventional band theory that assume a perfect interface. The difference between this value and our frequency dependent results clearly demonstrate the important role of the ionic defect in shaping the characteristics of complex oxide *pn* junctions. It has also been theorized that Nb stripes on the Nb doped $SrTiO_3$ may facilitate the formation of defects at the junction.[212] The built-in voltage in thin film heterojunctions has also been seen to vary with thickness due to lattice strain.[213] In-plane strain may affect the mobility of carriers in the film and also lead to the distortion of the NiO_6 octahedral lattice.[213,214] Due to the low amount of strontium doping (x=0.125) in the lattice, LSNO should have a carrier concentration on the order of less than 10^{19} cm^{-3} which implies a large depletion layer. The Nb:STO is heavily doped and will act as an n^+ semiconductor. For the case of $La_{0.67}Ca_{0.33}MnO_3$/Nb:STO, Wang *et al.* reported that the depletion width varied with film thickness and could be on the order of 30nm.[213] In that study, the strain in those films affected the carrier density through modulating the Jahn-Teller effect. In our estimate, the depletion layer could be a significant part of the film as noted from Equation 6 and Equation 7. Ni^{2+} in the parent phase La_2NiO_4 is not a Jahn-Teller ion however; strontium doping introduces Ni^{3+} ions into the NiO_2 plane of LSNO leading to a weak Jahn-Teller distortion.[213] The depletion layer in correlated oxide thin films, due to variation in carrier concentration, defects and localization induced by coulombic repulsion, could be wider than that which conventional semiconducting junction theory predicts and therefore cause interaction on the order of the thickness studied.[215]

5.2.5 Conclusion

We have fabricated heteroepitaxial LSNO/Nb:STO junctions and their properties have been investigated as a function of temperature for different thickness LSNO films and substrate doping. Rectifying behavior was observed as seen from the current-voltage measurements showing a rectification ratio on the order of 300 dependent on substrate and thickness. Through *C-f-V* measurements, we are able to determine the effect the substrate plays on the interface characteristics. The varying built-in voltage estimated from capacitance measurements varies approximately from 0.5V to 2V depending on frequency, indicating the role of defects on the response of the *pn* junction.

5.3 Role of Strain in Thin Film LSNO

5.3.1 Abstract

Epitaxial thin films of $La_{1.875}Sr_{0.125}NiO_4$ (lanthanum strontium nickelate, LSNO) have been synthesized by sputtering onto single crystal oxide substrates (chosen to induce varying epitaxial strain) and their structural and dielectric properties are reported. High dielectric constants on the order of 10^7 have been measured up to 1MHz in interdigitated capacitors with a frequency dependence that correlates with substrate imposed strain and texture. The observation of a high dielectric constant albeit with moderate loss tangent at high frequencies motivates further explorations of charge ordering phenomena in such complex oxides and serves to examine size effects on dielectric response by comparison to studies on bulk single crystal LSNO.

5.3.2 Introduction

In recent years, thin film charge-ordered epitaxial and textured perovskites and perovskite-related oxide structures have received much attention due to their intriguing electronic and magnetic functionalities. Krohns *et al.*[216] have identified bulk single crystal $La_{1.875}Sr_{0.125}NiO_4$ (LSNO) as a colossal dielectric constant (CDC) material having a high frequency dielectric constant up to approximately 10^5. Colossal dielectric constant has been observed in charge-ordered systems such as $M_{2-x}Sr_xNiO_4$ where M = Sm, La, and Nd however their frequency dependence is rather severe. [217,218,219] While the dielectric constant can be of the order of 10^5 at low frequencies, the intrinsic dielectric constant is often much lower at around 10-100.[220] An interesting observation in the recent study by Krohns *et al.* was that LSNO retained its CDC well into the GHz range as opposed to other CDC materials (such as the more widely studied $CaCu_3Ti_4O_{12}$ (CCTO)) showing dispersion into the kHz and beyond. [221,222] This seems to suggest a distinct mechanism for the origin of the large dielectric response in this system. Of course, the dielectric loss in such systems is typically higher (around 0.5) compared to traditional dielectrics that may have loss of the order of 0.01 for comparable thickness range. Hence, it is not immediately obvious if they will be suitable for capacitor applications. Nevertheless, the retention of such large dielectric constant into the high frequency domain piques interest in applications and further suggests additional mechanisms involved in polarization compared to the CCTO system that requires a better understanding. In epitaxial form, LSNO grown on highly degenerate n-type $SrTiO_3$, displayed rectifying properties.[223] Motivated by the intriguing report by Krohns *et al.* mentioned above, we have carried out a detailed study on the dielectric properties of epitaxial LSNO films grown on various insulating substrates measured with interdigitated capacitor structures. We compare the properties of such films with those of

textured films and bulk single crystal literature data. To the best of our knowledge, these represent the first studies on dielectric response in this unique charge ordered system in epitaxial thin film form.

5.3.3 Experimental

Epitaxial and textured LSNO films of nominal composition $La_{1.875}Sr_{0.125}NiO_4$ were deposited by rf magnetron sputtering from stoichiometric targets of 99.9% purity. (ACI alloys). Deposition conditions were optimized at 4mTorr pressure, 1123K substrate temperature and 2% O_2 in Argon, without any post-deposition anneal. Single crystal substrates of (001) orientation were chosen due to the similar 'a' lattice parameters of bulk LSNO (extrapolated to be 3.853Å from JCPDS data[224]). Chosen substrates were cubic $SrTiO_3$ (STO), cubic $LaAlO_3$ (LAO) and tetragonal $SrLaAlO_4$ (SLA) (a, lattice parameter of 3.905Å, 3.790Å and 3.756 Å, respectively). Single crystal c-plane sapphire (ALO) (a=4.758, c=12.99) was also explored as a substrate to grow textured films for comparison. Thickness of the deposited films was estimated to be approximately 80nm from x-ray reflectivity. Epitaxial relationship, phase and reciprocal space mapping (RSM) was determined from high resolution x-ray diffraction (HRXRD) using a (022) Ge monochromated Cu K-α beam and Eulerian cradle (Bruker D8) while pole figure analysis was performed using 2D area detector (Bruker D8 with Vantec 2000 detector). Electrical contacts were deposited by photolithographic patterning of interdigitated capacitors (IDC) and consisted of 10nm adhesion layer of Ti and 100nm layer of Au. Capacitance measurements were carried out as a function of frequency up to 1MHz (Agilent E4980A LCR Meter). Surface roughness was measured to be <3nm RMS from atomic force microscopy.

5.3.4 Results

Figure 73A, B, C shows the θ-2θ diffraction pattern of the LSNO film grown on STO, LAO and SLA substrates, respectively. Films showed the (00*l*) family of peaks, namely (004), (006) and (008) from the tetragonal LSNO having a K_2NiF_4 structure (I4/mmm space group) as well as substrate peaks as expected from epitaxial cube-on-cube growth of LSNO on the lattice matched substrates. No other peaks are seen in the diffraction pattern suggesting phase purity. Epitaxy is verified in the lattice matched substrates by ϕ scans shown in Figure 73 D,E,F for LSNO grown on the STO, LAO, and SLA substrates, respectively. ϕ scans were performed from symmetric peaks at the appropriate χ value. The peaks from film planes of (103), (204), and (114) were obtained at the appropriate χ values on all substrates further indicating the *I4/mmm* space group as well as showing 4-fold tetragonal symmetry. Shown in Figure 73D4 and Figure 73D5, Figure 73E4 and Figure 73E5 and Figure 73F4 and Figure 73F5 are scans taken from the substrate as a reference for growth direction. In the LAO and STO cubic substrate, the ϕ scan were taken from the (111) and (101) film planes whereas in the SLA substrate, ϕ scans were taken from the (105) and (112) film planes as reference. From the location of the peak positions of the substrate, film orientation with respect to the substrate is deduced to be (010)//(010) and <001>//<001>. This indicates cube-on-cube growth with the c-axis of the LSNO film being normal to the surface of the film.

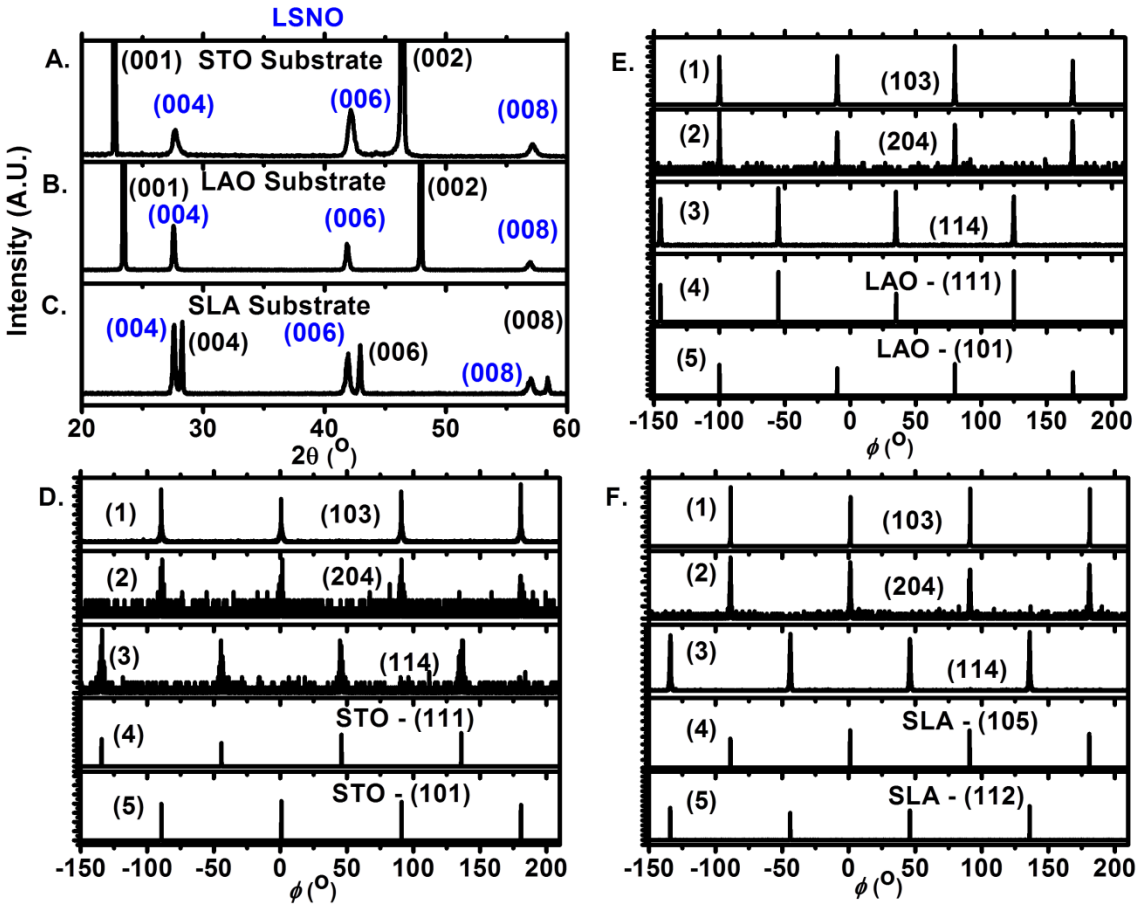

Figure 73: θ-2θ scans for LSNO films on (A) STO, (B) LAO and (C) SLA substrates. Phi scans from symmetric peaks for LSNO grown on (D) STO, (E) LAO and (F) SLA. Substrate ϕ scans are plotted as a reference.

Reciprocal space mapping (RSM) was performed around the (1 1 10) LSNO peak for film grown on STO and LAO and around the (1 0 11) LSNO peak for the film grown on SLA as shown in Figure 74A,B,C respectively. The high order asymmetric peaks were chosen due to their proximity to the substrate peaks ((113) LSNO plane for cubic STO and LAO and (1 0 10) plane for tetragonal SLA). Reciprocal space maps are plotted by scattered intensity in $(\mathbf{q_x},\mathbf{q_z})$ space where $\mathbf{q_x}$ and $\mathbf{q_z}$ are the components of the scattering vector q given by $\mathbf{q}=4\pi \sin\theta/\lambda$. LSNO on STO (Figure 74A) shows large shift from the substrate q_x position indicating the film is

relaxed with the broad and diffuse peak indicating a large density of defects. Extended defects such as dislocations are introduced to relieve stress. A distribution of microscopic rotations (known as a mosaic pattern) produces a broadening of the diffraction peak transverse to the radial direction and along the rotations.[225,226] LSNO on LAO (Figure 74B) shows coherent growth i.e. both film and the substrate peaks have the same in-plane q_x value indicating fully strained condition as well as compressive strain. Similar conditions are seen for LSNO on SLA (Figure 74C) however, a slight shift from the substrate q_x position indicates relaxation is occurring (partially strained). In all cases, there is a broadening of the LSNO peak along the q_x direction indicating the existence of defects and/or low angle grain boundaries.

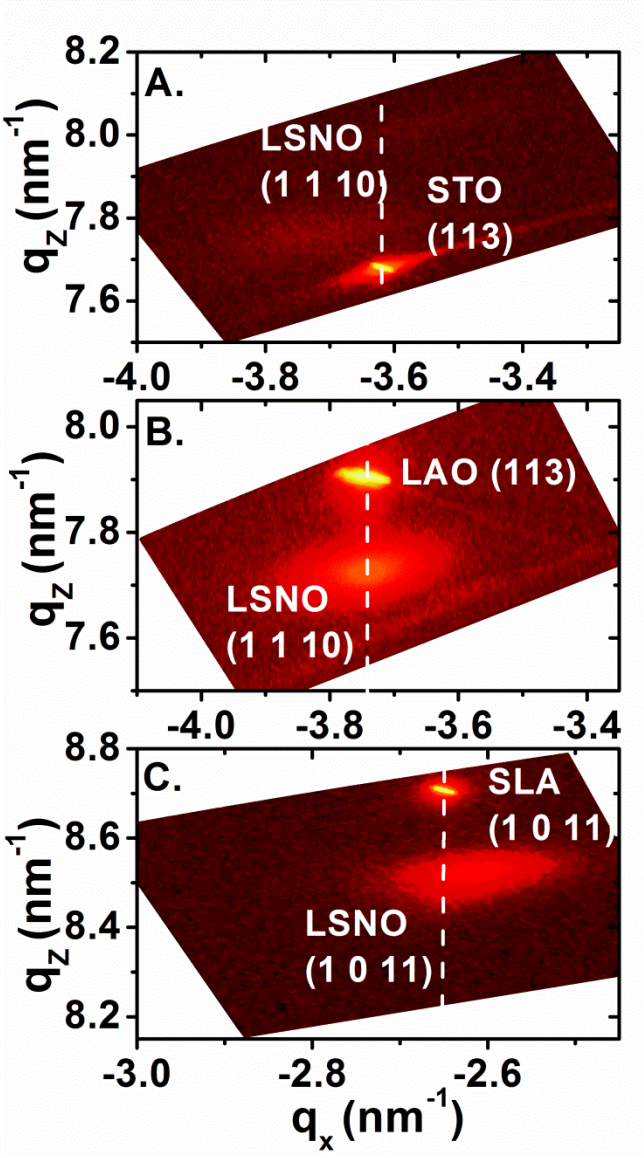

Figure 74: Reciprocal space maps of LSNO films grown on (A) STO, (B) LAO and (C) SLA substrate. LSNO on STO is shown to be grown under tensile strain whereas LSNO on LAO and SLA are under compressive strain. Dashed vertical line is used to visualize coherent growth i.e. same in-plane q_x value.

Lattice parameters of the epitaxial LSNO thin film was calculated from the out-of-plane θ-2θ scan shown as well as reciprocal space mapping around the in-plane direction as indicated in Table 1 . All data were obtained with a high resolution x-ray diffractometer using (022) Ge

monochromated Cu Kα1 radiation and point detector. From a comparison to the extrapolated JCDPS data, lattice parameters appeared to vary significantly even when compared to the fully relaxed film (LSNO on STO). It has previously been reported in bulk LSNO data that as a function of decreasing oxygen content in the film, the *a*-lattice parameter reduces systematically whereas the *c*-parameter increases.[227] Our films show the same relation whereas the 'a' lattice parameter is decreased in reference to the bulk and the *c*- lattice parameter is increased indicating role of oxygen vacancies in the film.

Table 1: Calculated lattice parameters for LSNO grown on STO, LAO and SLA.

Substrate	Calculated Film Lattice Parameter, 'a' (Å)	Calculated Film Lattice Parameter, 'c' (Å)	Substrate Film Lattice Parameter, 'a' (Å)
STO	3.808	12.866	3.905
LAO	3.795	12.931	3.790
SLA	3.779	12.920	3.756
JCDPS Data (extrapolated)	3.853	12.691	

LSNO grown on sapphire showed only the (200) film peak and the (006) sapphire peak in the θ-2θ diffraction pattern as seen in Figure 75A. Other peaks marked with the asterisks are due to the substrate holder. In order to understand the growth of LSNO on sapphire, pole figures were obtained using a 2D detector. Pole figures were measured by scanning the tilt angle of the goniometer, χ, in the range 0-60° and the azimuthal angle, ϕ, in the range 0-360°. Pole figure for the (200) LSNO peak is shown in Figure 75B. The position of the peak in the center of the

stereographic projection indicates the film to be strongly textured with the (200) reflection normal to the surface; however it should be noted that the due to the spread in intensity in the χ direction (i.e. radial) we can infer that this is weakly textured. Analyzing the pole figure at 44.0° (Figure 75C) shows strong 6-fold diffraction of the (113) sapphire peaks as well as a diffused ring around a χ value of approximately 57.5°. The diffuse ring is attributed to the (114) LSNO reflection. The location of the ring at approximately 57.5°, as calculated from the interplanar angle between the (114) and the (100) plane, further indicates the (100) orientation of the film. The large spread is again associated with the weak texture and polycrystallinity. From these patterns, we can infer LSNO grown on ALO has a fiber texture with the *a*-axis of the film normal to the surface.

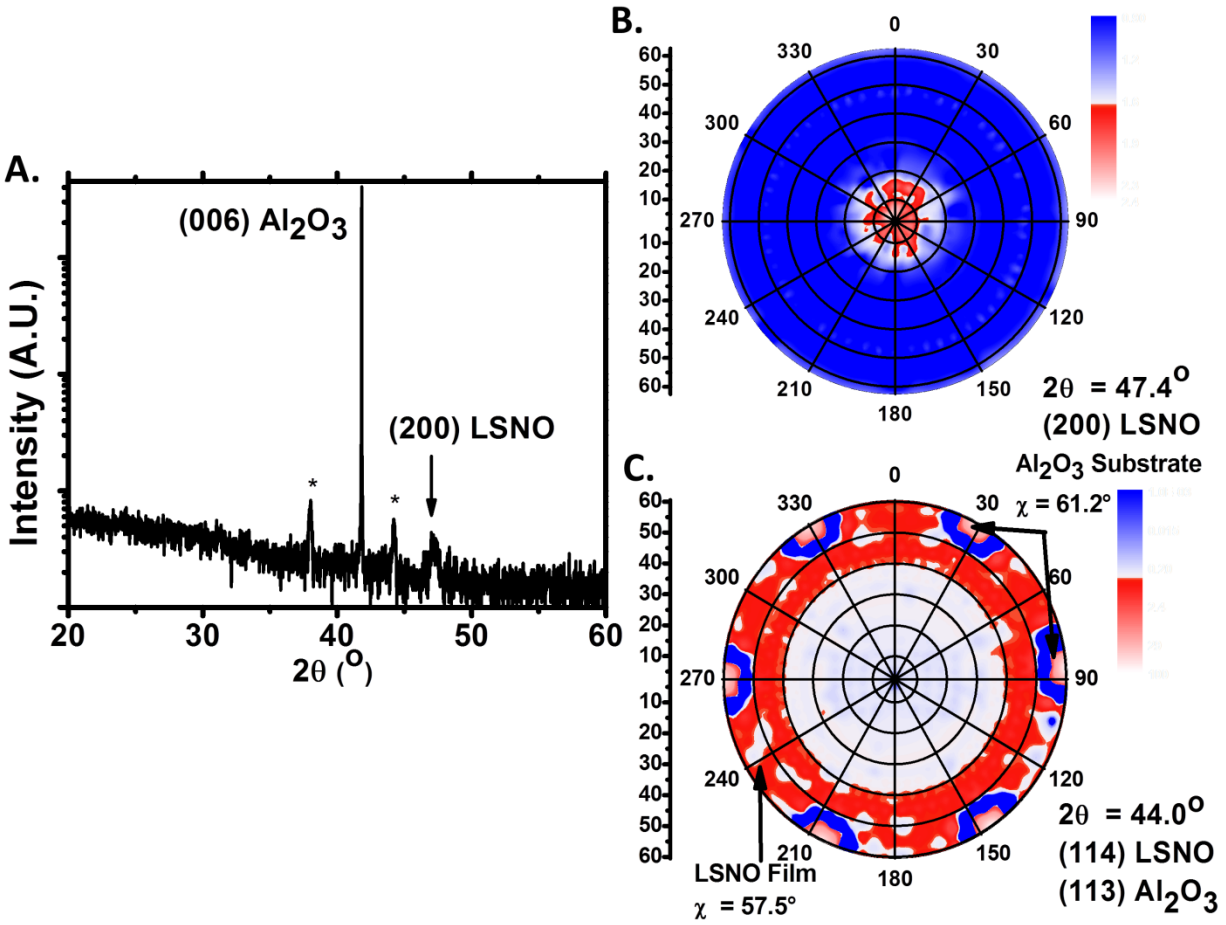

Figure 75: (A) Diffraction pattern of LSNO film grown on ALO. * indicated reflections from substrate holder. (B) Pole figure of the (200) LSNO reflection. (C) Pole figure take at 44° showing reflections from both the (113) sapphire (six-fold symmetry) and the (114) LSNO. χ is the radial direction and ϕ is the angular coordinate.

To characterize dielectric properties of the various LSNO films, interdigitated capacitors were prepared with a broad current collector on either side through photolithographic patterning. Close up view of an IDC test device is shown in the inset in Figure 76A. Dielectric constant of the film was calculated using the known semi-empirical relations as described in Chapter 3.4.2

The effective length of the individual fingers in the interdigitated capacitor was 2000μm and ended 50 μm from the opposite current collector. Several different electrode configurations

were deposited onto the epitaxial films consisting of gaps between fingers ranging from 100 μm to 10 μm coinciding with an increasing amount of fingers from 10 to 100. A similar approach for measuring the dielectric constant of thin films is given by Tselev *et al*. who used a difference method between measured substrate and film.[228] Comparison of the results obtained for both methods is shown for LSNO on LAO (Figure 76A). Both analysis methods gave approximately the same results. Dielectric loss was calculated from the relationship $\tan\delta = \frac{G_m}{C_m 2\pi f}$ where G_m is the measured conductance, C_m is the measured capacitance and f is the applied frequency.

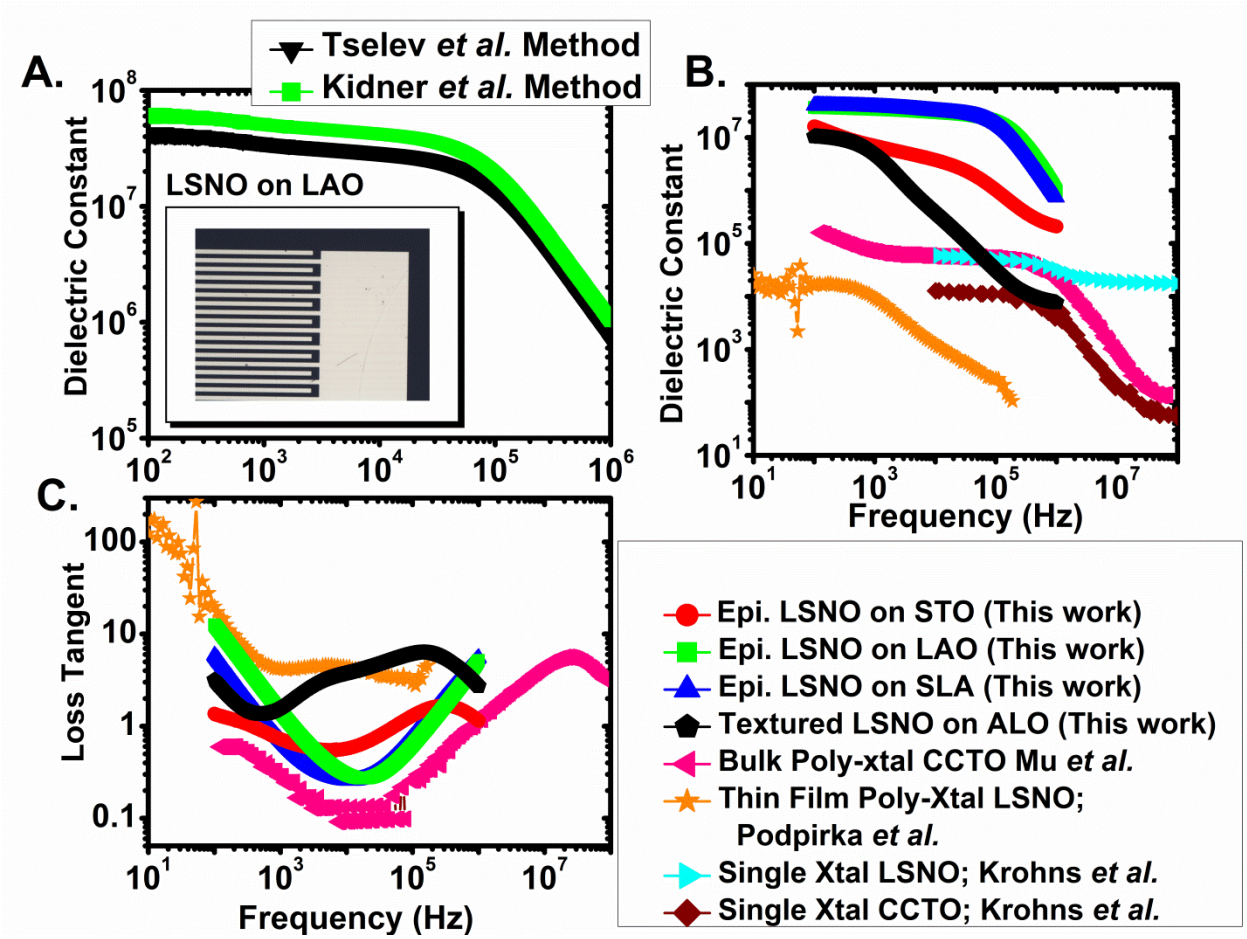

Figure 76: (A) Comparison between two methods used for analysis of dielectric response of LSNO on LAO substrate. Inset shows a close up of the IDC structure. (B) Dielectric constant as a function of frequency for LSNO on LAO, STO, SLA and ALO substrates taken at 303K

Dielectric constant and the loss tangent data taken at 303K are shown in Figure 76B and Figure 76C, respectively. The loss tangent also varied as a function of frequency with a minimum value of 0.25 for LSNO on LAO and SLA, 0.6 for LSNO on STO and 1 for LSNO on ALO. As previously stated, LSNO on LAO and SLA are in compressive strain, LSNO on STO is under tensile strain and LSNO on ALO is fiber textured. Similar trends in dielectric response and loss tangent are seen between the LAO and SLA (both compressively strained) in Figure

76B and Figure 76C. The permittivity of the LSNO on LAO and SLA was seen to have minimal dispersion well into the 10^5 Hz range. In LSNO on STO and on ALO, much larger and earlier onset of dispersion was observed as a function of frequency. As a reference, we plot published data for CCTO and LSNO in both polycrystalline and single crystal bulk form taken at room temperature in Figure 76B and Figure 76C.[216,229,230] Our results show approximately 2-3 orders of magnitude greater dielectric response for epitaxial and textured films whereas the loss tangent is comparable to polycrystalline data of CCTO and LSNO. In the fiber textured film (LSNO on ALO), the low frequency permittivity is at approximately the same value as epitaxial films however decreases steeply as a function of frequency. Loss tangent results for single crystal LSNO was not available as a function of a continuous frequency sweep however at room temperature it was shown to lie between 0.1 and 1 in the frequency range of 356 kHz and 1 Ghz.216 Our results show a decrease in loss tangent in comparison to those we previously observed on polycrystalline LSNO. This arises from the lower density of grain boundaries which was shown to cause high losses in the polycrystalline film.[229]

Evolution of the dielectric constant and loss tangent as a function of temperature is shown in Figure 77 for epitaxial LSNO on (A) LAO, (B) SLA, (C) STO and fiber textured LSNO on (D) ALO, respectively. In all cases, there was a shift to higher frequencies and enhancement in dielectric response corresponding to an increase in temperature. The loss tangent also experiences a shift to higher frequencies of the minima as temperature increases. For the loss tangent of LSNO grown on STO and ALO (Figure 77C and Figure 77D inset), a peak is seen, which evolves to high frequencies with an increase in temperature. This may also be present in LSNO on LAO (Figure 77A inset) and SLA (Figure 77B inset) however beyond the frequency range in this study. These peaks may be associated with relaxation arising from the resonance of

localized charged carriers which contribute to the giant dielectric response.[216,231] As the temperature increases, a larger number of carriers become de-localized. The frequency at which relaxation occurs therefore moves to higher frequencies with the increase in temperature.

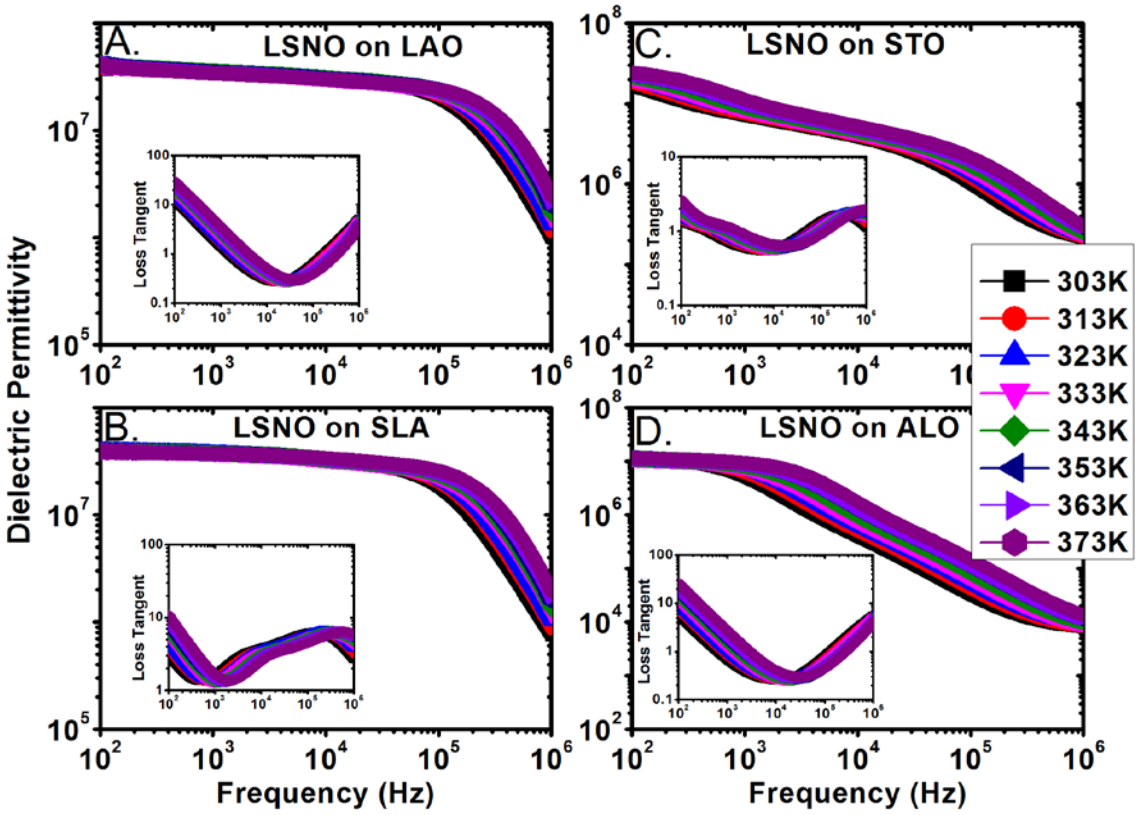

Figure 77: Dielectric constant as a function of temperature for LSNO on (A) LAO, (B) SLA, (C) STO and (D) ALO. Insets show the loss tangent as a function of temperature.

It is known that in semiconducting materials such as CCTO and LSNO, localized charge carriers hopping between spatially fluctuating lattice potentials gives rise to dipolar effects. The frequency dependent dielectric response caused by the localized carriers can be described by Jonscher's power law i.e. universal dielectric response. In the LSNO system, so-called charge ordering manifested by the stripe-like ordering of holes, has been associated with the creation of a giant dielectric response.[232] This ordering leads to an enhanced dielectric response due to

charge induced heterogeneities in what is known as a Maxwell-Wagner type behavior. It has been reported that nickelates grown under differing strain conditions may also contain differing oxidation states for the transition element i.e. nickel due to strain stabilization.[233] In LSNO, the nickel should be mostly in the Ni^{+2} state with the low concentration of strontium and oxygen non-stoichiometry (vacancies) in the lattice leading to Ni^{+3}.[234] It has also been reported that in $LaNiO_3$, the chemical bonding in the lattice is not purely ionic but shows covalent (Ni-O and La-O) and metallic (Ni-O-Ni) characteristics and can therefore perturb the electronic states.[235] The unstable Ni-O-Ni bonding created by the tensile LSNO on STO and the fiber textured LSNO on ALO could therefore lead to an increased dispersion as shown in Figure 76B, Figure 77C and Figure 77D. The compressive strained LSNO will stabilize the lattice and in turn stabilize the charge-order induced heterogeneities leading to a high dielectric constant which may manifest as delayed onset of dispersion. The non-epitaxial nature of the film on ALO is likely responsible for the large dispersion, similar to results previously reported for LSNO growth on metal underlayers.[229] The enhancement in the dielectric constant is seen in all films however the stabilization of the lattice by epitaxy leads to a delay in dispersion onset. This may account for the dielectric properties of single crystal LSNO into the gigahertz ranger reported by Krohns *et al.* as well as the increased dispersion seen in LSNO on STO and ALO with respect to that observed for LSNO on LAO and SLA.

5.3.5 Conclusion

To summarize, we have grown epitaxial and textured $La_{1.875}Sr_{0.125}NiO_4$ thin films on various single crystal oxide substrates by sputtering. Dielectric constant on the order of 10^7 has been observed with loss tangent of ~0.5. These preliminary results suggest LSNO may be

interesting for further explorations into the nature of dielectric response in this charge ordered system and potentially towards applications that benefit from large dielectric constant oxides.

5.4 Growth and Reorientation in Epitaxial LSNO on $SrTiO_3$

5.4.1 Abstract

Charge-ordered oxides are of interest in condensed matter studies to explore electronic phase diagram in compositionally complex materials systems and in emerging energy technologies. We report on orientation transition and strain relaxation in oxygenated epitaxial $La_{1.875}Sr_{0.125}NiO_{4+\delta}$ (LSNO) thin films grown by sputtering onto single crystal $SrTiO_3$ (STO) substrates. Structural evolution has been studied as a function of film thickness by x-ray diffraction, reciprocal space mapping and transmission electron microscopy. We observe a crystallographic re-orientation of the growth mode at a thickness of ~ 15 nm. The LSNO layer grows epitaxial (OR1) with respect to the STO substrate with an orientation $((001)_{OR\text{-}1}//(001)_{STO}$ and $<001>_{OR\text{-}1}$ //$<001>_{STO.}$ This orientation is maintained up to approximately 15 nm, at which point it relaxes by lattice mismatch strain and re-orients. The growth continues with a new orientation (OR2) given as $(100)_{OR\text{-}2}//(001)_{OR\text{-}1}$ and with $<100>_{OR\text{-}2}//<001>_{OR\text{-}1}$ and $<001>_{OR\text{-}2}//<001>_{OR\text{-}1}$ with respect to the epitaxial LSNO layer. Interdigitated capacitors are then fabricated on these various films and trends in dielectric properties are discussed.

5.4.2 Introduction

The La_2NiO_4 system with Sr doping is of broad interest in materials physics and chemistry. It has structural similarity to the superconductor La_2CuO_4, exhibits giant dielectric

constant, has a rich electronic phase diagram and is also explored for fuel cell applications.[236,237,238,239] The series $La_{2-x}Sr_xNiO_4$ promises high oxygen ionic mobility due to their perovskite-like K_2NiF_4 type structure and their tendency to oxygen hyperstoichiometry and with a possible high mobility in interstitial lattice sites.[240] A better understanding of the structural properties in thin film form is therefore of importance.

The lattice mismatch between a thin film and substrate is an important parameter that greatly influences the film structure, morphology and its strain state. Competition between the thermal strain energy minimization and surface energy minimization leading to orientation transition have been observed in metallic thin films.[241,242]However, the lattice mismatch strain becomes predominant in epitaxial, oxide thin films. Typically, first few layers of thin film may accommodate the mismatch strain by elastic deformation and maintain the atomic registry with the substrate leading to epitaxial growth with coherent interface for small mismatch. However, the homogeneous elastic energy stored within an epitaxial film due to the lattice misfit strain increases with film thickness. At a certain critical thickness, h_c it is energetically favorable to relieve the misfit strain by formation of dislocations or other mechanisms at or near the substrate/film interface.[243] In the present study, we report on the microstructure of LSNO on $SrTiO_3$ (STO) grown at high oxygen partial pressure as a function of thickness. We report on the existence of a critical thickness associated with epitaxial growth followed by crystallographic reorientation at larger thickness that likely is created by the hyperstoichiometry of oxygen in the lattice and driven by strain relaxation and surface energy minimization.

La_2NiO_4 and related compounds, exhibit large anisotropy arising from the complex crystal structure of the ruddlesden-popper phase. Anisotropic oxygen diffusion at high temperatures has been predicted by molecular dynamic calculations showing the *a-b* plane to be

most active.[244] Electronic conductivity at low temperature was also seen to be highly anisotropic. Hopping conduction is seen in the *c* direction whereas the diffusive character of the charge transport is due to the (001) plane. It has also been seen that negative charge carriers (electrons) are also present, mainly in the LaO layer.[245] The deposition of pure *c*-axis oriented La_2NiO_4, the related La_2CuO_4 and LSNO on STO has been done using numerous methods and by the authors.[246,247,248,266,267] By simply changing the deposition conditions, we have shown that a crystallographic reorientation is obtainable. The ability to vary the orientation through deposition parameters would allow to development of devices utilizing the anisotropy of the material on substrates once thought to be unfavorable for its growth.

5.4.3 Experimental

Epitaxial LSNO films of nominal composition $La_{1.875}Sr_{0.125}NiO_4$ (space group 139, I 4/mmm) were deposited by rf magnetron sputtering from stoichiometric targets of 99.9% purity. (ACI alloys). Deposition conditions were optimized at 10mTorr pressure, 923K substrate temperature and 50% O_2 in Argon, without any post-deposition anneal. Samples were allowed to cool to room temperature in the deposition chamber. Single crystal substrates of (001) orientation cubic STO were chosen due to the similar lattice parameters (3.905Å) to that of bulk LSNO. Film thickness was controlled by deposition time and varied from 25nm to 150nm in steps of 25nm. Growth rate of the films was approximately 6.5Å/min. x-ray diffraction was performed using a (022) Ge monochromated Cu K-α beam (Bruker D8 with pathfinder detector) and general area 2-D dectors (Bruker D8 with Vantec 2000 Dector). Cross sectional transmission electron microscopy (TEM) was performed using JEOL 2010-FEG microscope operated at 200 KV. TEM specimens were prepared by mechanical thinning followed by Ar ion milling. Composition of LSNO film on STO was confirmed by electron energy loss spectroscopy

analysis (EELS) performed in Zeiss Libra TEM with omega filter operated at 120 kV. Background subtraction was performed using the power law model in digital micrograph. Electrical contacts were patterned by photolithography of interdigitated capacitors (IDC) and consisted of 10nm adhesion layer of Ti and 100nm layer of Au deposited by electron beam depositon. Capacitance measurements were carried out as a function of frequency up to 1MHz (Agilent E4980A LCR Meter).

5.4.4 Results

X-ray diffraction studies were carried out on all thin film samples and showed features related solely to STO and LSNO over a wide 2θ range. Figure 78 shows the evolution of the diffraction pattern as a function of thickness plotted from 35^{o} to 55^{o} for reference. The 25nm film only showed (001) peaks related to both the substrate and film. Figure 79 shows detailed diffraction data for the 25nm thin film. Modeling the x-ray reflectivity data confirms thickness of ~25nm as well as a homogenous layer (i.e. no secondary oscillations). Epitaxial relationship (Figure 79 inset A) was confirmed by phi scan from symmetric (103) peak showing four-fold tetragonal symmetry. Rocking curve data (Figure 79 inset B) for the LSNO (006) peak shows strong orientation with a full width half maximum of 467 arc seconds thus confirming an epitaxial layer. Lattice parameter along the c-axis was calculated from the (006) peak and determined to be 12.81 Å. Bulk LSNO lattice parameter was extrapolated to be 3.853Å from JCPDS data in the *a*-direction.[249] Lattice parameter of cubic STO is 3.905Å. We can expect the LSNO films grown on STO will be under tensile strain.

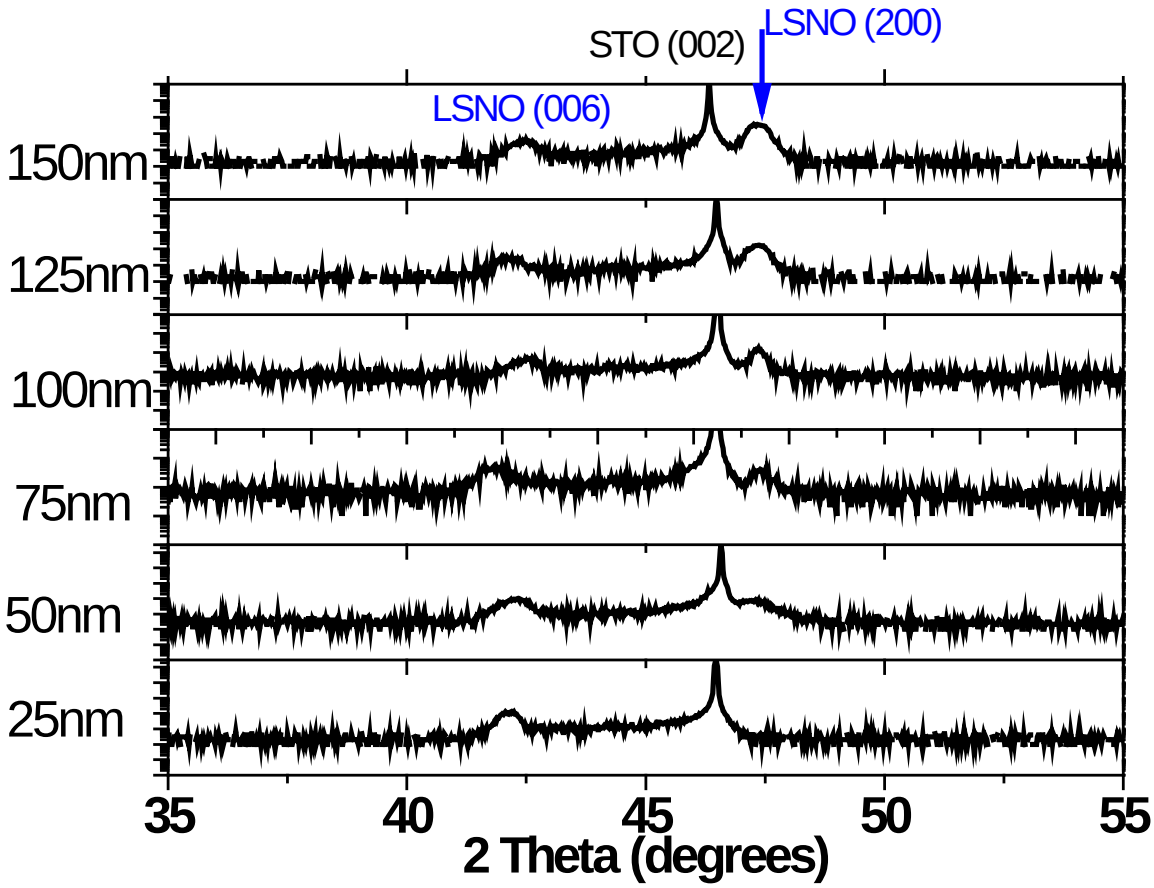

Figure 78: Diffraction pattern of LSNO on STO as a function of thickness showing the formation of the (200) phase.

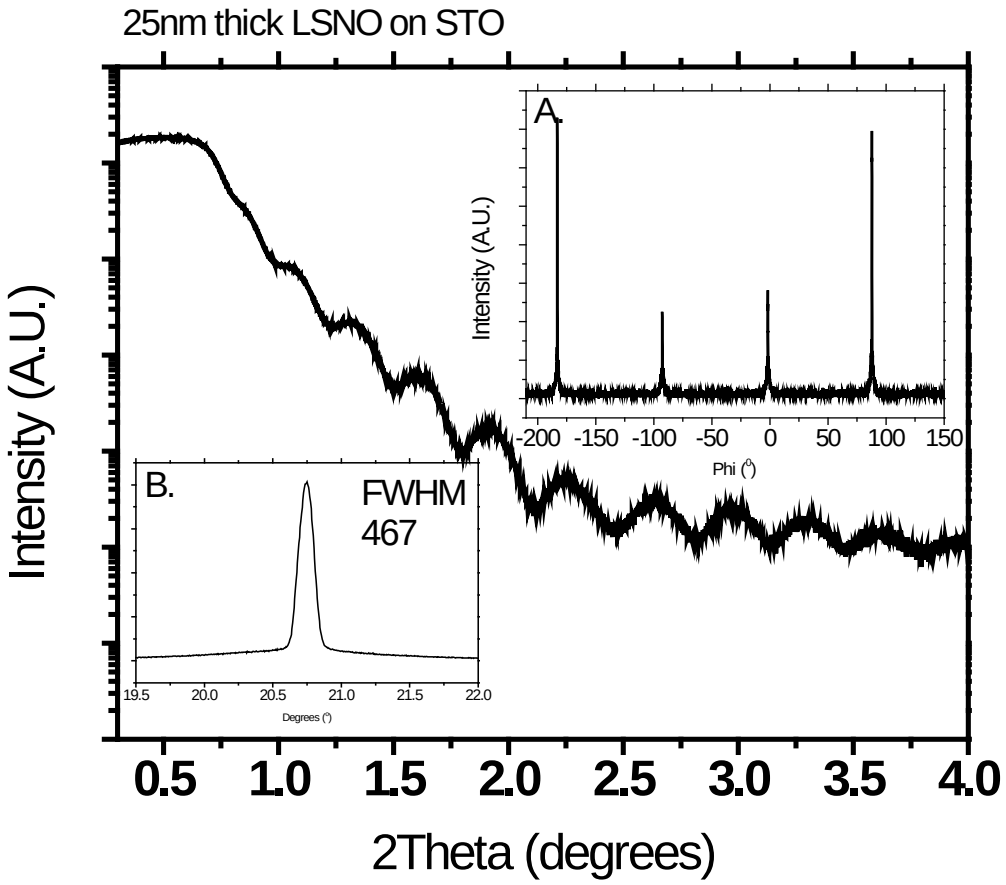

Figure 79: x-ray reflectivity of 25nm thick LSNO on STO. Inset (A) Phi scan showing of 25nm thick (103) LSNO on STO. Inset (B) Rocking curve data for 25nm thick LSNO (006).

Beyond 25nm, in addition to the (001) peaks, a (200) peak begins to develop which becomes more intense as the thickness of the film is increased while still maintaining the (00*l*) peaks. This indicates that between 25nm and 50nm, there exists a crystallographic re-orientation in order to accommodate the stress induced by the epitaxial growth mode. *a* plane lattice parameter for the 150nm film was measured to be 3.835 Å from the (200) peak which matches closely with that reported in literature.[249] Since we are performing symmetric 2θ-θ scans, diffraction planes must be parallel to the surface. Schematically, the crystal structure of LSNO is given in Figure 80 with (100) and (001) planes highlighted in black and blue, respectively.[250]

Therefore, as the films become thicker, crystallographic reorientation is occurring to change from the (001) plane being parallel to the STO surface to (100) parallel to the surface. Rocking curve data for the (200) peak is plotted in Figure 81 for 50nm and 150nm. As the thickness of the films increases, the rocking curve becomes much stronger indicating an increase in texturing as a function of growth. This likely arises from the minimization of surface free energy.[251] Instead of relieving the stress due to interface dislocations which is much more common, we observe the crystallographic reorientation of the film at a critical thickness. This crystallographically reorientation phenomena has been seen in other systems such as TiN and most recently in La_2NiO_4 which will be discussed in detail in a later section.[252,253,254] To confirm the orientation transition, TEM studies were carried out on the 100 nm thick LSNO film.

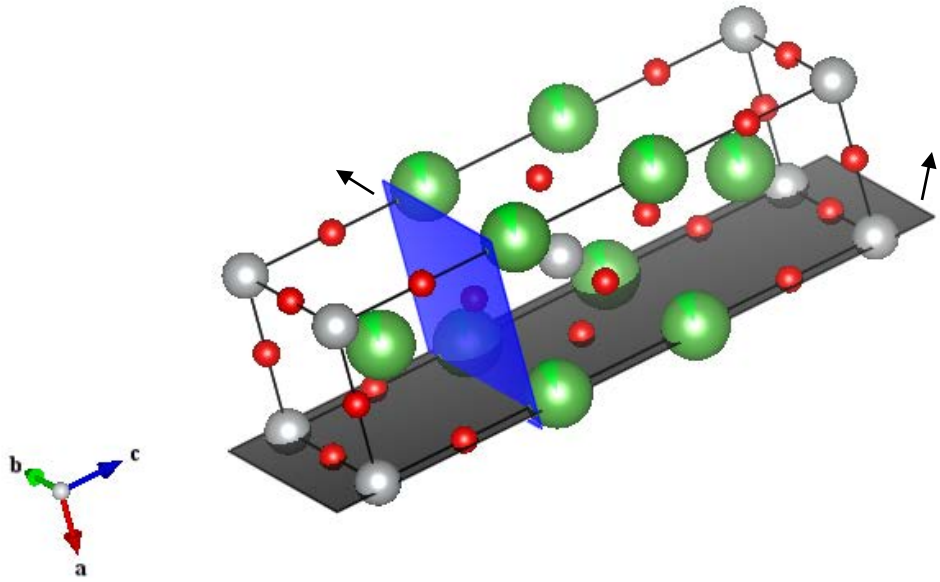

Figure 80: Crystal structure of LSNO. (100) and (001) planes are shown in gray and blue, respectively. Created with Ref.[13].

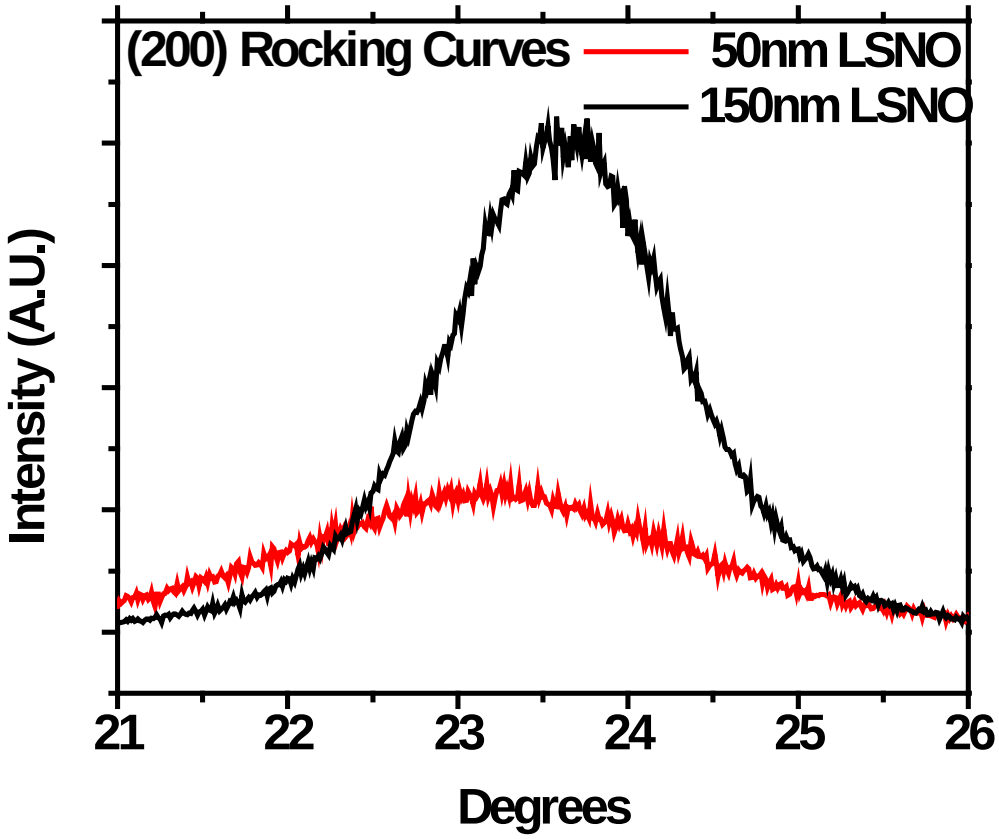

Figure 81: Rocking curve data as a function of thickness for the (200) LSNO peak. Broadness of 50nm LSNO indicates weak texturing. Offset of peak position is due to alignment of substrate.

Figure 82 shows the TEM bright field images of the 100 nm thick LSNO film on STO substrate. The corresponding SAED patterns obtained from LSNO film and STO substrate are shown as inset. LSNO thin film appears darker as compared to the STO substrate owing to mass/thickness contrast arising from heavier elements present in LSNO. No contrast is seen in LSNO film up to 15 nm of thickness with smooth appearance close to the LSNO-STO interface, whereas columnar growth is evident from the LSNO film edge region, suggesting possible microstructural heterogeneity in LSNO film with varying thickness (Figure 82). Interestingly, the

SAED pattern recorded from the LSNO film shows overlapping diffraction pattern from two different orientations; LSNO (001)//STO (001) – OR1 and LSNO (100)//STO (001) – OR2. This can be visualized using the crystal structure in Figure 80 with the lattice planes labeled. Lattice image of LSNO film on STO indicates the existence of critical thickness (~ 15 nm) favoring two different orientations in LSNO film (Figure 83). The boundary line separating the two orientations is shown by arrow marks. While the LSNO-STO interface is sharp, the interface separating the two orientations of LSNO film is rough and varies between 12 and 18 nm which is evident from the arrow marks pointing the boundary. In order to confirm the orientation change, FFT patterns were obtained from the film edge to LSNO-STO interface region. It is evident from Figure 83A-E, the orientation of LSNO film is changing across the critical thickness of ~15 nm. FFT from the STO region is shown in Figure 83f for reference. HRTEM image recorded from the LSNO-STO interface clearly shows the existence of critical layer thickness with two different orientations of LSNO film (Figure 84). Below 15 nm, OR1-LSNO (001)// STO (001) is observed and OR2-LSNO (100)//STO (001) is observed above this thickness with columnar microstructure. Inset in Figure 84 show the FFT patterns of STO and LSNO with two different orientations consistent with the SAED pattern. The bright field and lattice image recorded from LSNO film shows dense columnar growth parallel to the substrate normal (Figure 85). The columnar microstructure of OR-2 region of LSNO is marked in bright field and lattice image for guidance.

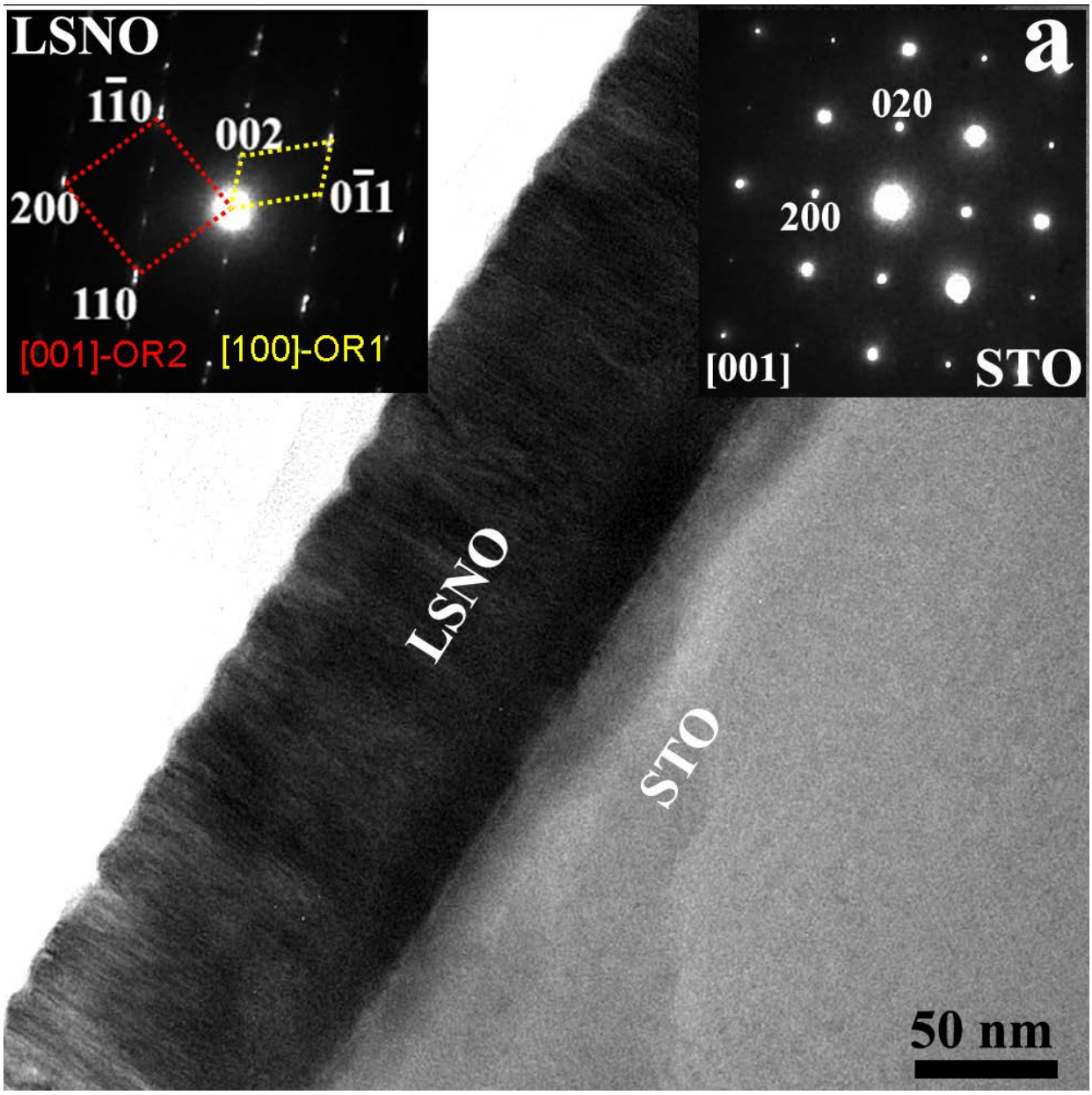

Figure 82: TEM-Bright field image shows the of LSNO film of 100 nm thickness on STO substrate. SAED pattern from LSNO film and STO substrate are shown as insets.

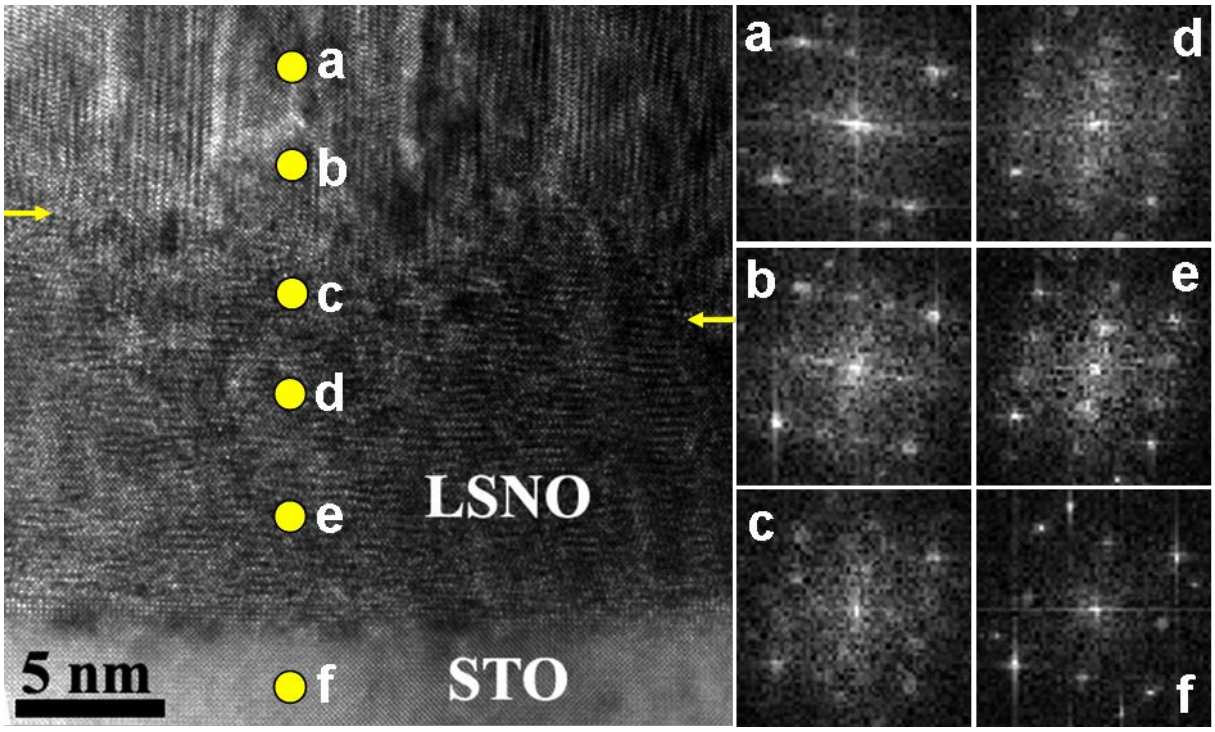

Figure 83: TEM lattice image of LSNO on STO shows the orientation evolution of LSNO film grown on STO. FFT patterns (A-E) show the changes in the orientation of LSNO film across the critical thickness of 15 nm.

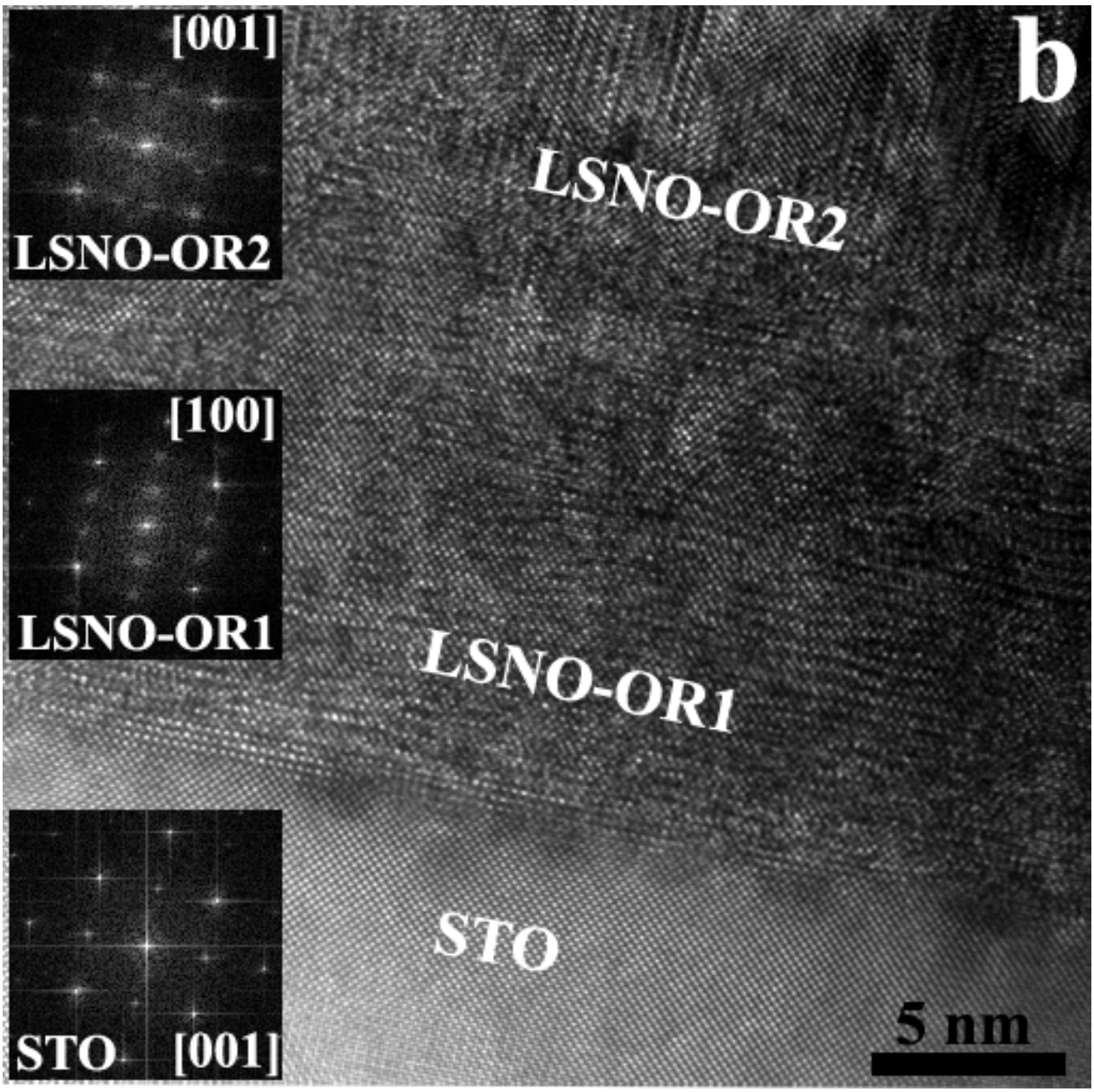

Figure 84: HRTEM image reveals the existence of critical thickness favoring LSNO [100]//STO [001]-OR-1 and LSNO[001]//STO[001]-OR-2 at low and high thicknesses respectively. The corresponding FFT patterns obtained from different layers are shown as insets.

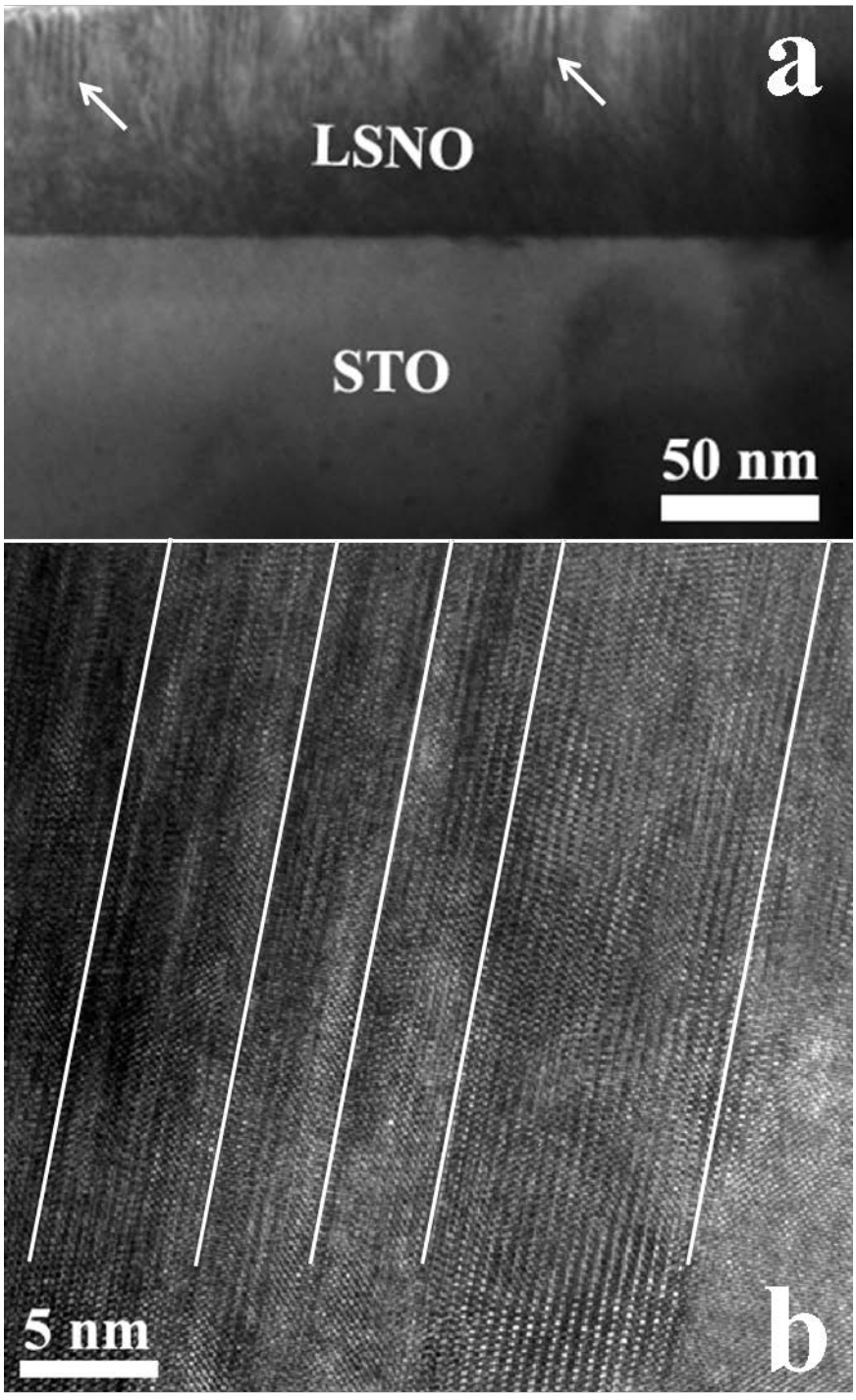

Figure 85: TEM (A) bright field image and (B) lattice image recorded from LSNO film showing dense columnar microstructure of OR-2 region. Columnar structure is marked using arrow marks and lines in bright field and lattice image respectively.

The composition of the LSNO film has been investigated using EELS in order to check whether the microstrutural heterogeneity/orientation change is related to compositional segregation or not. Figure 86 show the EELS spectra of LSNO film of 100 nm thickness grown on STO substrate with the signatures of both LSNO(A-C) and $SrTiO_3$(D-F). In STO, energy loss at 462 eV, 532 eV and 1943 eV can be assigned to Ti-L_2, O-K and Sr-L_3 edges respectively. In LSNO thin film, the observed energy loss at 825 eV and 850 eV are due to La-M_5 and La-M_4 respectively. Note that the overlap of strong La-M_4 edge with Ni-L_3 edge at 850 eV makes the measurement/analysis of Ni-L_3 edge challenging. However, the weak Ni-L_2 edge at 864.3 eV confirms the presence of Ni. Similarly, energy loss edges at 532 eV and 1943 eV in thin film confirm the presence of O and Sr respectively. The relative intensities of Sr in LSNO appears weaker compared to that of Sr in STO as the Sr content in LSNO is much lower. The energy loss near edge structure (ELNES) observed within 50 eV above the O-K edge (~532 eV) gives further insights to the composition of LSNO film on STO substrate. LSNO film shows 2 peaks at the O-K edge that can be corroborated to excitations of O 1s core state to the O 2p orbitals in the planar La-O layers hybridized with La 5d, 4f states and NiO_2 sheets hybridized with Ni 3dConsiderable difference between STO and LSNO in the shape of ELNES spectra is evident from the Figure 86A and D. Notably, intensity ratios, splitting between the peaks are different. In addition, the pre peak below 531 eV is present in STO while the pre peak intensity is negligible in LSNO. Typically, the pre-peak strength below the O-K is related to the oxygen as well as the Sr content. While the Sr doping increases the pre-peak strength, the oxygen vacancy ordering is known to introduce pre-peak.[255,256] Hence the absence of pre peak in the case of LSNO may be suggestive of high oxygen content as well as low Sr dopingin LSNO film deposited at high oxygen pressure.

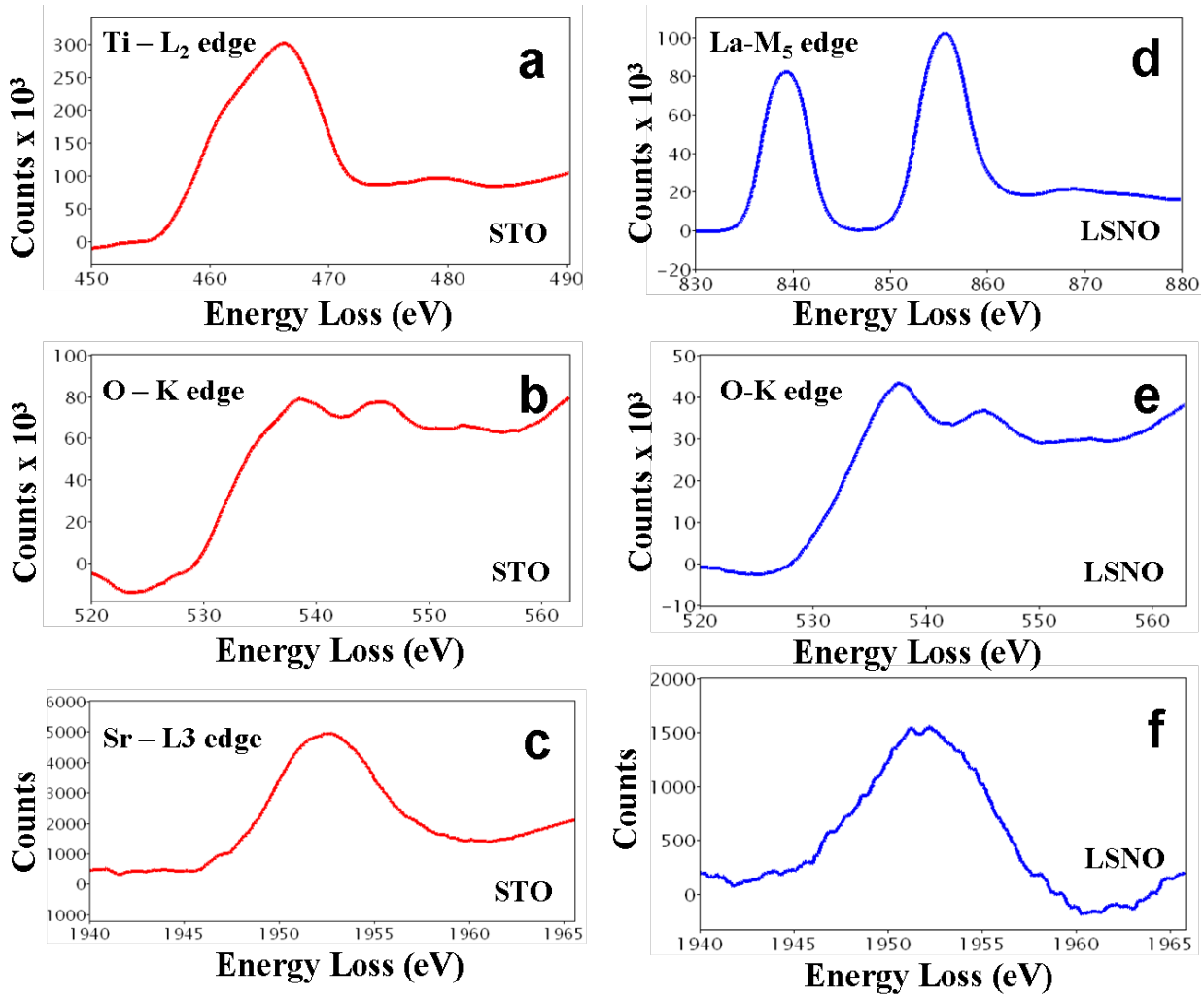

Figure 86: EELS spectra collected from STO substrate (A-C) and LSNO film (D-F) regions are shown with their characteristic energy loss edges and energy loss near edge structures (ELNES) that confirm the formation of phase pure LSNO film on STO.

General area diffraction is used to understand the oriented growth as a function of thickness. Pole figures were constructed from the (006) and the (114) LSNO planes and shown in Figure 87 and Figure 88, respectively. Due to the lattice spacing and structure, (105) plane has the same d-spacing as the (006) diffraction leading to reflections corresponding to both sets of planes. Figure 87A shows the 25nm sample that corresponds to the simulated pole figure in

Figure 87E which shows the (001) oriented simulation with the (006) reflection in the center of the stereographic projection and a four-fold symmetry of the (105) reflection at a psi of 33.6°. At 50nm (Figure 87B), another set of reflections appears at a psi of 56.5° which corresponds to the orientation change mentioned above. The location of the reflections at a psi of 56.5° correspond to (100) orientation. At a thickness of 100nm and 150nm, only the reflections at a psi of 56.5° are visible due to the intensity with respect to the (001) orientation. The simulation of the pole figure in Figure 85F however only shows two reflections, whereas we clearly see four-fold symmetry in the 100nm (Figure 87C) and 150nm (Figure 87D) samples. As observed in the TEM images in Figure 85, columnar growth exists in the second re-oriented layer. The $(100)_{OR\text{-}2}//(001)_{OR\text{-}2}$ orientation is present however from the pole figures we see that the OR-2 layer contains two distinct in-plane growth direction which are orthogonal to each other. The position of the pole figures allows us to deduce that the growth direction. To confirm this, pole figures from the (114) planes are analyzed.

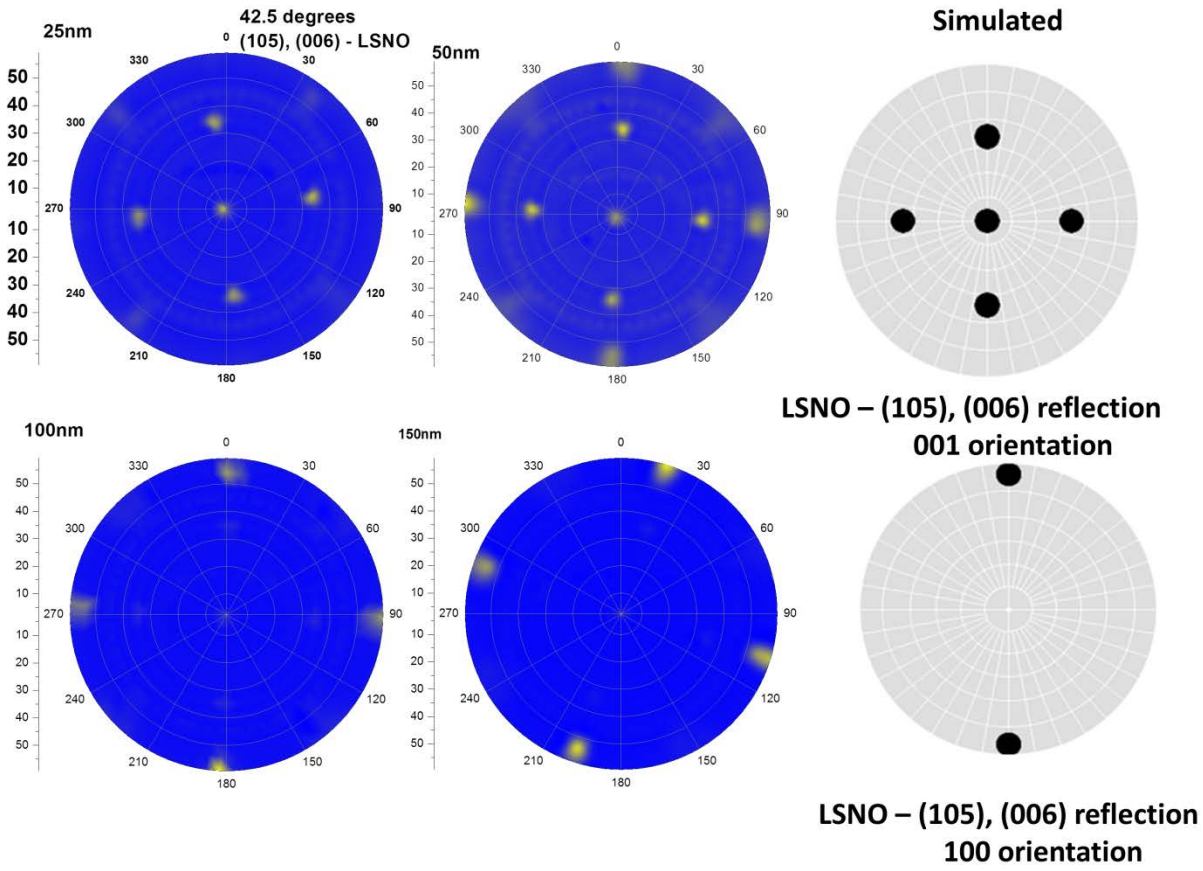

Figure 87: Pole figure for the (105), (006) reflection of thin film LSNO at 25nm, 50nm 100nm and 150nm. Simulation pole figure for the (105),(006) reflection with (001) orientation and (100) orientation.

The reflections of the (114) plane further confirm the analysis seen above. The 25nm sample (10A) shows reflections at a psi of 49.5° associated with the (001) oriented growth, which is also simulated in Figure 88E. At 50nm, a second set of reflections begins to appear at a psi of 57.5°. The psi angle indicates the film is (100) oriented. Films of thickness 100nm and 150nm (Figure 88C and Figure 88D, respectively) show distinct reflections at 57.5°. Again, the simulation (Figure 88F) does not match the films in that another set of reflections is seen. This again would correspond to the bicrystal orientation in the plane of the film. The fact that in both

Figure 87 and Figure 88 show sharp distinct reflections indicates that the films are highly textured, even after the reorientation see at approximately 15 nm and no polycrystalline random orientation is noticed. In both pole figures, the in-plane orientation direction is orthogonal to each other leading to a distinct 90° rotation in the pole figure. OR1 is grown on STO as $(001)_{OR-1}//(001)_{STO}$ and $<001>_{OR-1}$ //$<001>_{STO}$ as indicated from the diffraction data. From the pole figures, OR-2 on OR-1 is grown $(100)_{OR-2}//(001)_{OR-1}$ and with both $<100>_{OR-2}//<001>_{OR-1}$ and $<001>_{OR-2}//<001>_{OR-1}$ directions present. This accounts for the patterns seen in both pole figures and confirm the distinct columnar growth see in cross sectional TEM image of OR-2 (Figure 84B) which shows dense columnar in-plane growth incorporating two distinct domains. It should be noted that in both sets of pole figures, data is plotted on a linear scale which prevents the observation of the OR-1 layer in the thicker films. OR-1 orientation is still present however the intensity of the OR-2 layer is greater and allows for easier interpretation of data.

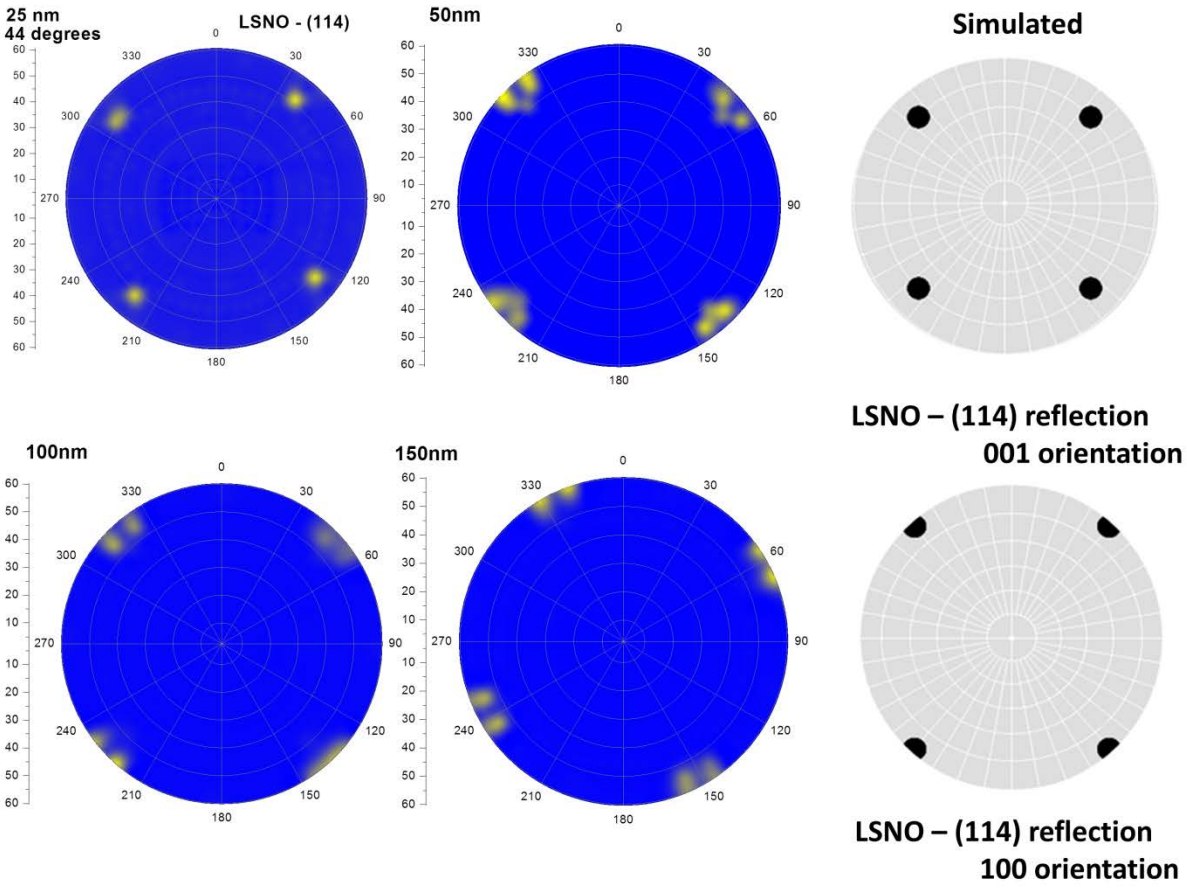

Figure 88: Pole figure for the (114) reflection of thin film LSNO at 25nm, 50nm 100nm and 150nm. Simulation pole figure for the (114) reflection with (001) orientation and (100) orientation.

Electrical characterization allows us to immediately observe the importance of understanding the reorientation phenomena observed. As stated earlier, bulk crystal LSNO has been observed to have colossal dielectric properties due to its charge ordered properties as previously observed by Krohns *et al.*[257] To further understand the functionality of the film with respect to reorientation, electrical characterization was performed with interdigitated capacitor structures (IDC) micro-fabricated on the surface of the film. Detailed explanation of the data analysis methods is given in chapter 3.4.2. Figure 89 plots the dielectric data for the thicknesses

(A) 25nm and 50nm and (B) 75nm, 125nm and 150nm. It is observed, that differing dielectric response is present as a function of thickness, further indicating the importance of reorientation in the films. The 25nm film, which is completely strained, behaves similar to that observed in a previous work on epitaxial LSNO (chapter 5.3). The lattice is completely tensile strained leading to an unstable Ni-O-Ni bonding which leads to capacitance dispersion through the entire frequency sweep. As the film gets thicker, a mixed dispersion begins to take shape in the 50nm thick film which arises from the 25nm strained layer OR-1 and the 25nm relaxed OR-2. This mixed dispersion manifests itself as the formation of a plateau and multiple relaxations as indicated in Figure 89A. The enhancement of the dielectric properties may arise from the interplay in the two distinct layers and grains present. Increased density of grain boundaries have been shown to lead to increased low frequency dielectric constant in LSNO due to Maxwell-Wagner polarization.[258] In the 50nm sample, a broad rocking curve of the (200) peak was observed in Figure 81. This indicates that multiple grains are present and have not yet fully reoriented themselves. This mismatch could lead to a dielectric enhancement as well as the layered structure being approximately 50% OR-1 and 50% OR-2. This may also lead to the two distinct relaxation mechanisms present where a low and high frequency mechanism being present due to the large fraction of both phases present.

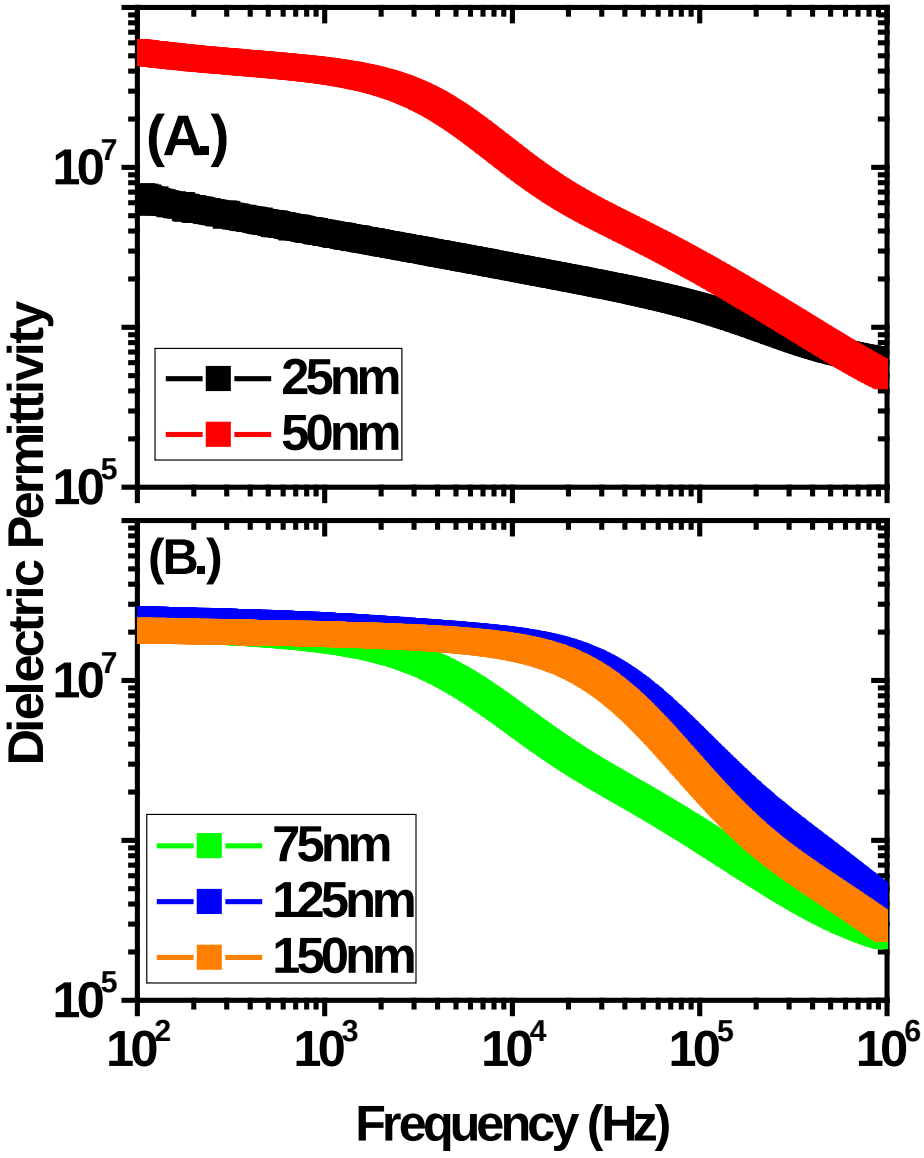

Figure 89: Dielectric properties of LSNO thin film of (A) 25nm and 50nm and (B) 75nm, 125, and 150nm grown on STO.

At 75nm, the dielectric constant seems to stabilize with a plateau at $2*10^7$. A low frequency plateau is usually observed in giant dielectric constant materials such as $CaCu_3Ti_4O12$, $Sm_{1.5}Sr_{0.5}NiO_4$, LSNO and other systems.[259,260,261] This data shows frequency

dependent relaxation process occurring at approximately 2kHz which is similar to that observed in the 50nm thin film however characteristic frequency dependence similar to 125nm films is beginning to manifest itself. At 125nm and 150nm, with dense columnar growth, the dielectric properties observed match closely with one another. The form of the dielectric response showing dispersion at high frequency is similar to that observed in other charge ordered systems showing giant dielectric response. In both, we see a delayed onset of dispersion with respect to the thinner films.

Similar trends can be seen in the dielectric loss tangent of the films shown in Figure 90. 25nm thick film shows exhibits a much different response to that of the 50nm response as seen in Figure 90A. It can be inferred from this that the low frequency local minima can be associated with OR2 formation however trends for the 50nm and 75nm samples show great similarity in their shape. As observed in Figure 80 and Figure 85, as the film becomes thicker, the columnar growth and surface normal plane orientation becomes more pronounced. In the 75nm sample, shown in Figure 90B, due to these crystallographic properties described, the response from OR-1 becomes suppressed. At 125nm and 150nm (Figure 90B), the shape of the dielectric response changes significantly with the local minima moving to approximately 10 kHz and no longer a flat plateau being observed in the 10-100kHz range as was present in the loss tangents for the 50nm and 75nm thick films. Crystallographic anisotropy in the electrical properties is observed thus explaining the differences between the OR-1 and OR-2 orientations however the role of domain boundaries in the OR-2 layer cannot be fully decoupled. Domains have been shown to play a significant role in the dielectric response in materials exhibiting Maxwell-Wagner type polarization.[262,263] Due to differences in the local chemical stoichiometry of the grain-grain

boundary domains and the anisotropy of crystallographic direction, dielectric response will indeed vary through the thicknesses measured.

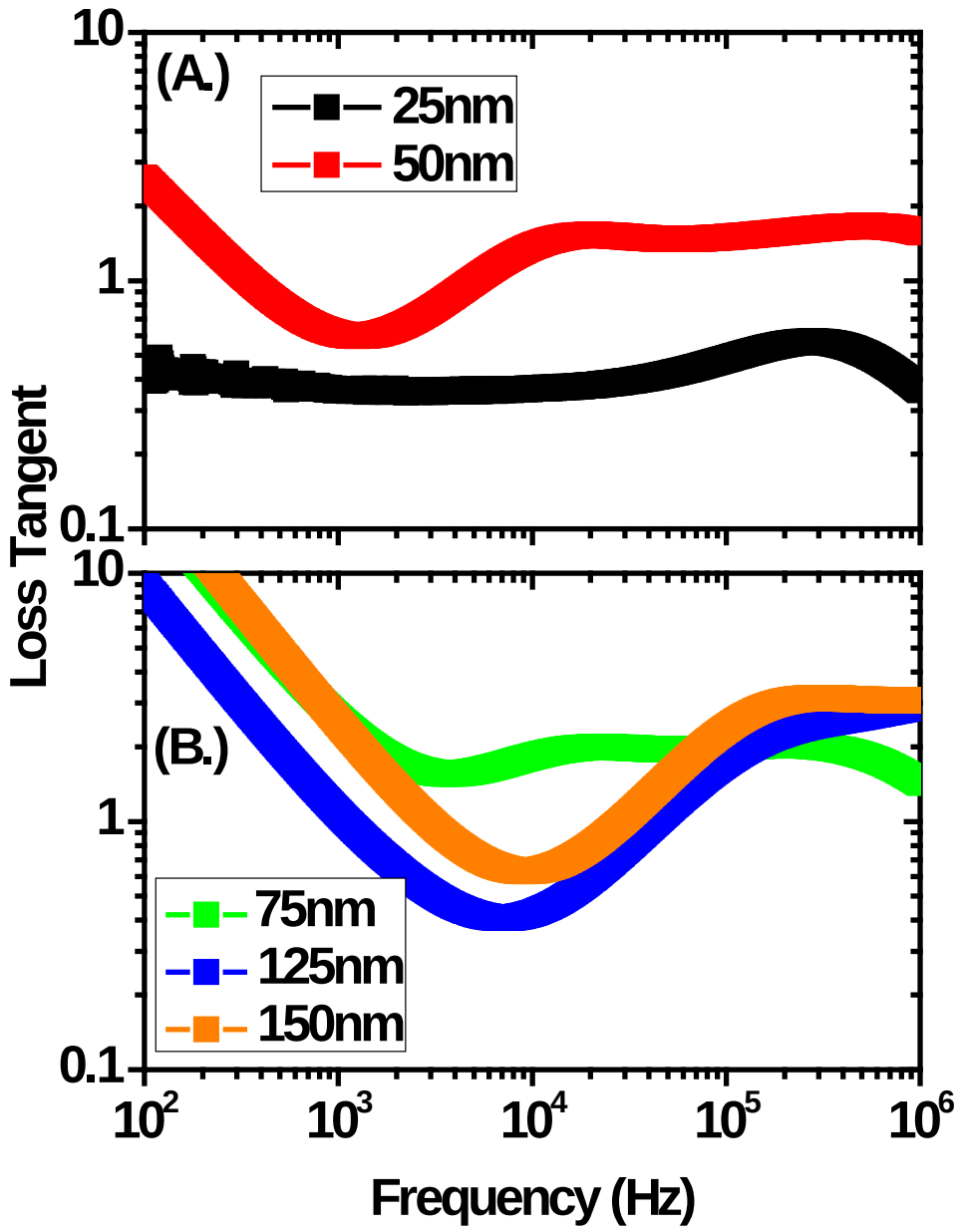

Figure 90: Dielectric loss tangent for LSNO thin film of (A) 25nm and 50nm and (B) 75nm, 125, and 150nm grown on STO.

In the isostructural La_2CuO_4 (LCO) system, tensile strain is accommodated by the creation of misfit dislocations.[264] In many oxide systems, misfit dislocations accommodate the strain energy thereby allowing continued epitaxial growth.[265] In our previous study, epitaxial LSNO films that were grown at lower oxygen partial pressures and faster deposition rates up to a thickness of 220 nm with epitaxial (001) orientation. [266,267] We can thus eliminate the role of Ni in LSNO as a cause for the crystallographic re-orientation when compared to LCO. Due to the K_2NiF_4 structure, LSNO can accommodate interstitial oxygen within the rock salt layer of the lattice which arises from the large concentration of oxygen during sputtering.[268,269.] The interstitial oxygen may increase the elastic energy of the film and therefore relaxation through misfit dislocations at the LSNO-STO interface is impeded.

It has been reported that the K_2NiF_4-type structure incorporates oxygen readily into the lattice leading to hyperstoichiometric phases.[270] The rock salt La_2O_3 layer may accommodate a significant oxygen excess charge-compensated by the formation of electron holes in the perovskite sheets.[271] This places the NiO_2 plane under pressure. In La_2NiO_4, the strain may be released by either a tilting of the NiO_6 octahedra in the stoichiometric compound, which leads to an orthorhombic *Bmab* structure, or an oxygen intercalation in the La_2O_2 double layer, resulting in overstoichiometric phases of $La_2NiO_{4+\delta}$. In this case, the release of strain in the NiO_2 plane arises both from the partial oxidation of Ni^{2+} into $Ni^{3+}$and from a tilting of NiO_6.[272] The doping of oxygen and strontium into the La_2NiO_4 lattice significantly affects the phase diagram of the system.[273] Substitution of Sr^{2+} for La^{3+} into the La_2NiO_4 lattice has been shown to induce holes just as excess oxygen does. The formal valence of the NiO_2 plane is negative while that of the (La,Sr)O bilayer is positive. Doping with interstitial oxide ions of Sr^{2+} reduces the positive net charge in the rocksalt bilayer. Similarly, the compensating holes serve to reduce the negative net

charge in the NiO_2 planes. Overall, doping decreases the charge separation inherent to the structure, providing a stabilizing effect.[273] For a doping of above x=0.08, Hucker *et al*. have reported that no orthorhombic-tetragonal transition takes place due to oxygen interstitials and the Sr defects, and the reduction of the octahedral tilt angle by Sr doping contributions to this effect. However, in our study, due to the hyperstoichiometric nature of the deposition, lattice effects from the hole doping may play a significant role in the layer reorientation. At the moment, it is unclear the exact mechanism for how the reorientation is formed from oxygen interstitial interaction, however more studies are being performed to elucidate the effect. The subtle interplay between strontium and oxygen co-doping may also lead to the resulting critical thickness and should be explored further.

However beyond a critical thickness, the film needs to lower its overall energy by strain relaxation and/or surface energy minimization. According to Read *et al.*, in the LNO system the surface energy of the un-relaxed and relaxed (100) plane is 3.07 J/m^2 and 0.98 J/m^2, respectively which is the lowest among all planes. As a reference, (001) plane has an unrelaxed and relaxed surface energy of 3.55 J/m^2 and 1.55 J/m^2 respectively.[274] Once layer-by-layer growth stops, plastic deformation occurs and the film reorients itself by having the (100) plane normal to the surface of the film, which leads to the observation of the (200) peak as shown in Figure 78. The driving force is the decrease in surface energy to accommodate the driving strain. The thermal strain should play a minimal role in the reorientation due to the nearly equal thermal expansion coefficients of the materials; LSNO being approximately $11.5*10^{-6}$ K^{-1} whereas STO being approximately $11*10^{-6}$ K^{-1}.[275,276] The critical thickness was determined to be ~15nm by TEM though no sign of the (200) plane was visible in the 25nm sample in x-ray diffraction the intensity of the thin LSNO layer on top of the epitaxial film are expected to be low. As stated

previously, as the film grows thicker, the surface energy is minimized and the (200) layer becomes more textured. This texturing allows (200) orientation to be seen in both x-ray and electron diffraction. It should also be noted that from the XRD pattern in Figure 78 and the pole figures in Figure 86 and Figure 87, there is no increase in intensity of the (006) peak as a function of growth, nor is there any (006) continuation of the growth, indicating that the orientation of OR2 is solely that of the (200) parallel to the growth. TEM images further this understanding. This is in support of that observed in the recent work by Telesca *et al.* on La_2NiO_4 who interpreted the results as two distinct layers rather than mixed domains. Telesca *et al.* also reported observing four distinct orientations associated with domain tilting and tensile/compressive strain. We observed only two distinct orientations orthogonal to each other as confirmed by pole figure analysis and simulation. We do not see any reflections arising from tensile/compressive strain since only our 25nm thick layer was highly strained and the columnar growth in the second layer can be said to be relaxed.

5.4.5 Conclusion

Our results suggest that crystallographic reorientation occurs in growth of highly oxygenated LSNO thin films grown on STO substrate under tensile strain. At a critical thickness epitaxial growth is transformed to a highly textured film. This appears to be a result of energy minimization arising from the competition between surface energy and strain energy. Due to the interest currently associated with LSNO, namely in the ionic conductivity and dielectric properties, a detailed understanding of the crystallographic anisotropy to its electrical properties is of great interest. We show that the dielectric properties vary significantly as a function of strain and strength of reorientation. The ability to vary the anisotropy through simply varying

deposition parameters may allow for the use of LSNO in applications once thought to be unobtainable due to its crystallographic orientation.

6 Future Work

Since the very recent discovery of the giant dielectric constant in LSNO, there has been a giant stimulus to pursue a closer look at the dielectric properties. Unfortunately, many more interesting aspects of the material are still unexplored. In this section, I will describe a short list of possible routes that I see interesting to pursue as well as am currently pursuing. This will focus primarily on LSNO since BST has been studied to a much greater extent.

- Due to the crystal structure of LSNO, properties should be highly anisotropic. This was observed in chapter 5.3 and 5.4 where the reorientation of the film showed different dielectric behavior. This arises from the conduction and space layer that was discussed previously. By change in the orientation, will allow us to careful study the dielectric properties in both the *c* and *a* direction. This could easily be done by the growth on LSNO on substrates such as $LaAlSrO_4$. Since the substrate has a same K_2NiF_4 crystal structure, similar lattice parameter as well as can be purchased with different orientations, a deeper understanding of the anisotropy can be obtained.
- LSNO is a doped material, with the hole creating arising from the addition of strontium in the lattice. This also changes the charge ordering temperature significantly as shown in the work by Freeman *et al.*[41] Depending on the doping, stripe and checkerboard ordering can be explored. Stripe ordering usually occurs in the range of 100-200K however, checkerboard ordering has been shown to be above 250K. A thorough understanding of these charge ordering effects should be investigated. In the same light, the effect of lattice strain on the ordering temperature should be explored. We already saw the effect of lattice strain on the dielectric

properties in chapter 5.3 Can this lattice strain change the stripe ordering temperature? By using strain engineering, can we tailor new properties? Charge ordering would also manifest itself in the *pn* junction (chapter 5.2) study if those were now measured at cryogenic temperatures.

- The dielectric properties, namely the dielectric loss of BST, are highly desirable for device application. BST however has a significantly smaller dielectric constant when compared to LSNO, which suffers from high dielectric losses. Superlattice growth has been shown to greatly enhance dielectric properties in thin films.[277] Can the coupling of a colossal dielectric constant material with a ferroelectric enhance play a significant role in the dielectric properties?
- As seen in Chapter 5.4 , reorientation phenomena occurs in LSNO thin films. This was attributed to the oxygen concentration during the sputtering process. The amount of oxygen that is able to interstitially incorporate into the LSNO lattice is proportional to the doping of strontium. A greater understanding of the mechanism for the orientation can be developed by investigating the critical thickness associated with the growth of oxygenated LSNO films of differing Strontium content. In particular, when x= 0 and x=0.5. This will give a better understanding to the control needed for reorientation.
- LSNO has recently been identified as a cathodic material suitable for intermediate temperature solid oxide fuel cells (SOFC).[278] The ability of conduct ions interstitially due to the ability of incorporate a large concentration of interstitial, may be of great interest for fuel cell applications. This is due in large part to the high catalytic properties of Sr, Ni and La. Throughout this thesis, we have shown the ability to grow

phase pure LSNO. In a previous work (not present in this thesis), we measured the mixed ionic and electronic conductivity in Gadolinia doped Ceria.[279] Similar thin film experiments should be performed on LSNO in order to determine the suitability for SOFCs. This could be done as a function of orientation (using epitaxial growth as mentioned before) and as a function of strontium content (by co-sputtering with LSNO targets of different compositions).

7 Conclusion

Transition metal complex oxides, due to their intricate processing steps and defect chemistry, leads to many interesting physical properties. This thesis shows the importance of structure, strain and oxygen stoichiometry on the dielectric properties of BST and LSNO thin films.

With BST, we have explored the interaction of UV assisted annealing allowing for a novel route to lower processing temperature. This is of great significance for industrial applications that require lower temperatures in order to integrate BST into the supply chain. The ability to grow BST on non-noble electrodes significantly lowers cost and makes the processing route attractive to the semiconductor industry. Through UV assisted annealing, oxygen defects are eliminated, giving more robust dielectric properties.

We have studied the dielectric properties of LSNO for the first time in polycrystalline and epitaxial thin film form. We note the dielectric properties are dependent on the microstructure, with the mechanism being of a Maxwell-Wagner type. In epitaxial form, the substrate induced strain effects the frequency dependence, with compressive strain delaying the onset of dispersion and tensile strain leading to early onset. When these same films are grown epitaxially on Nb-doped $SrTiO_3$, a degenerate *n*-type conductor, we experience the formation of *pn* junctions due to the hole concentration in the LSNO. Conventional semiconductor band bending may not be applicable due to the variation in dielectric properties as a function of frequency as observed when the dielectric properties were measured on tensile strained LSNO on STO. Finally, we observe a crystallographic reorientation phenomena associated with the growth of epitaxial films

with high oxygen partial pressure. This allows for controlled oriented growth in order to reach certain anisotropic properties.

Where the first part of the thesis was working on the processing techniques in a well-studied material system, BST, the second part dealt with the basic underlying physics and material science of a novel system, LSNO. These studies attempt to overcome hurdles the electronic industry will face in the coming year, with both novel processing routes and materials. Our understanding into complex oxides is still in its infancy with more questions arising as we answer existing ones. Though this may complicate our understanding of complex oxides, from a practical point of view, this is not negative, since the control and manipulation of certain properties can lead to other interesting and potentially beneficial applications.

8 References

[1] V. Fiorentini and G. Gulleri *Phys. Rev. Lett.* **89**[26] 266101(2002).

[2] B. Hude, K. Husekova, E. Dobrocka, T. Lalinsky, J. Aarik, A. Aidla and F. Frohlich *IOP Conf. Ser. Mat. Sci. and Eng.* **8** 012024 (2010).

[3] D. Oh, C. Ko, S. Ramanathan and D.G. Cahill, *Appl. Phys. Lett.*, **96**, 151906, (2010).

[4] T. Kikuzuki and M. Lippmaa *Appl. Phys. Lett.* **96**, 132107 (2010).

[5] http://modelscience.com/PeriodicTable.html

[6] P. Lunkenheimer, R. Fichtl, S. G. Ebbinghaus and A. Loidl *Phys. Rev. B* **70**, 172102 (2004).

[7] S. Q. Liu, N. J. Wu and A. Ignatiev *Appl. Phys. Lett.* **76** 2749 (2000).

[8] R. Moazzami *IEEE Transaction on Electron Devices* **39**[9] 2044 (1992).

[9] Y. Koval, F. Chowdhury, X. Jin, Y. Simsek, F. Lichtenberg, R. Pentcheva and P. Muleer *Physica Status Solidi* **208**[2] 284 (2011).

[10] P. K. Davies, H. Wu, A. Y. Borisevich, I. E. Molodetsky and L. Farber *Annu. Rev. Mater. Res.* **38** 369 (2008).

[11] P. Zubko, S. Gariglio, M. Gabay, P. Ghosez and J.-M. Triscone *Annu. Rev. Condens. Matter. Phys.* **2** 141 (2011)

[12] J. G. Bednorz, K. A. Muller and M. Takashige *Science* **236**73 (1987).

[13] K. Momma and F. Izumi *J. Appl. Crystallogr.*, **44** 1272 (2011).

[14] K. C. Kao *Dielectric Phenomena in Solids* Elsevier (2004).

[15] K. Maex, M. R. Baklanov, D. Shamiryan, F. Lacopi, S. H. Brongersma, and Z. S. Yanovitskaya *J. Appl. Phys.* **93**[11] 8793 (2003).

[16] W. J. Merz *Phy. Rev.* **76**[8] 1221 (1949).

[17] P. Lunkenheimer, S. Krohns, S. Riegg, S. G. Ebbinghaus, A. Reller and A. Loidl *Eur. Phys. J.*

[18] P. Lunkenheimer, V. Bobnar, A. V. Pronin, A. I. Ritus, A. A. Volkov and A. Lodil *Phys. Rev. B* **66** 052105 (2002).

[19] M. A. Subramanian, D. Lin, N. Duan, B. A. Resiner, A. W. Sleight *J. Sol. Stat. Chem.* **151**, 323 (2000).

[20] S. Krohns, P. Lunkenheimer, S. G. Ebbinghaus and A. Loidl *J. Appl. Phys.* **103**, 084107 (2008).

[21] P. R. Bueno, R. Tararan, R. Parra, E. Joanni, M. A. Ramirez, W. C. Ribeiro, E. Longo and J. A. Varela *J. Phys. D:appl. Phys.* **42** 055404 (2009).

[22] S. Krohns, P. Lunkenheimer, Ch. Kant, A. V. Pronin, H. B. Brom, A. A. Nugroho, M. Diatoro and A. Loidl *Appl. Phys. Lett.* **94**, 122903 (2009).

[23] Z.-Y. Cheng, R. S. Katiyar, X. Yao and A. S. Bhalla *Phys. Rev. B* **57**[14] 8166 (1998).

[24] I. Rivera, A. Kumar, N. Ortega, R. S. Katiyar and S. Lushnikov *Sol. Sta.Com.***149** 172 (2009).

[25] J. Dumas, C. Schlenker, J. Marcus, R. Buder, Phys. Rev. Lett. 50, 757 (1983).

[26] C. C. Wang and L. W. Zhang *New J. Phys.* **9** 210 (2007).

[27] J. Sichelschmidt, M. Paraskevopoulos, M. Brando, R. Wehn, D. Ivannikov, F. Mayr, K. Pucher, J. Hemberger, A. Pimenov, H.-A. Krug von Nidda, P. Lunkenheimer, V.Yu. Ivanov, A.A. Mukhin, A.M. Balbashov, A. Loidl, *Euro. Phys. J. B* **20**, 7 (2001).

[28] D. Capsoni, M. Bini, V. Massarotti, G. Chiodelli, M.C. Mozzatic and C. B. Azzoni *J. Sol. Stat. Chem.* **77**[12] 4494 (2004).

[29] B. Renner, P. Lunkenheimer, M. Schetter, A. Loidl, A. Reller and S. G. Ebbinghaus *J. Appl. Phys.* **96** 4400 (2004).

[30] A. R. West, T. B. Adams, F. D. Morrison and D. C. Sinclair *J. Euro. Ceram. Soc.* **24**[6] 1439 (2004).

[31] L. Zhang and Z.-J. Tang *Phys. Rev. B* **70** 174306 (2004).

[32] A. K. Jonscher *Nature* **267** 673 (1977).

[33] P. Lunkenheimer, T. Gotzfried, R. Fichtl, S. Weber, T. Rudolf, A. Loidl, A. Reller and S. G. Ebbinghaus *J.Sol. Stat. Chem.* **179**, 3965 (2006).

[34] A. von Hippel *Dielectrics and Waves* Artech House (1995).

[35] J. C. Maxwell, Electricity and Magnetism, Vol. 1 (Clarendon Press, Oxford, 1892).

[36] K. W. Wagner, Die Isolierstoffe der Elektrotechnik, ed. H. Schering (Springer-Verlag, Berlin, 1924).

[37] W. Li, O. Auciello, R. N. Premnath and B. Kabius *Appl. Phys. Lett.***96**, 162907 (2010).

[38] A. F. Gibson, F. A. Kr□oger and R. E. Burgess, Progress in Semiconductors, Vol. 4 (Heywood & Co. Ltd., London, 1960).

[39] C. C. Wang, H. B. Lu, K. J. Jin and G. Z. Yang *Mod. Phys. Lett. B* **22**[13] 1297 (2008).

[40] A. Bianconi and N. L. Saini *Stripes and Related Phenomena* Kluwer Academic/Plenum Publisher (2000).

[41] P. Freeman *Thesis: Magnetism and the Magnetic Excitation of Charge Ordered* $La_{2-x}Sr_xNiO_{4+\delta}$ Oxford University.

[42] R. R. Tummala *IEEE Spectrum* **6** 44 (2006).

[43] Y. Chase *Introduction to choosing MLC Capacitors for Bypass/Decoupling Applications* AVX Corporation.

[44] R. R. Tummala *Fundamentals of Microsystems Packagin* McGraw-Hill (2001).

[45] H. Kwak and T. Hubing Technical Report: Clemson Vehicular Electronics Laboratory-07-0001.

[46] M. W. Cole, E. Ngo, S. Hirsch, J. D. Demaree, S. Zhong and S. P. Aplay *J. Appl. Phys.* **102** 034104 (2007).

[47] T. S. Kalkur, N. M. Sebrockey, G. S. Tompa, P. Alpay, J. E. Spanier, E. N. Galow and M. W. Cole *Int. Ferro.* **112**[1] 1 (2010).

[48] B. A. Baumert, L.-H. Chang, A. T. Matsuda, T.-L. Tsai, C. J. Tracy, R. B. Gregory, P. L. Fejes, N. G. Cave, W. Chen, D. J. Taylor, T. Otsuki, E. Fujii, S. Hayashi and K. Suu *J. Appl. Phys.* **82** 2558 (1997).

[49] D. M. Smyth *Ann. Rev. Mat. Sci* **15** 329 (1985).

[50] M. Hucker, K. Chung, M. Chand, T. Vogt, J. M. Tranquada and D. J. Buttrey *Phys. Rev. B* **70**, 064105 (2004).

[51] V. V. Kharton, A. P. Viskup, E. N. Naumovich and F. M. B. Marques *J. Mater. Chem.* **9** 2623 (1999).

[52] M. L. Fontaine, C. Laberty-Robert, M. Verelst, J. Pielaszeck, P. Lenormand, F. Ansart and P. Tailhades *Mat. Res. Bul.* **41**[9] 1747 (2006).

[53] F. Mauvy, J.-M. Bassat, E. Boehm, J. P. Manaud, P. Dordor, J.-C. Grenier *Sol. Sta. Ion.* **158** 17 (2003).

[54] S. Krohns, P. Lunkenheimer, Ch. Kant, A.V. Pronin, H. B. Brom, A. A. Nugroho, M. Diantoro, and A. Loidl, *Appl. Phys. Lett.* **94**, 122903 (2009).

[55] K. Wasa, M. Kitabatake and I. Adachi *Thin Films Materials Technology: sputtering of compound materials* William Andrew, Inc (2004).

[56] L. B. Freund and S. Suresh *Thin Film Materials: Stress, defect formation and surface evolution* Cambridge (2003).

[57] J. A. Thornton *Ann. Rev. Mat. Sci.* TA401-A7 **7** 239 (1977).

[58] D. A. Porter and K. E. Easterling *Phase Transformations in Metals and Alloys 2nd Edition* Chapman & Hall (1981).

[59] S. M. Aygun, P. Daniels, W. Borland and J.-P. Maria *J. Appl. Phys.* **103**, 084123 (2008).

[60] E.M. Young and W. A. Tiller Appl. Phys. Lett. **50**(2) 80 (1987).

[61] E.M. Young and W.A. Tiller, Appl. Phys. Lett. **50**, 46 (1987).

[62] H. Okabe, *Photochemistry of Small Molecules* John Willey and Son (1978).

[63] C. R. Cracium, K. Ramani, V. Craciun and R. K. Singh *Appl. Phys. Lett.* **88**, 182902 (2006).

[64] A. Srivastava, V. Craciun, J. M. Howard and R. K. Singh *Appl. Phys. Lett.* **75**, 3002 (1999).

[65] M. Tsuchiya, S. K. R. S. Sankatanarayanan, and S. Ramanathan *Prog. Mat. Sci.* **54**[7] 981 (2009).

[66] J. Als-Nielsen and D. McMorrow *Elements of Modern X-ray Physics* Wiley (2001).

[67] W. Rontgen *Nobel Prize in Physcis (*1901).

[68] E. Chason and T.M. Mayer *Crit. Rev. in Sol. Stat. and Mat. Sci.* **22**(1) 1 (1997).

[69] M. A. Moram and M. E. Vickers *Rep. Prog. Phys.* **72** 036502 (2009).

[70] T. Konya *x-ray diffraction techniques for thin films* Rigaku Corporation.

[71] M. Li, C. R. Becker, R. Gall, W. Faschinger and G. Landwehr *Appl. Phys. Lett.* **71**[13] 1822 (1997).

[72] *x-ray user guide*, Technical University Munich..

[73] B. B. He, U. Preckwinkel and K. L. Smith *Advances in x-ray Analysis* **43** 273 (2000).

[74] H.J. Nam, D.K. Choi, W.J. Lee. Thin Solid Films, Vol. 371, pp. 264-271, (2001).

[75] N. J. Kidner, A. Meier, Z. J. Homrighaus, B. W. Wessels, T. O. Mason and E. J. Garboczi *Thin Solid Films* **515** 4588 (2007).

[76] N. J. Kidner, Z. J. Homrighaus, T. O. Mason and E. J. Garboczi, *Thin Solid Films* **496** 539 (2006).

[77] E. Barsoukov and J. R. Macdonald *Impedance Spectroscopy: Theory, Experiment, and Applications 2nd edition* Wiley and Sons, Inc (2005).

[78] Y. K. V. Reddy, D. Nergel and W. Osswald *Mat. Sci. Eng.* **130** 237 (2006).

[79] N. P. Choudhary *Dielectric Materials: Introduction, Research and Applications* Nova Science Pub. Inc (2009).

[80] S. M. Sze and K. K. Ng *Physics of Semiconductor Devices* Wiley (2007).

[81] D. B. Williams and C. B. Carter *Transmission Electron Microscopy* Springer (1996).

[82] C. L. Chen, J. Shen, S. Y. Chen, G. P. Luo, C. W. Chu, F. A. Miranda, F.W. Van Keuls, J. C. Jiang, E. I. Meletis, and H. Y. Chang, Appl. Phys. Lett. **78**, 652 (2001).

[83] A. Kumar, S.G. Manavalan, V.Gurumurthy, S. Jeedigunta, and T. Weller, Mater. Sci. Eng. B **139**, 177 (2007).

[84] J. Park, C.S. Hwang, and D.Y. Yang, J. Mater. Res. **16**, 1363 (2001).

[85] Z. –G. Ban and S. P. Alpay, J. Appl. Phys. **93**, 504 (2003).

[86] W. Zhu, J. Cheng, S. Yu, J. Gong, and Z. Meng, Appl. Phys. Lett. **90**, 032907 (2007).

[87] P. C. Joshi and M. W. Cole, Appl. Phys Lett. **77**, 289 (2000).

[88] S. Hyun, J.H. Lee, S.S. Kim, K. Char, S.J. Park, S. Sok, and E.H. Lee, Appl. Phys. Lett. **77**, 3084 (2000).

[89] H. S. Kim, T. S. Hyun, H. G. Kim, I. D. Kim, T. S. Yun, and J. C. Lee, Appl. Phys. Lett. **89**, 052902 (2006).

[90] S. K. Sahoo, D. C. Agrawal, Y. N. Mohapatra, S.B. Majumder and R.S. Katiyar, Appl. Phys. Lett. **85**, 5001 (2004).

[91] W. Choi, B.S. Kang, Q.X. Jia, V. Matias, and A.T. Findikoglu, Appl. Phys. Lett. **88**, 062907 (2006).

[92] V. Craciun, A. Srivastava, J.M. Howard, R.K. Singh and J. Perriere, Appl. Phys. A **69**, S787 (1999).

[93] W.J. Kim, W. Chang, S.B. Qadri, J.M. Pond, S.W. Kirchoefer, D.B. Chrisey, and J.S. Horwitz, Appl. Phys. Lett., **76**, 1185 (2000).

[94] H.J. Nam, D.K. Choi, and W.J. Lee, Thin Solid Films **371**, 264 (2000).

[95] V. Craciun and R.K. Singh, Appl. Surf. Sci. **168**, 239 (2000).

[96] J.S. Horwitz, W. Chang, W. Kim, S.B. Qadri, J.M. Pond, S.W. Kirchoefer and D.B. Chrisey, J. Electroceram. **4**, 357 (2000).

[97] S. Saha and S. B. Krupanidhi, J. Appl. Phys. **87**, 3056 (2000).

[98] M. W. Cole, P. C. Joshi, and M. H. Ervin, J. Appl. Phys. **89**, 6336 (2001).

[99] M. W. Cole, A. Podpirka, and S. Ramanathan, ARL Technical Report **27**, 1 (2007).

[100] C.S. Hwang et al., J. Appl. Phys. **83**, 3703 (1998).

[101] D.C. Shye, C.C. Hwang, M.J. Lai, C.C. Jaing, J.S. Chen, S. Huang, M.H. Juang, B.S. Chiou, and H.C. Cheng, Jpn. J. Appl. Phys. **42**, 549 (2003).

[102] V. Craciun and R.K. Singh, Appl. Phys. Lett. **76**, 1932 (2000).

[103] S. Ramanathan, D.A. Muller, G.D. Wilk, C.M. Park, and P.C. McIntyre, Appl. Phys. Lett. **79**, 3311 (2001).

[104] J.H. Joo, J.M. Seon, Y.C. Jeon, K.Y. Oh, J.S. Roh, and J.J. Kim, Appl. Phys. Lett. **70**, 3053 (1997).

[105] S. K. Bhattacharya and R.R. Tummala, J. Mat. Sci: Mat. in Electr. **11**(3), 253 (2000).

[106] C.S. Hwang, Mat. Sci. and Eng. B **56**(2-3), 178 (1998).

[107] M.W. Cole, C. Hubbard, E. Ngo, M. Ervin, M. Wood, and R.G. Geyer. J. Appl. Phys. **92**, 475 (2002).

[108] S. Zhong, S.P. Alpay and J.V. Mantese,Appl. Phys. Lett. **89**, 042906 (2006).

[109] Z.-G. Ban and S.P. Alpay, J. Appl. Phys. **93**, 504 (2003).

[110] R. K. Ulrich and L. W. Schaper, *Integrated Passive Component Technology*, (IEEE Press, 2003).

[111] R. R. Tummala, IEEE Spectrum. 43(6) 44 (2006).

[112] P. Padmini, T.R. Taylor, M. J. Lefevre, A. S. Nagra, R. A. York, and J.S. Speck, Appl. Phys. Lett. **75**, 3186 (1999).

[113] M. W. Cole and R. G. Geyer, Mech. of Mat. **36**(10), 1017 (2004).

[114] B. Laughlin, J. Ihlefeld, and J.-P. Maria, J. Am. Ceram. Soc. **88**(9), 2652 (2005).

[115] S. M. Aygun, P. Daniels, W. Borlands, and J.-P. Maria, J. Appl. Phys. **103**, 084123 (2008).

[116] P.C. McIntyre, J. Appl. Phys. **89**(12), 8074 (2001).

[117] M. Tsuchiya, K.R.S.S. Sankaranarayanan, and S. Ramanathan, Prog. in Mat. Sci. **54**, 981 (2009).

[118] M. Tsuchiya, V. Shutthandan, M. Engelhard, and S. Ramanathan, Appl. Phys. Lett. **93** 263109 (2008).

[119] V. Craciun and R. K. Singh, Appl. Phs. Lett. **76**, 1932 (2000).

[120] R. Merkle and J. Maier, Angew. Chem. Int. Ed. **47**, 3874 (2008)**.**

[121] J.-S. Lee, Y. Li, Y. Lin, S. Y. Lee, and Q. X. Jia, Appl. Phys. Lett. **84**, 3825 (2004).

[122] Y.-L. Qin, C.-L. Jia, R. Liedtke, R. Waser, and K. Urban, J. Am. Ceram. Soc. **86**(7), 1190 (2003).

[123] S.-I. Jang and H. M. Jang, Ceram. Int. **26,** 421 (2000).

[124] R. Schafranek, J. Schaffner, and A. Klein. J. Euro. Cer. Soc. **30** 187 (2010).

[125] M.S. Tsai and T. Y. Tseng, J. Phys. D: Appl. Phys. **32**, 2141 (1999).

[126] M.W. Cole, W.D. Nothwang, C. Hubbard, E. Ngo, and M. Ervin, J. Appl. Phys. **93,** 9218 (2003).

[127] M. Shen, Z. Dong, Z. Gan, S. Ge, and W. Cao, Appl. Phys. Lett. **80**, 2538 (2002).

[128] S.C. Roy, G.L. Sharma, and M.C. Bhatnagar, Solid State Communications **141**, 243 (2007).

[129] C.-L. Chang and S. Ramanathan, J. Electrochem. Soc. **154**(7), G160 (2007).

[130] S. K. R. S. Sankaranarayanan, E. Kaxiras, and S. Ramanathan, Energy Environ. Sci. **2**, 1196 (2009).

[131] T. Hara, IEEE Trans. of Dev. and Mat. Rel. **4**(4), 640 (2004).

[132] M.B. Okatan and S.P. Alpay, Appl. Phys. Lett. **95**, 092902 (2009).

[133] R.A. de Souza, Phys. Chem. Chem. Phys. **8**, 890 (2006).

[134] J. A. Lane, and J. A. Kilner, Solid State Ionics **136-137**, 927 (2000).

[135] J.-H. Joo, J.-M. Seon, Y.-C. Jeon, K.-Y. Oh, J.-S. Roh, and J.-J. Kim, Appl. Phys. Lett. **70**, 3053 (1997).

[136] M.A. Subramanian, D. Li, N. Duan, B.A. Reisner, and A.W. Sleight, J. of Sol. Sta. Chem. **151**, 323 (2000).

[137] R.R. Tummala, *IEEE Spectrum*, June 2006.

[138] R. R. Tummala and M. Swaminathan, *Introduction to System-On-Package* The McGraw-Hill Companies, Inc. (2008).

[139] S. Krohns, P. Lunkehheimer, Ch. Kant, A. V. Pronin, H.B. Brom, A. A. Nugroho, M. Diantoro, and A. Loidl, Appl. Phys. Lett. **94**, 122903 (2009).

[140] C.C Homes, T. Vogt, S.M. Shapiro, S. Wakimoto, and A.P. Ramirez, Science **293**[5530], 673 (2001).

[141] T.-T. Fang and H.-K. Shiau, J. Am. Ceram. Soc. **87**, 2072 (2004).

[142] J. Yu, P.-F. Paradis, T. Ishikawa, and S. Yoda, Appl. Phys. Lett. **85,** 2899 (2004).

[143]J. Yu, T. Ishikawa, Y. Arai, S. Yoda, M. Itoh, and T. Saita, Appl. Phys. Lett. **87**, 252904 (2005).

[144] Y.K. V. Reddy, D. Mergel, and W. Osswald, Mat. Sci. and Eng. B **130,** 237 (2006).

[145] P. Lunkenheimer, V. Bodnar, A.V. Pronin, A. I. Ritus, A.A. Volvok, and A. Loidl, Phys. Rev. B **66**, 052105 (2002).

[146] K. Rivas, B. Rivas-Murias, A. Fondado, J. Mira, and M.A. Senaris-Rodrigues, Appl. Phys. Lett. **85,** 6224 (2004).

[147] S. Yanez-Vilar, M. Sanchez-Andujar, J. Rivas, and M.A. Senaris-Rodriquez, J. Alloys and Comp. **82,** 485 (2009).

[148] D.C. Sinclair, T.B. Adams, F. D. Morrison, and A.R. West, Appl. Phys. Lett. **80**[12], 2153 (2002).

[149] P. Lunkenheimer, T. Gotzfried, R. Fichtl, S. Weber, T. Rudolf, A. Loidl, A. Reller, and S. G. Ebbinghaus, J. Sol. Stat. Chem. **179**[12], 3965 (2006).

[150] W. Li, O. Auciello, R. N. Premnath, and B. Kabius, Appl. Phys. Lett. **96**, 162907 (2010).

[151] P. Thongbai, C. Masingboon, S. Maensiri, T. Yamwong, S. Wongsaenmai, and R. Yimnirun, J. Phys. Condens. Matter. **19,** 236208 (2007).

[152] A. Castro-Couceiro, M. Sanchez-Andujar, B. Rivas-Murias, J. Mira, J. Rivas, and M.A. Senaris-Rodriguez, Sol. Sta. Sci. **7,** 905 (2005).

[153] A. von Hippel, *Dielectrics and Waves* Artech House Publishers (1995).

[154] A.K. Jonscher, *Dielectric Relaxation in Solids* Chelsea Dielectric Press (1983).

[155] A.K. Jonscher, Nature (London) **267**, 673 (1977).

[156] Y. J. Wu, N. Wang, Y. Q. Lin, and X. M. Chen, Mat. Chem. and Phys. **121**[1-2], 326 (2010).

[157] S. Kumar and K.B.R. Varma, Sol. Stat. Comm. **146,** 137 (2008).

[158] K. Funke, Prog. Solid. St. Chem. **22,** 111 (1993).

[159] M. Vijayakumar, S. Selvasekarapandian, M.S. Bhuvaneswari, G. Hiran Kumar, G. Ramprasad, R. Subramanian, and P.C. Angelo, Physica B **334,** 390 (2003).

[160] C.C. Wang, Y. M. Cui, and L.W. Zhang, Appl. Phys. Lett. **90**, 012904 (2007).

[161] S. Sarkar, P. K. Jana, B.K. Chaudhuri, and H. Sakata, Appl. Phys. Lett. **89,** 212905 (2006).

[162] X.Q. Liu, Y.J. Wu, X.M. Chen, and H.Y. Zhu, J. Appl. Phys. **104,** 054114 (2008).

[163] S. Maensiri, P. Thongbai, and T. Yamwong, *Acta. Mater.* **55,** 2851 (2007).

[164] G. Wu and J. J. Neumeier, Phys. Rev. B **67**, 125116 (2003).

[165] C.H. Chen, S-W. Cheong, and A.S. Cooper, Phys. Rev. Lett. **71**, 2461 (1993).

[166] J.J. Zhu, X. G. Yang, X. L. Xu, and K. M. Wei, Sci. in China B: Chem. **50**[1], 41 (2007).

[167] N. Poirot, P. Odier, P. Simon, and F. Gervais, Sol. Stat. Sci **5,** 735 (2003).

[168] J. Li, A.W. Sleight, and M.A. Subramanian, Sol. Sta. Comm. **135,** 260 (2005).

[169] W.-X. Yuan, S.-K. Hark, and W.-N. Mei, J. Electrochem. Soc., **157**[5] G117 (2010).

[170] L. Zhang, Appl. Phys. Lett. **87**, 022907 (2005).

[171] F. Liu, Y. Ma, F. Yang, and Y. Zhou, Appl. Phys. Lett. **96**, 052102 (2010).

[172] C. Vallee, P. Gonon, C. Jorel, and F. El Kamel, Appl. Phys. Lett. **96**, 233504 (2010).

[173] K. Liu, X.-Y. Zhang, and J.-Z. Xiao, Chin. Phys. Lett. **26**[10], 107701 (2009).

[174] K. Majhi, S. Shri Prakash, and K.B. R. Varma, J. Phys. D. Appl. Phys. **40,** 7128 (2007).

[175] N. Biskup, A. de Andres, and J. L. Martinez, Phys. Rev. B **72**, 024115 (2005).

[176] G.-Z. Liu, C. Wang, C.-C. Wang, J. Qiu, M. H, J. Xing, K.-J. Jin, H.-B. Lu, and G.-Z. Yang, Appl. Phys. Lett. **92**, 122903 (2008).

[177] A. Podpirka, B. Viswanath, and S. Ramanathan, J. Appl. Phys. **108**, 024106 (2010).

[178] A. Podpirka, M.W. Cole, and S. Ramanathan, Appl. Phys. Lett. **92**, 212906 (2008).

[179] M. Tsuchiya, K.R.S.S. Sankaranarayanan, and S. Ramanathan, *Prog. in Mat. Sci.* 54, 981 (2009).

[180] V. V. Kharton, A. P. Viskup, E. N. Naumovich, and F. M. B. Marques, J. Mat. Chem. **9**, 2623 (1999).

[181] A. Bianconi and N. L. Saini *Stripes and Related Phenomena* (Kluwer Academic/Plenum Publisher, New York, 2000).

[182] H. Takagi and H. Y. Hwang, Science **327**, 1601 (2010).

[183] S. Ramanathan (Ed.) Thin *Film Metal-Oxides: Fundamentals and Applications in Electronics and Energy* (Springer-Verlag, New York, 2010).

[184] J. Matsuno, A. Sawa, M. Kawasaki, and Y. Tokura, *Appl. Phys. Lett.* **92**, 122104 (2008).

[185] B.T. Xie, Y. G. Zhao, C. M. Xiong, *Appl. Phys. Lett.* **93**, 072112 (2008).

[186] S. Krohns, P. Lunkenheimer, Ch. Kant, A.V. Pronin, H. B. Brom, A. A. Nugroho, M. Diantoro, and A. Loidl, *Appl. Phys. Lett.* **94**, 122903 (2009).

[187] C. H. Chen, S. W. Cheong, and A. S. Cooper, *Phys. Rev. Lett.* **71**, 2461 (1993).

[188] V. Sachan, D. J. Buttrey, J. M. Tranquada, J. E. Lorenzo, and G. Shirane, *Phys. Rev. B* **51**, 12742 (1995).

[189] C. Lei-Ming, L. Guang-Chang, Z. Yan, and G. Yan-Feng. *Chin. Phys. Lett.* **27** 077401 (2010).

[190] JCPDS # 01-070-9274

[191] M. Burriel, J. Santiso, M. D. Rossel, G. V. Tendeloo, A. Figueras and G. Garcia. *J. Phys. Chem. C* **112** 1098 (2008).

[192] G. Li, D.-b. Huang, S.-w. Jin, Y.-q. Ma, and X.-g. Li, *Sol. Stat. Com.* **150** 1737 (2010).

[193] M. Kanai, D. Matsuura, T. Kawai and H. Miki *Physica C* **289** 223 (1997).

[194] S. M. Sze, *Physics of Semiconductor Devices*, 2nd ed. (Wiley, New York, 1981).

[195] E. H. Rhoderick and R. H. Williams, *Metal-Semiconductor Contacts*, 2nd ed. (Clarendon, Oxford, 1988).

[196] A. Ruotolo, C. Y. Lam, W.F. Cheng, K. H. Wong, and C. W. Leung. *Phys. Rev. B* **76**, 075122 (2007).

[197] W. Ramadan, S. B. Ogale, S. Dhar, L.F. Fu, S.R. Shinde, C. Kundaliya Darshan, M. S. R. Rao, N. D. Browning and T. Venkatesan. *Phys. Rev.* B **72** 205333 (2005).

[198] R.T. Tung. *Phys. Rev.* B **45** 13509 (1992).

[199] Y. Hikita, Y. Kozuka, T. Susaki, H. Takagi and H.Y. Hwang *Appl. Phys. Lett.* **90**, 143507 (2007).

[200] F. Y. Bruno, J. Garcia-Barriocanal, M . Torija, A. Rivera, Z. Sefrioui, C. Leighton, C. Leon, and J. Santamaria. *Appl. Phys. Lett.* **92**, 082106 (2008).

[201] A. Yamamoto, A. Sawa. H. Akoh, M. Kawasaki and Y. Tokura. *Appl. Phys. Lett.* **90**, 112104 (2007).

[202] K. Morito, T. Suzuki, S. Sekiguchi, H. Okushi and M. Fujimoto. *Jpn. J. Appl Phys*. **39** 166 (2000).

[203] A. Podpirka and S. Ramamathan *J. Appl. Phys.* **109** 014106 (2011).

[204] T. Yamamoto, S. Suzuki, H. Suzuki, K. Kawaguchi, K. Takahashi and Y. Yoshisato. *Jpn. J. Appl. Phys.* **36** L390 (1997).

[205] C.-J. Liu, M.D. Mays, D. O. Cowan and M.G. Sanchez *Chem. Mater.* **3** 495 (1991).

[206] D. M. Fleetwood, S. T. Pantelides, R. D. Schrimpf. *Defects in microelectronic materials and devices (*CRC press, Florida, 2009).

[207] M. Schmeits, N. D. Nguyen and M. Germain *J. Appl. Phys.*89[3] 1890 (2001).

[208] G. H. Glover *Solid-State Electronics* **16** 973 (1973).

[209] S. Saraf, M. Markovich, and A. Rothschild. *Phys. Rev. B* **82**, 245208 (2010).

[210] T. Makino, H. Kato, S.-G. Ri, S. Yamasaki and H. Okushi. *Diamond and Related Materials* **17**[4-5] 782 (2008).

[211] T. Makino, N. Tokuda, H. Kato, M. Ogura, H. Watanabe, S-G. Ri, S. Yamasaki and H. Okushi. *Diamond and Related Materials* **16** 1025 (2007).

[212] M. C. Ni, S. M. Guo, H. F. Tian, Y. G. Zhao and J. Q. Li. *Appl. Phys. Lett.* **91**, 183502 (2007).

[213] D. J. Wang, J. R. Sun, Y. W. Xie, Y. B. Li, L. G. Zhang, R. W. Wang and B. G. Shen. *Appl. Phys. Lett.* **97**, 192503 (2010).

[214] J. R. Sun, C. M. Xiong, B. G. Shen, P. Y. Wang and Y. X. Weng, *Appl. Phys. Lett.* **84**[14] 2611 (2004).

[215] C. Wang, Z. F. Li, X.M. Chen, J.M. Liu, Z. M. Liu, H. Y. Cui, Y. ang and W. Lu, *Thin Solid Films* **516** 4282 (2008).

[216] S. Krohns, P. Lunkenheimer, Ch. Kant, A.V. Pronin, H. B. Brom, A. A. Nugroho, M. Diantoro and A. Loidl, *Appl. Phys. Lett.* **94**, 122903 (2009).

[217]X. Q. Liu, B. W. Jia, W. Z. Yang, J. P. Cheng and X. M. Chen, *J. Phys. D: Appl. Phys.* **43,** 495402 (2010).

[218] X. Q. Liu, Y. J. Wu and X. M. Chen, *Solid State Communications* **150**, 1794 (2010).

[219] X. Q. Liu, S. Y. Wu, X. M. Chen, and H. Y. Zhu, *J. Appl. Phys.* **104**, 054114 (2008).

[220] P. Lunkenheimer, S. Krohns, S. Riegg, S. G. Ebbinghaus, A. Reller and A. Loidl, *Eur. Phys. J. Special Topics* **180**, 61 (2010).

[221] M. A. Subramanian, D. Li, N. Duan, B. A. Reisner, and A. W. Sleight, *J. Solid State Chem.* **151**, 323 (2000).

[222] C. C. Homes, T. Vogt, S. M. Shapiro, S. Wakimoto, and A. P. Ramirez, *Science* **293**, 673 (2001).

[223] A. Podpirka and S. Ramanathan, *J. Electrochem. Soc.* **159**[2] H72 (2011).

[224] JCDPS Data #01-089-8308, #01-070-9274

[225] P. F. Miceli, C. J. Palmstrøn, and K. W. Moyers, *Appl. Phys. Lett.* **58**, 1602 (1991).

[226] S. Gariglio, N. Stucki, J.-M. Triscone, and G. Triscone, *Appl. Phys. Lett.* **90**, 202905 (2007).

[227] V. V. Vashook, N. E. Trofimenko, H. Ullmann, and L. V. Makhnach, *Solid State Ionics* **131** 329 (2000).

[228] A. Tselev, C. M. Brooks, S. M. Anlage, H. Zheng, L. Salamanca-Riba, R. Ramesh and M.A. Subramanian, *Phys. Rev. B* **70**, 144101 (2004).

[229] A. Podpirka and S. Ramanathan, *J. Appl. Phys.* **109**, 014106 (2011).

[230] C.-H. Mu, P. Liu, Y. He, J.-P. Zhou and H.-W. Zhang, *J. Alloys and Compounds* **471**[1-2] 137 (2009).

[231] C. C. Wang and L W. Zhang, *Appl. Phys. Lett.* **90**, 142905 (2007).

[232] V. Sachan, D. J. Buttrey, J. M. Tranquada, J. E. Lorenzo and G. Shirane, *Phys. Rev. B* **51** 12742 (1995).12742

[233] G. H. Aydogdu, S. D. Ha, B. Viswanath and S. Ramanathan, *J. Appl. Phys.* **109**, 124110 (2011).

[234] V. V. Vashook, S. P. Tolochko, I.I. Yushkevich, L.V. Makhnach, I. F. Kononyuk, H. Altenburg, J. Hauck and H. Ullmann, *Solid State Ionics* **110**[3-4] 245 (1998).

[235] J. J. Zhu, W. W. Li, Y. W. Li, Y.D. Shen, Z. G. Hu and J. H. Chu, *Appl. Phys. Lett.* **97**, 211904 (2010).

[236] Z. Tan, S.M. Heald, S.-W. Cheong, A.S. Cooper and A. R. Moodenbaugh *Phys. Rev. B* 47, 12365 (1993).

[237] J. Choisnet, R. A. Evarestov, I. I. Tupitsin and V. A. Veryazov *Physica Status Solidi (b)* **179**[2], 441 (1993).

[238] A. Podpirka and S. Ramanathan J. Appl. Phys. **109**, 014106 (2011).

[239] A. Yamada, Y. Suzuki, K. Saka, M. Uehara, D. Mori, R. Kanno, T. Kiguchi, F. Mauvy and J.-C. Grenier *Adv. Mater.* **20** 4124 (2008).

[240] V. V. Vashook, N. E. Trofimenko, H. Ullmann, and L.V. Makhnach *Solid State Ionics* **131** [3-4] 329 (2000).

[241] C. V. Thompson and R. Carel *J. Mech. Phys. Sol.* **44**[5] 657 (1996)

[242] B. Viswanath, C. Ko and S. Ramanathan *Phil. Mag.* **91** 4311 (2011).

[243] L. B. Freund and W. D. Nix *Appl. Phys. Lett.* **69**[2] 173 (1996).

[244] A. Chroneos, D. Parfitt, J. A. Kilner and R. W. Grimes *J. Mat. Chem.* **20** 266 (2010).

[245] J. M. Bassat, F. Gervais and P. Odier *Mar. Sci and Eng.* B3 *507 (1989).*

[246] M. Burriel, G. Garcia, J. Santiso, J. A. Kilner, R. J. Chater and S. J Skinner *J.Mat. Chem.* **18** 416 (2008).

[247] J. Santiso and M. Burriel *J. Sol. Sta. Electrochem* **15** 985(2011).

[248] F. Arrouy, J.-P. Locquet, E. J. Williams, E. Machler, R. Berger, C. Gerber, C. Monroux, J.-C. Grenier and A. Wattiaux *Phys. Rev. B* **54**[10]

[249] JCDPS Data #01-089-8308, #01-070-9274

[250] K. Momma and F. Izumi *J. Appl. Crystallogr.* **44** 1272 (2011).

[251] C. V. Thompson and R. Carel *Mat. Sci. and Eng. B* **32** 211 (1995).

[252] U.C. Oh, J. H. Je and J. Y. Lee *J. Mater. Res.***13**[5] 1226 (1998).

[253] U. C. Oh and J. H. Je *J. Appl. Phys.* **74**[3] 1693 (1993).

[254] D. Telesca, B. O. Wells, and B. Sinkovic *Surface Science* (2012) article in press

[255] E. Pellegrin, J. Zaanen, H. J. Lin, G. Meigs, C. T. Chen, G. H. Ho, H. Eisaki, and S. Uchida *Phys. Rev. B* 53[16] 10667 (1996).

[256] A. Travlos, N. Boukos, G. Apostolopoulos, A. Dimoulas and C. Giannakopoulos *Mat. Sci and Eng:B* **109**[1-3] 52 (2004).

[257] Krohns S, Lunkenheimer P, Kant Ch, Pronin A V, Brom H B, Nugroho A A, Diantoro M and Loidl A 2009 *Appl. Phys. Lett.* **94** 122903

[258]A. Podpirka A and S. Ramanathan *J. Appl. Phys.* **109** 014106 (2011).

[259] Subramanian M A, Li D, Duan N, Reisner B A, and Sleight A W 2000 *J. Solid State Chem.* **151** 323

[260] Liu X Q, Wu Y J and Chen X M 2010 *Solid State Ionics* **150** 1794

[261] Podpirka A and Ramanathan S 2011 *J. Appl. Phys.* **109** 014106

[262] W. Li and R. W. Schwartz *Phys. Rev. B* **75**, 012104 (2007).

[263] T.-T. Fang and H.-K. Shiau *J. Am. Ceram. Soc.* **87**[11] 2072 (2004).

[264] L. Houben *J. Mater. Sci.* **41** 4413 (2006).

[265] N. Wakiya, K. Kuroyagi, Y. Xuan, K. Shinozaki, N. Mizutani *Thin Solid Films* **357[2]** 166 (1999).

[266] A. Podpirka and S. Ramanathan *J. Electrochem. Soc*. **159**(2) H72 (2012).

[267] A. Podpirka, A. Tselev and S. Ramanathan (in preparation).

[268] T. Nakamura, K. Yashiro, K. Sato and J. Mizusaki *Solid State Ionics* **181** 292 (2010).

[269] V. V. Kharton, A. P. Viskup, A. V. Kovalevsky, E. N. Naumovich and F. M. B. Marques *Solid State Ionics* **143** 337 **(**2001).

[270] V. V. Kharton, A. P. Viskup, A. V. Kovalevsky, E. N. Naumovich, and F. M. B. Marques *Solid State Ionics* 143[3-4] 337 (2001).

[271] E. N. Naumovich and V. V. Kharton *J. Mol. Struct.: THEOCHEM* **946** 57 (2010).

[272] C. Frayret, A. Villesuzanne, and M. Pouchard *Chem. Mater.* **17**, 6538 (2005).

[273] M. Hucker, K. Chung, M. Chand, T. Vogtm J. M. Tranquada, and D. J. Buttrey *Phys. Rev. B* **70**, 064105 (2004).

[274] M. S. D. Read, M. S. Islam, G. W. Watson and F. E. Hancock J. Mat. Chem. **11** 2597 (2001).

[275] A. Aguadero, M. J. Escudero, M. Perez, J. A. Alonso, V. Pomjakushin and L. Daza *Dalton Trans.* 4377 (2006).

[276] J. Kawashima, Y. Yamada and I. Hirabayashi *Physica C: Superconducitivty* **306**[1-2] 114 (1998).

[277] H.-Y. Lee, H.-J. Liu, Y.-C. Liang, K.-F. Wu, and C.-H. Lee *J. Electrochem. Soc.*, **156**[8] G144 (2009).

[278] F. Mauvy, J.-M. Bassat, E. Boehm, J. P. Manaud, P. Dordor, J.-C. Grenier *Sol. Sta. Ion.* **158** 17 (2003).

[279] A. Podpirka and S. Ramanathan *J. Am. Cera. Soc.* **92**[10] 2400 (2009).